

# **HYDROTHERMALLY SYNTHESIZED FUNCTIONAL NANOMATERIALS FOR DIELECTRIC, TRIBOELECTRIC AND PHOTOCATALYTIC APPLICATIONS**

Thesis

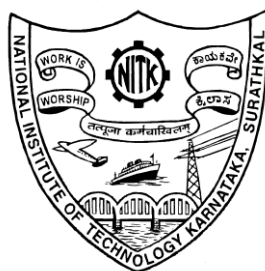
Submitted in partial fulfilment of the requirements for the degree of

**DOCTOR OF PHILOSOPHY**

By

**SUNIL**

(Registration No: 155065MT15F05)




DEPARTMENT OF METALLURGICAL AND MATERIALS  
ENGINEERING  
NATIONAL INSTITUTE OF TECHNOLOGY KARNATAKA,  
SURATHKAL, MANGALORE - 575025

OCTOBER, 2021



## DECLARATION

I hereby *declare* that the Research Thesis entitled “**HYDROTHERMALLY SYNTHESIZED FUNCTIONAL NANOMATERIALS FOR DIELECTRIC, TRIBOELECTRIC AND PHOTOCATALYTIC APPLICATIONS**” which is being submitted to the National Institute of Technology Karnataka, Surathkal in partial fulfillment of the requirements for the award of the Degree of **Doctor of Philosophy** in the Department of **Metallurgical and Materials Engineering**, is a *bonafide report of the research work carried out by me*. The material contained in this Research Thesis has not been submitted to any University or Institution for the award of any degree.



**SUNIL**

Registration number: 155065-MT15F05

Department of Metallurgical and Materials Engineering

Place: NITK, Surathkal

Date: 06-10-2021



## CERTIFICATE

This is to certify that the Research Thesis entitled "HYDROTHERMALLY SYNTHESIZED FUNCTIONAL NANOMATERIALS FOR DIELECTRIC, TRIBOELECTRIC AND PHOTOCATALYTIC APPLICATIONS" submitted by Mr. Sunil (Register Number: 155065MT15F05) as the record of the research work carried out by him, is *accepted as the Research Thesis submission* in partial fulfillment of the requirements for the award of degree of Doctor of Philosophy.

Research Supervisor

  
Prof. Udaya Bhat K.

Professor

Department of Metallurgical and Materials

Engineering

NITK Surathkal



Chairman- DRPC

Department of Metallurgical and Materials Engineering

NITK Surathkal

**Chairman - DRPC**  
Dept. of Metallurgical and Materials Engineering  
National Institute of Technology Karnataka, Surathkal  
Post Srinivasnagar, Mangaluru - 575 025  
Karnataka, India



**DEDICATED  
TO  
MY FAMILY....**





## ACKNOWLEDGEMENTS

I express my sincere thanks to the almighty whose divine intervention was instrumental in the proceedings of this work. I express my sincere gratitude to my mother-Smt. Lakshmibai, father-Virupakshappa Meti, sister-Sneha, wife-Smt. Ashwini Sunil Meti and my family for their constant and encouraging support throughout my doctoral study.

My sincere graceful acknowledgement to my research supervisor Prof. Udaya Bhat K., Professor, Department of Metallurgical and Materials Engineering, National Institute of Technology Karnataka Surathkal, for his valuable guidance, support and motivation throughout the research.

I would like to thank Prof. Narayan Prabhu, Head of the Department, Metallurgical and Materials Engineering, National Institute of Technology Karnataka Surathkal, for the constant encouragement and support. I would like take this opportunity to thank members of my research programme assessment committee (RPAC), Prof. Anandhan Srinivasan, Department of Metallurgical and Materials Engineering and Dr. Uday Kumar D., Department of Chemistry, National Institute of Technology Karnataka, Surathkal for their valuable suggestions and the comments during the progress and pre-synopsis seminars. I would also convey my sincere regards to Dr. Saumen Mandal, Dr. M. R. Rahman, Prof. Anandhan Srinivasan and other faculties, Department of Metallurgical and Materials Engineering, Prof. M. N. Satyanarayan, Department of Physics and Dr. Basavaraj Manu, Department of Civil Engineering, National Institute of Technology Karnataka, Surathkal for sharing their lab facility to carry out the experiments during my research work. I also express my sincere thanks to all the research colleagues of NITK Surathkal for their constant help and support and fruitful discussions on concepts.

I express my deep and sincere thanks to Dr. Pavan Pujar, Dr. Prashant Huilgol, Dr. Kishor Kumar M J, Dr. Komalkrushna Hadagalli, Dr. Jayalakshmi, Dr. Sanjeev Sangami, Mr. Uday Patil, Dr. Ningappa B. A., Mr. Vijaykumar A. S., Mr. Robbi Vivek Vardhan, Ms. Ashritha Salian, Dr. Anjan, Dr. Basavaraj N., Dr. Sachin, Dr. Mohammad Khalifa,

Mr. Prabhukumar C., Mr. Sudhish, Dr. Arun A., Dr. Nandan, Dr. Kiran, Mr. Chethankumar Gowda, Mr. Pandith, Dr. Deepak M. D., Mr. Hemanth, Dr. Anup S., Mr. Pramod K., Dr. Rajesh, Mr. Pandu, Dr. Arun Yadav, Mr. Sagar H P, Mr. Arun D. S., Mr. Akash, Mr. Pavan, Mr. Basavaraj P., Mr. Ravi, Mr. Aruna M. N., Mr. Govinda Ekbote, Mr. Mohan, for their help and constant support throughout my research work.

I am thankful to all the teaching staff of the Department of Metallurgical and Materials Engineering, National Institute of Technology Karnataka, Surathkal for constant support and help in various aspects of my course. I am thankful to the non teaching staff, Mr. Yashwanth, Mr. Dinesh, Mr. Satish, Mr. Lokesh, Mr. Sundar and Mr. Sachin, Department of Metallurgical and Materials Engineering, National Institute of Technology Karnataka Surathkal, for helping me directly/indirectly in carrying out my research work in the department. Special thanks to Mrs. Sharmila Dinesh and Mrs. Vinaya for helping me in necessary documentation at various stages of Ph.D. I extend my special thanks to Ms. Rashmi Banjan, Mr. Vinay, Mr. Manas, Mr. Vinayak for their support in conducting Scanning Electron Microscopic studies. Finally, I thank all those who directly and indirectly helped me to complete my research work.

SUNIL  
NITK Surathkal

## ABSTRACT

Hydrothermally synthesized functional nanomaterials are utilized for various applications. The functional nanomaterials, like  $\text{TiO}_2$ ,  $\text{La}_2\text{O}_3$ ,  $\text{ZnO}$ , GO and rGO/ZnO were synthesized and used for various applications, like parallel plate capacitor, triboelectric nanogenerators and photocatalytic applications. This method not only yielded nanomaterials with uniform dimensions, but also permitted to tailor the dimensions and morphologies. The materials were characterized to examine the structure, morphology and nature. The primary objective was to explore the potential of hydrothermally synthesized  $\text{TiO}_2$  in parallel plate capacitor applications. The flexibility of the  $\text{TiO}_2$  was achieved by incorporating  $\text{TiO}_2$  nanoparticles in Nylon-6 polymer. These materials were characterized to find the dielectric permittivity ( $\epsilon$ ) using impedance spectroscopy. The results showed that the  $\epsilon$  value is 124 at 1 kHz for Nylon-6/ $\text{TiO}_2$  polymer nanocomposites and 4472 at 1 kHz for hydrothermally grown unique microstructural films exhibiting colossal dielectric permittivity. The  $\text{La}_2\text{O}_3$ -based and  $\text{ZnO}$ -based triboelectric nanogenerator (TENG) devices were fabricated by screen-printing the hydrothermally synthesized  $\text{La}_2\text{O}_3$  and  $\text{ZnO}$  nanomaterials on copper foil (conductive substrate), respectively, with Teflon film (back coated on copper foil) as counter material. The TENG was subjected to mechanical motion by means of a in-house built motorized fixture. The maximum power density generated by  $\text{La}_2\text{O}_3$ -based TENG device was  $7.125 \text{ W/m}^2$  at an external load resistance of  $30 \text{ M}\Omega$  and  $\text{ZnO}$ -based TENG was  $0.58 \text{ W/m}^2$  at  $3 \text{ M}\Omega$ . The operation life-cycle of the TENG device was analyzed by decay in the voltage after prolonged cycle of operations. The decay in the voltage generated by the TENG devices was negligible after  $10^5$  cycles of tapping operations. The TENG device generated enough power and was capable to carry out the smooth functioning of the self-powered devices. The hydrothermally synthesized graphene oxide (GO) was used in the preparation of rGO/ZnO nanocomposites for the methyl orange dye degradation. The advantages of the hydrothermal synthesis of GO over Modified Hummers' method is the use of less harmful chemicals, less instrumentation and eco-friendly nature. The nanocomposite was capable of degrading the methyl orange with

almost equal kinetic rate constant ( $0.0523 \text{ min}^{-1}$ ) compared to the rGO/ZnO nanocomposite, where GO prepared following the Modified Hummers' method.

Low-cost, low-temperature, eco-friendly and industrial scalability are the main advantages of the hydrothermally synthesized functional nanomaterials, which can be further used in various applications.

**Keywords:** *Hydrothermal synthesis; low-temperature process; dielectrics; triboelectric nanogenerators; photocatalytic applications.*

## CONTENTS

ACKNOWLEDGEMENT	
ABSTRACT	
CONTENTS	i
LIST OF FIGURES	vii
LIST OF TABLES	xiv
NOMENCLATURE	xv
<b>CHAPTER 1. INTRODUCTION</b>	<b>1</b>
1.1 Capacitors	4
1.2 Introduction to Self-powered (triboelectric) Device Materials	8
1.3 Introduction to the Graphene Based-ZnO Nanocomposites for Photocatalytic Dye Degradation Applications	10
1.4 Hydrothermal Synthesis	11
1.5 Organization of the Thesis	13
<b>CHAPTER 2. LITERATURE REVIEW</b>	<b>15</b>
2.1 Theory of a Capacitor	17
2.1.1 Dielectrics	19
2.1.2 Nylon-6 (N6/Polycaprolactam)	22
2.1.3 Filler materials	25
2.1.4 Nylon-6 and titanium oxide (TiO <sub>2</sub> ) composites	28
2.2 Introduction to TENG Devices	29
2.2.1 The working principle of TENGs	31
2.2.1.1 <i>Vertical contact-separation mode</i>	32
2.2.1.2 <i>In-plane sliding mode</i>	33
2.2.1.3 <i>Single electrode mode</i>	33
2.2.1.4 <i>Free standing triboelectric-layer mode</i>	33
2.2.2 Applications of the TENGs	34

2.2.3	TENG materials	34
2.2.4	Zinc oxide based TENGs	34
2.2.5	Lanthanum oxide (La <sub>2</sub> O <sub>3</sub> ) based TENGs	38
2.3	Hydrothermal Synthesis of Graphene-Based ZnO Nanocomposites for Photocatalytic Applications	40
2.3.1	Graphene/graphene oxide	40
2.3.2	Advantages of GO	40
2.3.3	Different methods to synthesize graphene/GO	41
	<i>2.3.3.1 Bottom-up synthesis of large scale graphene oxide nanosheets</i>	41
	<i>2.3.3.2 Modified Hummers method</i>	42
	<i>2.3.3.3 Decisions on the synthesis of GO</i>	42
2.3.4	Zinc oxide and rGO-ZnO nanocomposites	43
2.3.5	Different methods to produce ZnO and rGO-ZnO nanocomposites	44
	<i>2.3.5.1 Hydrothermal method</i>	44
	<i>2.3.5.2 Microwave-assisted hydrothermal synthesis</i>	45
	<i>2.3.5.3 Electrochemical growth of the ZnO</i>	45
	<i>2.3.5.4 Sol-gel synthesis of the graphene-based ZnO</i>	46
2.3.6	Effect of synthesis parameters on morphology and dimensions	49
2.3.7	Microwave-assisted hydrothermal method	50
2.4	The Synthesis Route	52
	2.4.1 Factors influencing the hydrothermal synthesis of nanostructures	53
2.5	Objectives of the Work	53
2.6	Scope of the Study	54
	<b>CHAPTER 3. MATERIALS, METHODS, FUNCTIONAL DEVICE FABRICATION AND CHARACTERIZATION</b>	55

3.1	Materials	57
3.2	Synthesis of Functional Materials	57
	3.2.1 Synthesis and reinforcement of high permittivity TiO <sub>2</sub> in polymer nanocomposites	57
	3.2.2 Direct growth of high permittivity TiO <sub>2</sub> on the substrate	58
	3.2.3 Synthesis of lanthanum oxide (La <sub>2</sub> O <sub>3</sub> ) nanocrystals for screen printable paste in triboelectric energy generation	60
	3.2.4 Synthesis of zinc oxide (ZnO) nanoparticles for screen printable paste in triboelectric energy generation	61
	3.2.5 Synthesis of graphene oxide (GO), ZnO and reduced graphene oxide (rGO)-ZnO for photocatalytic studies	62
	3.2.5.1 <i>Synthesis of GO</i>	62
	3.2.5.2 <i>Synthesis of rGO-ZnO nanocomposites</i>	63
3.3	Thin Film Fabrication	63
	3.3.1 Fabrication of Nylon-6/TiO <sub>2</sub> composite polymer thin films for dielectrics applications	63
	3.3.2 The direct growth of TiO <sub>2</sub> thin film on glass/FTO substrate for dielectrics applications	65
	3.3.3 Fabrication of screen printed La <sub>2</sub> O <sub>3</sub> thin films for triboelectric applications	65
	3.3.4 Fabrication of screen printed ZnO thin films for triboelectric applications	65
3.4	Applications of Various Functional Materials	66
	3.4.1 High permittivity dielectrics application	66
	3.4.2 Triboelectric characterization of screen-printed films	66
	3.4.3 Observation of photocatalytic activity of bare-ZnO and rGO-ZnO	67
3.5	Characterization Techniques Employed in the Present Study	68
	<b>CHAPTER 4. DIELECTRIC BEHAVIOUR OF NYLON-6/TITANIUM DIOXIDE POLYMER COMPOSITE</b>	<b>73</b>
4.1	Introduction	75

4.2	Electron Microscopic Analysis of the Synthesized TiO <sub>2</sub> Nanoparticles	76
4.3	Structural Analysis of TiO <sub>2</sub> and NT Polymer Nanocomposites	79
4.4	Raman Spectroscopic Analysis of NT Polymer Nanocomposites	80
4.5	Chemical Composition of NT Polymer Nanocomposites Using XPS	80
4.6	FTIR Analysis of NT Polymer Nanocomposites	82
4.7	Thermal Analysis of NT Polymer Nanocomposites Using DSC	83
4.8	Frequency Dependence Dielectric Study of NT Polymer Nanocomposites	84
4.9	Summary and Conclusions	87
	<b>CHAPTERS 5. SINGLE STEP GROWTH OF POROUS TITANIUM OXIDE VIA THE HYDROTHERMAL METHOD</b>	89
5.1	Introduction	91
5.2	Structural Analysis of the TiO <sub>2</sub> Films	93
5.3	Electron Microscopic Analysis of TiO <sub>2</sub> Films	96
5.4	Raman Spectroscopic Analysis of the TiO <sub>2</sub> Films	98
5.5	XPS Analysis of the TiO <sub>2</sub> Film	98
5.6	BET Analysis of TiO <sub>2</sub> Sample (T2)	100
5.7	Thermal Analysis of TiO <sub>2</sub> Films	100
5.8	Studies on Dielectric Permittivity of TiO <sub>2</sub> Films	101
5.9	Conclusions	104
	<b>CHAPTER 6. ASSESSMENT OF TRIBOELECTRIC PROPERETY OF DIFFERENT NANOCRYSTALS PREPARED BY HYDROTHERMAL TECHNIQUE</b>	105
6.1	Introduction.	107
6.2	Results and Discussion of Triboelectric Property Assessment of La <sub>2</sub> O <sub>3</sub> Nanocrystals	109
	6.2.1 Morphology of La <sub>2</sub> O <sub>3</sub> nanocrystals	109



6.2.2	Morphology of La <sub>2</sub> O <sub>3</sub> screen-printed film	111
6.2.3	Crystal structure of La <sub>2</sub> O <sub>3</sub> using XRD	112
6.2.4	Chemical composition of La <sub>2</sub> O <sub>3</sub> nanocrystals using XPS	113
6.2.5	BET surface area analysis	114
6.2.6	Identification of chemical bonding by FTIR	115
6.2.7	DSC spectrum of lanthanum oxide nanoparticles	116
6.2.8	Raman spectrum of lanthanum oxide nanoparticles	116
6.2.9	Output characteristics of triboelectric nanogenerators	117
6.3	Results and Discussion of Triboelectric Property Assessment of ZnO Nanoparticles	119
6.3.1	Morphology of ZnO nanoparticles	119
6.3.2	XRD characteristics of ZnO nanoparticles	121
6.3.3	Rietveld refinement study of ZnO nanoparticles	122
6.3.4	SEM micrographs of screen printed ZnO film	123
6.3.5	XRD spectrum of screen printed ZnO film	124
6.3.6	Triboelectric property assessment of ZnO film	124
6.4	Conclusions	126
	<b>CHAPTER 7. PHOTOCATALYTIC ACTIVITY OF REDUCED GRAPHENE OXIDE – ZINC OXIDE NANOCOMPOSITES</b>	129
7.1	Introduction	131
7.2	Characterization of Hydrothermally Synthesized GO	132
7.3	The Structural Characterization of the rGO-ZnO Nanocomposite	135

7.4	Chemical Composition Analysis of rGO-ZnO Nanocomposites Using XPS	137
7.5	Raman Spectroscopic Analysis of rGO-ZnO and ZnO	139
7.6	Morphological Analysis of rGO-ZnO Nanocomposites Using FESEM and TEM	140
7.7	Growth Mechanism of the ZnO and rGO-ZnO Nanorods During Microwave Heating	141
7.8	Dye Degradation Studies Using rGO-ZnO and ZnO	143
7.9	Photocatalytic Performance Comparison of rGO-ZnO Prepared from Different Zinc Precursors	145
7.10	Photocatalytic Degradation Performance Comparison of rGO-ZnO Nanocomposites with GO Prepared from Tang Lau Method and Hummer's Method	146
7.11	The Recycling Ability of rGO-ZnO Nanocomposites	147
7.12	Conclusions	148
	<b>CHAPTER 8. SUMMARY AND CONCLUSIONS</b>	149
	<b>REFERENCES</b>	155
	<b>LIST OF PUBLICATIONS</b>	191
	<b>BIO DATA</b>	193

## LIST OF FIGURES

Fig. 1.1	The schematic showing the hydrothermal technique for synthesizing various nanoparticles	12
Fig. 2.1	Schematic representation of a parallel plate capacitor	17
Fig. 2.2	Symbolic representation of (a) electrostatic capacitor and (b) electrochemical capacitor	19
Fig. 2.3	Orientations of polar dipole molecules when (a) $\vec{E}_0 = 0$ and (b) $\vec{E}_0 \neq 0$	20
Fig. 2.4	Orientations of the non-polar dipole molecules when (a) $\vec{E}_0 = 0$ and (b) $\vec{E}_0 \neq 0$	21
Fig. 2.5	FTIR spectra of electrospun pure Nylon-6 and its variants	23
Fig. 2.6	(a) Caprolactam molecule, (b) the ring opening polymerization reaction from the caprolactam molecule to Nylon-6	23
Fig. 2.7	An example for core shell nanoparticle; TEM micrograph of the titanium core and the titanium oxide shell	27
Fig. 2.8	An example for the core shell nanoparticle; the TEM micrograph of aluminium nanoparticle with the aluminium oxide ( $\text{Al}_2\text{O}_3$ ) shell (thickness 2.8 nm) casing and the aluminium core	27
Fig. 2.9	Schematic representation of the alternate layer deposition for PNCs	28
Fig. 2.10	(a) A cross-sectional schematic representation of PNC based capacitor with a thickness of each layer of the dielectric, (b) the corresponding schematic showing micro capacitor network within the device and (c) the variation of dielectric constant with thickness $t$ of the deposited nylon-6 layer in Ti-PNC and Ag + Ti-PNC based capacitors at 1 kHz and 40 °C	28
Fig. 2.11	Four working modes of triboelectric nanogenerator: (a) vertical contact-separation mode, (b) in-plane sliding mode, (c) single electrode mode and (d) free standing triboelectric-layer mode	32

Fig. 2.12	Schematics of the ZnO based TENG device fabrication process	35
Fig.2.13	Schematic representation of fabricated TENG device consisting of ZnO microballoons grown on PDMS film coated with the PTFE on the acrylic substrate	36
Fig. 2.14	The SEM micrographs of (a) PDMS film showing pyramid pattern and (b) ZnO microballoons grown on the PDMS pyramids	37
Fig. 2.15	SEM micrograph of the hydrothermally synthesized ZnO using zinc nitrate and NaOH aqueous solution as reagents at 80 °C	49
Fig. 2.16	SEM micrograph of the hydrothermally synthesized ZnO using zinc nitrate and NaOH aqueous solution as reagents at 180 °C	50
Fig. 2.17	SEM micrograph of the ZnO nanoparticles, synthesized by microwave assisted hydrothermal method using NaOH as reagent at 700 W power	51
Fig. 2.18	FESEM micrograph of the rGO/ZnO synthesized by microwave assisted hydrothermal method using NaOH as reagent	51
Fig. 3.1	Flowchart of synthesis procedure followed for the synthesis of TiO <sub>2</sub> nanoparticles	58
Fig. 3.2	Pictorial representation of the TiO <sub>2</sub> film growth on the FTO coated glass slide for dielectric application	59
Fig. 3.3	(a) Schematic representation of synthesis procedure for the La <sub>2</sub> O <sub>3</sub> and fabrication of TENG device by using screen-printing technique and (b) flowchart for the synthesis procedure of La <sub>2</sub> O <sub>3</sub> nanocrystals.	60
Fig. 3.4	Schematic representation of step-by-step procedure for the synthesis and fabrication of the ZnO based TENG device	61
Fig. 3.5	Schematic representation of the hydrothermally synthesized GO in the preparation of microwave hydrothermal synthesis of rGO-ZnO nanocomposite	62
Fig. 3.6	Schematic representation of the thin film fabrication of the Nylon-6/TiO <sub>2</sub> on the FTO coated glass slides	64

Fig.3.7	Architecture and working principle of contact-separation mode triboelectric device	67
Fig. 3.8	Figure showing the schematic representation of the impedance measurement	70
Fig. 3.9	Pictorial representation of the triboelectric properties assessment using motorized fixture	71
Fig. 4.1	(a-d) Scanning electron micrographs of TiO <sub>2</sub> nanoparticles at different magnifications (e & f) histogram of variation of crystallite size distribution, (g-i) low and high magnification transmission electron micrographs depicting size, shape and fringe pattern of TiO <sub>2</sub> nanorods, (j) SAED pattern and (k) TEM-EDS spectrum of TiO <sub>2</sub> nanorods.	78
Fig. 4.2	The XRD spectra of NT5, NT10, NT20 and pure TiO <sub>2</sub> nanoparticles	79
Fig. 4.3	Raman spectra showing characteristic bands of the TiO <sub>2</sub> in the NT polymer nanocomposites	80
Fig. 4.4	XPS survey spectrum of (a) NT polymer nanocomposite showing the presence of only C, O, N and Ti elements, (b) Ti 2 <i>p</i> , (c) O 1 <i>s</i> , (d) C 1 <i>s</i> and (e) N 1 <i>s</i>	81
Fig. 4.5	The FTIR spectra of NT5, NT10 and NT20 polymer nanocomposites	82
Fig. 4.6	The DSC spectra show the NT nanocomposite samples with different weight fractions of the TiO <sub>2</sub> filler	83
Fig. 4.7	Schematic representation of the parallel plate capacitor device for impedance testing	84
Fig. 4.8	The cross sectional SEM micrograph of the spin coated NT polymer nanocomposite film	84
Fig. 4.9	The graph showing frequency dependency of (a) dielectric constant, (b) schematic illustration of variation of dielectric constant at 1 kHz and 1 MHz frequency, (c) dielectric loss and (d) AC conductivity of NT polymer nanocomposites for different samples	85

Fig. 5.1	XRD spectra of TiO <sub>2</sub> samples (a) T1 (150 °C) and T2 (180 °C) and corresponding Rietveld refined pattern of (b) T1 sample (synthesized at 150 °C) and (c) T2 sample (synthesized at 180 °C), respectively, (d) T sample (synthesized at 120 °C) and (e) schematic representation of crystallographic structure of tetragonal anatase phase TiO <sub>2</sub> (blue atoms are titanium and red atoms are oxygen)	93
Fig. 5.2	SEM micrographs of porous flower-like TiO <sub>2</sub> microstructure for samples at T (120 °C) (a, b and c), T1 (150 °C) (d, e, and f) and T2 (180 °C) (g, h and i) at different magnifications, (j) SEM-EDS of TiO <sub>2</sub> sample and (k) schematic representation of the crystallographic structure of TiO <sub>2</sub> grown on FTO coated glass	97
Fig. 5.3	Raman spectrum showing the characteristic bands of TiO <sub>2</sub> anatase phase for the samples T1 (150 °C) and T2 (180 °C)	98
Fig. 5.4	(a) The XPS survey spectrum of the TiO <sub>2</sub> sample, (b) core level 2p spectrum of titanium and (c) core level 1s spectrum of oxygen	99
Fig. 5.5	The BET surface area estimations for TiO <sub>2</sub> sample synthesized at 180 °C for 24 h constant heating	100
Fig. 5.6	The TGA weight loss curves for T1 (150 °C) and T2 (180 °C) TiO <sub>2</sub> samples	101
Fig. 5.7	(a) The schematic representation of crystallographic structure of TiO <sub>2</sub> -dielectric material grown on FTO coated glass in parallel plate capacitor setup, (b) variation of dielectric constant against frequency for TiO <sub>2</sub> samples, (c) schematic representation of variation of dielectric constant for T1 and T2 TiO <sub>2</sub> samples and (d) graphical abstract showing variation of dielectric constant for T1 and T2 samples at 1 kHz and 1 MHz	102
Fig. 5.8	The plots of (a) dielectric loss and (b) conductivity vs. frequency for the T1 and T2 TiO <sub>2</sub> samples	103
Fig. 6.1	Morphology of La <sub>2</sub> O <sub>3</sub> nanocrystals captured using, (a) & (b) SEM, (c) TEM, (d) corresponding magnified high-resolution micrograph and (e) selected area electron diffraction (SAED) ring depicting the polycrystalline nature of La <sub>2</sub> O <sub>3</sub> nanocrystals	110
Fig. 6.2	(a) SEM morphology of La <sub>2</sub> O <sub>3</sub> screen printed film on copper foil, (b) photograph of La <sub>2</sub> O <sub>3</sub> screen printed film on copper foil and (c)	111

	cross sectional SEM micrograph showing the film thickness	
Fig. 6.3	(a) The XRD spectrum of hydrothermally synthesized $\text{La}_2\text{O}_3$ nanocrystals, (b) the crystal structure of $\text{La}_2\text{O}_3$ (green-lanthanum and red-oxygen) and (c) the crystal structure of $\text{La}_2\text{O}_3$ on copper (Blue-copper, red-oxygen and green-lanthanum)	112
Fig. 6.4	XPS spectra of the $\text{La}_2\text{O}_3$ showing both (a) low and high-resolution scans, (b) La 3d region and (c) O 1s region	113
Fig. 6.5	Nitrogen ( $\text{N}_2$ ) adsorption/desorption isotherms for $\text{La}_2\text{O}_3$ nanocrystals	114
Fig. 6.6	FTIR analysis of $\text{La}_2\text{O}_3$ nanocrystals	115
Fig. 6.7	DSC spectrum of lanthanum oxide	116
Fig. 6.8	The Raman spectrum of $\text{La}_2\text{O}_3$ nanocrystals	116
Fig. 6.9	(a) The schematic of TENG device circuit connection, the characteristic electrical output of the $\text{La}_2\text{O}_3$ triboelectric device showing its dependency of (b) voltage and (c) power output on external load resistance	117
Fig. 6.10	The schematic representation of fluorine tending to hold the electrons in the carbon-fluorine bonds closely to itself, creating highest electron negative polarity over the surface	118
Fig. 6.11	(a) and (b) high resolution SEM micrographs, (c) and (d) particle size distribution with Gauss fit for length and diameter of the ZnO nanoparticles and (e) SEM-EDS spectrum of ZnO nanoparticles	120
Fig. 6.12	The XRD spectrum of ZnO nanoparticles	121
Fig. 6.13	(a) Rietveld refined XRD spectra of the ZnO nanoparticles and (b) crystallographic atomic structure of the ZnO (red colour-oxygen and grey colour-zinc)	122
Fig. 6.14	(a) SEM micrographs of screen-printed ZnO (b) cross sectional SEM micrographs of ZnO film showing the thickness	123
Fig. 6.15	(a) The XRD spectrum of screen-printed ZnO film on copper tape and (b) the crystal structure of screen-printed ZnO on the copper	124

(Blue-copper, red-oxygen and grey-lanthanum)

- Fig. 6.16 (a) Dependence of voltage, current and the peak power output on the external load resistance (The points represent peak value of electric signals while lines are fitted results), (b) Durability test for TENG active layer: voltage waveform at the beginning, after 25,000 cycles, 50,000 cycles, 75,000 cycles and one lakh cycles of operation and (c) image of the screen-printed ZnO tribo active layer after one lakh cycles of operation 125
- Fig. 7.1 (a) Raman spectrum, (b) FTIR spectrum, (c) XRD spectrum, (d) SEM and (e) TEM micrographs of the hydrothermally synthesized GONs 134
- Fig. 7.2 (a) rGO-ZnO nanocomposite and ZnO XRD pattern, (b) Rietveld refined XRD spectra of rGO-ZnO nanocomposite, (c) Synchrotron XRD pattern and (d) magnified image of the synchrotron XRD pattern showing the presence of the carbon species, graphene (<10%), in the rGO-ZnO nanocomposite 136
- Fig. 7.3 (a) X-ray photoelectron survey spectrum and high-resolution responses of (b) Zn 2*p*, (c) O 1*s* and (d) C 1*s* of rGO-ZnO nanocomposite 138
- Fig. 7.4 Raman spectra of the ZnO and the rGO-ZnO nanocomposite 139
- Fig. 7.5 (a) FESEM micrograph presenting morphology of the rGO-ZnO nanocomposite, (b) and (c) TEM micrographs of the microwave-assisted hydrothermally synthesized rGO-ZnO nanocomposite showing ZnO nanorods decorated with rGO, (d) TEM micrograph with selected area electron diffraction (SAED) pattern and (e) TEM-energy dispersive spectroscopy (EDS) of the rGO-ZnO nanocomposite 141
- Fig. 7.6 (a) The absorbance spectra of the MO aqueous solution in rGO-ZnO composite after different irradiation time, (b) photocatalytic degradation of the MO aqueous solution in the presence of the rGO-ZnO and the ZnO and (c) the graphical abstract showing the mechanism of MO dye degradation using rGO-ZnO nanocomposite in presence of UV light source. 143
- Fig. 7.7 The comparison of absorbance spectra of the MO aqueous solution in the presence of the rGO-ZnO nanocomposite prepared using 145



zinc chloride and zinc nitrate after different UV irradiation times

- Fig. 7.8 The comparison of absorbance spectra of the MO aqueous solution in the presence of the rGO-ZnO nanocomposite prepared using GO synthesized from Tang Lau method and Hummer's method 146
- Fig. 7.9 The recycling ability of rGO-ZnO nanocomposite for MO aqueous solution 147

## LIST OF TABLES

Table 2.1	Dielectric constants of different materials	21
Table 2.2	Triboelectric materials	30
Table 2.3	Table of comparison for TENG power density for different materials	37
Table 2.4	Comparison of photocatalytic conditions and performance of GO/rGO based ZnO nanocomposites in degrading organic dyes	47
Table 5.1	The refined parameters and crystal data of T1 and T2 TiO <sub>2</sub> samples	94
Table 6.1	Reported specific surface area of La <sub>2</sub> O <sub>3</sub> nanocrystals	114
Table 6.2	Respective elemental composition of ZnO nanoparticles (in Fig. 6.11 (a)) obtained from the SEM-EDS spectrum is tabulated	120
Table 6.3	The refined parameters and crystal data of ZnO nanoparticles	122
Table 7.1	Variables in the preparation of GO by hydrothermal method	133

## NOMENCLATURE

<b>Symbols</b>	<b>Abbreviations</b>
nm	Nanometer
W	Watt
K	Kelvin
M	Meter
Pa	Pascal
N	Newton
G	Gram
°C	Degree Celsius
$\Theta$	Diffraction angle
K	Dielectric constant
kHz	Frequency in kilo Hertz
M	Molarity
Rpm	Rotation per minute
eV	Electron volt
GPa	Giga Pascal
La(OH) <sub>3</sub>	Lanthanum hydroxide
KMnO <sub>4</sub>	Potassium permanganate
Q	Charge
C	Capacitance
$\epsilon_0$	Absolute permittivity
$\epsilon_r$	Relative permittivity
F	Farad
V	Volt
C	Coulomb charge

E	Electric field strength
$\epsilon$	Permittivity of the material
W	Work done to remove charge from one plate
$\Omega$	Ohm
$\mu\text{m}$	Micrometer
J	Joules
$\vec{E}$	Electric field
e	Charge of electron
mL	Millilitre
Bar	Unit of pressure
$\text{\AA}$	Angstrom, $10^{-10}$ meter
s	Second
PVDF	Polyvinylidene fluoride
GO	Graphene oxide
rGO	Reduced graphene oxide
N6	Nylon-6 polymer
PTFE	Polytetrafluoroethylene
PDMS	Polydimethylsiloxane
PMMA	Poly(methyl methacrylate)
RTP	Rapid thermal processing
CVD	Chemical vapour deposition
PNCs	Polymer nanocomposites
meV	milli electron volts
H	Hours
MHz	Mega Hertz

# CHAPTER 1

*Page intentionally left blank*

## CHAPTER 1

### INTRODUCTION

*This chapter gives a brief introduction about the various materials used in the energy (dielectric and triboelectric) and photocatalyst materials. Further, different routes to synthesize the functional nanomaterials for such applications are briefed. Finally, the importance and characteristic features of the hydrothermal method in the synthesis and preparation of functional nanomaterials is detailed.*

Nanomaterials play a pivotal role in the devices and applications. Nanomaterials are defined as materials having any-one external dimension measuring below 100 nm (Motta et al. 2010). Nanomaterials are now being used in the everyday life. The demand for industrial machinery, advanced medical devices, sensors and thin film-electronic devices has increased tremendously due to the increased comfort life of human being. To synthesize these nanomaterials, various synthesis techniques have been proposed, over the years. Amongst them, the hydrothermal technique is a simple and low cost method. It offers benefits of uniform control of size and shape for the nanoparticles, takes less time and a low-temperature process. According to heating methods, the method is divided into conventional hydrothermal and microwave-assisted hydrothermal techniques. In the conventional hydrothermal method, the nanoparticles are synthesized by precipitation or by a direct mixture of metal salts with a base solution. The solution is transferred to the Teflon cup, sealed in a stainless steel autoclave and heated in a hot air oven. In the microwave-assisted hydrothermal heating, the heat is internally generated within the material with the assist of microwave sources (Möhmel et al. 2002). This method increases the reaction kinetics, and hence, it is a low energy and less time required operation. This method is carried out at low temperature, which yields uniform and high purity nanoparticles (Motta et al. 2010). The hydrothermally synthesized nanomaterials have found their usage in many applications, like gas sensors, functional dielectrics, active materials for lithium-ion batteries, piezoelectric and triboelectric materials, photocatalytic materials, self-cleaning coatings, solar cells, bio-medical applications.

The human race for its comforts is now concentrating on automation of all the equipments/machines. Electricity is the most essential need of the automation process. The energy requirement for such devices is a challenging task in the present scenario. The need for the storage of energy and self-powering devices has opened many challenging areas for research. Out of these, one major thrust area is the development of energy storage and self-powered devices with compact size, high shelf life, compatibility to versatile applications and flexibility. The capacitors and self-powered devices, like piezoelectric and triboelectric devices can be used as an energy source for thin film and flexible nano devices. The hydrothermally synthesized nanomaterials are the best-suited materials for these applications (Darr et al. 2017; Kango et al. 2013; Kolodziejczak-Radzimska and Jesionowski 2014; Low et al. 2017; Rui et al. 2014; Shandilya et al. 2016; Xiao et al. 2014a).

## **1.1 Capacitors**

Capacitors are the electrical energy storage elements in the circuits. They are divided into two main categories, electrochemical and electrostatic capacitors. In electrochemical capacitors (or supercapacitors), two electrodes are separated by an electrolyte. The electrolyte assists in the transferring and balancing charges between the electrodes. The electrochemical capacitors are also called as electrical double-layer capacitor (EDLC) or supercapacitors or ultracapacitors. Here, the electrodes used are made up of high surface area carbon (*i.e.*, graphite). The electrical charge is stored at the surface-electrolyte interface of the carbon electrodes. In contrast, the electrostatic capacitor uses two parallel plate electrodes separated by a dielectric material. The most commonly used dielectrics are oxides of metals (silicon dioxide, hafnium oxide, aluminum oxide etc.), nitrides, carbides, polymers and composites (Srinivasan and Bandyopadhyay 2017)). The electrostatic capacitors are non-hazardous compared to the electrochemical capacitors. It is attributed to the use of dielectrics in the place of electrolytes; which are susceptible to fire hazards. In order to fabricate compact size capacitors, the research is focused on reducing the thickness of the dielectric material of the electrostatic capacitor. With the development of nanoscience and nanotechnology, significant attention is being paid towards nanomaterials for preparing these dielectric materials. The efficiency of the electrical



charge storage capacity of the capacitor is mainly dependent on the dielectric materials. The large capacitance of a capacitor is the outcome of a thin dielectric with a large dielectric constant. In contrast, the thickness scaling of the dielectric is limited by the adverse current flow through it, termed as leakage current (Liu et al. 2018). The increased magnitude of leakage current leads to the breakdown of the capacitor. The advancements in nanomaterials and nanocomposites, in particular, have resulted in the retainment of high capacitance with minimum leakage current. The nanomaterials of different morphologies, like nanorods, nanofibres, nanoneedles, nanospindles, nanospheres, nanotubes, nanolayers are studied and found to have different properties (Avinash B et al. 2016; Béguin et al. 2014; Nan 2001a; Siddabattuni and Schuman 2014).

The ceramic nanoparticles, like BaTiO<sub>3</sub>, TiO<sub>2</sub>, Al<sub>2</sub>O<sub>3</sub> and ZnO have been examined as dielectric materials to fabricate high-strength thin film capacitors due to high dielectric constant ( $\kappa$ ) (Amoghavarsha et al. 2014; Jianwen et al. 2006; Mahadevegowda et al. 2014). Amongst them, TiO<sub>2</sub> is a well-studied oxide material as it is chemically stable, easily available and cost-effective (Mahadevegowda et al. 2015). The TiO<sub>2</sub> possesses unique physical and chemical characteristics with abundance in availability and nontoxicity, as well as high thermal and chemical stability (Tao et al. 2012). The TiO<sub>2</sub> is used in areas, like gas sensors, biomedical implants, self-cleaning glasses, dye-sensitized solar cells, cosmetics and photocatalytic applications (Fan et al. 2014; Lee and Sung 2012; Low et al. 2017; Pai et al. 2014; Ben Yahia et al. 2009). Besides, the TiO<sub>2</sub> is actively used in integrated optics and electronics (Atuchin et al. 2005, 2018; Hu et al. 2018; Kalabin et al. 2003). The TiO<sub>2</sub> possesses three different crystalline modifications, namely, anatase, rutile and brookite (Low et al. 2017; Sajan et al. 2016).

There are varieties of TiO<sub>2</sub> synthesis techniques reported, namely, sol–gel, combustion synthesis, sputtering, hydrothermal synthesis, etc. (Jin et al. 2006; Kruchinin et al. 2017; Meti et al. 2015; Troitskaia et al. 2012). Amongst these, the hydrothermal synthesis technique has unique advantages, such as uniform crystal growth, less instrumentation, rapid and easy method (Cheng et al. 2014a; Sajan et al. 2016). In the hydrothermal method, the morphology, microstructure and phase

composition of the TiO<sub>2</sub> are easily altered by varying the process parameters (Cheng et al. 2014a). Different morphologies of the TiO<sub>2</sub> and their properties are reviewed in the literature (Sajan et al. 2016). The TiO<sub>2</sub> material is already been tested as a superior dielectric material (Avinash B et al. 2016; Gritsenko et al. 2006; Kalygina et al. 2016, 2017). The TiO<sub>2</sub> is a high dielectric constant material with a dielectric constant ranging from 12-114 (Mahadevegowda et al. 2015). TiO<sub>2</sub> is to be moulded into different shapes in the case of various electronic thin film applications (Džunuzović et al. 2009; Jin et al. 2013; Liu et al. 2012a; PRATAP et al. 2013; Qi et al. 2014; Qureshi et al. 2009; Ramadoss and Kim 2013; Yang and Kofinas 2007). The low mechanical strength, hardness and high sintering temperature limit the applicability of the ceramic nanoparticles as dielectric materials. The TiO<sub>2</sub>-polymer nanocomposites are explored to overcome these limitations. The TiO<sub>2</sub> nanoparticles are characterized by good dispersion in the polymer matrix and it results in uniformity of the properties (Agrawal et al. 2014; Džunuzović et al. 2009; Grabowski et al. 2016; Wang et al. 2017; Xu et al. 2017; Yang and Kofinas 2007).

The polymer nanocomposites (PNCs) have emerged as one of the promising classes of nanomaterials. A wide range of polymers are used as matrix materials in PNCs. Some of them are polyethylene, polyaniline, polypropylene, polycaprolactam, polyvinyl difluoride, etc (Hashim et al. 2016). The application of the PNCs as the dielectric material in electrostatic capacitors has many advantages, like flexibility, low cost, low density and ease of processing (Srinivasan and Bandyopadhyay 2017). The PNCs are used as high-performance materials at low electric potential and current across variable frequencies. The PNCs can be readily cast into thin films with high specific surface area. The PNCs possess a breakdown strength as high as  $\sim 10^5$  kV/m (Dang et al. 2003). The polymers are good insulators owing to their wide band gap of 2 eV - 7 eV between the valence and conduction bands (Qi et al. 2014). The nano-fillers in the polymer-ceramic composites form a “micro-capacitor network” within the material which enhances the effective dielectric constant observed around the current percolation threshold (Dang et al. 2003, 2007; He et al. 2009; Huang et al. 2003, 2009; Pecharromás and Moya 2000; Shen et al. 2007; Xu and Wong 2005; Zhao et al. 2009). The presence of nanoscale filler materials in the polymer matrix is

responsible for the excellent breakdown strength shown by the PNCs (Callister 2002 and Dissado 1992).

The polycaprolactam (Nylon-6/N6/PA6) possesses good mechanical, chemical and thermal properties. Nylon-6 (N6) is an extensively used synthetic polymer comprising of polyamides group (Dong et al. 2008). From the literature, it has been seen that N6 is used in many fields, like fabrics, automotive, electronic, medicine, insulating material and commercial applications. The N6 polymer is of great interest due to its high mechanical and chemical stability, excellent stability to human body fluid, water-resistance nature, and high dimensional stability. The dielectric properties of N6 are of special interest due to its partial crystallinity and complex structure (Mahadevegowda et al. 2015). According to the semi-crystallinity of the N6, the polymer chains at some regions are highly ordered, while, in other regions, the material is amorphous. This property of the N6 enhances the dielectric strength as well as exhibits complicated dielectric relaxation behaviour. These characteristic features of the N6 polymer are also improved by the addition of some inorganic fillers and thus formed end product based on the N6 polymer which is tailored to particular applications (Rusu and Rusu 2011). The carboxyl and amino groups present in N6 interact with the ceramic fillers with hydrogen bonding while forming ceramic-polymer nanocomposites (Kango et al. 2013).

Combining N6 with the filler materials, like two-dimensional graphene oxide nanosheets and metal oxide nanoparticles have shown good potential to be used as dielectric materials. The use of nanofillers with less volume fraction in the N6 matrix raises the dielectric constant of the composites. The overall capacitance also increases with such composite dielectric materials (Mahadevegowda et al. 2015). Various nanofillers are tested for N6 PNCs as dielectric material (O'Neill et al. 2014). They have shown promising results for N6 to be highly recommended polymer matrix in PNCs for dielectric applications. Due to various advantages of N6 based composites, we have chosen N6 matrix and high dielectric strength  $\text{TiO}_2$  as filler material to prepare composites with high flexibility, permittivity and strength. The potential polymer-ceramic nanocomposite,  $\text{TiO}_2/\text{Nylon-6}$  (NT) heterogeneous system, is chosen to enhance the flexibility of  $\text{TiO}_2$ . The semicrystalline polymer N6 with  $\text{TiO}_2$

inorganic fillers have not been explored explicitly. Based on these observations, we made attempt to fabricate Nylon6/TiO<sub>2</sub> composite dielectric film with improved dielectric properties. The attempt is also made to fabricate the parallel plate capacitor from the directly grown unique morphological flower-like structure on the conductive substrate with high surface area TiO<sub>2</sub> film.

## **1.2 Introduction to Self-powered (Triboelectric) Device Materials**

The hunt for renewable energy is tremendously growing due to the depletion of fossil fuels and to reduce the global warming due to carbon emissions. Self-powered devices are the answers for such renewable energy powering applications. The devices which require less power wattage (in terms of milli to micro watts) can be powered with such mechanisms. Vibration is a common mechanical motion in daily life in different forms, from the heart pulse to body motions. The vibration energy can be used to power the self-powered devices. The self-powered device can be used as an alternative to battery-operated devices. The mechanism of vibration energy harvesting can be transduced into electrical energy based on the electromagnetic effect, electrostatic effect and piezoelectric effect. These techniques have many limitations, like structural complexity, reliance on an external source and high-quality materials. The devices have a major drawback that they can work only under a low-frequency range (below a few hundred hertz). With the presently available mechanism and device architecture parameters, it's necessary to fabricate and evaluate the different materials producing maximum power output. The triboelectric nanogenerator (TENG) is a new technology invented in 2012 by Wang's group (Fan et al. 2012). The most fundamental theory of TENG is based on Maxwell's displacement current. The term polarization induced current is directly related to the output current of the TENG. The triboelectric devices work on the principle of contact electrification and electrostatic induction of charges on the surface of the two dissimilar materials. Triboelectric devices are used as self-powered devices, due to their advantages, like simple device fabrication, high efficiency, cost-effective and large power output. The triboelectric performance undergoes negligible decay even after 10<sup>6</sup> cycles of operation. The triboelectric is a surface phenomenon. The working principle of the triboelectric device is explained further.

The two dissimilar materials via physical contacts develop electrostatic charges on their surfaces. The electric potential difference can be induced between the two contacted surfaces when the space between them is mismatched by mechanical motions. This phenomenon drives the electrons back and forth between the electrodes under the external load resistance and thus power is generated (Wang 2017). Recently, notable work has been carried out on the TENGs as self-powered devices in various applications. Currently, the efforts of many researchers are focused on enhancing the conversion efficiency and output performance of the TENGs. This is achieved by selecting suitable triboelectric materials, with large triboelectric polarity differences and nanomaterials having high effective surface area (Chen et al. 2020; Lowell and Rose-Innes 1980; Niu et al. 2013; Seol et al. 2015; Zhang et al. 2017a). The TENG materials do not degrade on prolonged usage and operates even at lower frequencies, which make it a highly suitable device for many critical applications in biomedical implants (Chen and Wang 2017; Wen et al. 2014). The Teflon (polytetrafluoroethylene/PTFE) is a commonly used polymer in the TENG devices due to its highly tribo negative polarity of the fluorine atoms. Teflon is selected as counter surface against the triboelectric positive polarity materials (Wen et al. 2017). Recent literatures suggest that the materials with high dielectric constant and highly negative triboelectric polarity are selected as counter surface for the TENG devices. ZnO and La<sub>2</sub>O<sub>3</sub> nanocrystals are selected for TENG applications as counter material along with the Teflon polymer owing to their various advantages. The hydrothermally synthesized nanocrystals of La<sub>2</sub>O<sub>3</sub> and ZnO are selected for the triboelectric performance study (Badawy and Ibrahim 2016; Jafari Nejad et al. 2010; Kim et al. 2020; Wojnarowicz et al. 2020; Zhen Wen et al. 2017). This hydrothermal method produces materials with high-effective surface area which further enhances the triboelectric efficiency (Mi et al. 2018a; b; Ramaswamy et al. 2019; Saadatnia et al. 2019b; Tang et al. 2017; Wang et al. 2016). The triboelectric performance of the ZnO is already reported. There is a scope to increase the power density of the ZnO triboactive material by exploring different morphology and synthesizing techniques (Saadatnia et al. 2019a; Zhang et al. 2017a; Zhou et al. 2020). The recent reports suggest that, the La<sub>2</sub>O<sub>3</sub> is proven to be a material with high dielectric constant and PTFE is having a high triboelectric negative polarity. There are fewer or no reports on

TENGs using  $\text{La}_2\text{O}_3$  as active material. The  $\text{La}_2\text{O}_3$ -based TENG devices can be tested for the power density and longer life cycle of the materials. The hydrothermally synthesized  $\text{La}_2\text{O}_3$ -based and ZnO-based TENG along with the PTFE as counter materials can be tested as the self-powered TENG devices for their power output and working life-cycle.

### **1.3 Introduction to the Graphene Based-ZnO Nanocomposites for Photocatalytic Dye Degradation Applications**

Graphene is a two-dimensional single-atomic-thick sheet of graphite, which possesses extraordinary physical, chemical and mechanical properties (Yang et al. 2010). The oxidized form of graphene, graphene oxide, has attracted attention towards research in various aspects of material science with a wide variety of possible applications (Zhao et al. 2017). The GO has found many applications in the functional devices, such as fuel cells, supercapacitors, batteries, nanofluids, photovoltaics, etc. (Baby and Ramaprabhu 2010; Bunch et al. 2007; Kavitha et al. 2012; Li et al. 2016b; Liu et al. 2008; Mohanty and Berry 2008; Seger and Kamat 2009; Stoller et al. 2008; Tang et al. 2012; Vivekchand et al. 2008; Xiang et al. 2012b).

Several synthesis methods for GO has been reported. Most notable methods are chemical vapour deposition (CVD) (Sun et al. 2012), mechanical exfoliation method (KS et al. 2004), SiC pyrolysis (Kellar et al. 2010), e-beam evaporation (Sellappan et al. 2013a), Modified Hummer's method (Héctor et al. 2008) and so on. By far, Hummer's method has been most widely used technique for the synthesis of GO/rGO (Choi et al. 2011; Song et al. 2012; Wu et al. 2012; Zhang et al. 2016). However, these techniques require either high end instrumentation or usage of extremely strong chemical agents. The small lateral sizes of synthesized product remained the major drawbacks of these techniques (Tang et al. 2012). Most of the processing methods involve multiple-steps where in controlling the layer growth is difficult (Chen et al. 2015; Sellappan et al. 2013a).

Recently, Tang et al. (2012) reported a facile and low cost method for synthesis of GO utilizing glucose, fructose and sugar as major ingredients. By employing hydrothermal processing, GO was synthesized at much lower temperatures

while, at the same time, by varying processing parameters such as temperature, sugar concentration and duration of heating, the number of layers could be controlled (Tang et al. 2012). The synthesis of GO by Tang Lau method is not explored much in the context of the preparation of the nanocomposite. The ZnO is one of the highly attractive wide band gap semiconducting materials (3.37 eV, which is similar to that of GaN) with a large binding energy (60 meV) at room temperature (Kavitha et al. 2012). Recently, there have been attempts of growing nanocomposite of ZnO nanostructure with carbonaceous species to improve the properties of the bare ZnO (Akhavan 2011; Feng et al. 2014; Hashim et al. 2016; Kumar et al. 2015b; Kumar and Rao 2015; Lv et al. 2011; Stankovich et al. 2006; Sushma and Girish Kumar 2017; Yu et al. 2007; Zhang et al. 2009). The rGO content in the rGO-ZnO nanocomposite assist charge transfer between the metal oxide and pollutants, thereby improving optoelectronic property, energy storage property and photocatalytic ability (Dou et al. 2015).

#### **1.4 Hydrothermal Synthesis**

The processing of nanomaterials by various techniques has been reported. Amongst, the hydrothermal technique is the best suited technique. The hydrothermal method, a simple and facile solution synthesis technique, is selected due to its various advantages. In the hydrothermal method, the aqueous mixture of soluble metal salts and the suitable surfactants are heated under elevated temperature (below 200 °C) and relatively high-pressure conditions. According to heating modes of the autoclave, it is divided into conventional hydrothermal and microwave-assisted hydrothermal methods.

In the conventional hydrothermal method, the nanoparticles are synthesised by precipitation or by a direct mixture of metal salts with a base solution and then transferred to Teflon cup (Fig. 1.1). It is sealed in a stainless steel autoclave and heated in a hot air oven.

The hydrothermal method has the following advantages (Sheng et al. 2007)

- Feasibility of uniform control of size and shape of the particles

- Less time and temperature required for completing the reaction or synthesis process
- The end product will have least or no impurities in it

Direct growth of film can be achieved by keeping the FTO coated glass slides in the stainless steel autoclave during hydrothermal heating.

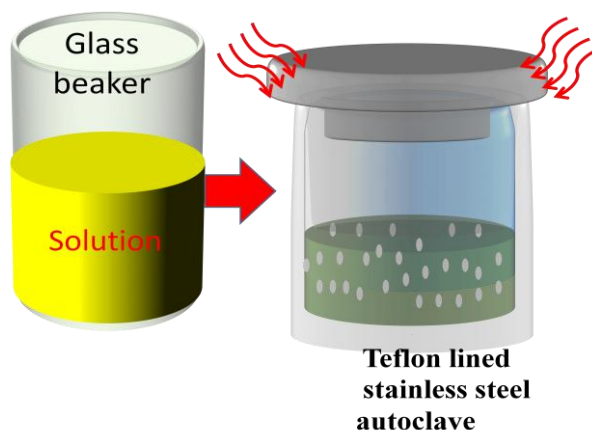


Fig. 1.1 The schematic showing the hydrothermal technique for synthesizing various nanoparticles.

In the microwave-assisted hydrothermal method, the heat is internally generated within the material using microwaves as external heating sources (Möhmel et al. 2002). This method has many advantages, like increased reaction kinetics, less energy consuming and less time required. This method can be carried out at low synthesis temperature, which yields uniform and high purity nanoparticles (Motta et al. 2010).

Various thin film deposition techniques are followed to fabricate the devices. This film deposition technique utilizes hydrothermally synthesized nanoparticles as precursors. The spin coating is a simple technique to deposit the nanomaterials on a substrate of interest. The spin coating solution can be prepared by dispersing a colloidal mist constituting of nanoparticles in a suitable volatile solvent(s). Later, the solution on the substrate is spun at a prescribed angular acceleration. The spinning parameters, like solution viscosity and spinning speed are tuned to get a uniform film with a maximum surface coverage of the substrate. On the other hand, the screen printing is also another film deposition technique, which enables the fabrication of



functional thin-film devices. The hydrothermally synthesized nanoparticles are mixed with the volatile solvent and a suitable binder(s). The solution is ground and high viscous paste is collected. The films are deposited on the substrate to fabricate the functional TENG device.

Here, an attempt is made to explore the applicability of the hydrothermally synthesized functional nanomaterials in various applications, like parallel plate capacitors, self-powered triboelectric devices and photocatalytic degradation of the methyl orange dye.

### **1.5 Organization of the Thesis**

**CHAPTER 1** introduces various concepts on dielectrics, triboelectric energy generators and photocatalytic applications.

**CHAPTER 2** deals with the literature of various methods to synthesize nanomaterials. The effect of hydrothermal synthesis parameters on the nanostructures is detailed. The theory of dielectrics, thin-film capacitor, classification of dielectrics, triboelectric nanogenerators, materials used in triboelectric applications, modes of triboelectric power generation and photocatalytic dye degradation is detailed.

**CHAPTER 3** deals with the detailed procedure for synthesizing  $\text{TiO}_2$ ,  $\text{La}_2\text{O}_3$  and  $\text{ZnO}$  nanoparticles. The detailed procedure of characterization, fabrication and device performance is discussed.

**CHAPTER 4** discusses the application of hydrothermally synthesized  $\text{TiO}_2$  nanorods in the fabrication of  $\text{N6/TiO}_2$  thin-film for dielectric application.

**CHAPTER 5** presents the single-step unique microstructural growth of  $\text{TiO}_2$  flower-like morphological thin films for dielectric application.

**CHAPTER 6** details the characterization and fabrication of  $\text{La}_2\text{O}_3$  and  $\text{ZnO}$ -based TENG devices.

**CHAPTER 7** details the usage of hydrothermally synthesized GO in the preparation of  $\text{rGO-ZnO}$  nanocomposites for methyl orange dye degradation. The effect of

various zinc precursors and GO (synthesized by Hummers' method) in the photocatalytic performance of rGO-ZnO nanocomposites is also compared.

**CHAPTER 8** details the summary, key findings and conclusions of the present work.

## CHAPTER 2

The content of this chapter have been published in the book chapter *Graphene as Energy Storage Material for Supercapacitors* 64, 181, 2020, [doi.org/10.21741/9781644900550-7](https://doi.org/10.21741/9781644900550-7).

*Page intentionally left blank*

## CHAPTER 2

### LITERATURE REVIEW

*This chapter gives the brief literature on exploring the synthesis of functional nanomaterials, like  $TiO_2$ ,  $La_2O_3$ ,  $ZnO$ ,  $GO$ ,  $rGO-ZnO$  by following the hydrothermal method. An overview of concepts of dielectrics (using  $TiO_2$  and  $TiO_2$ -based polymer nanocomposites), triboelectric nanogenerators ( $La_2O_3$  and  $ZnO$  based) and photocatalytic dye degradation (graphene based  $ZnO$ ) and advancements in these areas are presented. A brief literature on the hydrothermal synthesis of nanomaterials for various applications, such as energy and photocatalysis is also discussed. Finally, the problem identification along with the objectives of the present study is detailed.*

#### 2.1 Theory of a Capacitor

The capacitor is a device that stores electric charge and potential energy. Capacitors vary in shape and size. There are different configurations for capacitors, available commercially. One amongst those configurations is the electrostatic parallel plate capacitor. The basic design of a parallel plate capacitor consists of two parallel plates of area ' $A$ ' separated by distance ' $d$ ' (Barratt 1965; Matsch 1964) (Fig. 2.1).

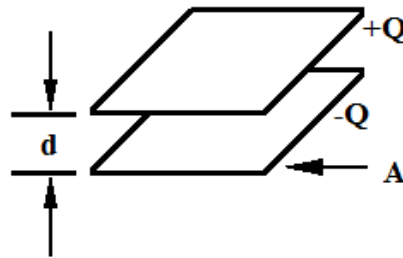


Fig. 2.1 Schematic representation of a parallel plate capacitor.

The space between two parallel plate electrodes may be occupied with a layer of air of absolute permittivity ' $\epsilon_0$ ' or a dielectric material of relative permittivity ' $\epsilon_r$ '. In the uncharged state, the charge on those parallel plates is zero. During the charging process, charge ' $Q$ ' is moved from one plate to another plate which results in the potential difference ( $\Delta V$ ) between the two parallel plates. The positively charged ( $+Q$ ) plate is at a higher potential by donating the charge ' $Q$ ' to the negatively charged ( $-Q$ )

lower potential plate. The net charge of the capacitor remains zero. The quantity of charge stored in the capacitor is directly related to the potential difference across the two parallel electrodes (Barratt 1965). Thus, charge  $Q$  is given by the equation,

$$Q = C[\Delta V] \quad (\text{Eq. 2.1})$$

where,  $C$  is the proportionality constant called the capacitance. The SI unit of the capacitance is farad ( $F$ ):

$$1 F = 1 \text{ farad} = 1 \text{ coulomb/volt} = 1 C/V.$$

According to Gauss's law, the potential difference between the parallel plates is given by,

$$\Delta V = Ed \quad (\text{Eq. 2.2})$$

where,  $E$  is the electric field applied.

The capacitance of a parallel plate capacitor is given by the following equation,

$$C = \frac{k\epsilon A}{d} \quad (\text{Eq. 2.3})$$

Where,  $k$  is the dielectric constant of the material,  $\epsilon$  is the permittivity of the dielectric material which is given by the following equation,

$$\epsilon = \epsilon_0 \epsilon_r \quad (\text{Eq. 2.4})$$

where,  $\epsilon_0$  has the value of  $8.85 \times 10^{-12} \text{ C}^2/\text{Nm}^2$ .

The symbols employed to represent the capacitors are shown in Fig. 2.2 (a) and (b). The work done ( $W$ ) to remove the charge from one plate and to deposit it on another, in the case of a parallel plate capacitor, is equal to electrical potential energy ' $U_E$ ' of the system and is given by the formula,

$$W = U_E = \frac{1}{2} \frac{Q^2}{C} \quad (\text{Eq. 2.5})$$

The electrical energy density ( $u_E$ ) of the system in the case of a parallel plate capacitor is given by,

$$u_E = \frac{U_E}{\text{Volume between the parallel plates}} = \frac{1}{2} \epsilon_0 E^2 \quad (\text{Eq. 2.6})$$



Fig. 2.2 Symbolic representation of (a) electrostatic capacitor and (b) electrochemical capacitor.

The breakdown field strength at which dry air loses its insulating ability and allows the discharge to pass through is  $E_b = 3 \times 10^6$  V/m. The electric energy density in this field is calculated using Eq. 2.6. It gives  $u_E = 40$  J/m<sup>3</sup>.

The capacitor should be chosen based on the application and its operating voltage (either AC or DC). The working voltage of the capacitor should be at least 50% smaller than the highest effective voltage to be applied to it, just at the point of discharge.

### 2.1.1 Dielectrics

$C_o$  is the capacitance of the capacitor without dielectric material in between the plates (means there is only an air gap in between the plates). The value of  $C_o$  increases when the distance between the parallel plates is filled with the good dielectric material of strength  $k$ , then the capacitance of the capacitor  $C$  is given by

$$C = kC_o \quad (\text{Eq. 2.7})$$

Every dielectric material has a dielectric strength which is the upper limit value of the electric field, above which breakdown occurs and the charges begin to flow. It is found that the value of dielectric strength is always more than one ( $k > 1$ ). The desired feature of the dielectric material is that it should not allow charge leakage when high voltage is applied. The dielectric material should have a 'k' value as high as possible.

There are two types of dielectrics, namely, polar dielectrics and non-polar dielectrics. Polar dielectrics possess polar molecules which inherently have permanent dipole moments. These dipoles are oriented randomly when there is no external

electric field applied as shown in Fig. 2.3(a). The dipoles orient in a direction when the field ( $\vec{E}$ ) is applied as shown in Fig. 2.3(b). Only a small amount of the electric field is used for changing the orientation of the dipoles along the direction of the applied field. The majority of the applied field is used to remove the electric charge from one plate and to deposit it on the other plate (Dissado and Fothergill 1992).

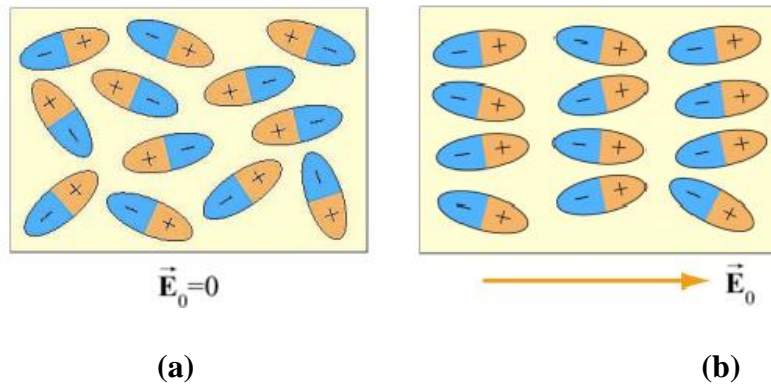


Fig. 2.3 Orientations of polar dipole molecules when (a)  $\vec{E}_0 = 0$  and (b)  $\vec{E}_0 \neq 0$  (Matsch 1964).

The non-polar molecule doesn't have an inherent dipole moment as shown in Fig. 2.4(a). There are no dipoles present inherently in the material. When the electric field is applied, the field is used initially for developing the dipoles in the molecules. These dipoles orient in the direction of the applied electric field as shown in Fig. 2.4(b).

The conductivity of any material in the case of capacitor application depends on three components,

- The applied frequency
- The auto ionisation or polarisation
- The free metal ions entrapped inside the crystal lattice may generate defects in the oxide crystals. The capacitance initially decreases sharply at a lower frequency and then slowly and then nearly become constant. The behaviour is due to space charge polarisation from the inhomogeneous dielectric structure (Xiao et al. 2014b).



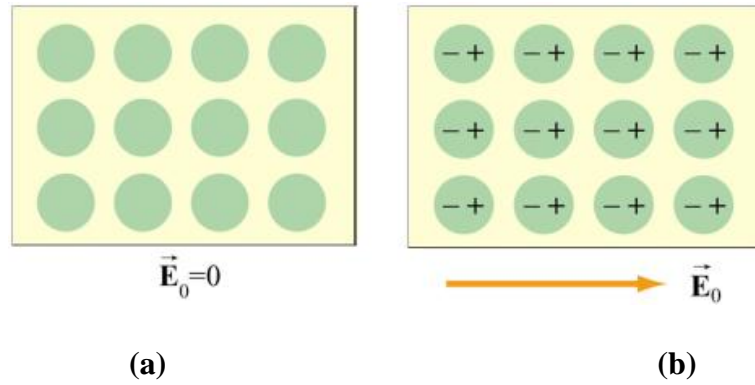


Fig. 2.4 Orientations of the non-polar dipole molecules when (a)  $\vec{E}_0 = 0$  and (b)  $\vec{E}_0 \neq 0$  (Matsch 1964).

Table 2.1 Dielectric constants of different materials (Dissado and Fothergill 1992; Srinivasan and Bandyopadhyay 2017)

Material	Dielectric constant ( $k$ )
Polyethylene	3.2
Polypropylene	2.2
Polycaprolactam	4.3
Vacuum	1
Air	1.0006
Paper	2.5-3.5
Glass	3-10
Mica	5-7
Wood	3-8
Metal oxide powder	6-20

According to the theory and the literature, an increase in the dielectric constant ( $k$ ) increases the capacitance of the capacitor. It is recommended from the literature (Dissado and Fothergill 1992; Matsch 1964) that higher dielectric constant ( $k$ ) is obtained by using the composites rather than a single material. The capacitors may consist of an individual layer or a combination of two or more sandwiched layers of dielectric and electrode plate arrangements. The dielectric material may be a composite having a matrix and filler materials of high dielectric constant. Over a decade, polymer nanocomposites are explored extensively for the fabrication of high-

performance capacitors. The polymer with nanofiller material is expected to give a higher dielectric constant ( $k$ ) by forming the micro capacitor network developed within the PNCs (Mahadevegowda et al. 2015; Srinivasan and Bandyopadhyay 2017).

Table 2.1 shows the list of dielectric constants of different materials. The polycaprolactam (N6) has a dielectric constant of 4. It also has other advantages, like high chemical stability, high mechanical strength, etc. Some of the research works are focused on the N6 polymer composite dielectric layer for the parallel plate capacitors (Mahadevegowda et al. 2015). The composite with N6 polymer as a matrix and fillers of nanoparticles has yielded good results as the dielectric material. This composite has also shown good breakdown strength when high voltage is applied.

### **2.1.2 Nylon-6 (N6/Polycaprolactam)**

Nylon-6/Polyamide-6 (N6/PA6) or polycaprolactam is a polymer developed by Paul Schlack at IG Farben to reproduce the properties of Nylon-6,6 without violating the patent on its production (Pant et al. 2013a). The Nylon-6,6 is made of two monomers each containing 6 carbon atoms, hexamethylenediamine and adipic acid. The caprolactam has 6 carbons, hence the name 'Nylon-6/N6/PA6'. Nylon-6 is semicrystalline polyamide and formed by ring-opening polymerization. A polyamide is a macromolecule with repeating units linked by amide bonds. The polyamides occur both naturally and artificially. The natural polyamides are proteins, such as wool and silk. The artificial polyamides can be prepared through step-growth polymerization or solid-phase synthesis yielding materials, such as nylons, aramids, and sodium poly-aspartate (Lewin and Pearce 1998; Pant et al. 2013a; Pant et al. 2013b; Srinivasan and Bandyopadhyay 2017). Nylon-6 and Nylon-6,6 are the aliphatic polyamides having an aliphatic main chain as the backbone. Nylon-6 (PA6/Polyamide-6) is an aliphatic polyamide with straight-chain without any rings. Nylons must specifically include a straight-chain (aliphatic) monomer.

During polymerization, the amide link is produced from an amine group (alternatively known as an amino group) and a carboxylic acid group. The hydroxyl group from the carboxylic acid combines with the hydrogen from the amine. The byproduct of the reaction is water.

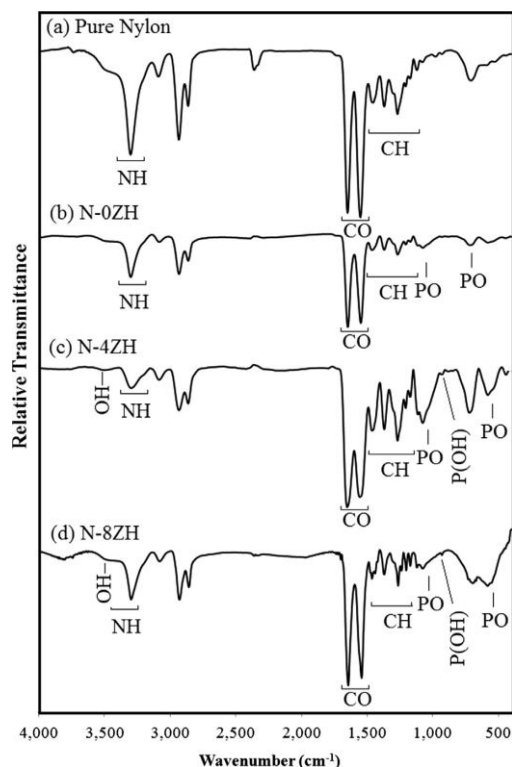


Fig. 2.5 FTIR spectra of electrospun pure Nylon-6 and its variants (Pant et al. 2013a).

A peptide bond (amide bond) is a covalent chemical bond linking two consecutive amino acid monomers along a peptide or protein chain. Amides are usually considered derivatives of carboxylic acids. Here, the hydroxyl group is supplemented by amine or ammonia. These compounds can both donate and accept hydrogen bonds. The FTIR spectrum of N6 is shown in Fig. 2.5. The amides exhibit a moderately intense  $\nu_{\text{CO}}$  band near  $1650\text{ cm}^{-1}$  in the FTIR spectrum.

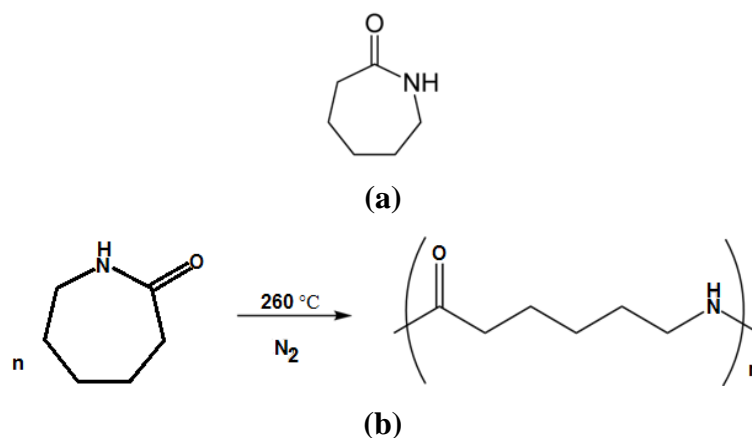


Fig. 2.6 (a) Caprolactam molecule, (b) the ring opening polymerization reaction from the caprolactam molecule to Nylon-6 (Wang and Lin 1998).

Nylon-6 is excellently resistant to oils, greases, aliphatic and aromatic hydrocarbons, as well as, to most halogenated hydrocarbons. It is not resistant to acids and alkalis. The UV stability of N6 is better than that of most other engineering polymers. N6 fibers are tough, possessing high tensile strength, high elasticity and luster (shine). They are wrinkle-proof and extremely immune to abrasion and chemicals, like acids and alkalis. The N6 fibers can absorb water up to 2.4%, although this lowers its tensile strength. The glass transition temperature of N6 is 47 °C. As a synthetic fiber, N6 is generally white but can be coloured by the application of dyes. Its tenacity is between 6 - 8.5 g/den (gram/denier) with a density of 1.14 g/cc. The melting point of N6 is 215 °C and withstands heat up to 150 °C on average. The autoignition temperature of N6 is 434 °C. IUPAC name of N6 is poly (hexane-6-lactam). N6 is a good polyelectrolyte and having band-gap energy of 4.9 eV. The electrical conductivity is very low and hence it is a good insulator (Lewin and Pearce 1998). When caprolactam (Fig. 2.6 (a)) is heated to about 260 °C in an inert atmosphere of nitrogen for about a period of 4 - 5 h, the ring breaks and undergoes polymerization, as shown in Fig. 2.6 (b). Further, the molten mass is passed through spinnerets to form fibers of Nylon-6.

Nylon-6 finds application in a broad range of products requiring materials of high strength. It is widely used for gears, fittings, and bearings, in the automotive industry for under-the-hood parts and as a material for power tool housings. Nylon-6 is used as a thread in bristles for toothbrushes, surgical sutures, and strings for acoustic and classical musical instruments, including guitars, sitars, violins, violas and cellos. It is used in the fabrication of big assortments of threads, ropes, filaments, nets, tire cords, as well as hosiery and knitted garments. It can also be used in gun frames which are made with a composite of Nylon-6 and other polymers. In the manufacturing sector, Nylon-6 is used as washers. It holds the potential to be recycled as a raw material for the production of new Nylon-6, by depolymerization to caprolactam. It is also used in the area of application in the electronics industry as electrical insulation material. It has consumption in textiles industries, carpets and sportswear due to its high durability and strength. The transportation industry is the

major consumer, accounting for 35% of polyamide (PA) consumption (Esfahani et al. 2015; Koltzenburg et al. 2017).

### 2.1.3 Filler materials

The PNCs with N6 polymer matrix and the high dielectric strength fillers have shown high dielectric constant (Hashim et al. 2016; Pant et al. 2013b). Nylon-6 with metal oxide nanoparticles and ceramic oxide nanoparticle fillers have also shown great scope in these dielectric applications (Amoghavarsha et al. 2014; Cao et al. 2020; Dong et al. 2008; Mahadevegowda et al. 2014; Pant et al. 2011; Rusu and Rusu 2011; Shinde et al. 2016; Zhou et al. 2020).

Titanium is a reactive metal that undergoes oxidation. TiO<sub>2</sub> is a semiconductor that is highly polarizable with a high dielectric constant ( $k$ , ranges from 12 to 114). The production details and role of this material are drastically increased recently. TiO<sub>2</sub> is commonly utilized in most applications due to its wide availability, chemical stability, low-cost, non-toxic nature and good photocatalytic properties. It has exhibited polymorph crystal phases, like anatase, rutile, brookite, etc. The anatase phase of TiO<sub>2</sub> is stable at low temperature and the rutile phase is thermodynamically stable at high temperature (Boukrouh et al. 2008; Constantin et al. 2012; Mukherjee et al. 2014). The nanosized anatase is being explored in the application of photocatalytic, chemical treatment of organic pollutants, organic light-emitting diodes. The rutile phase exhibits high dielectric constant and is used as filler in hybrid composite materials. TiO<sub>2</sub> (rutile phase), an inorganic filler in the polymer nanocomposite, has good dielectric properties. The rutile TiO<sub>2</sub> nanoparticle with nanometer size has low dispersion rate and strong dielectric permittivity. It enables its use in modern electronic applications (Wypych et al. 2014b).

Recently, Marinel et al. (2013) reported the dielectric properties of TiO<sub>2</sub> ceramics produced by the conventional and the microwave sintering over the temperatures 1000 - 1300 °C. The dielectric constant values were high and equal to about 100 for measurement performed at room temperature and the frequency of 100 Hz. These high values were achieved by the preparation of high-density ceramic sinters (Marinel et al. 2013). Wypych et al. (2014) synthesized the TiO<sub>2</sub> nanoparticles,

via three types of wet chemical methods, like sol-gel, precipitation method as well as by using layered ammonium titanate as a source of TiO<sub>2</sub>. Within the wet chemical methods, one can find thermohydrolysis, sol-gel, and precipitation as well as the hydrothermal route that required autoclave. The wet chemical methods were valued for synthesizing oxide nanoparticles, because of the ease, simplicity and economical nature. Homogeneous nanoparticles of desired morphologies were achieved by using simple techniques. They also studied the effect of thermal treatment on the structure, morphology and dielectric properties of rutile nanoparticles. The synthesized nano powder was used as a filler material in high  $k$  (dielectric strength) nanocomposites. The results showed that the dimension of the TiO<sub>2</sub> rutile nanoparticles synthesized by following the sol-gel method was 20 nm at 850 °C. These TiO<sub>2</sub> nanoparticles were found to exhibit high dielectric strength. The value of dielectric permittivity was 63.7 and loss tangent equal to 0.051 at MHz frequencies. Other techniques yielded lower values compared to those produced by the sol-gel technique.

Cortes and Phillips (2015a) worked on the porous TiO<sub>2</sub> material. Any non-conductive porous material filled with a liquid having sufficient concentration of dissolved ions is shown to exhibit a high dielectric constant. The value of  $k$  was 10<sup>4</sup> times more than the barium titanate (the best solid dielectric material). Fromille et al. (2014) used boric acid and dissolved sodium chloride salts. The electronic double-layer capacitor (EDLC) with super dielectric material had two limitations. The first limitation was the thickness of (few micrometers) thin layered dielectric material. The second limitation was the ultimate voltage rating of the thin EDLC, which is of the order of ~1.2 V (Cortes and Phillips 2015a; b). When the electric field was applied across such dielectric material, the ions which were filling pores of the solid material formed giant dipoles within the liquid. This phenomenon resulted in a higher dielectric strength (Gould 2020; Jackson 2013). Cortes and Phillips (2015b) also depicted that the thinner the dielectric layer higher is the energy density.

Mahadevegowda et al. (2015) examined the TiO<sub>2</sub> core-shell nanoparticles. The core-shell nanoparticles trapped the electric charge at the core/shell and shell/matrix interfaces, which enhanced the interface polarisability. The outer shell of the core-shell nanoparticles fulfilled the role of an interphase. Few examples for core-

shell nanoparticles have been shown in Fig. 2.7 and Fig. 2.8. The choice of the particulate phase forming the oxide shell and the nature of the shell affected the performance of the dielectric material.

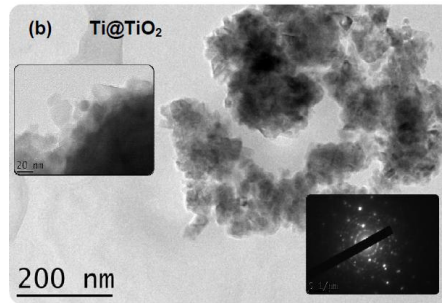


Fig. 2.7 An example for the core shell nanoparticle; TEM micrograph of the titanium core and the titanium oxide shell (Nikitenko et al. 2015).

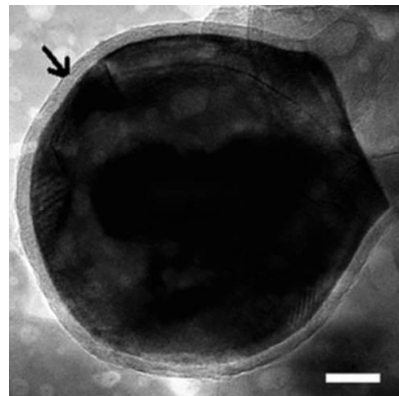


Fig. 2.8 An example for the core shell nanoparticle; the TEM micrograph of aluminium nanoparticle with the aluminium oxide ( $\text{Al}_2\text{O}_3$ ) shell (thickness 2.8 nm) casing and the aluminium core (Xu and Wong 2005).

Cheng et al. (2014b) examined the photocatalytic properties of  $\text{TiO}_2$ .  $\text{TiO}_2$  being photosensitive, when illuminated by light, generated electron-hole pairs that created  $\text{O}^{2-}$  and OH radicals. Graphene (2D nanolayers) based  $\text{TiO}_2$  materials split the electron-hole pairs more efficiently by providing high surface area and electron mobility. The properties of graphene/ $\text{TiO}_2$  composite completely depended upon graphene content, the degree of interfacial contact, the heterojunction between graphene- $\text{TiO}_2$  and the surface area of the  $\text{TiO}_2$  nanocrystals (Cheng et al. 2014b).

### 2.1.4 Nylon-6 and titanium oxide (TiO<sub>2</sub>) composites

Mahadevegowda et al. (2015) worked on the titanium-based core-shell nanoparticles as filler materials for PNC films to enhance the dielectric properties. Thermal evaporation was done in Edwards Auto 306 Cryo evaporator with a base pressure of  $5 \times 10^{-4}$  Pa. Titanium wire (99.7% pure), nylon-6 (Aldrich) and aluminum wire (99.999% pure) were thermally evaporated onto the glass slide, sequentially, using different tungsten (W) boats. The top and bottom (1st and 5th) layers of Al (40 nm each) formed the electrodes of a simple parallel plate capacitor. Ti, Ag-Ti and N6 layers were coated one above the other in a configuration as shown in Fig. 2.9 and Fig. 2.10. Reactive metal titanium was selected as it oxidizes to TiO<sub>2</sub> which can be formed in versatile forms, ranging from amorphous TiO<sub>2</sub> to crystalline TiO<sub>2</sub> (anatase, rutile and brookite).

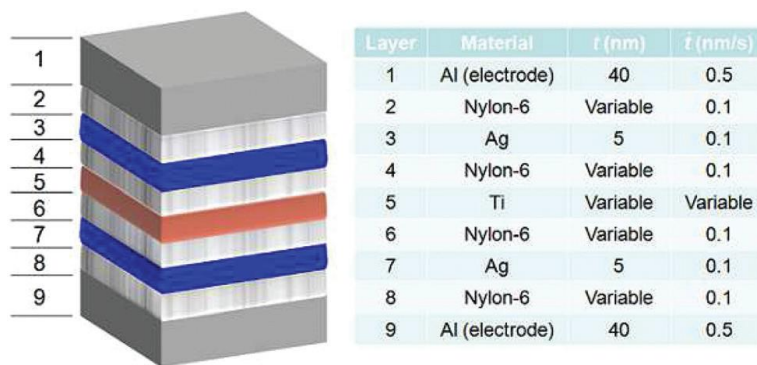


Fig.2.9 Schematic representation of the alternate layer deposition for PNCs (Mahadevegowda et al. 2015)

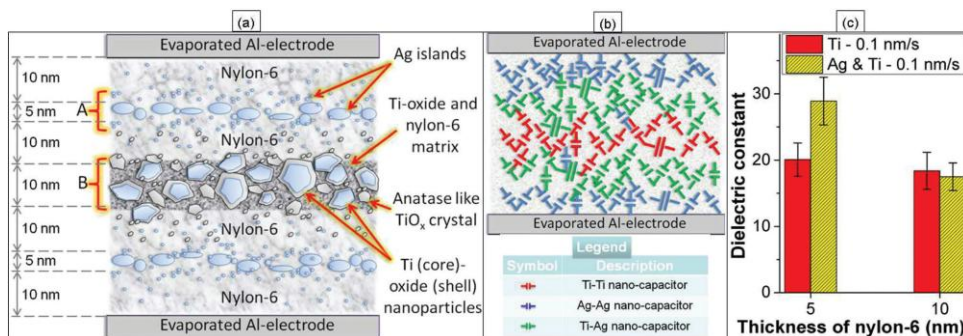


Fig. 2.10 (a) A cross-sectional, schematic representation of PNC based capacitor with thickness of each layer of the dielectric, (b) the corresponding schematic showing micro capacitor network within the device and (c) the variation of dielectric constant with thickness  $t$  of the deposited nylon-6 layer in Ti-PNC and Ag + Ti-PNC based capacitors at 1 kHz and 40 °C (Mahadevegowda et al. 2015).



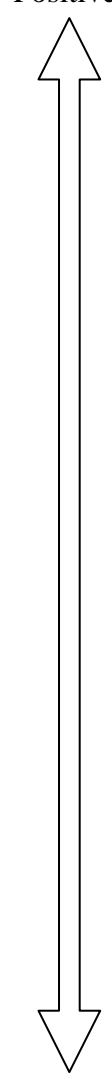
TiO<sub>2</sub> is a semiconducting and highly polarizable material having  $k$  in the range of 12-114. In core-shell particulate fillers, the outer “shell” fulfills the role of the interphase and also inhibits the excessive current percolation effects. The dielectric constant ( $k$ ) achieved was as high as  $\sim 73$ . This survey brought out that the core-shell nanoparticle increases the interfacial polarisability by trapping the charge in the interface of core-shell particles and the matrix. Very low volume of the secondary phase of Ag was deposited as discrete, non-continuous islands, which was sandwiched by polymer layers. They provided additional contributions in enhancing the dielectric strength of the device by forming a micro-capacitor network.

Mahadevegowda et al. (2014) had also worked on the polymer sandwich parallel plate capacitor with alternate layers of highly polarisable minority phase fillers, like conductive metal Al/Ag and N6 polymer matrix. Vacuum deposited aluminum (Al) yielded angular core-shell nanoparticles in Al-oxide/N6 matrix whereas Ag yielded round and discrete nanoparticles in the N6 matrix. The electrochemical impedance spectroscopy and microstructural characterization techniques were used for examining the thin film parallel plate capacitor. The electron microscopy investigations showed the morphology, nanostructure and phase of nano-scale core (metal) - shell (oxide) particles and metallic nano-islands in Al and Ag-based PNCs, respectively. Experimental and computational studies on the core-shell nano-particles suggested that the shell thickness influences their polarisability, along with the morphology of the filler and distribution of the nanofiller material. The survey also suggested that Al-based PNCs showed two times higher  $k$  values than the Ag-based PNCs. It was attributed to the formation of a polarizable Al<sub>2</sub>O<sub>3</sub> shell around the Al nanoparticle core.

## **2.2 Introduction to TENG Devices**

Electricity is the most essential need for the automation process. The need for the storage of energy/electricity has opened many challenging areas for research. Presently, batteries and capacitors are used to power these devices. The energy storage gadgets in the miniaturized devices resulted in bulky devices. The life and efficiency of the powering devices were found to diminish after prolonged usage.

Table 2.2 Triboelectric materials (Chen and Wang 2017).

Insulator Name	Charge Affinity (nC/J)		Insulator Name	Charge Affinity (nC/J)
Polyurethane foam	+60		Sorbothane	+58
Hair, oily skin	+45		Solid polyurethane	+40
Magnesium fluoride	+35		Nylon, dry skin	+30
Machine oil	+29		Nylatron	+28
Glass (soda)	+25		Paper	+10
Wood (pine)	+7		Cotton	+5
Nitrile rubber	+3		Wool	0
Polycarbonate	-5		Acrylic	-10
Epoxy	-32		Styrene-butadiene rubber	-35
PET (mylar) solid	-40		EVA rubber	-55
Gum rubber	-60		Polystyrene	-70
Polyimide	-70		Silicones	-72
Vinyl: flexible	-75		LDPE	-90
Polypropylene	-90		HDPE	-90
Cellulose nitrate	-93		UHMWPE	-95
Polychloroprene	-98		PVC (rigid vinyl)	-100
Latex (natural) rubber	-105		Viton, filled	-117
Epichlorohydrin rubber	-118		Santoprene rubber	-120
Hypalon rubber, filled	-130		Butyl rubber, filled	-135
EDPM rubber, rubber	-140		PTFE (Teflon)	-190

There is a possibility of potential environmental pollution because of the difficulty in the recycling and even possibility of explosion of rechargeable batteries. To overcome these disadvantages, presently researchers are considering on self-powered devices, potential alternative to battery-powered devices. This has opened a research area towards the development of highly efficient, independent, environment friendly, maintenance-free, mobile, high power density and miniaturized nanodevices.

Zhong Lin Wang's group is the first inventor of the piezoelectric nanogenerator (PENG) using ZnO nanowires (Wang and Song 2006). This device worked on the principle of converting mechanical energy into electrical energy using the piezoelectric effect. Later in the year 2012, they have also invented the triboelectric nanogenerator (TENG), which was based on contact electrification and electrostatic induction (Fan et al. 2012). Based on their studies, it was concluded that TENG devices were having high power output, more environmental friendly devices and fabricated using commonly available materials. The TENGs can harvest energy using conventional mechanical movements in our daily activities. TENGs are also useful in many applications, such as self-powered sensors to detect vibration, humidity, gas sensing and temperature sensing. Table 2.2 lists the materials and respective charge affinities.

### 2.2.1 The working principle of TENGs

Wang (2017) studied the fundamental theory of nanogenerators with the help of Maxwell's equations and predicted the "Displacement current" equation for the nanogenerators.

$$J_D = \epsilon_0 \frac{\partial E}{\partial t} + \frac{\partial P}{\partial t} \quad \text{Eq. 2.8.}$$

The second term  $\frac{\partial P}{\partial t}$  in Eq. 2.8 was related to the polarization induced current (or output electric current), which was the fundamental characteristics of the nanogenerators, like piezoelectric nanogenerators and triboelectric nanogenerators (Wang 2017). The nanogenerators are the applications of Maxwell's displacement current in energy and sensors. By analyzing the output electric signals ( $V_{oc}$ ,  $I_{sc}$ , frequency, etc.), the input signals (magnitude and frequency) were analyzed easily. There was no need for an external power source for the nanogenerators. They were found to produce the output electric signals on their own. This makes the device self-powered and unique when compared to conventional devices. The TENGs were found to work on the principle of contact electrification and electrostatic induction. The contact electrification occurs when the two materials with different polarities were brought close to each other. Thus, the energy was produced and the potential between the two electrodes was induced in response to the mechanical agitation and drives the

electrons through the external loads. The triboelectric charges flow back and forth among the electrodes, thus producing the electric output signals. Based on the movement of the electrodes and dielectric system, four different working modes of the TENGs were presented.

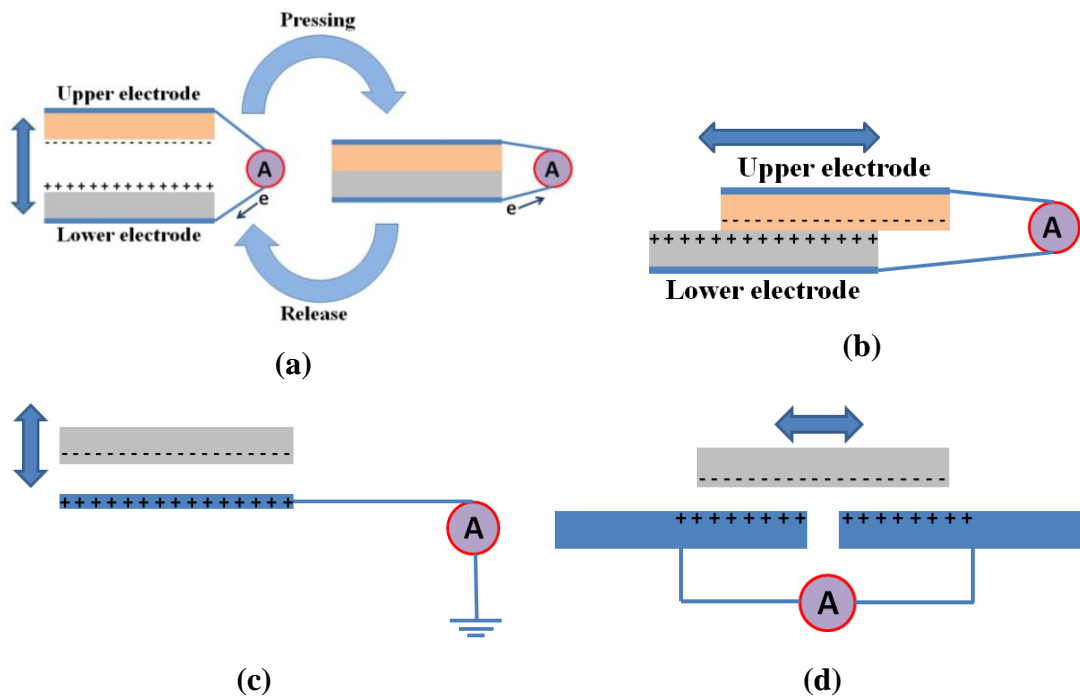


Fig. 2.11 Four working modes of triboelectric nanogenerator: (a) vertical contact-separation mode, (b) in-plane sliding mode, (c) single electrode mode and (d) free standing triboelectric-layer mode (Wang 2014).

### 2.2.1.1 Vertical contact-separation mode

Figure 2.11(a) illustrates the vertical contact - separation mode of the TENGs. It consists of two materials (insulator/dielectric) having dissimilar electron affinity with electrode material being back coated on both the surfaces. When the physical contact between the two materials is held with a small separation, the triboelectric charges get generated on the surfaces. When the external load is connected across the electrodes, the triboelectric charges are flown from one electrode to the other electrode to balance the electrostatic field. When the gap is closed, the triboelectric charges disappear and flow back. A periodic contact and separation between two such dissimilar materials induce the triboelectric charges to flow back and forth resulting in

an AC output in the external circuit (Yang et al. 2013a). This is the basic mode in the TENG, where the polarization is in the vertical direction. It can be easily achieved.

#### ***2.2.1.2 In-plane sliding mode***

Figure 2.11 (b) illustrates the in-plane sliding mode of TENGs. The relative reciprocating motion, between the two dielectric materials of different triboelectric polarities, generates the triboelectric charges on the surface. This mode is similar to the vertical contact-separation mode. When the two contact surfaces are disengaged, the positive charges on one surface are not fully compensated by the negative charges on the disengaged area. This results in the creation of the triboelectric charge polarization in parallel to the direction of sliding motion. Therefore, a potential difference across the two electrodes is generated and hence the alternating current output (Zheng et al. 2015). This mode is also used for cylindrical rotation mode even in the vacuum condition.

#### ***2.2.1.3 Single electrode mode***

A single electrode mode system is developed to overcome the constraint in the motion of the two electrodes. This mode utilizes only one electrode (which is ground) and one dielectric system. When the dielectric material (Fig. 2.11 (c)) approaches or leaves the electrode, it induces the triboelectric charge polarization on the electrode surface (Yang et al. 2013b). The single electrode allows the electrons to flow between the electrode and ground. Here, the relative motion of the triboelectric layers is in vertical contact-separation mode and in-plane sliding mode.

#### ***2.2.1.4 Free standing triboelectric-layer mode***

The system consists of two symmetrical electrodes, which are of the same order as the size of the moving object (dielectric layer) situated above the electrodes. The electrodes and the dielectric object are placed with a small gap. The object approaching and departing from the electrodes creates asymmetric triboelectric charges to flow between the electrodes to balance the potential distribution (Fig. 2.11 (d)). Thus, the AC output is induced in the external circuit (Wang et al. 2014). This system does not have any physical contact between the dielectric layer and electrodes.

The electrodes need not be grounded and hence prevents abrasion during the TENG operation. This mode harvests the energy from the moving object and the entire system is mobile without grounding. The system can sustain a longer duration of charges on the contact surface during the working cycle.

### **2.2.2 Applications of the TENGs**

The TENGs are mainly used in sensors, such as vibration sensors, motion sensors, gas sensors, pressure sensors, acoustic sensors, UV radiation sensors, electronic skin, air filtering, MEMS, robotics, water wave energy and implantable biomedical applications.

### **2.2.3 TENG materials**

The materials used in the TENG devices should have the ability to get polarized when they come in contact with the materials of different electron affinity. Since, the invention of TENG in 2012, extensive works are being carried out by many researchers on TENGs with different materials. Researchers have worked on developing and increasing the high potential triboelectric charge generation. The materials used for the TENG tribo-active surfaces are ZnO, aluminum, CdS, polytetrafluoroethylene (PTFE), polydimethylsiloxane (PDMS), polyvinyl chloride, fluorinated ethylene propylene (FEP) and also fluorine rich polymer (Kim et al. 2020; Mathew et al. 2021; Pace et al. 2020; Wen et al. 2017).

### **2.2.4 Zinc oxide based TENGs**

ZnO is a semiconducting material with a bandgap of 3.37 eV. It has high electron mobility and large binding energy. ZnO is used in various applications, like light-emitting diodes, transparent electrodes, bio-sensors, gas sensors, UV filters and as a photocatalyst. In recent times, lead-free piezoelectric and triboelectric materials, like ZnO-based piezoelectric nanogenerators (PENG) and TENG have attracted the research community in a wide variety of applications.

Although ZnO is not a tribo-material, it exhibits triboelectricity due to its finite conductivity characteristics. The surface of the ZnO nanorods is desirable and efficient for contact and interface at the junction of the triboelectric polymer materials

in TENG devices (Wang and Song 2006). ZnO exhibits tremendous piezoelectric and triboelectric properties. The main advantage of choosing ZnO in TENGs is due to its bio-safe nature, strong orientation effect, excellent flexibility, abundant availability and a variety of possible morphologies. The ZnO with different morphologies are easily synthesized using the simple, low-cost, and low-temperature growth hydrothermal method. The ZnO, also exhibits one-dimensional structure and shows high sensitivity for small applied external load and large deformation.

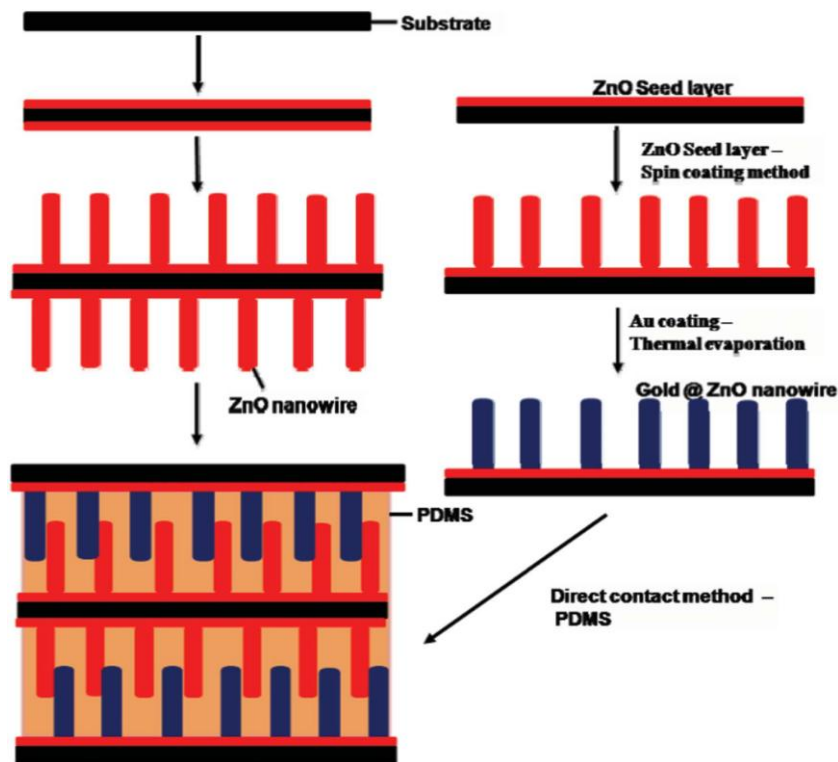


Fig. 2.12 Schematics of the ZnO based TENG device fabrication process (Saravankumar et al. 2013).

There are many reports on various methods for synthesizing 1D ZnO-based TENGs. The TENG devices were fabricated by sandwiching the ZnO with different polymers/metal films. The ZnO-based TENGs were fabricated based on the four different modes of operation. Many devices of ZnO were reported by coupling with tribo-negatively charged polymers for the TENG devices (Guo et al. 2013; Orlov et al. 2016; Wang and Song 2006). When the dimension of the ZnO was reduced, it produced a good response to the mechanical motion and thus taking care of TENG output (Wen et al. 2017; Zhang et al. 2017b). The ZnO was used with most tribo-

negatively charged polymers, like PTFE, Kapton, PVC, polyesters, polyimide, PVDF, polyethylene, etc. There is a literature gap on the fabrication of TENGs using ZnO with increased power density output.

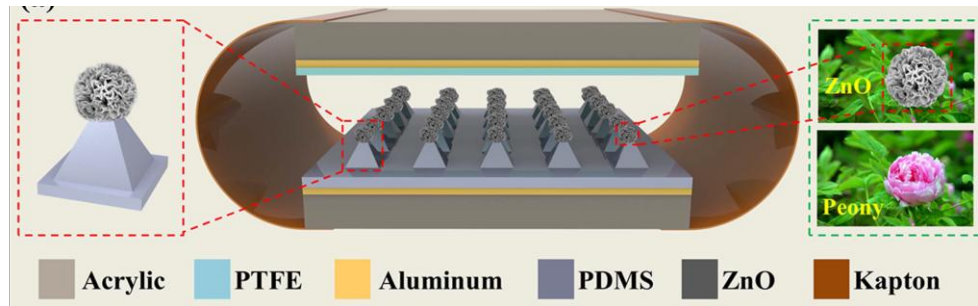


Fig. 2.13 Schematic representation of fabricated TENG device consisting of ZnO microballoons grown on PDMS film coated with the PTFE on the acrylic substrate (Deng et al. 2017).

Narasimulu et al. (2017) have successfully demonstrated the TENGs of aligned ZnO nanosheets with PVDF/PA6 on the aluminum substrate. It was found that there is a significant increase in the TENG performance, with a high value of  $V_{oc}$  and  $I_{sc}$  of 625 V and 40 mA/m<sup>2</sup> (charge density of 100.6  $\mu\text{C}/\text{m}^2$ ), respectively. The ZnO nanostructures were grown on the substrates, with the alignment of (0002) along the contact force direction, which significantly enhanced the performance of the TENGs (Narasimulu et al. 2017). The well-aligned ZnO was found to contribute to the effective increase of high surface area, preferential polarisation and growth direction of the dipoles. The power density reported here is 1.8 W/m<sup>2</sup>. Another work on the fabrication of ZnO nanogenerator for bio-safe energy harvesting is reported by Saravanakumar et al. (2013). The schematic of fabricated devices is shown in Fig. 2.12. The device consists of a double-sided layer of ZnO nanowire array sandwiched between the gold-coated ZnO nanowire arrays with polydimethylsiloxane as a counter tribonegative surface (Saravanakumar et al. 2013). This ZnO nanogenerator device extracts the energy from the human body movements, such as stretching, folding and pressing of the fingers. The  $V_{oc}$  and  $I_{sc}$  recorded from the device are found out to be 30 V, 300 nA with a power density of 0.39 mW cm<sup>-2</sup>. This energy produced by the device is enough to operate wearable electronic devices.



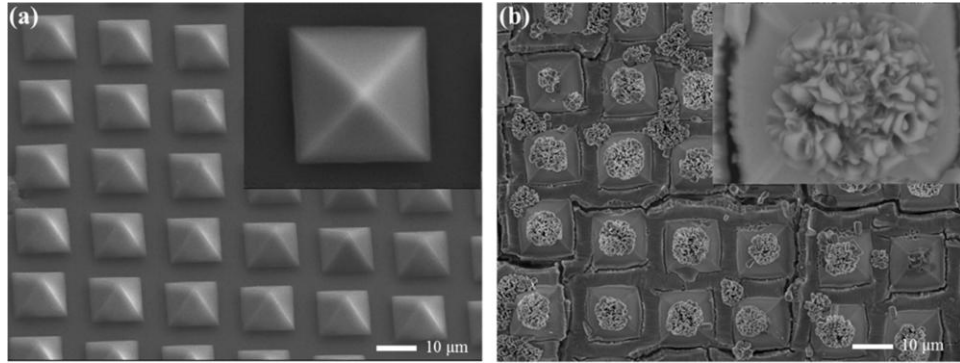


Fig. 2.14 The SEM micrographs of (a) PDMS film showing pyramid pattern and (b) ZnO microballoons grown on the PDMS pyramids (Deng et al. 2017).

Deng et al. (2017) have reported ZnO microballoons array on top of the PDMS pyramids films coated with the PTFE film, as shown in Fig. 2.13 and Fig. 2.14. The triboelectric output  $V_{oc}$  and  $I_{sc}$  produced by the device are 57 V and 59 mA/m<sup>2</sup>, at 100 Hz. The corresponding power density reported is 1.1 W/m<sup>2</sup>, at 2 MΩ.

Table 2.3 Table of comparison for TENG power density of different materials.

Material	Power (W/m <sup>2</sup> )	Reference
Al nanopores - kapton film	2.76 @ 6 MΩ	(Hu et al. 2013)
Aluminum – PTFE	0.0602 @ 6 MΩ	(Yang et al. 2014)
Copper-PTFE	0.121 @ 0.8 MΩ	(Fan et al. 2015)
Kapton-PDMS-Aluminum	0.00844 @ 10 MΩ	(Zi et al. 2015)
Microgrooved architectural PTFE – Aluminum	25.2 mW/cm <sup>-2</sup> @ 500 MΩ	(Dudem et al. 2018)
PVDF/TrFE – Nylon 11/PMMA	42 mW/cm <sup>-2</sup>	(Cao et al. 2020)
Micrograting films	50 mW/cm <sup>-2</sup>	(Zhu et al. 2014)
Aluminum-Nylon-conductive liquid-Rubber	0.035	(Yi et al. 2016)
Aluminum – PTFE	0.77	(Liang et al. 2015b)
Aluminum-PTFE-copper-acrylic	0.7261 @ 5 MΩ	(Chen et al. 2013)
ZnO-gold-PDMS	0.390 mW/cm <sup>-2</sup>	(Saravanakumar et al. 2013)
ZnO-polystyrene	2.3*10 <sup>-4</sup>	(Gupta et al. 2020)

Table 2.3 lists a few TENG devices and corresponding output power density. The tremendous performance of the TENG device demonstrates that the surface modification enhances the power output of the TENG devices. Thus, there is a need for producing highly aligned nanocrystals to extract the highest performance from the TENG devices.

### **2.2.5 Lanthanum oxide (La<sub>2</sub>O<sub>3</sub>) based TENGs**

Lanthanum is the lightest material in the lanthanide series. It has been widely studied in its compound states, such as oxides, hydroxides and phosphate forms. These nanoparticles are extensively used in optoelectronic devices, sensors, catalysis, and solid electrolyte (Xiao et al. 2014c). Lanthanum and its compounds have most of the applications in optical, electrical, magnetic domains and the most important are in the impurity extraction of As (III) (Stouwdam et al. 2003). Lanthanum oxide has found great attention in the area of piezoelectric materials, galvanothermy materials, thermoelectric materials, automobile exhaust-gas convertors and as a catalyst. Numerous techniques for synthesizing the lanthanum oxide nanoparticles have been proposed, such as thermal decomposition, super-molecular template route, micelles, homogeneous precipitation, solvothermal, hydrothermal and other chemical routes (Murugan and Viswanath 2006; Sheng et al. 2007; Wang et al. 2010). Murugan and Viswanath (2006) examined microwave-assisted hydrothermal synthesis. Lanthanide compounds with one-dimensional nanostructure were highly functionalized as a consequence of specific shapes and quantum size effects. They have unique electronic structures and exhibit numerous transition modes involving 4f shells of their ions. The properties of the nanosized materials depend on the size, shape and morphology (Yang et al. 2019). Solution phase synthesis of nanowires, nanobelts, nanorods and nanotubes favoured agglomeration and spherical particle formation due to the high surface energy of lanthanum oxide nanoparticles. To reduce the agglomeration of the one-dimensional lanthanum oxide nanoparticles, suitable capping agents, like surfactants, polymers or templates were employed (Murphy et al. 2005; Sreepasad and Pradeep 2013).

Many researchers have synthesized La(OH)<sub>3</sub> nanotubes and nanorods by using the hydrothermal process. The prepared nanostructures were uniform nanorods with

diameters up to 10 nm and lengths in the range of 100 - 150 nm (Fang et al. 2008a; Hu et al. 2007; Sheng et al. 2007; Wang et al. 2013, 2010, 2006). Hu et al. (2007) demonstrated the transformation of the lanthanum hydroxide to lanthanum oxide with suitable calcination techniques. Microwave-assisted synthesis was quicker, simpler and very energy efficient. During the synthesis of lanthanum oxide, there was a microwave-induced rotation of the dipoles within the liquid. This rotation forced the polar molecules to align and relax in the direction of the oscillating electromagnetic radiations (Murugan and Viswanath 2006). The synthesized lanthanum oxide nanoparticles were found to be porous. The surfactants were removed by air calcination at 450 °C. This porosity was examined by nitrogen adsorption and desorption isotherms. Sheng et al. (2007) examined the surfactant-assisted La<sub>2</sub>O<sub>3</sub> nanorods, nanoneedles and nanorod bundles.

The exploitation of such lanthanum oxide architectures may provide an area of interest for innovative ceramic nanoparticles with tunable material properties, required for electronic, magnetic and catalytic applications. Recent literature on the La<sub>2</sub>O<sub>3</sub> materials has revealed that it could be used in solid fuel cells, dielectric material and high-temperature superconductors (Allenspach and Gasser 2000; Niewa et al. 2011). Lanthanum oxide is ceramic, brittle and offers high dielectric properties. The materials La(OH)<sub>3</sub> and La<sub>2</sub>O<sub>3</sub> were used in the fabrication of the super-capacitors and also as dielectric material in the case of parallel plate thin film capacitors (Xiao et al. 2014c). Lanthanum oxide nanomaterials are highly functionalized materials due to shape-specific and quantum size effects. Based on the literature, the lanthanum oxide nanoparticles have shown good results as a dielectric material. The literature suggests that the high dielectric strength materials are best suited for the triboelectric energy generator. Lanthanum oxide has been used as a highly efficient dielectric material. Based on this observation, an attempt would be made to utilize the lanthanum oxide nanoparticles as triboelectric nanogenerators (TENGs). It is also observed that limited literature is available in the case of lanthanum oxide-based TENGs.

## **2.3 Hydrothermal Synthesis of Graphene-Based ZnO Nanocomposites for Photocatalytic Applications**

### **2.3.1 Graphene/graphene oxide**

Graphene is a two-dimensional (2D) single atomic layer of graphite (single atomic layer of carbon atoms). It has a strong covalent bond between two carbon atoms. The carbon atoms are arranged in a “honeycomb” like hexagonal structure. It is an allotrope of carbon, whose structure is a single planar sheet of  $sp^2$ -bonded carbon atoms. Each carbon atom occupies each corner of a hexagonal structure (Liao and Duan 2010). The carbon-carbon bond length in graphene is about 0.142 nm and interlayer distance is measured to be 0.33 nm. Depending on the nature and character of the border, graphene exhibits different electronic, mechanical and chemical properties. Armchair and zigzag are the most usual types of edge configuration with chiral edge configuration of  $0^\circ$  (armchair) and  $30^\circ$  (zigzag), respectively (Fan et al. 2017; Liao and Duan 2010).

### **2.3.2 Advantages of GO**

GO has a large surface area and much-increased adsorption capacity. The strong electron transferability of the thermally reduced graphene oxide in the composite is the unique physicochemical property. Due to defects in the basal plane of GO and due to  $Sp^2$ - $Sp^3$  conversion after functionalization with  $-OH$  and  $-COOH$  groups,  $\Pi \rightarrow \Pi$  transitions of electrons are restricted (Kumar et al. 2015a).

Oxidation of graphene gives rise to graphene oxide (GO). GO is a single atomic layer of carbon atoms with hydroxyl and carboxyl molecules attached to the carbon atoms. Oxford chemist Benjamin C. Brodie first demonstrated the synthesis of graphene oxide in 1859 by adding a portion of potassium chlorate to a slurry of graphite in fuming nitric acid. In 1958, Hummer reported an alternative method for the synthesis of graphene oxide by using  $KMnO_4$  and  $NaNO_3$  in concentrated  $H_2SO_4$ . GO prepared by this method could be utilized for preparing large graphene films. It was thought that graphene is not stable in its free form until it was isolated in 2004 by researchers (Andre Geim and Kostya Novoselov - 2010; to which Nobel Prize was

conferred) at The University of Manchester. The name “graphene” was first mentioned in 1987 by S. Mouras and co-workers (Shahriary and Athawale 2014).

### **2.3.3 Different methods to synthesize graphene/GO**

The primary objective of this part of literature survey is to find out which method is practicable and suitable to synthesize GO with available lab resources. It is expected that the synthesis method is free of strong chemicals which are harmful in handling. The selected method should be capable to synthesize the GO in mass, less time-consuming and cost-effective. Considering the above requirements, different methods for the GO synthesis are discussed here (Hashim et al. 2016; Sellappan et al. 2013b).

- Bottom-up synthesis of large-scale graphene oxide nanosheets (also called as Tang Lau method)
- Mechanical exfoliation method (also called as “Scotch tape method”)
- Modified Hummers method
- E-Beam deposition of graphene
- Catalyst-free growth of graphene by CVD
- Catalyst assisted growth of graphene by CVD
- Growth of large-area graphene from sputtered films
- SiC pyrolysis
- Graphite oxide reduction
- Epitaxial growth of the graphene by chemical vapour deposition.

#### ***2.3.3.1 Bottom-up synthesis of large scale graphene oxide nanosheets (Tang et al. 2012)***

This method is also known as the Tang-Lau method. The graphene oxide nanosheets (GONs) were grown by using a hydrothermal method. Glucose, sugar and fructose were used as a source of carbon and were dissolved in deionized water (DI water). The sugar solution concentration was ranging from 0.075 - 0.8 M. A 40 ml source solution was poured into a 50 ml Teflon-lined autoclave. The growth temperature was ranging from 160 to 220 °C with a growth period in the range of 70 -

660 minutes. Later, the autoclave was allowed to cool to room temperature; the layers floating on the solution were GONs. The layers were skimmed out into a separate container. The GONs were rinsed with deionized water and then transferred onto a desirable substrate for thermal annealing. The substrate was annealed using a rapid thermal processor to control 'O' (oxygen) content in the GONs. It was carried under a nitrogen atmosphere at 1 sccm. This was a self-assembly method to synthesize GO with thickness ranging from ~ 1 nm (monolayer) to ~ 1500 nm. The annealing temperature and time were ranging from 450 to 1300 °C and 2 to 5 minutes, respectively.

### ***2.3.3.2 Modified Hummers method***

1 g of graphite and 0.5 g of sodium nitrate were mixed in a glass beaker. 23 mL of concentrated sulphuric acid was added drop-wise under constant stirring. After 1 hour, 3 g of  $\text{KMnO}_4$  was added gradually to the above solution while maintaining the temperature less than 20 °C to prevent overheating and detonation. The mixture was stirred at 35 °C for 12 h duration. The resulting solution was diluted by adding 500 mL of water under vigorous stirring. To ensure completion of the reaction with  $\text{KMnO}_4$ , the suspension was further treated with 30 %  $\text{H}_2\text{O}_2$  solution (5 mL). The resulting mixture was washed with HCl and  $\text{H}_2\text{O}$ , respectively, followed by filtration and drying. Graphene oxide sheets were thus obtained from graphite (Backes et al. 2020; Pace et al. 2020; Shahriary and Athawale 2014).

### ***2.3.3.3 Decisions on the synthesis of GO***

Many methods of synthesis for graphene/graphene oxide involve a bunch of chemicals, instrumentation and time consuming (Sellappan et al. 2013). From literature, many researchers have mostly used Modified Hummer's method for GO and rGO (reduced graphene oxide) production. Amongst various methods, hydrothermal synthesis of graphene oxide has used only water and sugar as reagents. Tang et al. (2012) successfully demonstrated the hydrothermal synthesis of graphene oxide using sugar (sucrose, glucose and fructose, which are having a molecular formula with C, H O in the ratio of 1:2:1). The GO sheets produced were having a large lateral size. It was also demonstrated that the synthesized GO sheets were

converted to graphene by heating the samples to 450 - 1100 °C for a few minutes. The thickness was altered by altering the solution concentration, heating temperature and time of heating. This method has shown many advantages, like environmental friendly, facile, low-temperature operation, affordability and capable of scaling up for mass production. The instrumentation for this method was less. Here, the stainless steel autoclave and Teflon cup were used, which were of the least cost.

#### **2.3.4 Zinc oxide and rGO-ZnO nanocomposites**

Nanorods based on semiconducting materials have been investigated for application as energy harvesting and light-emitting devices. The optical bandgap of ZnO nanorods was tuned by variables, like morphology, composition and size. ZnO is also a good semiconducting material utilized for light-emitting diode, transparent electrodes, pH sensors, biosensors, acoustic wave devices, UV-photodiodes, photocatalytic units, laser diodes and gas sensor applications. ZnO has shown a large exciton binding energy at room temperature (Akhavan 2011; Chen et al. 2017a; Lv et al. 2011; Qi et al. 2017; Qurashi et al. 2009; Yu et al. 2016b). ZnO nanostructures have a great advantage to use in a catalytic reaction process due to their large surface area and high catalytic activity. Zinc oxide shows different physical and chemical properties depending upon the morphology of nanostructures and various synthesis methods. The physical and chemical properties of the synthesized zinc oxide were investigated in terms of its morphology (Chen et al. 2019a; Chen et al. 2019b; Hosseini and Babaei 2017; Liu et al. 2012b; Lv et al. 2011; Lv et al. 2012a; Lv et al. 2012b; Maruthupandy et al. 2020; Terzioglu et al. 2020; Tiwari et al. 2020; Yu et al. 2020).

Graphene-based ZnO materials have improved the properties of host ZnO nanomaterials. The hybrid nanomaterial of GO-ZnO nanocomposites resulted in unique properties, like ultrafast nonlinear optical switching property, optoelectronic property and energy storage property. Carbon-based materials incorporated with the metal oxides have resulted in the highest charge transfer between metal oxides and pollutants (Liu et al. 2012b; Lv et al. 2011; Lv et al. 2012a; Lv et al. 2012b). The addition of rGO to ZnO resulted in remarkable improvement in the photocatalytic activity when compared to that of the bare ZnO. This is due to the reason that ZnO

and graphene are expected to display unique properties and functionalities due to synergistic interaction between them. There are many innovative approaches to synthesize graphene-based zinc oxide (G/ZnO, GO/ZnO or rGO/ZnO) nanocomposites and their possible beneficial characteristics (Bu and Huang 2015a; Jayachandiran et al. 2018; Wang et al. 2018). There are multiple reports on the synthesis of graphene-based ZnO nanocomposites. A few of them are hydrothermal, sol-gel, electrochemical and vapour-phase processes. Generally used synthesis procedures with a few examples are briefed in the further section. It is also possible to tune morphologies, such as nanowires, nanorods, nanoneedles, hollow structures, and self-assembled architectures of the G-ZnO nanocomposites (Ashkarran and Mohammadi 2015; Bai et al. 2013; Bu and Huang 2015a; b; Du et al. 2013; Fang et al. 2014; Jayachandiran et al. 2018; Jayalakshmi et al. 2008; Kajbafvala et al. 2009; Li et al. 2013, 2015; Liu et al. 2012b; Lu et al. 2011; Marlinda et al. 2012; Rajeswari et al. 2017; Wang et al. 2011b, 2018; Wu et al. 2010; Zhao et al. 2014; Zou et al. 2011). Most of the reported work shows the need for higher temperature, sophisticated instruments and vacuum systems. Complex reaction procedures are requirements for the growth of ZnO onto the graphene oxide nanosheets. Therefore, there is a need for producing cost effective graphene-based ZnO nanocomposites with improved properties for their potential applications.

### **2.3.5 Different methods to produce ZnO and rGO-ZnO nanocomposites**

#### ***2.3.5.1 Hydrothermal method***

Absolute ethanol is utilized as a solvent for ZnO production using non-aqueous-based solutions. The advantage of using ethanol is to improve the dispersion of gel-like GO (Li and Cao 2011; Marlinda et al. 2012; Rajeswari et al. 2017; Xu et al. 2011; Zhou et al. 2012). One-pot synthesis of ZnO nanoparticles and the ZnO/graphene nanocomposites is carried out using Zn salt and GO. They have reported that the ZnO nanoparticles are chemically bonded to the graphene sheets during the reaction. ZnO nanoparticles with the dimensions of 10 - 15 nm are covered with graphene sheets (Liu et al. 2013). Zhou et al. (2012) have utilized the hydrothermal method to synthesize the ZnO-rGO nanocomposite with a high degree of photocatalytic degradation performance. Zinc nitrate hexahydrate and ammonia are



the raw materials. Hydrothermal conditions are 180 °C heating temperature and 10 h duration. Li and Cao et al. (2011) have synthesized ZnO-graphene composite. They reported that graphene sheets are incorporated onto ZnO by chemically reducing the mixture of graphite oxide and zinc acetate in an aqueous solution in the presence of NaBH<sub>4</sub>. Xu et al. (2011) have synthesized graphene–ZnO nanocomposites by reducing GO with the help of hydrazine. The graphene sheets are coated on the surface of the ZnO nanoparticles.

#### ***2.3.5.2 Microwave-assisted hydrothermal synthesis***

The dimensions of the ZnO nanoparticles synthesized by this method ranges from 10 to 100 nm. Microwave-assisted graphene-ZnO nanocomposites synthesis is also reported (Kajbafvala et al. 2009; Ke and Wang 2016; Lu et al. 2011; Zhu and Chen 2014). Graphene sheets constrain the growth of the ZnO nanostructures. Lu T. et al. (2011) carried out significant work on the synthesis of graphene-ZnO nanocomposites with high specific capacitance, via microwave-assisted reduction. Zinc sulphate, NaOH and GO were used as the target materials. Amir et al. (2009) have worked on the synthesis of the ZnO wires (sword shape) by using microwave energy. Methanol, tri-ethanol amine, zinc acetate dihydrate and sodium hydroxides were used as the raw materials. The width of the ZnO nanowires was ranging from 80 – 250 nm and length ~ 1-4 µm.

#### ***2.3.5.3 Electrochemical growth of the ZnO***

Effective control of the ZnO dimensions is possible through electrochemical growth. Dimension of the ZnO was tuned by controlling the growth variables, like solution concentration and applied potential (Run Liu et al. 2001; Zeng et al. 2010). ZnO deposition is carried out at lower temperatures (<100 °C) from an aqueous salt solution saturated with the oxygen. The variation in growth conditions results in a change from the planar film growth to the nanosized islands. The growth of the ZnO microstructure is depending on the substrate lattice parameter, the electrolyte used (nitrate, chloride or perchlorate), the amount of the oxygen content in the electrolyte, the applied potential and pre-activation surface treatment (Izaki and Omi 1998; Peulon and Lincot 1996; Run Liu et al. 2001; Wong et al. 2003; Zeng et al. 2010)

Wong et al. (2003) has studied the electrochemical growth of the ZnO nanorods. The ZnO nanorods were grown on the polycrystalline Zn foil by following the cathodic electrodeposition method. Aqueous zinc chloride/calcium chloride was used in this reaction at 80 °C. Zeng et al. (2010) synthesized the ZnO nanorods array on the GaAs substrate by electrochemical deposition without any buffer layer. Aqueous zinc nitrate was used as the electrolyte solution. Peulon and Lincot (1996) deposited the ZnO by using an electrochemical deposition approach. Zinc chloride (ZnCl<sub>2</sub>) salts and potassium chloride (KCl) electrolytes were used. Run Liu et al. (2001) deposited ZnO nanopillars on the single-crystal gold by following the electrochemical deposition method using ZnCl<sub>2</sub>/KCl solution. Izaki and Omi (1998) deposited transparent ZnO films by the ECD method by using zinc nitrate aqueous solution.

#### ***2.3.5.4 Sol-gel synthesis of the graphene-based ZnO***

This method uses GO, zinc precursors, additives and solvents for the nanocomposite synthesis. The basic reactions involved in sol-gel method are hydrolysis and condensation reactions. For example, zinc salt is used with alcohol or water in a solution medium. The hydrolysis reactions take place and form zinc hydroxide as the intermediate product. This product is condensed to form amorphous ZnO. The ZnO particles further need annealing to form ZnO nanocrystals. The morphology of the formed ZnO crystals ranges from spherical nanoparticles to percolated gels. Different variables like precursors, water content, solute and solvent ratios and aging decide the morphology of the ZnO. The sol-gel synthesis is a simple and inexpensive technique compared to other techniques (Alvarado et al. 2013; Ayana et al. 2016; Chebil et al. 2016; Demes et al. 2016; Haarindraprasad et al. 2016; Li et al. 2016a; Para et al. 2016; Pourshaban et al. 2016; Singh et al. 2016; Zhou et al. 2016; Zimmermann et al. 2016).

Pourshaban et al. (2016) has used zinc acetate as the zinc precursor with amino-additives in alcoholic solvents, like methanol and ethanol. The ZnO nanorods are synthesized by following the calcination technique at 500 °C for 60 min. Alvarado et al. (2013) have synthesized ZnO nanoparticles by using zinc acetate and KOH as the target materials with an annealing temperature of 600 °C. Singh et al. (2016) has

used zinc acetate and ethanol with a calcination temperature of 395 °C. Zhou et al. (2016) developed the ZnO porous film with the wood template method. Zinc acetate and ethanol were used as the targeting agents with sintering temperatures of 600, 800 and 1000 °C for 3 hours.

Table 2.4 Comparison of photocatalytic conditions and performance of GO/rGO based ZnO nanocomposites in degrading organic dyes.

<b>Material-Microstructure-Method</b>	<b>Organic dye</b>	<b>Light source</b>	<b>Removal (%) and Kinetic constant (min<sup>-1</sup>)</b>	<b>Time (min)</b>	<b>References</b>
rGO-ZnO nanorods-hydrothermal method	Methylene blue	Visible light	93 & -	120	(Ranjith et al. 2017)
rGO-ZnO nanorods-hydrothermal method	Direct red	UV light	91 & (7.3*10 <sup>-3</sup> )	180	(Mazarji et al. 2017)
GO-ZnO nanoparticles-hydrothermal method	Methylene blue	Visible light	99 & (1.1*10 <sup>-2</sup> )	120	(Mohamed et al. 2019)
GO-ZnO nanoplates-hydrothermal method	Azure B	UV light	99 & -	20	(Rabieh et al. 2016)
rGO-ZnO spindle-hydrothermal method	Methylene blue	Visible light	93 & -	180	(Prabhu et al. 2018)
rGO-ZnO nanosheets-hydrothermal method	Methylene blue	Visible light	100 & -	80	(Liu et al. 2020)
rGO-ZnO nanoparticles-hydrothermal method	Methylene blue	Visible light	100 & (1.4*10 <sup>-2</sup> )	60	(Van Tuan et al. 2020)

rGO-ZnO core-shell nanostructure- sol-gel method	Methylene blue	Visible light	93 & ( $4 \times 10^{-2}$ )	15	(Wang et al. 2020)
GO-ZnO nanoparticles- sol-gel method	Rhodamine B	Visible light	99 & ( $2 \times 10^{-1}$ )	100	(Yao et al. 2016)
rGO-ZnO lotus structure- sol-gel method	Phenol	Solar light	86 & ( $1 \times 10^{-1}$ )	20	(Yadav et al. 2019)
GO-ZnO nanoparticles- solution method	Safranin T	Visible light	100 & ( $4.9 \times 10^{-2}$ )	90	(Nenavathu et al. 2018)
GO-ZnO nanoparticles- solution method	O-xylene	UV light	75 & -	45	(Ahmed et al. 2018)
GO-ZnO nanoparticles- solution method	Rhodamine B	UV light	100 & ( $9.5 \times 10^{-2}$ )	65	(Tie et al. 2017)
GO-ZnO microspheres- solution method	Rhodamine B	UV light	99 & ( $6.9 \times 10^{-2}$ )	45	(Bera et al. 2016)
GO-ZnO nanoparticles - solvothermal method	Neutral red	UV light	99 & ( $3 \times 10^{-1}$ )	20	(Atchudan et al. 2017)
GO-ZnO nanoparticles - solvothermal method	Methylene blue	UV light	98 & ( $2.5 \times 10^{-1}$ )	15	(Atchudan et al. 2016)
GO-ZnO nanorods- solvothermal method	Orange II	Solar light	99 & ( $6.6 \times 10^{-2}$ )	180	(Moussa et al. 2016)
rGO-ZnO nanowires- electrodeposition method	Methylene blue	UV light	23 & ( $1.0 \times 10^{-3}$ )	240	(Pruna et al. 2017a)
GO-ZnO prong structure- hydrothermal method	Rhodamine B	UV light	91 & ( $5 \times 10^{-3}$ )	40	(Chamoli et al. 2021)

Chebil et al. (2016) has synthesized the ZnO thin film by using zinc acetate, isopropanol and monoethanolamine as a precursor, solvent and stabilizer, respectively. Haarindraprasad et al. (2016) has developed the ZnO nanowires by using zinc acetate alcohol and amine as the target chemicals. Para et al. (2016) has synthesized the ZnO nanoparticles using zinc acetate, glacial acetic acid and ammonium acetate as target materials. Li et al. (2016a) have synthesized the ZnO/graphene nanocomposite film as the anode material for the lithium-ion batteries using zinc acetate, ethanol, graphene and lithium hydroxide aqueous solution. Demes et al. (2016) have studied the effect of different amine agents, like mono and diethanolamine on the morphology of the ZnO nanowires. Ayana et al. (2016) have developed multilayer ZnO thin films using ethanol, zinc acetate monoethanolamine as target materials. They have also studied the effect of different substrates on the development of ZnO films. Zimmermann et al. (2016) have synthesized ZnO quantum dots and examined the effect of ethylene glycol on their growth. They have used zinc acetate, NaOH, 2-propanol and ethylene glycol. Table 2.4 lists the GO and rGO based ZnO nanocomposite materials with their corresponding microstructure and kinetic constants for different organic dye degrading.

### 2.3.6 Effect of synthesis parameters on morphology and dimensions

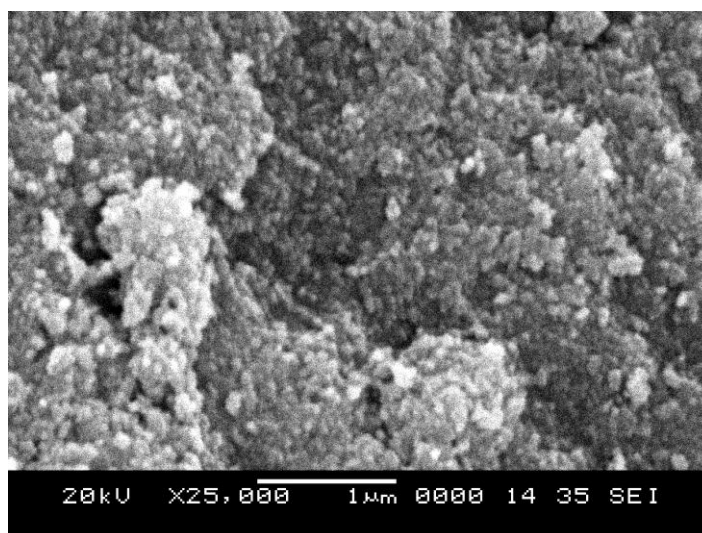


Fig. 2.15 SEM micrograph of the hydrothermally synthesized ZnO using zinc nitrate and NaOH aqueous solution as reagents at 80 °C.

The effect of various precursors, hydrothermal heating temperatures and methods on the synthesis of the ZnO nanostructures is studied by the authors. Figure 2.15 shows the SEM micrograph of the ZnO, wherein zinc nitrate along with NaOH reagent was used. The solution prepared was hydrothermally heated to 80 °C in a Teflon-lined stainless steel autoclave. The effect of hydrothermal temperature on the ZnO morphology was studied. The solution prepared with zinc nitrate and NaOH was kept same throughout the study and the effect of hydrothermal heating was studied over the temperature range of 80 to 180 °C.

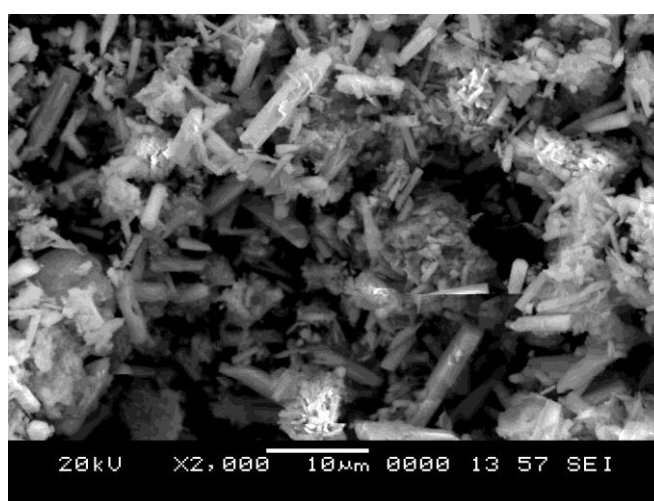


Fig. 2.16 SEM micrograph of the hydrothermally synthesized ZnO using zinc nitrate and NaOH aqueous solution as reagents at 180 °C.

Figure 2.16 shows the ZnO nanostructures with rod-like morphology. The increase in temperature provided sufficient activation energy and nucleation sites for the production of rod-like morphology of ZnO nanostructures.

### **2.3.7 Microwave-assisted hydrothermal method**

The ZnO nanostructures were synthesized by following the microwave-assisted hydrothermal method. Zinc nitrate and NaOH were added to the DI water. The mixture was then transferred to a Parr acid digester vessel. The Parr microwave autoclave was heated in a microwave oven at 700 W power for a few minutes. The resulting constituent was then washed with ethanol and DI water many times. The final powder was then dried in an oven at  $60 \pm 2$  °C for 12 hours. Figure 2.17 shows the SEM micrograph of the ZnO nanoparticles.

There are many reports on the ZnO nanoparticles decorated on the graphene/GO/rGO nanosheets. The ZnO nanostructures anchored on the graphene sheets improve the electron transferability of the ZnO. In our previous work, we have synthesized rGO/ZnO nanocomposites using the microwave-assisted hydrothermal method. We used hydrothermally synthesized GO nanosheets, zinc nitrate and NaOH as the target chemicals (Meti et al. 2018).

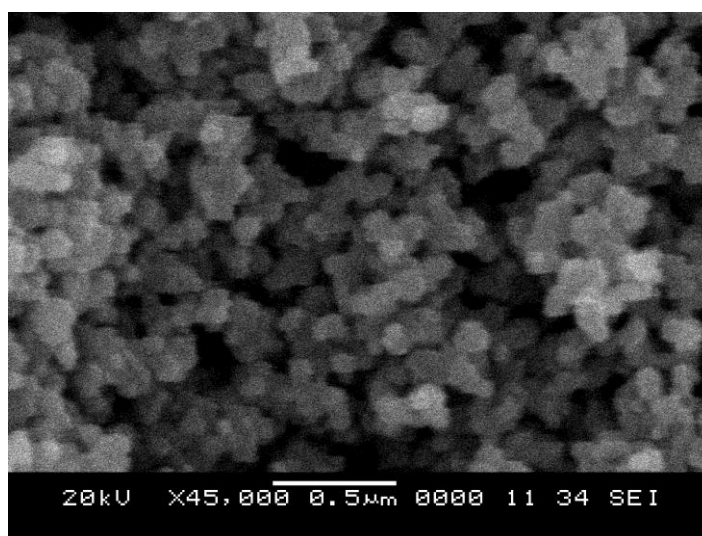


Fig. 2.17 SEM micrograph of the ZnO nanoparticles, synthesized by microwave assisted hydrothermal method using NaOH as reagent at 700 W power.

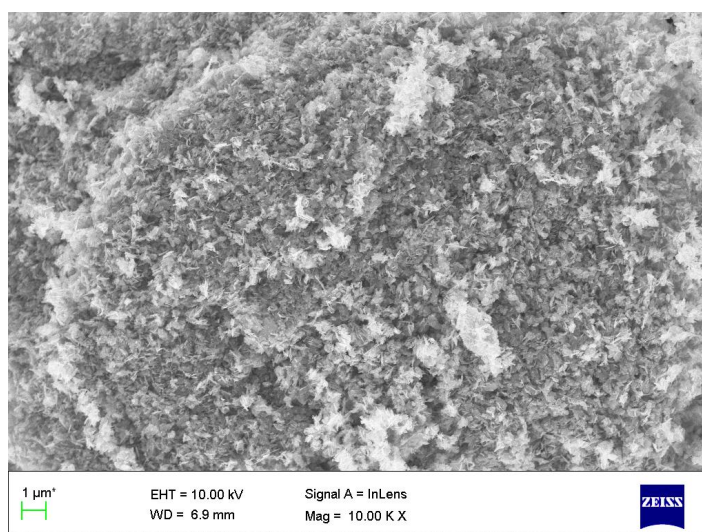


Fig. 2.18 FESEM micrograph of the rGO/ZnO synthesized by microwave assisted hydrothermal method using NaOH as reagent (Meti et al. 2018).

The synthesis of the GO was carried out using the hydrothermal method (Tang et al. 2012). The GO was dispersed in DI water. Zinc nitrate and NaOH were added to the same solution. The solution was then heated in a Parr microwave acid digester vessel at 700 W power for few minutes. The FESEM micrograph in Fig. 2.18 shows the ZnO nanorods anchored on the rGO nanosheets. The properties of the ZnO were improved by anchoring the ZnO onto the rGO nanosheets.

Based on the observations, it is seen that for the preparation of GO/rGO based ZnO nanocomposite the researchers are following Modified Hummers' method to synthesize the GO. From the literature, it is known that the hydrothermally synthesized GO, using only water and sugar as target chemicals, possibly replace GO prepared via Hummers' method. Based on these observations, we have identified the research gap that hydrothermally synthesized GO can be the best replacement for GO prepared via Hummers' method, in the preparation of rGO-ZnO nanocomposites.

## **2.4 The Synthesis Route**

The hydrothermal method is widely used for the production of a variety of inorganic nanoparticles under controlled pressure and temperature. This method has various advantages, like low processing temperatures and less reaction time. The hydrothermal method is used to produce various single and multi-component powders with ultrafine size, chemically homogeneous, high purity and high crystallinity. The method is also called a solvothermal process if the solutions are non-aqueous. A closed system of Teflon-lined stainless steel autoclave is used in the hydrothermal synthesis. When the temperature of the vessel is increased, the pressure inside the vessel increments over the critical pressure of the water. This phenomenon intensifies the disintegration of the thermodynamically unstable compounds. The macromolecules in the aqueous solution fracture to form nano-sized particles (Shandilya et al. 2016).

Microwave heating is done using the microwave frequency of 2.45 GHz. The heating depends on the molecular properties and reaction conditions. Any complex binary or a ternary metal oxide could be synthesized by using this method. The



nanoparticles produced from this method are having fine and uniform particle size due to minimal synthesis time and highly concentrated localized heating.

#### **2.4.1 Factors influencing the hydrothermal synthesis of nanostructures**

The synthesis of the nanostructure is found to be influenced by many factors such as temperature, time, pH value, alkaline source, surface energy and surfactants. By setting the pH value of the solution to the alkaline medium, the morphology could be changed. The alkalinity of the solution controls the preferential growth and orientation of nanocrystals. The alkaline solution will have high hydroxyl ion concentration and hence high chemical potential. The nucleation process occurs faster and more crystals are formed, resulting in the high surface area to volume ratio of the nanoparticles. The surfactants will also serve the purpose of a growth controller for nanoparticles as well as agglomeration inhibitor by forming a covering film on the nanoparticles (Xiao et al. 2014a).

#### **2.5 Objectives of the Work**

Based on the literature review, it can be summarized that the hydrothermal synthesis of the functional nanomaterials is simple and low-temperature method. The nanomaterials synthesized here can be utilized for capacitors, triboelectric devices and in photocatalytic applications.

The following objectives are defined for this study,

- Hydrothermal synthesis and characterization of GO, TiO<sub>2</sub>, La<sub>2</sub>O<sub>3</sub> and ZnO
  - Detailed study on phase, morphology and nature of the synthesized material
- Synthesis, preparation, characterization and fabrication of Nylon-6/TiO<sub>2</sub> thin films as dielectric material
- Synthesis, preparation, characterization and fabrication of the TiO<sub>2</sub> thin films as dielectric material
- Hydrothermally synthesized ZnO and La<sub>2</sub>O<sub>3</sub> nanocrystals in the TENG application
- Hydrothermally synthesized rGO/ZnO nanocomposite in the photocatalytic application.

## **2.6 Scope of the Study**

The study will help in exploring the hydrothermal synthesis of functional nanostructures. Understanding the synthesis mechanism will help in tailoring the growth of the nanostructures by controlling the parameters. Further, the applicability of the synthesized nanostructures in fabricating devices, like parallel plate capacitors, triboelectric nanogenerators and photocatalytic dye degradation materials will be examined.

# **CHAPTER 3**

*Page intentionally left blank*

## CHAPTER 3

### MATERIALS, METHODS, FUNCTIONAL DEVICE FABRICATION AND CHARACTERIZATION

*This chapter details with the step-by-step procedure of hydrothermal synthesis and characterization of functional nanomaterials ( $\text{TiO}_2$ ,  $\text{La}_2\text{O}_3$ ,  $\text{ZnO}$ ,  $\text{GO}$  and  $\text{rGO-ZnO}$ ). Further, the fabrication of functionalized devices for dielectric (Nylon-6/ $\text{TiO}_2$  and  $\text{TiO}_2$ ), triboelectric ( $\text{La}_2\text{O}_3$  and  $\text{ZnO}$  based) and photocatalytic ( $\text{rGO-ZnO}$ ) applications is described.*

#### 3.1 Materials

The chemicals used in the study were analytical-grade reagents and used as received, without additional purification. Nylon-6 ( $M_w \approx 35,000$ ), ammonium hexafluorotitanate ( $((\text{NH}_4)_2\text{TiF}_6)$  with 99.999% purity), diethylene tri-amine ( $\text{HN}(\text{CH}_2\text{CH}_2\text{NH}_2)_2$ ), formic acid, zinc nitrate hexahydrate ( $\text{Zn}(\text{NO}_3)_2 \cdot 6\text{H}_2\text{O}$ ), sodium hydroxide ( $\text{NaOH}$ ) and sucrose ( $\text{C}_{12}\text{H}_{22}\text{O}_{11}$ ) were purchased from Sigma-Aldrich Chemicals, Mumbai, India and Alfa Aesar Delhi, India. The deionized (DI) water was used throughout the experiments.

#### 3.2 Synthesis of Functional Materials

##### 3.2.1 Synthesis and reinforcement of high permittivity $\text{TiO}_2$ in polymer nanocomposites

In these experiments, the low-temperature hydrothermal synthesis technique was used. The process was begun by weighing 1.25 g ammonium hexafluorotitanate ( $((\text{NH}_4)_2\text{TiF}_6)$ ) as the titanium source. The hexafluorotitanate was initially added to a glass beaker containing 100 ml of DI water and rigorously stirred for 10 min. About 50 ml of diethylene tri-amine was then added gradually to the solution under constant stirring for an elaborated time of 30 min. Further, the solution was poured into the Teflon lined stainless steel autoclave (having a capacity of 200 ml). The autoclave was heated in a hot air oven for 48 h. The temperature of the autoclave was

maintained to be  $180 \pm 2$  °C. Schematic representation of the synthesis procedure is shown in Fig. 3.1. The cooling of the autoclave was then accomplished under the ambient condition. The resultant solution was washed subsequently in DI water and ethanol in repeated cycles. Finally, the solution was dried in a vacuum oven at a temperature of 80 °C for a time span of 12 h. The synthesized powder was then separated from the container and stored in an airtight glass vial under dark condition.

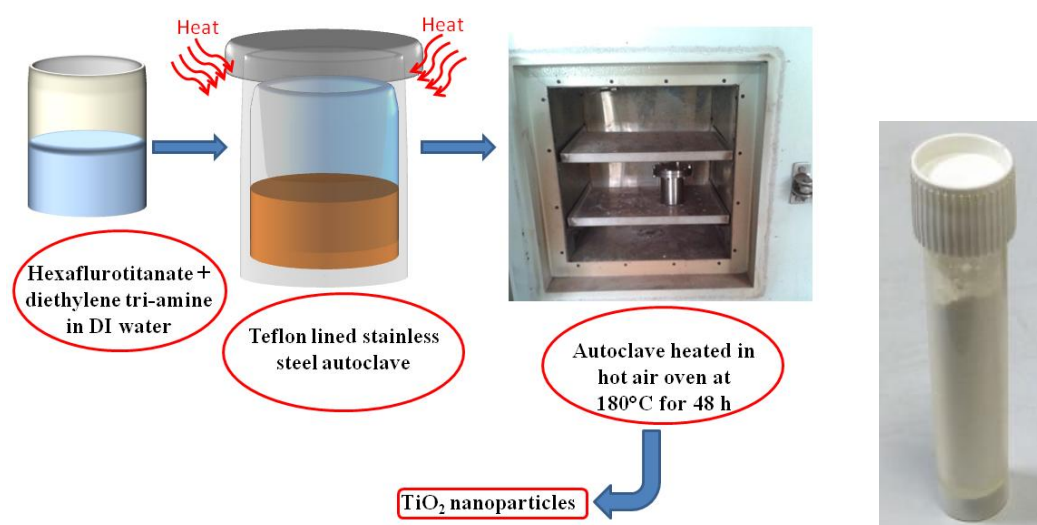


Fig. 3.1 Flowchart of synthesis procedure followed for the synthesis of TiO<sub>2</sub> nanoparticles.

The procedure is divided into two subsections, namely, the synthesis and the fabrication of composite films. First, low-temperature hydrothermal synthesis technique was used to synthesize titanium oxide (TiO<sub>2</sub>) nanoparticles. Secondly, the synthesized nanoparticles were used in the formation of composites using Nylon-6 polymer. The composite (Nylon-6/TiO<sub>2</sub>) was then utilized to fabricate thin films via spin casting. The following subsections provide details of both synthesis methodology as well as fabrication of the functional thin films.

### 3.2.2 Direct growth of high permittivity TiO<sub>2</sub> on the substrate

The process was begun by weighing 0.5 g of (NH<sub>4</sub>)<sub>2</sub>TiF<sub>6</sub> (purity: 99.99%, Sigma Aldrich) and followed by adding it to a glass beaker having 40 ml DI water. Further, 20 ml of diethanolamine (Sigma Aldrich) was added gently under constant stirring for a time span of 30 min. The colour of the solution was observed to be

turning into dark brown. Then, the resulting solution was transferred into a Teflon-lined stainless steel autoclave. FTO glass substrates (dimensions: 10 cm×2.5 cm×0.5 cm) possessing a sheet resistance of 12-15 Ω/sq were kept inside the autoclave. The FTO substrate was expected to provide the heterogeneous nucleation sites for the growth of TiO<sub>2</sub> thin film.

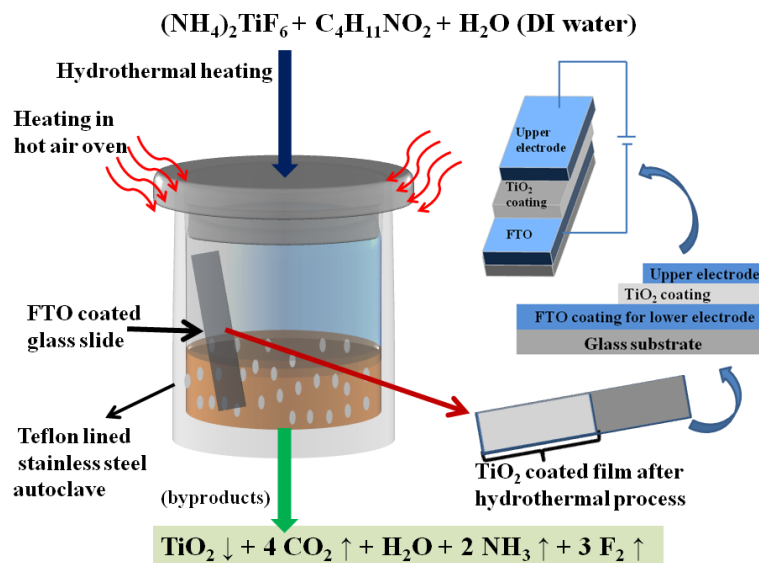
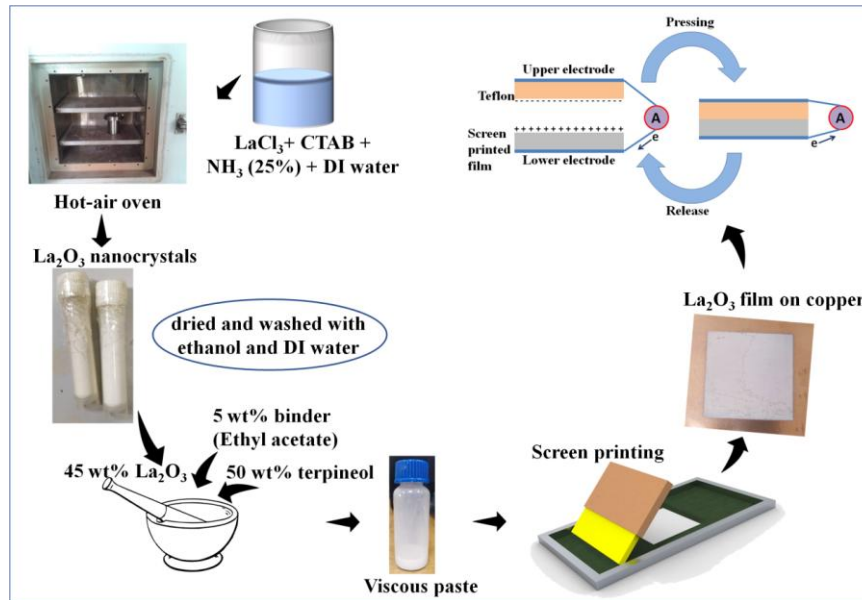


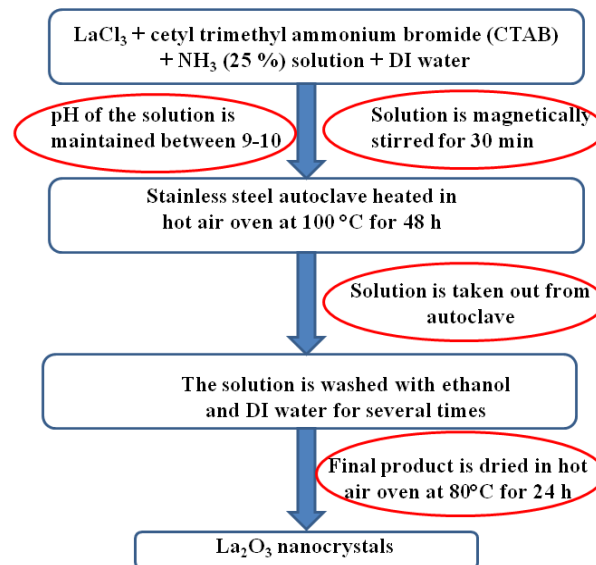
Fig. 3.2 Pictorial representation of the TiO<sub>2</sub> film growth on the FTO coated glass slide for dielectric application.

The nucleation followed by the growth of TiO<sub>2</sub> with a specific morphology is schematically presented in Fig. 3.2. The autoclave was subjected to thermal heating in a hot air oven for 24 h at different temperatures, i.e., 120 °C (termed as sample T), 150 °C (termed as sample T1) and 180 °C (termed as sample T2). The sample “T (at 120 °C)” had not yielded any output. In other words, the sample “T” has been characterized to confirm no deposition of TiO<sub>2</sub> on the glass slide. The autoclave was removed from the oven and was allowed to cool naturally. The deposited FTO substrates were collected and washed several times with the help of absolute alcohol and DI water. Finally, the coated FTO substrates were dried at 60 °C for 12 h (Cheng et al. 2014a).

### 3.2.3 Synthesis of lanthanum oxide ( $\text{La}_2\text{O}_3$ ) nanocrystals for screen printable paste in triboelectric energy generation



(a)



(b)

Fig. 3.3 (a) Schematic representation of synthesis procedure for the  $\text{La}_2\text{O}_3$  and fabrication of TENG device by using screen-printing technique and (b) flowchart for the synthesis procedure of  $\text{La}_2\text{O}_3$  nanocrystals.

In similar lines with  $\text{TiO}_2$  nanoparticles synthesis (in section 3.2.1) a pre-determined weight of (1.4 g) cetyl trimethyl ammonium bromide (CTAB) was added to a beaker containing 100 ml of DI water. The solution was stirred vigorously for few



min. Then, 3 g of  $\text{LaCl}_3$  salt was added to the same solution and stirred magnetically. Further, 3 ml of  $\text{NH}_3$  (25 %) solution was added dropwise to the solution so as to maintain a pH level of 9-10. The solution was stirred for twelve hours and a colloidal translucent appearance was noted. The prepared solution was poured into 200 ml Teflon lined stainless steel autoclave and kept in an oven at  $100\text{ }^\circ\text{C}$  for 48 h (as shown in Fig. 3.3). The products were subjected to various cycles of washing using DI water and ethanol, so to make the products free of residuals. Finally, the  $\text{La}_2\text{O}_3$  nanoparticles were dried in an oven at  $80\text{ }^\circ\text{C}$  for 24 h (Salavati-Niasari et al. 2011a).

### 3.2.4 Synthesis of zinc oxide (ZnO) nanoparticles for screen printable paste for triboelectric energy generation

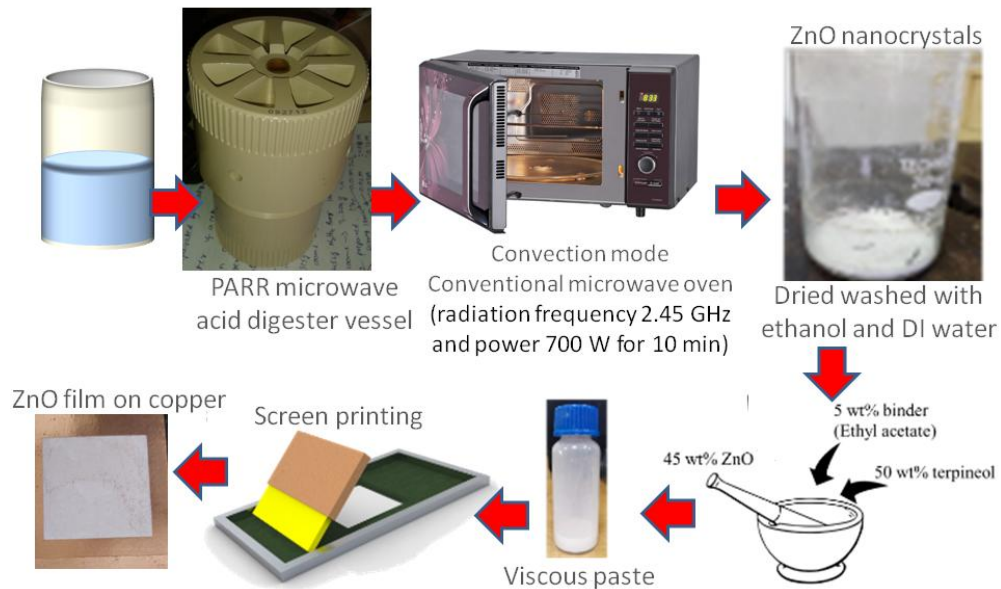


Fig. 3.4 Schematic representation of step-by-step procedure for the synthesis and fabrication of the ZnO based TENG device.

The aqueous precursor (0.5 M) of zinc nitrate hexahydrate ( $\text{Zn}(\text{NO}_3)_2 \cdot 6\text{H}_2\text{O}$ ) was prepared and stirred for 30 min to achieve a clear, homogeneous, and suspension-free liquid. Further, 0.5 M potassium hydroxide (KOH) was gradually added to the formed precursor under continuous mechanical stirring. Finally, ammonia solution (25 %) was added drop wise under vigorous stirring for 45 min to maintain the pH level between 10-11. The prepared precursor was found to be clear and suspension-free. The precursor was stored in an airtight bottle to check the time stability. The timely visual inspection ensured the stability of the precursor for several months.

Further, the aged precursor was poured into a beaker and placed in a convection-mode microwave oven for 10 min at a power rating of 700 W. The resulting solution was then cooled to room temperature and washed several times with DI water and alcohol to remove the impurities. Finally, the solution was allowed to dry in a hot air oven at 60 °C for 24 h to obtain ZnO nanoparticles. Schematic flow diagram for the procedure is shown in Fig. 3.4. The ZnO nanoparticles were stored in an airtight glass vial and stored in the dark.

### 3.2.5 Synthesis of graphene oxide (GO), ZnO and reduced graphene oxide (rGO)-ZnO for photocatalytic studies

#### 3.2.5.1 Synthesis of GO

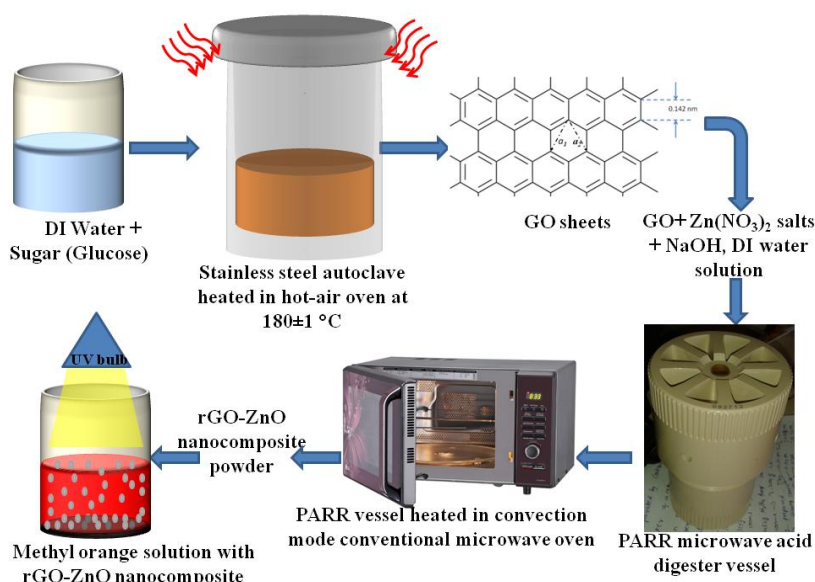


Fig. 3.5 Schematic representation of the hydrothermally synthesized GO in the preparation of microwave hydrothermal synthesis of rGO-ZnO nanocomposite.

The GO was synthesized by adopting the hydrothermal route (Tang Lau method). 0.5 M sugar solution was prepared by the complete dissolution of sugar crystals in DI water. Further, Teflon lined stainless steel autoclave (volume capacity: 200 ml) was filled with the as-prepared sugar solution up to half the capacity (~ 100 ml). The autoclave was heated in a hot air oven to a temperature of 180±2 °C for an elaborated time span of 80 min. The autoclave was then cooled to room temperature. GO was then scooped from the resultant solution and washed with DI water, multiple

times to make the product-GO free of residues. The obtained GO powder was then stored in an airtight bottle and stored in the dark for future usage.

### **3.2.5.2 Synthesis of rGO-ZnO nanocomposites**

The schematic of synthesis procedure is as shown in Fig. 3.5. The rGO-ZnO nanocomposites were synthesized using microwave-assisted hydrothermal method. A known weight corresponding to a magnitude of 140 mg GO was added to 20 ml DI water and allowed to sonicate under intense ultrasound waves for a time span of 30 min. 1.785 g (0.3 M) of  $\text{Zn}(\text{NO}_3)_2 \cdot 6\text{H}_2\text{O}$  was added to the resulting solution. The entire solution was maintained under constant stirring and 2 M NaOH solution in DI water was added drop wise to achieve the pH level of 10-11. Further, the prepared solution was transferred to a 24 ml capacity Parr acid digestion vessel. The digestion vessel was heated in a microwave oven (radiation frequency 2.45 GHz and power 700 W) in convection mode for 10 min. After the microwave heating, it was found that the colour of the suspension had changed into grayish-black, which indicates the successful chemical reduction of GO nanosheets (GONs) (Wu et al. 2012). The solution was transferred to a beaker and washed with DI water and ethanol several times; finally, the sample-solution was dried at a temperature of 70 °C for 12 h. For the comparison and consistency in the results, bare-ZnO nanoparticles were synthesized by employing the following procedure, without the addition of GO. In order to assess the effect of Zn-precursor, the rGO-ZnO nanocomposite was synthesized using  $\text{ZnCl}_2$  as the source of zinc instead of  $\text{Zn}(\text{NO}_3)_2 \cdot 6\text{H}_2\text{O}$  and maintaining other crucial parameters of the synthesis as same. The rGO-ZnO nanocomposite was also prepared from the GO synthesized using well-known and standard Hummer's method (Wang et al. 2011a) to compare the catalytic performance with that of Tang Lau method (Tang et al. 2012) derived GO.

## **3.3 Thin Film Fabrication**

### **3.3.1 Fabrication of Nylon-6/TiO<sub>2</sub> composite polymer thin films for dielectrics applications**

The composite, Nylon-6/TiO<sub>2</sub> is required to be in the solution form to cast it onto the substrate of interest. To accomplish the same, the synthesized TiO<sub>2</sub>

nanocrystals (as explained in section 3.2.1) was initially dispersed into 20 ml formic acid and kept on the shelf to check its stability over a week. Further, the dispersion was firmly stirred on a hot plate at room temperature, followed by the gradual addition of a known weight of Nylon-6. The resulting composite solution was sealed in conical flask and stirred for a day to attain uniform distribution of the Nylon-6 and TiO<sub>2</sub> nanoparticles. Three different mixtures of Nylon-6/TiO<sub>2</sub> solution were prepared with varied concentrations of the TiO<sub>2</sub> nanoparticles, which are namely, 5 %, 10 % and 20 % (hereafter are denoted by NT5, NT10, NT20, respectively) and fixed concentration of Nylon-6. On the other hand, the fluorine-doped tin oxide (FTO, sheet resistance: 10-15 Ω/sq) substrates of dimension 2.5 cm× 2.5 cm× 0.5 cm were subjected to cleaning with the help of organic solvents and flowing nitrogen gas drying.

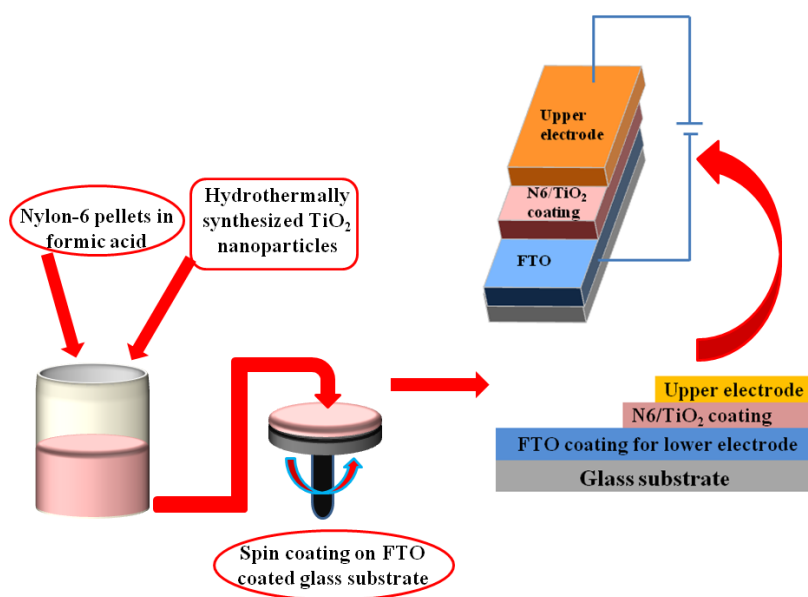


Fig. 3.6 Schematic representation of the thin film fabrication of the Nylon-6/TiO<sub>2</sub> on the FTO coated glass slides.

The standard cleaning procedure constituting acetone/DI water/isopropyl alcohol/DI water was used. Further, without any time-lapse, the solution was loaded to a spin coating chamber and the composite solutions were spin-coated with spinning parameters of 3000 rpm and 30 s. The dielectric film fabrication is explained in Fig. 3.6. The coated glass substrates were vacuum dried in an oven at 40 °C for 30 min.

The samples were characterized for their dielectric response to the applied electric field using an impedance analyzer (IM3536, Hioki, Japan).

### **3.3.2 The direct growth of TiO<sub>2</sub> thin film on glass/FTO substrate for dielectrics applications**

The hydrothermal TiO<sub>2</sub> film deposition procedure is already explained (in the section 3.2.2). As deposited TiO<sub>2</sub> on FTO coated glass-slides were not further treated and directly used for characterization to examine their various properties. The films were later subjected to impedance analysis to estimate the dielectric response under the input electric field.

### **3.3.3 Fabrication of screen printed La<sub>2</sub>O<sub>3</sub> thin films for triboelectric application**

The screen-printable quality paste with embedded La<sub>2</sub>O<sub>3</sub> nanoparticles was prepared (explained in section 3.2.3). The paste was formulated using 45 wt. % La<sub>2</sub>O<sub>3</sub> nanoparticles, 5 wt. % ethylcellulose-binder and 50 wt. % of terpinol solvent. The resultant mixture was then ground rigorously in a Mortar-pestle for 30 min to achieve highly viscous and agglomeration-free screen printable La<sub>2</sub>O<sub>3</sub> paste. The mask for the screen printing was created on the other hand with the help of a screen having #120 mesh. The snap-off distance of 5-10 mm was maintained to facilitate the quick release of screen during the course of printing. The substrate for the screen printing was intentionally and intelligently selected to fulfill the requirements of a flexible electrode for the device. The flexible and conductive copper adhesive tape was found to fit within the requirements and was directly employed for the thin film fabrication. The printed thin films were allowed to dry under the continuous irradiation of infrared beam for a prolonged time of three hours, which makes the film free of deteriorating solvent by allowing it evaporate to the surrounding ambiance.

### **3.3.4 Fabrication of screen printed ZnO thin films for triboelectric applications**

The synthesized ZnO nanoparticles (explained in section 3.2.4) was used for preparing screen printable paste. Screen with #120 mesh was used to create the mask and used for screen printing. While screen printing, 5 to 10 mm of snap-off distance was maintained to ensure non-adhesive quick release of the screen without leaving an

unwanted permanent texture onto the as-printed wet film. Solvent cleaned (i.e., cleaned with isopropyl alcohol, acetone, and DI water in exact order) and dried copper adhesive tape/foil was directly used as a supporting substrate for the screen printing process, since, copper acts as an electrode and the adhesive gum helps in effortless device fabrication with acceptable mechanical flexibility. The printed film was then dried under IR irradiation for 2 h for the complete evaporation of the solvent. The processed ZnO film was found to possess an optimized thickness of 2  $\mu\text{m}$ , which were measured using Dektak<sup>®</sup> profilometer.

### **3.4 Applications of Various Functional Materials**

#### **3.4.1 High permittivity dielectrics application**

The Nylon-6/TiO<sub>2</sub> composite polymer thin films (explained in section 3.3.1) and directly grown TiO<sub>2</sub> films on FTO coated glass-slides (explained in section 3.3.2) were subjected to impedance studies to find out the effective relative permittivity.

#### **3.4.2 Triboelectric characterization of screen-printed films**

The triboelectric device was fabricated with screen-printed La<sub>2</sub>O<sub>3</sub> (in section 3.3.3) and ZnO (in section 3.3.4) film as an active layer in the architecture. The device assembly has two major parts, namely, a rigid stationary part and an oscillating part. The rigid frame was fabricated using laser-cut acrylic sheets, which were directly procured from a local vendor. Here, a 4 mm thick acrylic sheet was used as the bottom substrate, and 8 mm thick sheet was used as the structural support for the oscillating part. The screen-printed film adheres to the bottom acrylic substrate, which acts as a stationary tribo-active layer. While for the counter tribo surface, the copper-cladded PTFE is adhered onto the brass block with PTFE exposed towards the active (La<sub>2</sub>O<sub>3</sub> and ZnO) layer. The assembly was then suspended using a commercially available 180 GSM elastic band, which was pre-stretched to  $\approx 120\%$ .

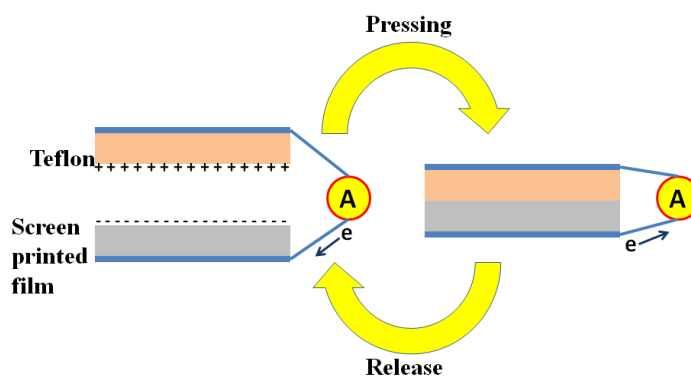


Fig.3.7 Architecture and working principle of contact-separation mode triboelectric device.

Here, cyanoacrylate (fevi-kwik<sup>®</sup>) was used for bonding brass to elastic and the elastic band to the acrylic support member. Enough spacing was machined inside the copper block to compensate for the solder bumps as and where required so that the exposed PTFE surface was expected to remain smooth. The device architecture and working principle of TENG device is explained with the pictorial diagram in Fig. 3.7. When the two surfaces of the active film (ZnO or La<sub>2</sub>O<sub>3</sub>) and Teflon are separated by a small distance, the charges segregate on the surface due to triboelectric effect. When they are sliding with each other, the contact between their surface increases and hence energy is generated (Saravanakumar et al. 2013).

### 3.4.3 Observation of photocatalytic activity of bare-ZnO and rGO-ZnO

The photocatalytic ability of the prepared rGO-ZnO nanocomposite (section 3.2.5) and ZnO nanopowders were evaluated by monitoring the degradation of standard methyl orange (MO) dye (25 mg/L) in aqueous solution. A 15 W deuterium lamp was used as the UV light source as the photocatalytic stimulus. 50 ml each of the above-prepared MO dye solution were taken in two separate beakers where 25 mg of catalyst (rGO-ZnO and ZnO) was added separately. Initially, the solution was stored in the dark and stirred for 30 min to establish absorption-desorption equilibrium between the dyes and photocatalysts. The solution was then placed under the UV light, and it was continuously stirred during the exposure. 5 ml solution from the system was then collected at every 20 min time interval. The collected solution was centrifuged for a few minutes to separate the catalyst in the solution. The

absorbance was measured at the wavelength of 464 nm using UV-visible double beam spectrophotometer (Systronics, Model-2201, NITK Surathkal, India). The relative degradation activity was expressed as  $(C_f/C_o)$  vs.  $t$ ; where,  $C_f$  stands for the real-time concentration of MO and  $C_o$  designates the initial concentration soon-after the absorption-desorption equilibrium.

### 3.5 Characterization Techniques Employed in the Present Study

Phase identification of the sample was carried out by using X-ray diffractometer (XRD, make-JEOL-JPZ 8 and thin film XRD, make-Rigaku) using copper target (Cu  $K_\alpha = 1.54 \text{ \AA}$ ). The interlayer spacing was estimated using Bragg's relation as expressed in equation 3.1

$$d = \frac{n\lambda}{2 \sin\theta} \quad (\text{Eq. 3.1})$$

Where,  $d$  is the interlayer spacing (in Armstrong units),  $\lambda$  is the wavelength of the X-rays used and  $\theta$  is the diffraction angle or Bragg angle. The Rietveld refinement of the procured XRD pattern of the material was carried out by using the General Structural Analysis System (GSAS) software suite (Larson and Dreele 2004; Toby and Expgui 2001). The Bragg peak profiles were modeled with pseudo-Voight type-3 function.

Further, to identify the presence of rGO in rGO-ZnO nanocomposite (explained in section 3.2.5), XRD patterns were also recorded at Stanford Synchrotron Radiation Light-source (SSRL), Menlo Park, U.S.A. (Ahmad et al. 2015). The diffraction pattern was recorded at an incident X-ray energy of 12 keV, while  $\omega$  was fixed at  $3^\circ$ . To improve powder averaging, the sample was rocked for  $1^\circ$  during recording. The response of the diffracted intensity against the scattering vector "Q" was plotted. The relation between the scattering vector and  $d$ -spacing is given by the equation 3.2

$$Q = \frac{2\pi}{d} \quad (\text{Eq. 3.2})$$

Combining equation 3.2 with Bragg's law equation 3.1, the scattering vector can be expressed as equation 3.3.



$$Q = \frac{4\pi \cdot \sin(\theta)}{\lambda} \quad (\text{Eq. 3.3})$$

The X-ray photoelectron spectroscopy (XPS- Kratos Analytical, UK, monochromatic Al K $\alpha$  ~1486.6 eV as X-ray source and XPS; PHI5000VersaProbeII) was performed to analyze the chemical nature (composition and oxidation states) of the samples. Prior to the XPS measurements, the samples were treated under Argon gas to remove the surface contamination, mainly physically adsorbed carbonaceous impurities and moisture. The binding energy scaled was referred to in electron volts (eV) and to an accuracy of 0.2 eV. All the XPS data were calibrated with the standard C 1s peak centered at 284.7 eV. The deconvolution of the individual elemental shells (such as O 1s, C 1s, N 1s, La 3d, Ti 2p and Zn 2p) was performed by subtracting the background using Shirley background function and utilizing the Gaussian-Lorentzian product function with area resolution of 1 eV.

The surface features, elemental composition and morphology of the samples were investigated by using field emission scanning electron microscopy (FESEM, make-JEOL, Tokyo, Japan) and transmission electron microscopy (TEM, JEOL-JEM-2100, operating voltage: 200 kV, Tokyo Japan) while the chemical composition was carried out by using energy-dispersive X-ray spectroscopy (Oxford Instruments, Oxfordshire, UK). The TEM samples were prepared by drop casting the colloidal sample on a carbon-coated Cu grid and allowing it to evaporate by heating under the bulb (60 W) for 8 h.

The quality and the formation of synthesized materials and ceramic nanoparticles samples were examined by using Fourier transform infrared (FTIR, make-JASCO-4200) spectrometer in attenuated total internal reflection (ATR) method as well as KBr pellet method. The band energy was studied at room temperature using Raman spectroscopy (Raman, machine-Horiba Jobin Yvon - LabRAM HR spectrometer). The wavelengths of the laser source used were 325 and 514 nm.

DSC (Netzsch; Model DSC-404 F1, Germany) measurements for synthesized materials were performed by heating the aliquots of the samples from room temperature to different temperatures depending on the nature of the materials at different heating rates under the nitrogen atmosphere using aluminum/alumina pans.

The nitrogen gas flow rate was maintained at 80 ml/min inside the DSC furnace throughout the measurement, to avoid the undesired reaction of the sample with ambient atmosphere.

The TG analysis for the samples was carried out by using (Thermo-Gravimetric Analyzer; PerkinElmer, TGA 4000) over the temperature range of 50 – 800 °C at a heating rate of 20 °C/min. The specific surface area measurement was performed using a Brunauer-Emmett-Teller (BET) apparatus under the standard protocols at 77 K. The samples were degassed under flowing N<sub>2</sub> at 300 °C for overnight prior to BET measurements (Sivasankaran and Kishor Kumar 2015).

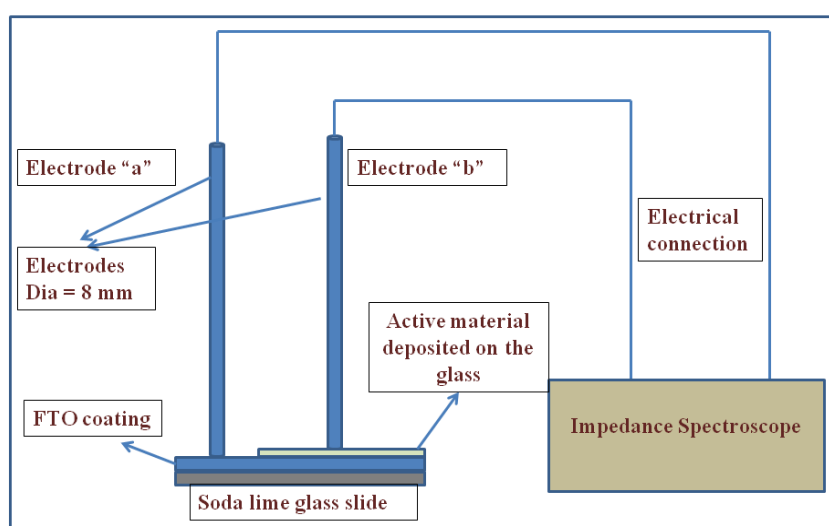


Fig. 3.8 Figure showing the schematic representation of the impedance measurement.

The impedance analyzer (IM3536, Hioki, Japan) was used for measuring dielectric constant, dielectric loss and AC conductivity of the samples in the frequency range of 4 Hz to 1 MHz. The details of the electrode parameters and dielectric properties measurement of films are schematically presented in Fig. 3.8. The impedance measurement of the film samples (explained in section 3.3.1 and 3.3.2) was performed using the same setup, as shown in Fig. 3.8.

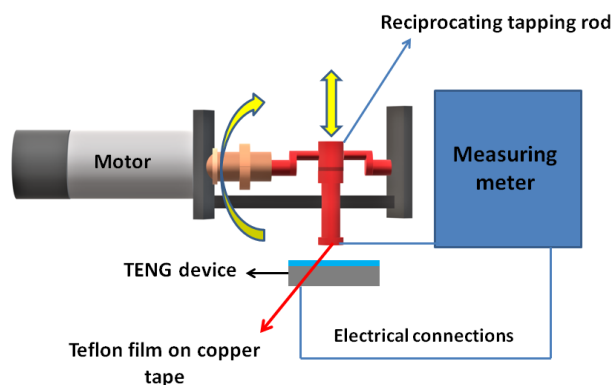


Fig. 3.9 Pictorial representation of the triboelectric properties assessment using motorized fixture.

To elucidate the triboelectric response of synthesized functional metal oxides, the screen-printed film counterparts of the oxides were tested in an in-house built motorized fixture, as shown in Fig. 3.9. The Teflon was used as a counter surface for testing the triboelectric performance of films since Teflon is fluorine rich, highly electronegative, and cost-effective. The tribonegative characteristics of Teflon produce maximum voltage with any material. While testing, the fixture was operated at around 10 Hz with a contact load of around 300 g. The electrical parameters (i.e., voltage and current) were logged using an oscilloscope (Tektronix DPO 2014B) and Keithley parameter analyzer (4200s), respectively. The triboelectric measurement of the film samples (explained in section 3.3.3 and 3.3.4) was performed using the same setup, as shown in Fig. 3.9.

*Page intentionally left blank*

# CHAPTER 4

The content of this chapter have been published in *Journal of Applied Physics A*,  
*126 (4), 1-11, 2020, doi.org/10.1007/s00339-020-3445-4.*

*Page intentionally left blank*

## CHAPTER 4

### DIELECTRIC BEHAVIOUR OF NYLON-6/TITANIUM DIOXIDE POLYMER COMPOSITE

*This chapter deals with the hydrothermal growth and characterization of the TiO<sub>2</sub> nanorods. Further, the as grown TiO<sub>2</sub> nanorods were used in fabricating the Nylon-6-TiO<sub>2</sub> polymer nanocomposites for the parallel plate capacitor application.*

#### 4.1 Introduction

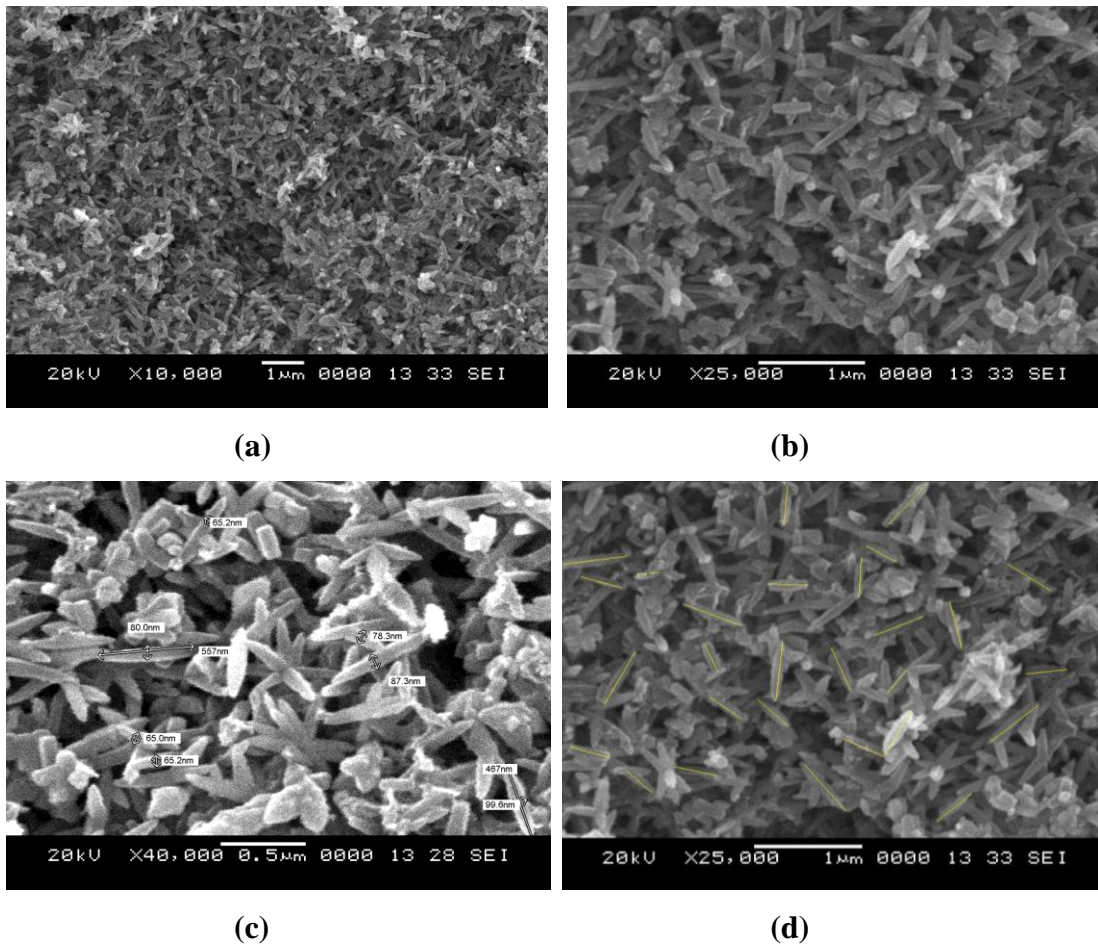
The polymer nanocomposites allow physical property tailoring using different types of conducting and semiconducting fillers. The properties of the polymer matrix can be tuned by usage of many types of the fillers with different particle size, particle shape, chemical nature and specific surface area. The mechanical, electrical, optical, magnetic and thermal properties of the polymer nanocomposites are tuned by introducing ceramic fillers into the polymer matrix. The polymer nanocomposites can be drawn into different shapes like wires and thin films due to their high elasticity and flexibility of the matrix. Owing to the continuous developments in the miniaturization of electronic devices, high-dielectric constant polymer-ceramic nanocomposites have become promising materials for capacitor applications. These polymer-ceramic nanocomposite capacitors, apart from showing high capacitance, exhibit the reduction in the dielectric loss compared to ceramic capacitors. In this regard, TiO<sub>2</sub> which is thermally stable up to 400 °C has been considered to explore its possible application in fabricating new generation composites with high dielectric permittivity in capacitor applications. Hence, it is essential to understand the dielectric behaviour of the polymer-ceramic composites as the property of the composites depend on the type of polymer and structure, type of filler and micro-capacitor network effect at the interface between polymer-ceramic. The Nylon-6, a widely used thermoplastic polymer with good mechanical properties associated with low cost and the composite with TiO<sub>2</sub> based films are studied in detail.

In the present chapter, the composite films of Nylon-6 (N6) matrix with hydrothermally synthesized TiO<sub>2</sub> nanoparticles at different weight fractions (5, 10 and

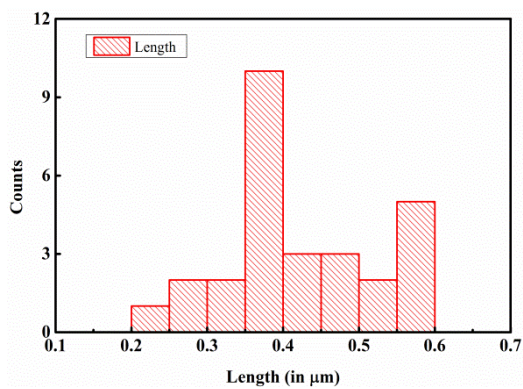
20 %) are subjected to dielectric permittivity measurements and the results are discussed systematically. Firstly, the solution constituting the matrix material-N6 and the reinforcement-TiO<sub>2</sub> is prepared. The details related to the synthesis and the quality of TiO<sub>2</sub> are discussed in chapter 3, section 3.2.1. The formulated precursor of the composite N6/TiO<sub>2</sub>, which is referred to as NT-nanocomposite hereafter (example: 5%-NT5 and so on.), was utilized for the fabrication of films on a glass substrate using spin coating. The produced films were tested for their dielectric response. The following subsections detail the results.

#### 4.2 Electron Microscopic Analysis of the Synthesized TiO<sub>2</sub> Nanoparticles

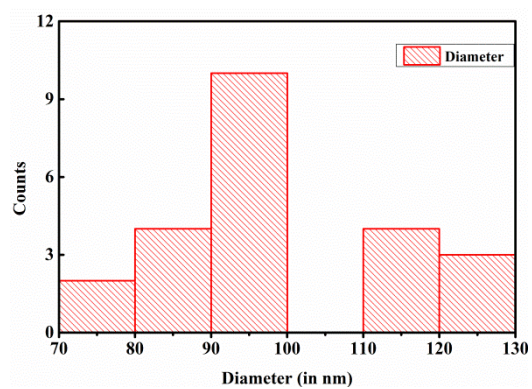
Initially the synthesized TiO<sub>2</sub> nanoparticles are characterized by using SEM, TEM and XRD to confirm the morphology, phase purity and composition. To study the morphology of the synthesized TiO<sub>2</sub> nanoparticles SEM and TEM were used and corresponding micrographs are presented in Fig. 4.1.



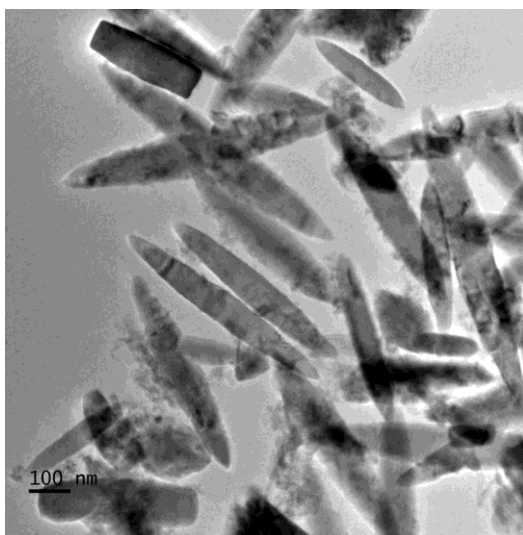




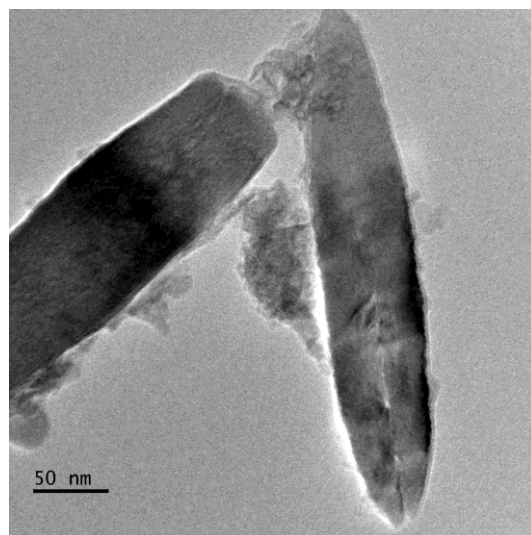
(e)



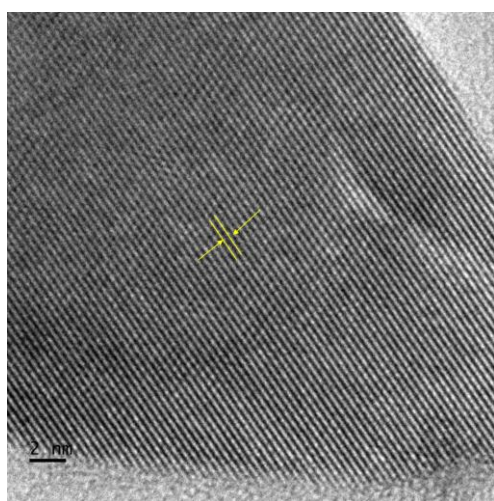
(f)



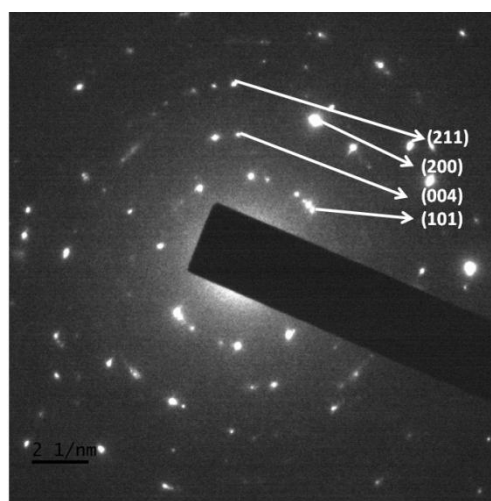
(g)



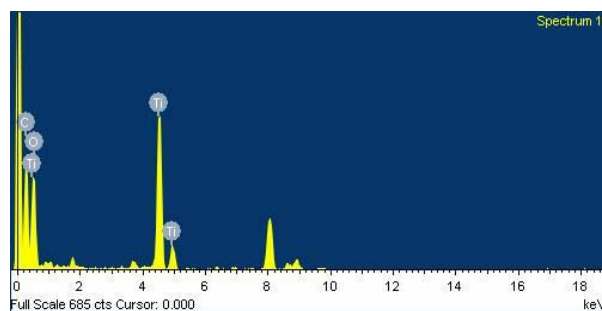
(h)



(i)



(j)



(k)

Fig. 4.1 (a-d) Scanning electron micrographs of TiO<sub>2</sub> nanoparticles at different magnifications (e & f) histogram of variation of crystallite size distribution, (g-i) low and high magnification transmission electron micrographs depicting size, shape and fringe pattern of TiO<sub>2</sub> nanorods, (j) SAED pattern and (k) TEM-EDS spectrum of TiO<sub>2</sub> nanorods.

The SEM micrographs in Fig. 4.1 (a) and (b) present the morphology of the TiO<sub>2</sub> nanoparticles. It could be observed that the synthesized nanoparticles are uniform and acicular in shape and size. Fig. 4.1 (c) and (d) shows that TiO<sub>2</sub> is having dimensions varying about 50 to 70 nm in diameter and length varying from 100 to 600 nm. The same has been inferred by plotting particle size distribution histogram. The histogram of particles is plotted in Fig. 4.1 (e) and (f). The histogram shows that TiO<sub>2</sub> nanoparticles length varies from 200 nm to 600 nm. The diameter varies from 70 to 130 nm. The representative high-resolution TEM micrograph of a single TiO<sub>2</sub> nanorod is shown in Fig. 4.1 (g) and (h). The high-resolution micrograph of TiO<sub>2</sub> nanorod shows a set of lattice fringes, with a spacing of 0.35 nm (Fig. 4.1 (i)), corresponding to the (101) planes of the anatase phase. The interplanar spacing ‘*d*’ is in good agreement with the *d*-space calculated using equation 3.1 from XRD data. The size of the crystallites is an essential factor affecting the dielectric constant of TiO<sub>2</sub>, since the exposed surface area in the single TiO<sub>2</sub> nanorod is high and the charge is stored on the surface of the crystal. The SAED pattern (Fig. 4.1 (j)) of TiO<sub>2</sub> showed that the synthesized material is polycrystalline in nature. The TEM-EDS spectrum and the corresponding atomic percentage are shown in Fig. 4.1 (k). The spectrum shows the presence of only two elements, that is Ti and O. The carbon peak is originated from the carbon-coated copper TEM grid and adsorbed carbon on TiO<sub>2</sub> nanorods during synthesis process.

### 4.3 Structural Analysis of TiO<sub>2</sub> and NT Polymer Nanocomposites

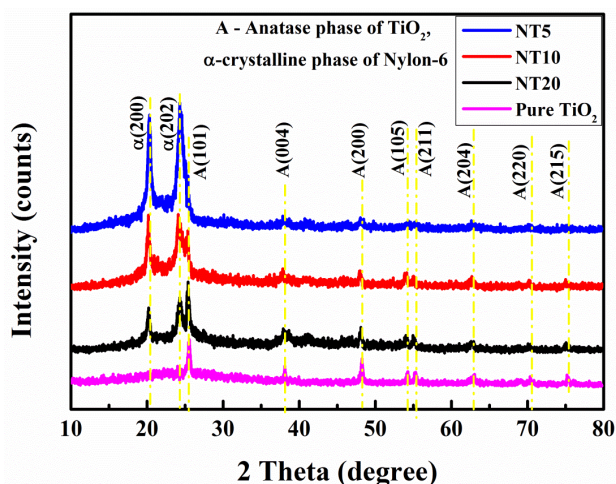


Fig. 4.2 The XRD spectra of NT5, NT10, NT20 and pure TiO<sub>2</sub> nanoparticles.

The XRD studies of the samples were over 10° to 80°, with a scanning speed of 1°/min. The XRD spectra of hydrothermally synthesized TiO<sub>2</sub> nanoparticles and NT nanocomposite films are shown in Fig. 4.2. The spin-coated NT polymer nanocomposites were analyzed by using XRD technique to understand the effect of variation of the weight of TiO<sub>2</sub> and subsequent formation of the NT polymer nanocomposites. For the TiO<sub>2</sub> nanoparticles, the diffraction peaks at 25.4°, 38.1°, 48.2°, 54.1°, 55.3°, 62.9°, 70.3° and 75.2° are observed to be the reflections from the planes (101), (004), (200), (105), (211), (204), (220) and (215), respectively, and are assigned to the pure anatase phase of TiO<sub>2</sub> (ICDD 21-1272) (Meti et al. 2015; Chowdhury et al. 2015). The interplanar spacing '*d*' calculated from the Eq. 3.1 for (101) reflection plane is 0.3503 nm. The observation of diffraction peaks for the samples NT5, NT10 and NT20 shows the corresponding XRD reflections for the N6 polymer and TiO<sub>2</sub> particles. The two intense diffraction peaks observed at 20.3° and 24.2° corresponds to (200) and (202) planes of the  $\alpha$ -phase of the N6 polymer in all the NT samples (Vasanthan and Salem 2001). The peak intensities of anatase TiO<sub>2</sub> are less for NT5 and become predominant in the case of NT10 and NT20. From the XRD results, it is concluded that the NT polymer nanocomposites exhibit similar diffraction peaks as pristine TiO<sub>2</sub> suggesting the presence of TiO<sub>2</sub> secondary phase in the NT

polymer nanocomposites. This is consistent in all XRD responses, irrespective of the weight fraction of TiO<sub>2</sub> reinforcement.

#### 4.4 Raman Spectroscopic Analysis of NT Polymer Nanocomposites

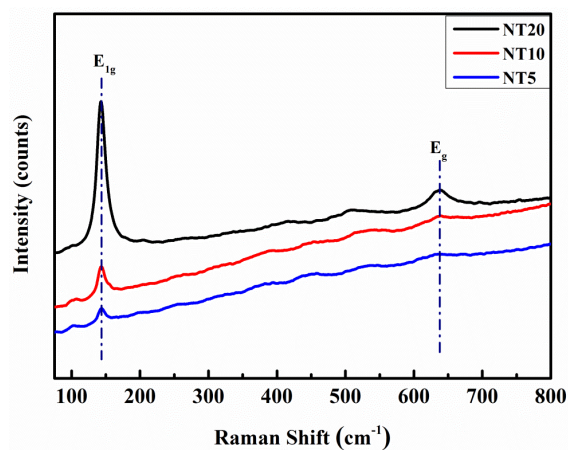
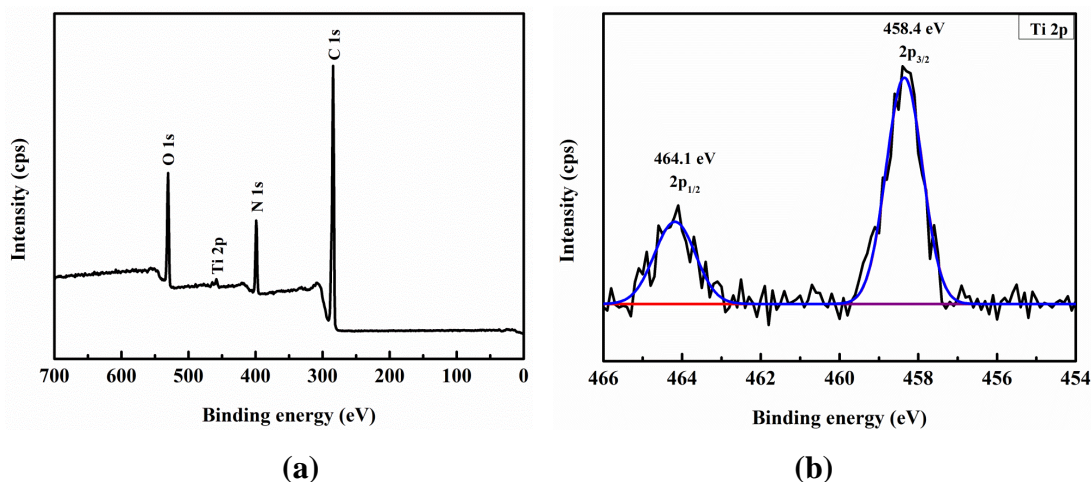


Fig. 4.3 Raman spectra showing characteristic bands of the TiO<sub>2</sub> in the NT polymer nanocomposites.

Figure 4.3 shows Raman spectra for the NT polymer nanocomposites. The specific (E<sub>1g</sub>) vibration mode of the typical anatase phase of TiO<sub>2</sub> exists at 144 cm<sup>-1</sup> for NT5 and NT10 samples. For the NT20 sample, the specific vibration modes at 144 cm<sup>-1</sup> (E<sub>1g</sub>) and 637 cm<sup>-1</sup> (E<sub>g</sub>) are predominantly seen in the spectra. The intensity of E<sub>1g</sub> vibration mode is higher for the NT20 sample because of the presence of a greater quantity of TiO<sub>2</sub> in the NT nanocomposite compared to NT10 and NT5 samples.

#### 4.5 Chemical Composition of NT Polymer Nanocomposites Using XPS



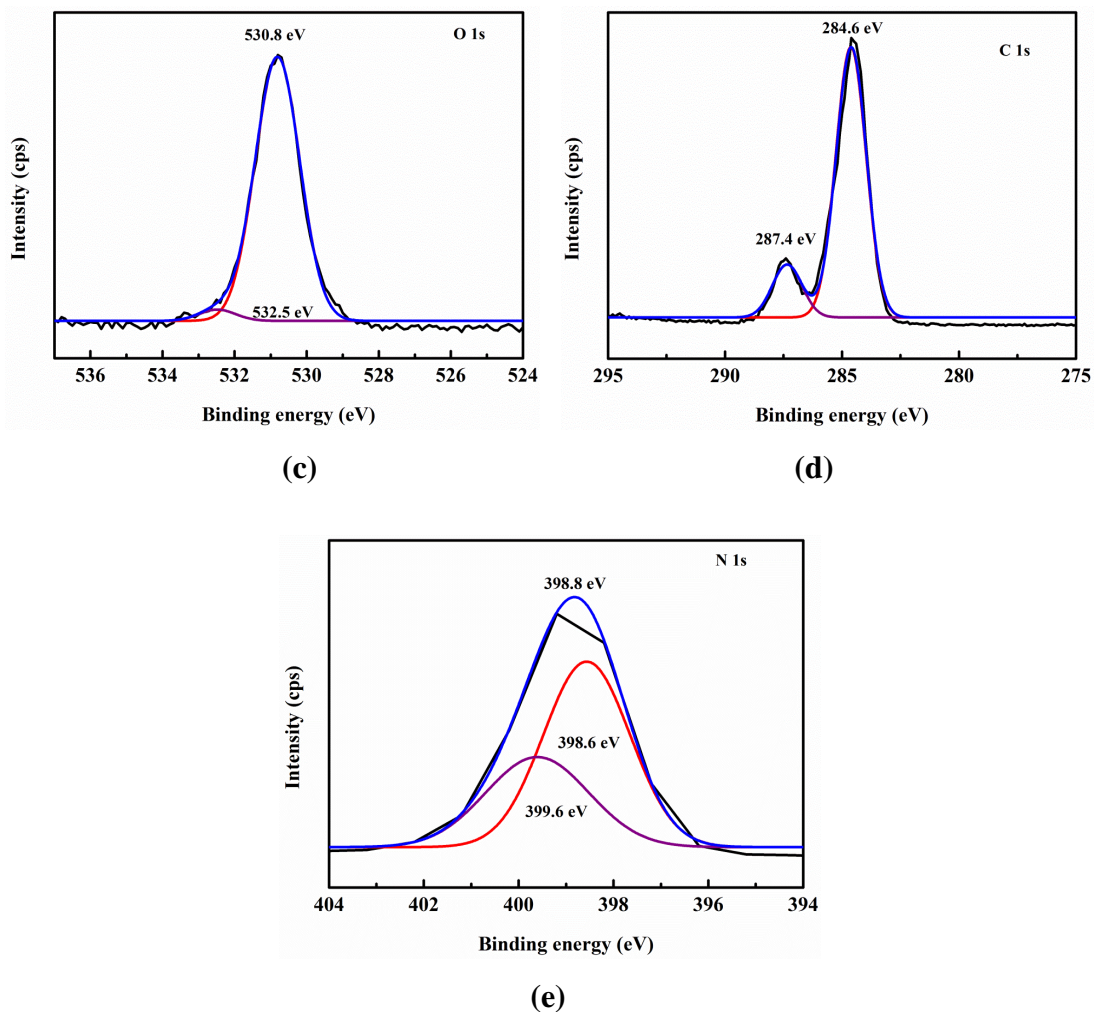


Fig. 4.4 XPS survey spectrum of (a) NT polymer nanocomposite showing the presence of only C, O, N and Ti elements, (b) Ti  $2p$ , (c) O  $1s$ , (d) C  $1s$  and (e) N  $1s$ .

The chemical states of elements in NT polymer nanocomposites are analyzed by using XPS, as shown in Fig. 4.4. The survey spectrum indicates responses, which correspond to four elements, namely, carbon, oxygen, titanium and nitrogen, as shown in Fig. 4.4 (a). Figure 4.4 (b) represents the high-resolution XPS Ti  $2p$  spectrum for the NT nanocomposite sample, where the spin-orbit doublet present at 458.4 and 464.1 eV are attributed to the Ti  $2p_{3/2}$  and Ti  $2p_{1/2}$ , respectively (Pu et al. 2013; Ramadoss and Kim 2013). The high-resolution O  $1s$  spectrum of the NT nanocomposite sample exhibited different peaks as shown in Fig. 4.4 (c). The peak at 530.8 eV corresponds to the Ti-O bonding state. The peak at 532.5 eV in the O  $1s$  spectrum supported the presence of oxyhydroxide group in the NT nanocomposite (Chen et al. 2017c; Liu et al. 2012a). Figure 4.4 (d) shows the deconvoluted C  $1s$

spectrum of NT sample. The minor peak present at 287.4 eV corresponds to C-O and C-OH functional group in the Nylon-6 polymer. The peak at 284.6 eV corresponds to methylidyne (CH) and ethynyl (CCH) functional groups of Nylon-6 polymer (Yu et al. 2016a). The high-resolution spectrum of N 1s in Fig. 4.4 (e) is deconvoluted into two peaks corresponding to 398.6 eV and 399.6 eV. The peaks are assigned to  $sp^2$  hybridized nitrogen (N) of (O=C-N) and [(H-N-(C)<sub>2</sub> or N-(C)<sub>3</sub>] groups.

#### 4.6 FTIR Analysis of NT Polymer Nanocomposites

To investigate the bonding state of the NT polymer nanocomposites, the FTIR analysis was carried out. As shown in the Fig. 4.5, the absorption peaks at 3302  $cm^{-1}$  and 692  $cm^{-1}$  belong to the O-H and N-H stretching and vibrating peaks of the N6 film. The peaks at 1640  $cm^{-1}$  and 1541  $cm^{-1}$  are attributed to the absorption peak of adsorbed water and polyamide configuration of the spin-coated N6 film (Esfahani et al. 2015). The peak at 1266  $cm^{-1}$  is assigned to the C-N stretching absorption peak of N6 polymer (Abdal-hay et al. 2013). The absorption peaks at 1372 and 2938  $cm^{-1}$  are attributed to the CH<sub>2</sub> asymmetric stretching vibrations.

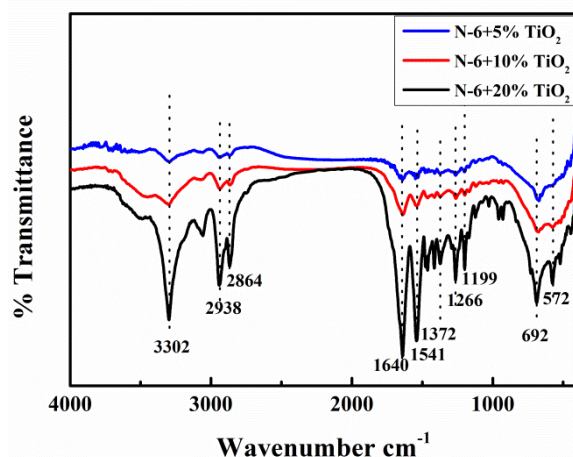


Fig. 4.5 The FTIR spectra of NT5, NT10 and NT20 polymer nanocomposites.

The characteristic CH<sub>2</sub> stretching and wagging vibration peaks are detected at 2864  $cm^{-1}$  and 1199  $cm^{-1}$  in the N6 structure (Esfahani et al. 2015). The broad Ti-O inorganic group stretching peak is observed in the range of 400-900  $cm^{-1}$  (Kaur and Verma 2014)(Fang et al. 2008b). The peak at 572  $cm^{-1}$  is ascribed to the absorption

bands of Ti-O and O-Ti-O flexion vibration (Lv et al. 2009). The Ti-O absorption peak is comparatively more intense for sample NT20, lesser for NT10 and still minor for NT5, due to the variation of TiO<sub>2</sub> weight percentage in the samples. Therefore, the existence of TiO<sub>2</sub> particles are confirmed in the N6 matrix and it is found that the TiO<sub>2</sub> nanoparticles have no or little effect on the atomic structure of the N6.

#### 4.7 Thermal Analysis of NT Polymer Nanocomposites Using DSC

Figure 4.6 shows the DSC spectra of the NT polymer nanocomposites. The DSC spectra show endothermic melting peak, associated with the  $\alpha$ -phase crystals for all NT polymer nanocomposites films. The melting temperature of the NT polymer nanocomposites film is measured from maximum of endothermic peaks. The melting temperatures for N6 matrix in the NT5, NT10 and NT20 samples are measured to be 210, 211 and 214 °C, respectively. It is also seen that the melting temperature of N6 in NT polymer nanocomposites increases slightly with an increase in loading of the TiO<sub>2</sub> nanoparticles filler content.

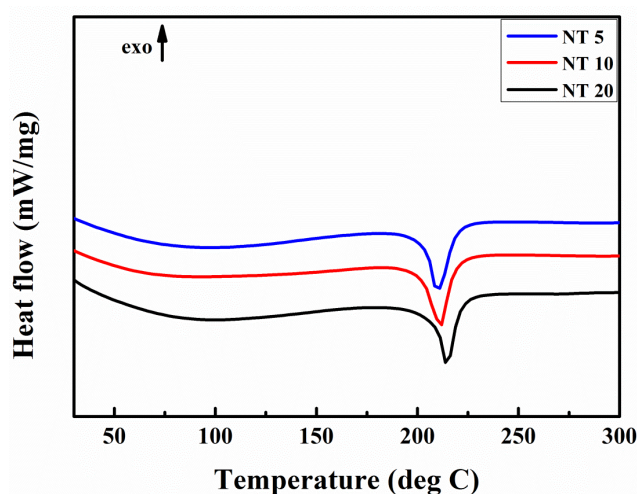


Fig. 4.6 The DSC spectra show the NT nanocomposite samples with different weight fractions of the TiO<sub>2</sub> filler.

The crystallization and degree of crystallinity of the NT polymer nanocomposites are influenced by the length of the repeated units and even-even state of N6 polyamide to form hydrogen bonds with the TiO<sub>2</sub> nanofillers (Ernest Ravindran

et al. 2017). The N6 polymer, having even-even carbon atoms, shows the tendency to crystallize in  $\alpha$ -phase at a higher temperature. The presence of  $\text{TiO}_2$  in the NT polymer nanocomposites induces the thermal interaction with the N6 matrix (Rusu and Rusu 2011). From the DSC results, it is concluded that the  $\gamma$ -phase of N6 matrix is absent in all NT polymer nanocomposites samples.

#### 4.8 Frequency Dependence Dielectric Study of NT Polymer Nanocomposites

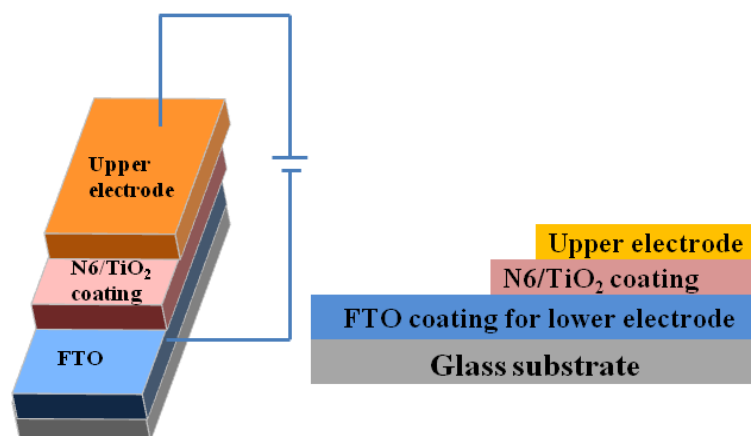


Fig. 4.7 Schematic representation of the parallel plate capacitor device for impedance testing.

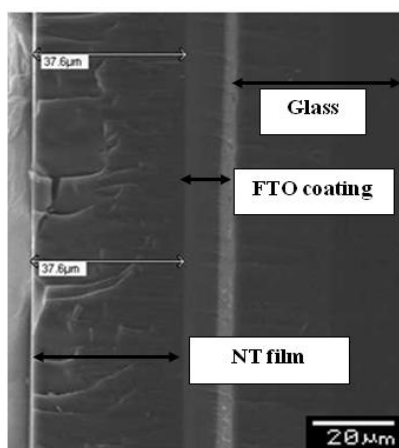


Fig. 4.8 The cross sectional SEM micrograph of the spin coated NT polymer nanocomposite film.

The schematic of parallel plate capacitor device with the spin-coated NT polymer composite on the FTO-coated glass slide is shown in Fig. 4.7. The FTO is



used as an electrode for the connection. The device is tested using the impedance analyzer. The cross sectional SEM micrograph in Fig. 4.8 shows the thickness of the spin coated NT polymer nanocomposite film. Prior to impedance measurements, the cross-sectional thickness and the effective surface area of film are useful for the calculation of dielectric properties of the NT polymer nanocomposites.

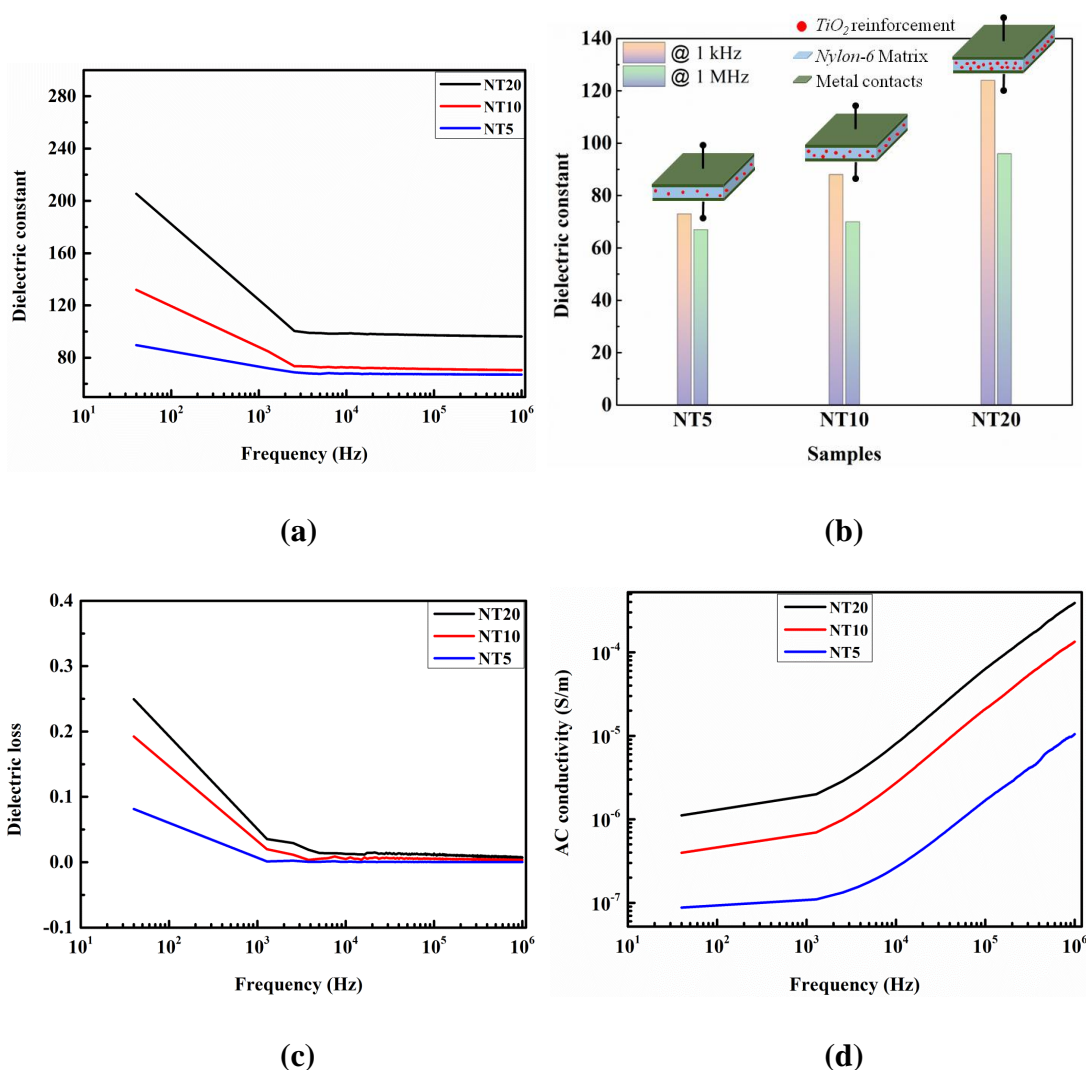


Fig. 4.9 The graph showing frequency dependency of (a) dielectric constant, (b) schematic illustration of variation of dielectric constant at 1 kHz and 1 MHz frequency, (c) dielectric loss and (d) AC conductivity of NT polymer nanocomposites for different samples.

Figure 4.9 (a) shows the frequency-dependent dielectric constant of the NT nanocomposite with different TiO<sub>2</sub> weight ratios. The increase in the TiO<sub>2</sub> filler

content in the NT polymer nanocomposites resulted in an increase of the effective dielectric constant ( $\epsilon$ ). The low-frequency dispersion increased with an increase in the TiO<sub>2</sub> filler content due to the increased surface charge effect on the nanoparticles. N6 is known to have stable  $\alpha$ -phase at room temperature. The NT polymer nanocomposites have a lower dielectric constant when compared to the pure TiO<sub>2</sub>. The dielectric constant ( $\epsilon$ ) of N6 is 4 at room temperature (Mahadevegowda et al. 2015). The  $\epsilon$  increases to 73 at 1 kHz when 5 weight percent of TiO<sub>2</sub> nanoparticles is added to the N6 matrix (NT5 sample). The  $\epsilon$  for NT5 is decreased to 67 when the frequency increases to 1 MHz.

The  $\epsilon$  becomes 88 at 1 kHz when the weight percent of TiO<sub>2</sub> increases to 10% (NT10 sample). Hence, a further increase in the TiO<sub>2</sub> content to 20 weight percent (NT20 sample) has exhibited  $\epsilon$  of 124 at 1 kHz, which is very high compared to Nylon-6/ceramic nanoparticles composites (Shinde et al. 2016)(Ernest Ravindran et al. 2017). As the frequency increases to 1 MHz, the NT polymer nanocomposites still retains a good magnitude of  $\epsilon$ . The  $\epsilon$  for NT5, NT10 and NT20 samples at 1 MHz are 67, 70 and 96, respectively. The variation of dielectric constant of NT polymer nanocomposites at 1kHz and 1 MHz, represented with bar chart, are shown in schematic diagram in Fig. 4.9 (b). The behaviour of increase in the value of  $\epsilon$  for NT polymer nanocomposites with an increase in the TiO<sub>2</sub> weight ratios is described based on the percolation phenomenon and is called as percolation threshold (Zhao et al. 2009). The effect of interfacial polarization and the high surface area of TiO<sub>2</sub> nanoparticles increase the value of  $\epsilon$  in the case of NT polymer nanocomposites (Ernest Ravindran et al. 2017)(Kilbride et al. 2002). This phenomenon is observed due to the conductive particle clusters of TiO<sub>2</sub> near the percolation threshold. The  $\epsilon$  is also dependent on the interface between the N6 and TiO<sub>2</sub> nanoparticles, size and shape of the TiO<sub>2</sub>, type of the polymer matrix and preparation method (Nan 2001b)(Bar-Cohen 2004). The dielectric loss for NT20 is 0.51 at 1 kHz, whereas for NT10 it is 0.31 and for NT5, it is 0.07, as shown in Fig. 4.9 (c). The increase in weight percent of TiO<sub>2</sub> results in much higher dielectric loss due to increased dissipation of energy through the movement of charges in the NT polymer nanocomposites. The NT20 sample has a higher number of polarisable particles

(TiO<sub>2</sub>) compared to NT10 and NT5 samples. These polarized TiO<sub>2</sub> particles switch the direction easily in the presence of an alternating electromagnetic field.

The variation of AC conductivity with frequency for different weight percent of TiO<sub>2</sub> in NT polymer nanocomposites is shown in Fig. 4.9 (d). The AC conductivity ( $\sigma$ ) is calculated from the data using the following equation 4.1

$$\sigma = \omega \varepsilon_0 \varepsilon (\tan \delta) \quad (\text{Eq. 4.1})$$

where  $\varepsilon_0 = 8.854 \times 10^{-12}$  F/m is the dielectric permittivity of free space and  $\omega = 2\pi f$  is the angular frequency. From the figure, the AC conductivity is high for NT20 and is calculated to be equal to  $1.82 \times 10^{-6}$  S/m, at 1 kHz. The AC conductivity decreases with a decrease in TiO<sub>2</sub> filler percentage in the NT composite. The AC conductivity for the NT5 and the NT10 is  $1.08 \times 10^{-7}$  S/m and  $6.69 \times 10^{-7}$  S/m, respectively. From Fig. 4.9 (d), it is also seen that the ' $\sigma$ ' increases with the increase in frequency for all the NT samples (Neher et al. 2015)(Bar-Cohen 2004). This phenomenon in ceramic-polymer nanocomposites is due to the interfacial polarization and the increase in the charge density of TiO<sub>2</sub> nanoparticles due to the movement of N6 polymer chain at low frequency. At 1 MHz, AC conductivity is higher due to the electronic polarization to hop charge carrier over a small height barrier. When the volume of TiO<sub>2</sub> nanoparticles filler content in the NT nanocomposite increases, the AC conductivity is found to be high due to better connectivity between the N6 and TiO<sub>2</sub> in the nanocomposite and increased number of charge density carriers. Therefore, an increase in the weight percent of TiO<sub>2</sub> nanoparticles supports the hopping of the charge carrier conduction mechanism (Hussien 2011)(Thomas et al. 2014).

#### 4.9 Summary and Conclusions

The TiO<sub>2</sub> nanoparticles were successfully synthesized by using the hydrothermal method. The different weight percent of TiO<sub>2</sub> nanoparticles were dispersed in the N6 polymer and spin coated the Nylon-6/TiO<sub>2</sub> polymer-ceramic nanocomposites film. At room temperature, the NT sample with 20 weight fraction TiO<sub>2</sub> filler was reported with the highest dielectric constant of 124 at 1 kHz. The XRD spectra showed the fabricated NT samples having an anatase form of TiO<sub>2</sub> and Nylon-

6 polymer peaks without any intermediate phases. SEM and TEM micrographs showed the uniformity of the synthesized TiO<sub>2</sub> nanoparticles. The d-spacing of the TiO<sub>2</sub> nanoparticles calculated from XRD data and TEM fringe images are in good agreement. The thermal analysis showed that the melting temperature was increased with an increase in the TiO<sub>2</sub> filler content. The formation of Nylon-6/TiO<sub>2</sub> polymer nanocomposites were also verified by FTIR spectra and the Raman spectra. The XPS confirmed the independent chemical state of components for the NT polymer nanocomposites. The dielectric behaviour of the NT polymer nanocomposites was influenced by the dispersion and different weight fraction of the TiO<sub>2</sub> in the N6 matrix. The lower content of TiO<sub>2</sub> in N6 leads to low dielectric constant and low dielectric loss, while the higher content of TiO<sub>2</sub> showed the highest dielectric constant and dielectric loss. In this work, we successfully fabricated semicrystalline N6 polymer-TiO<sub>2</sub> composite dielectric film with an improved  $\epsilon$  of 124, at 1 kHz, which is very high. Due to the flexibility and easy preparation of NT polymer nanocomposites, these composites have the potential to become high strength dielectric.

# CHAPTER 5

**The content of this chapter have been published in *Journal of Applied Physics A*,  
*125 (3), 1-10, 2019, doi.org/10.1007/s00339-019-2477-0.***

*Page intentionally left blank*

## CHAPTER 5

### SINGLE STEP GROWTH OF POROUS TITANIUM OXIDE VIA THE HYDROTHERMAL METHOD

*This chapter deals with the hydrothermal growth and characterization of the unique microstructural TiO<sub>2</sub> film on to the conductive surface. The fabricated device is examined for the parallel plate capacitor application.*

#### 5.1 Introduction

The major drawbacks in production of thin film dielectric material are adopting reproducible, single step growth mechanism, low temperature and budget friendly synthesis approach. Many parameters play a crucial role in the production of high dielectric materials, such as synthesis parameters, crystallinity, morphology, precursor chemical composition and temperature. The conventionally followed synthesis methods are sol-gel, hydrothermal, chemical vapour deposition (CVD), physical vapour deposition (PVD), lithography, screen printing, coating techniques, pyrolysis, etc. However, most of the methods require multiple step synthesis, high-cost instrumentation, high temperature environment and tedious process to produce high dielectric constant materials.

The hydrothermal method is one of the simplest, low-temperature, single-step, low-cost, easily reproducible, less instrumentation and cost-effective method to produce material. The morphology, phase and crystallinity of the material produced were tuned by varying the precursor, temperature and duration of heating. In hydrothermal method, Teflon lined stainless steel vessel was used for production of the material. By keeping the desired substrate in the autoclave, the material was directly grown on to the substrate. This step is used to produce thin film coating directly on to a substrate which is useful in applications, like parallel plate capacitors, piezoelectric sensors, optoelectronic, dye degradation systems and gas-sensors. The hydrothermally grown materials are directly used for applications without any further processing. This makes the hydrothermal process a viable and attractive technique for producing thin films on the desired substrate. The hydrothermal growth of a material

on the desired substrate is facile, greener, easily-reproducible and inherently safer technique, which is not easily achieved by other processing techniques.

The hydrothermal growth of  $\text{TiO}_2$  film on to the FTO-coated glass is adopted for the production of high dielectric material applications. FTO acts as a conducting surface which is useful for the electrical connections during the application. Here, initially an inorganic precursor was dissolved in the solvent (dispersant) and the desired reducing agents/ surfactants were then added to the above solution. The solution was thoroughly stirred for few minutes to ensure the uniformity. The autoclave was filled with the prepared solution to the half of its volume capacity. Pre-treated/ozone treated and thoroughly cleaned FTO-coated glass slides were kept in the autoclave to control the impurities. The autoclave was tightened with the bolts and heated in hot air oven for known time and temperature. During heating,  $\text{TiO}_2$  was reduced and the  $\text{TiO}_2$  film was directly grown on to the substrate. The FTO coated glass slides were seen to provide necessary growth site/substrate for  $\text{TiO}_2$  film growth. Later, the autoclave was removed from the oven and allowed to cool down to room temperature. The FTO-coated glass slides were removed from the autoclave and rinsed with the water. The glass slides were then dried in oven to remove the water and moisture content from the grown film. These are directly used for the application. Many conventional methods used for growing the thin  $\text{TiO}_2$  film on the substrates are multiple-steps methods, requires high vacuum, temperature, high-instrumentation processes and tedious.

In this chapter, the efficient and single-step hydrothermal growth of  $\text{TiO}_2$  dielectric film on the FTO-coated glass substrate was adopted. The synthesis of  $\text{TiO}_2$  with a unique porous morphology is detailed and followed by the deposition of  $\text{TiO}_2$  film on the substrate (section 3.2.2). The effect of hydrothermal processing temperature on the microstructural or morphological growth of the  $\text{TiO}_2$  was examined. The material was characterized in detail to confirm the morphology and phase composition. The dielectric behaviour of  $\text{TiO}_2$  film was examined in the flat band regime ranging from 40 Hz to 1 MHz. Further, the AC conductivity study was conducted to understand the electrical property of synthesized  $\text{TiO}_2$  nanofilms.



## 5.2 Structural Analysis of the TiO<sub>2</sub> Films

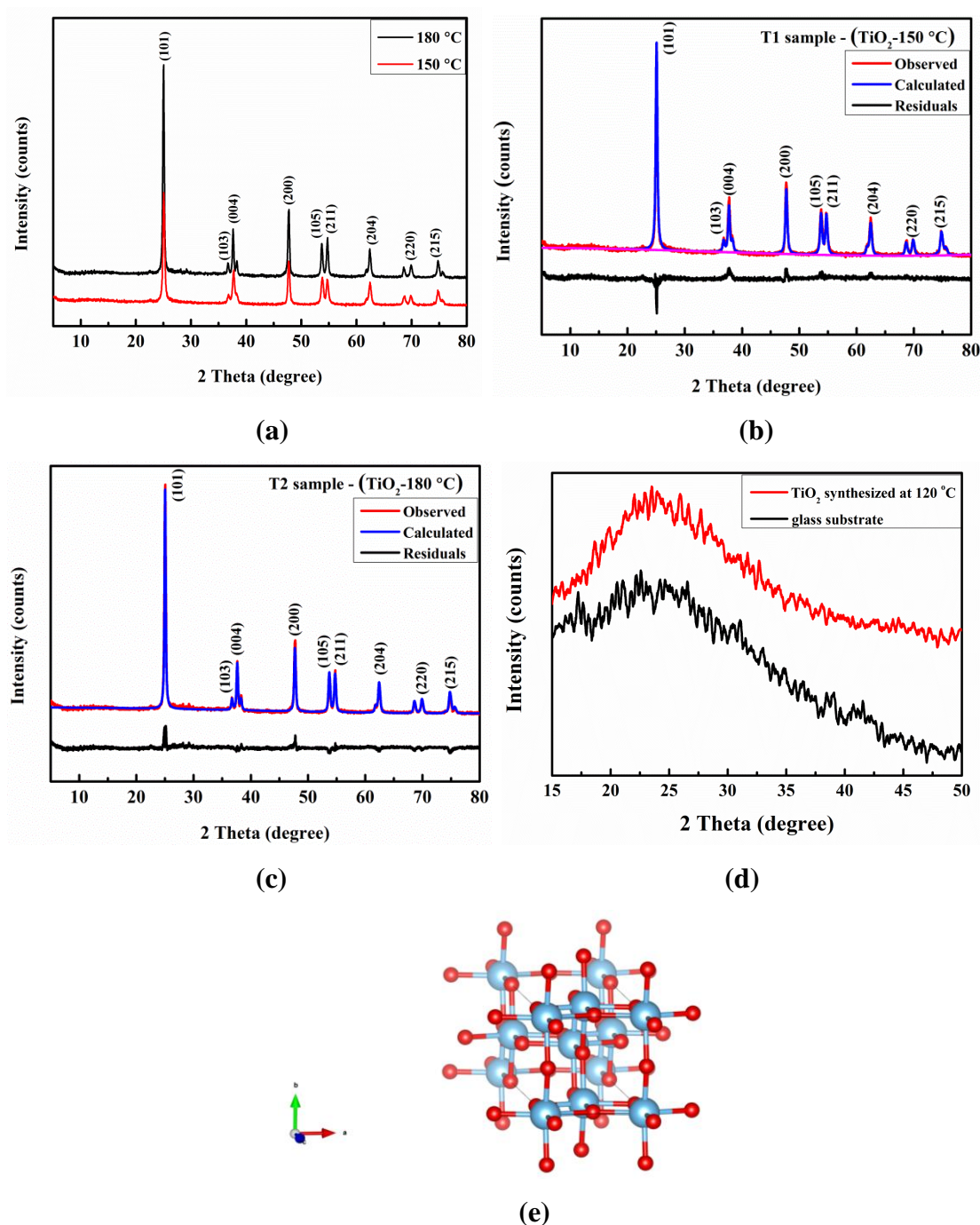


Fig. 5.1 XRD spectra of TiO<sub>2</sub> samples (a) T1 (150 °C) and T2 (180 °C) and corresponding Rietveld refined pattern of (b) T1 sample (synthesized at 150 °C) and (c) T2 sample (synthesized at 180 °C), respectively, (d) T sample (synthesized at 120 °C) and (e) schematic representation of crystallographic structure of tetragonal anatase phase TiO<sub>2</sub> (blue atoms are titanium and red atoms are oxygen).

Table 5.1 The refined parameters and crystal data of T1 and T2 TiO<sub>2</sub> samples.

Parameters	Obtained numerical magnitudes	
	Sample T1 (150 °C)	Sample T2 (180 °C)
Crystal structure	Tetragonal	Tetragonal
Space group	<i>I4<sub>1</sub>/amd</i>	<i>I4<sub>1</sub>/amd</i>
<i>a</i> (Å)	3.7986	3.7940
<i>b</i> (Å)	3.7986	3.7940
<i>c</i> (Å)	9.499	9.5016
$\alpha$ (°)	90	90
$\beta$ (°)	90	90
$\gamma$ (°)	90	90
$R_p$ (profile factor)	8.82 %	8.68 %
$R_{wp}$ (weighted profile factor)	10.96 %	10.92 %
Cell volume	137.068	136.775
$\chi^2$	1.641	2.066

In Fig. 5.1 (a), the XRD spectra of samples T1 and T2 are shown; the diffraction responses at various Bragg locations of the samples (T1 and T2) are entirely attributed to the anatase phase (ICDD 21-1272) (Chowdhury et al. 2015; Štengl et al. 2013b) without any impurities and secondary phases. The presence of diffraction peak (004) suggests the prominent single direction [001] growth (Pai et al. 2014; Tao et al. 2012), which is typical for the anatase TiO<sub>2</sub> thin film. The absence of peaks belonging to impurities suggests phase purity of the TiO<sub>2</sub>. The hydrothermal synthesis of TiO<sub>2</sub> affects the purity by the elimination of the surfactant. It results in the formation of a pure mesoporous structure (Kim and Kwak 2007). The strong and broad peaks indicate that the material has good crystallinity with small crystallites. The average crystallite size of TiO<sub>2</sub> in the thin films has been estimated from the full-

width at half-maximum  $\beta$  (in radian) of the diffraction response using the Scherrer equation 5.1

$$\tau = \frac{K\lambda}{\beta \cos \theta} \quad (\text{Eq. 5.1})$$

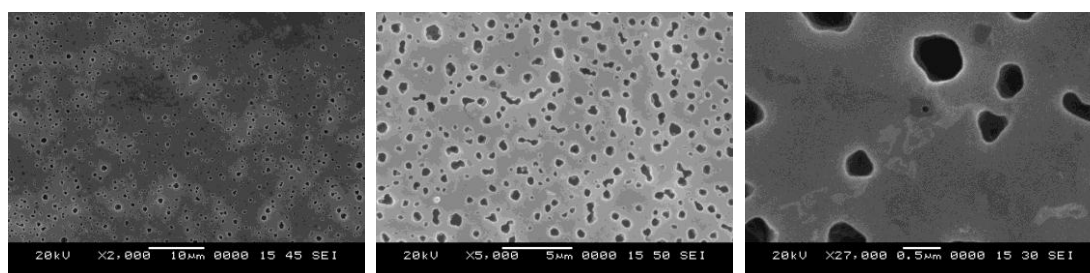
where  $\tau$  is the crystallite size,  $\theta$  is the diffraction angle,  $\lambda$  is 1.54 Å for the Cu K $_{\alpha}$  line and  $K$  is the Scherrer constant.

The value of  $K$  depends on the crystal shape and diffraction line indices (Uvarov and Popov 2007). The calculated crystallite size in the TiO $_2$  samples T1 and T2 are estimated to be 22.6 nm and 20.3 nm, respectively. The increase in heating temperature decreases the crystallite size for sample T2 compared to T1. The diffraction peaks of sample T2 are sharper than those of sample T1. It indicates that the sample T2 has better crystallization and smaller crystallites. It is attributed to the sample's exposure to the higher heating temperature (Chu et al. 2015).

The TiO $_2$  XRD data are further analyzed employing the Rietveld refinement technique with the help of GSAS software package, as shown in Fig. 5.1 (b-c) (McCusker et al. 1999). The TiO $_2$  samples are found to crystallize in single anatase tetragonal structure with space group  $I4_1/amd$  (ICDD 21-1272) without secondary phases. In Fig. 5.1 (b-c), the experimental pattern (observed) is shown by red colour and the theoretical data (calculated) is shown by blue colour. The difference between theoretical and experimental data is shown by the black curve. The main refined parameters, such as crystal system, cell parameters (a,b,c) and atomic position (x,y,z) are presented in Table 5.1. The value of goodness of fit ( $\chi^2$ ) for sample T1 and T2 is found to be equal to 1.64 and 2.06, respectively. The lattice parameters obtained agree with the literature (ICDD 21-1272). Fig. 5.1 (d) shows the XRD plot of bare or uncoated glass substrate and TiO $_2$  coated one, synthesized at 120 °C for 24 h (T sample). From diffraction response, it is visualized that the diffraction peaks corresponding to TiO $_2$  are absent. Figure 5.1 (e) shows the crystallographic structure of TiO $_2$  anatase phase. The lattice parameters obtained post Rietveld refinement is used for drawing the crystallographic structure of the TiO $_2$ .

### 5.3 Electron Microscopic Analysis of TiO<sub>2</sub> Films

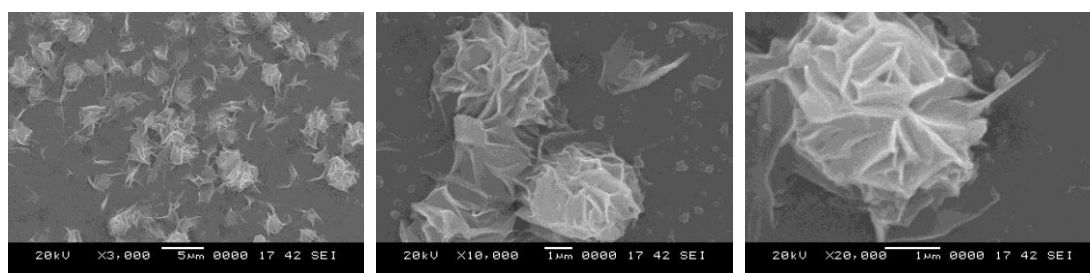
SEM micrographs of the T1 and T2 samples are shown in Fig. 5.2. The micrographs show that the sample T1 has the flower morphology and the T2 sample has a flower-like morphology with a higher dimension than that of the sample T1. The TiO<sub>2</sub> crystals grow predominantly in [001] direction, as indicated by XRD results. To understand the growth mechanism of 3D hierarchical TiO<sub>2</sub>, investigation of temperature-dependent evolution of the morphology and the crystal structure are investigated. Figure 5.2 shows the SEM micrographs of samples fabricated at different reaction temperatures for 24 h of constant heating. The sample obtained at 120 °C has not yielded any morphology due to the lower reaction temperature as shown in Fig. 5.2 (a, b and c).



(a)

(b)

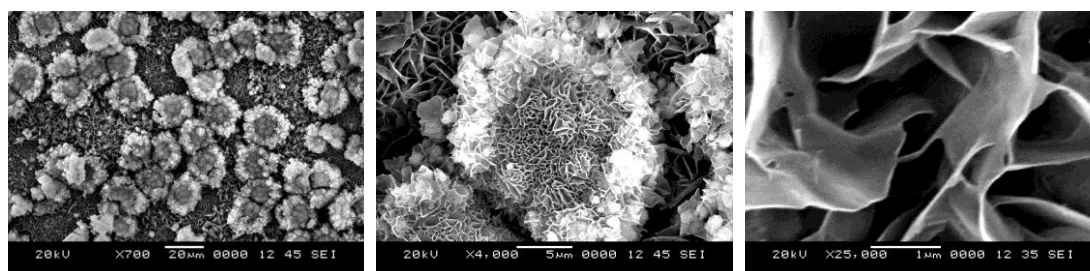
(c)



(d)

(e)

(f)



(g)

(h)

(i)

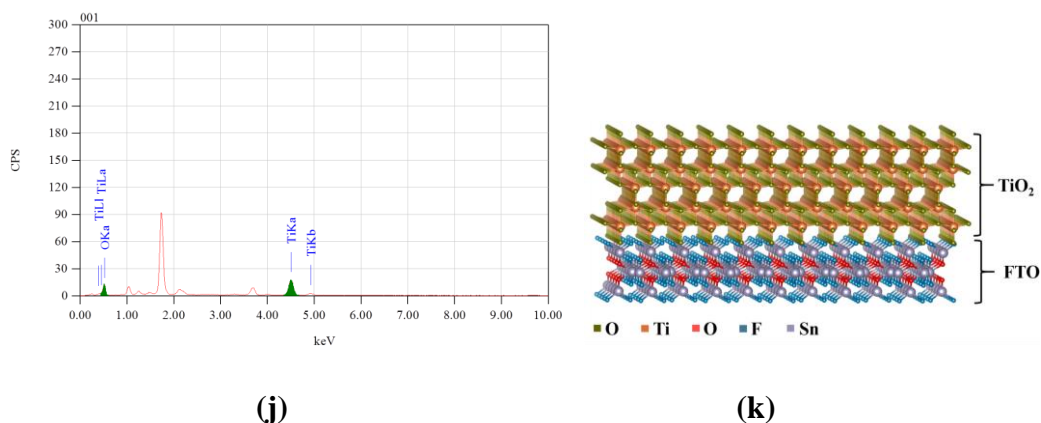


Fig. 5.2 SEM micrographs of porous flower-like TiO<sub>2</sub> microstructure for samples at T (120 °C) (a, b and c), T1 (150 °C) (d, e, and f) and T2 (180 °C) (g, h and i) at different magnifications, (j) SEM-EDS of TiO<sub>2</sub> sample and (k) schematic representation of the crystallographic structure of TiO<sub>2</sub> grown on FTO coated glass.

After hydrothermal heating at 150 °C (T1) for 24 h, the microspheres with an average diameter of 3.0  $\mu\text{m}$  are formed (Fig. 5.2 (d)). The high-resolution SEM micrographs (in Fig. 5.2 (e,f)) further confirms that the microspheres have a cluster of petals-morphology. After the hydrothermal reaction at 180 °C (T2) for 24 h, however, the morphology of the microspheres does change. Not only the diameter of microspheres increased to 20–30  $\mu\text{m}$ , but also the microsphere surface becomes dense. As shown in Fig. 5.2 (g), most of the microspheres start showing 3D flower-like morphology with dense petals of thin nano TiO<sub>2</sub> layers. The high-resolution micrographs in Fig. 5.2 (h,i), show that each petal in flower-like morphology is of nanometer thick. The size of each microsphere in the sample T2 is more significant than that in T1 due to increase in heating temperature. The increase in heating temperature resulted in higher mobility of Ti<sup>4+</sup> and O<sup>2-</sup> ions (Xiang et al. 2012a; Yang et al. 2009). The increase in temperature also resulted in higher porosity, increased surface area and the growth of highly crystalline TiO<sub>2</sub> layered flower morphology (T2 compared to T1).

Figure 5.2 (j) also shows the SEM-EDS spectra of TiO<sub>2</sub> film. It is found that Ti and O are the only elements present in the material. The average fractions (atomic weight) of Ti and O in the TiO<sub>2</sub> are found to be 33.89 % and 66.11 %, respectively, which is confirmed through systematic area analysis at various locations using a

number of micrographs. The EDS results verify the stoichiometric nature of the deposits; this depicts that the synthesized TiO<sub>2</sub> nanoparticles are compositionally robust. Figure 5.2 (k) shows the crystallographic structural growth of TiO<sub>2</sub> on the FTO coated glass slides. The parameters of TiO<sub>2</sub> obtained from the Rietveld refinement of XRD has been used for drawing. The lattice parameters of FTO are taken from the crystallographic database.

#### 5.4 Raman Spectroscopic Analysis of the TiO<sub>2</sub> Films

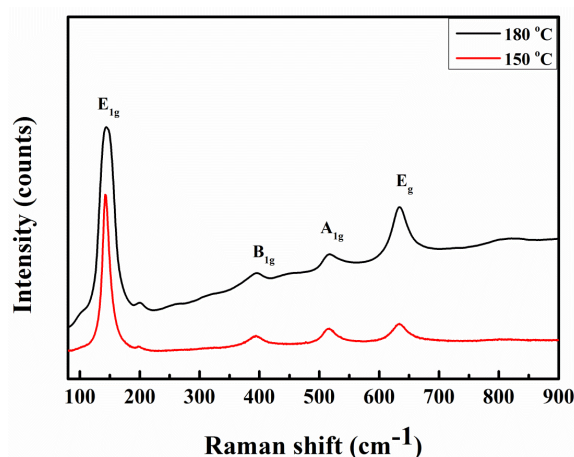


Fig. 5.3 Raman spectra showing the characteristic bands of TiO<sub>2</sub> anatase phase for the samples T1 (150 °C) and T2 (180 °C).

The characteristic vibration modes of anatase TiO<sub>2</sub> are located at 143 cm<sup>-1</sup> (E<sub>g</sub>), 395 cm<sup>-1</sup> (B<sub>1g</sub>), 516 cm<sup>-1</sup> (A<sub>1g</sub>) and 635 cm<sup>-1</sup> (E<sub>g</sub>). These characteristic positions added with Bragg locations of diffracted anatase phase consistently confirms the presence of pure TiO<sub>2</sub> (Chen et al. 2017b; Swamy et al. 2006). The percentage of {001} facets was calculated for both samples by measuring the peak intensity ratio of the E<sub>g</sub> (at 143 cm<sup>-1</sup>) and A<sub>1g</sub> (at 514 cm<sup>-1</sup>) (Chu et al. 2015). The percentage of {001} facets for sample T1 and T2 is calculated as 25% and 61%, respectively. Raman analysis results show the growth of the {001} facet is predominant for the T2 sample synthesized at 180 °C.

#### 5.5 XPS Analysis of the TiO<sub>2</sub> Film

Figure 5.4 (a) shows a survey and high-resolution XPS spectra of the sample T2. The survey spectrum showed that Ti and O are the only elements present in the

sample. The C 1s peak is present due to adsorbed hydrocarbons. In the XPS spectrum (Fig. 5.4 (b)), the Ti 2p doublet has the components Ti 2p<sub>3/2</sub> (binding energy 456.8 eV) and Ti 2p<sub>1/2</sub> (binding energy 462.8) arise from spin-orbit splitting (Atuchin et al. 2012, 2006).

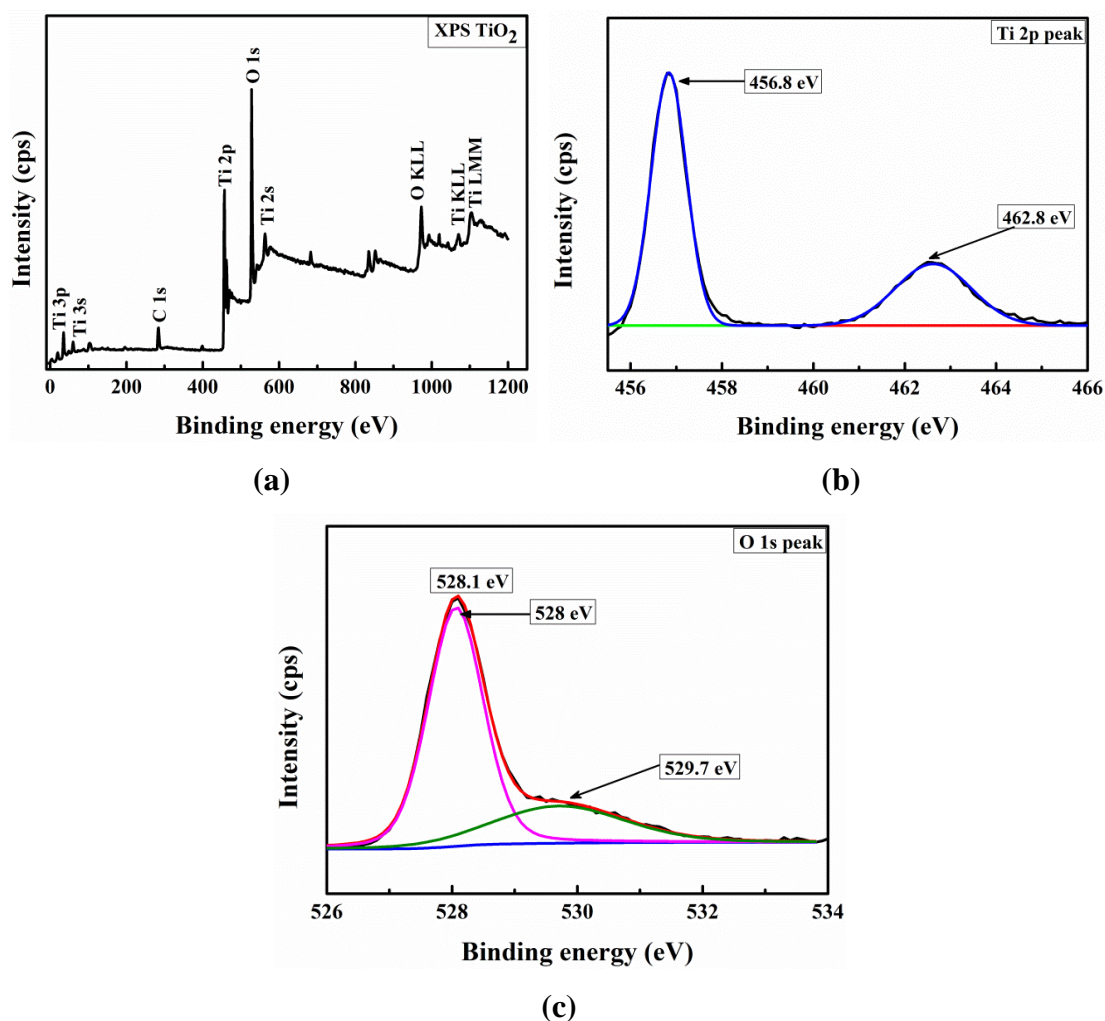


Fig. 5.4 (a) The XPS survey spectrum of the TiO<sub>2</sub> sample, (b) core level 2p spectrum of titanium and (c) core level 1s spectrum of oxygen.

The O 1s spectrum of the sample T2 is deconvoluted with two principal signatures, as shown in Fig. 5.4 (c) (Chen et al. 2017b). The components at binding energy 528 eV and 529.7 eV are attributed to lattice oxygen (Ti-O-Ti) and (-OH) groups adsorbed on the surface of the TiO<sub>2</sub>, respectively (Atuchin et al. 2008; Pai et al. 2014; Ramana et al. 2007).

## 5.6 BET Analysis of TiO<sub>2</sub> Sample (T2)

According to the nitrogen (N<sub>2</sub>) adsorption and desorption response (Fig. 5.5), the specific surface area calculated by the Brunauer-Emmett-Teller (BET) equation is found out to be 172.56 m<sup>2</sup>/g which is predominant compared to previously reported studies (Fig. 5.5) (Chu et al. 2015; Jin et al. 2006; Cheng et al. 2014). The higher surface area is useful for the charge polarization which results in increased dielectric strength.

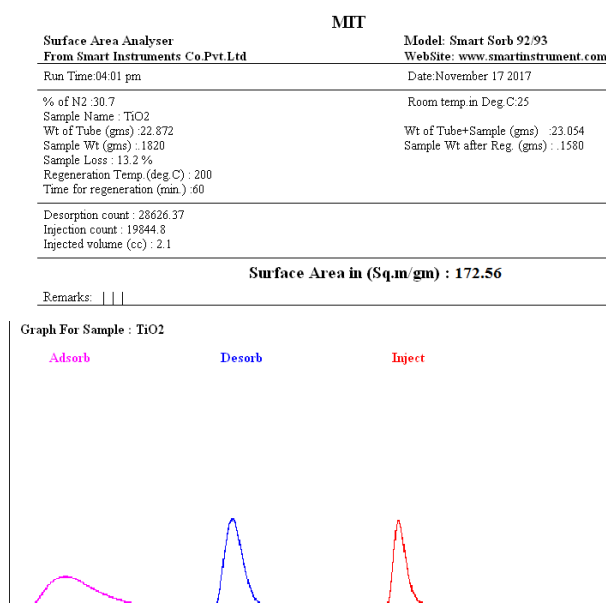


Fig. 5.5 The BET surface area estimation for TiO<sub>2</sub> sample synthesized at 180 °C for 24 h constant heating.

## 5.7 Thermal Analysis of TiO<sub>2</sub> Films

In the TGA experiments, the samples T1 and T2 were heated from room temperature up to 800 °C in nitrogen atmosphere. The TGA curve shown in Fig. 5.6 reveals that the weight losses for the samples T1 and T2 are 5.32 % and 5.46 %, respectively. The weight losses in the sample follow almost the same trend. The gradual weight loss occurring at around 220 °C up to 680 °C is attributed to surfactant decomposition (Kim and Kwak 2007). The TiO<sub>2</sub> being an oxide-ceramic which is thermally stable for a prolonged range of operating temperatures, results in negligible weight loss as observed in the TGA trace (Fig. 5.6). The samples show negligible weight loss up to 680 °C, beyond which the weight loss is almost nil.



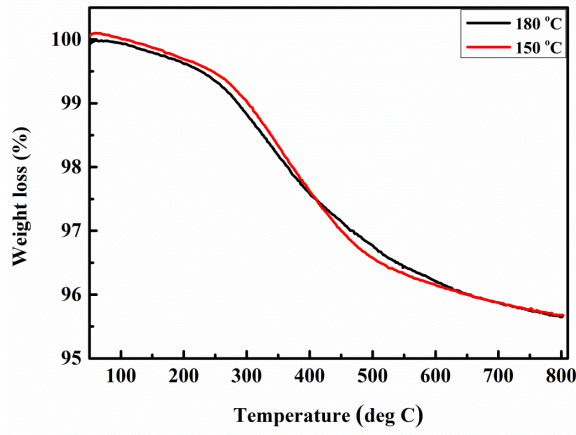


Fig. 5.6 The TGA weight loss curves for T1 (150 °C) and T2 (180 °C) TiO<sub>2</sub> samples.

### 5.8 Studies on Dielectric Permittivity of TiO<sub>2</sub> Films

The electrical connections and schematic of parallel plate capacitor with TiO<sub>2</sub> as dielectric material grown on FTO-coated glass slide is as shown in Fig. 5.7 (a). FTO and upper electrode from the impedance act as electrodes for connection. The fabricated parallel plate capacitor was directly fed to the impedance analysis. The dielectric constant (or permittivity) and the dielectric loss for the samples T1 and T2 were studied as a function of frequency, as shown in Fig. 5.7 and Fig. 5.8. The frequency during measurements was varied from 40 Hz to 1 MHz. The corresponding values were plotted against the frequency and the detailed explanation is discussed in the following section.

All the impedance measurements were done at room temperature conditions. The dielectric constant is evaluated using the relation,

$$\epsilon (r) = \frac{Cd}{\epsilon_0 A} \quad (\text{Eq. 5.1})$$

where  $d$  is the thickness of the dielectric film and  $A$  is the sample area. Fig. 5.7 (a) shows the variation of dielectric constant against the frequency for the T1 and T2 samples. At lower frequencies, the dielectric constant is high and it decays expeditiously with a small increment in frequency for both samples T1 and T2. The dielectric constant of the sample T2 is higher than that of the T1, due to the following reasons; the T2 sample compared to T1 has a higher {001} facet number, porosity, grain boundary as well as specific surface area. The increased space charge and ion

jump orientation effect, observed in the porous flower-like morphology of the sample T2, results in a high value of dielectric constant compared to that of T1 (Maliakal et al. 2005).

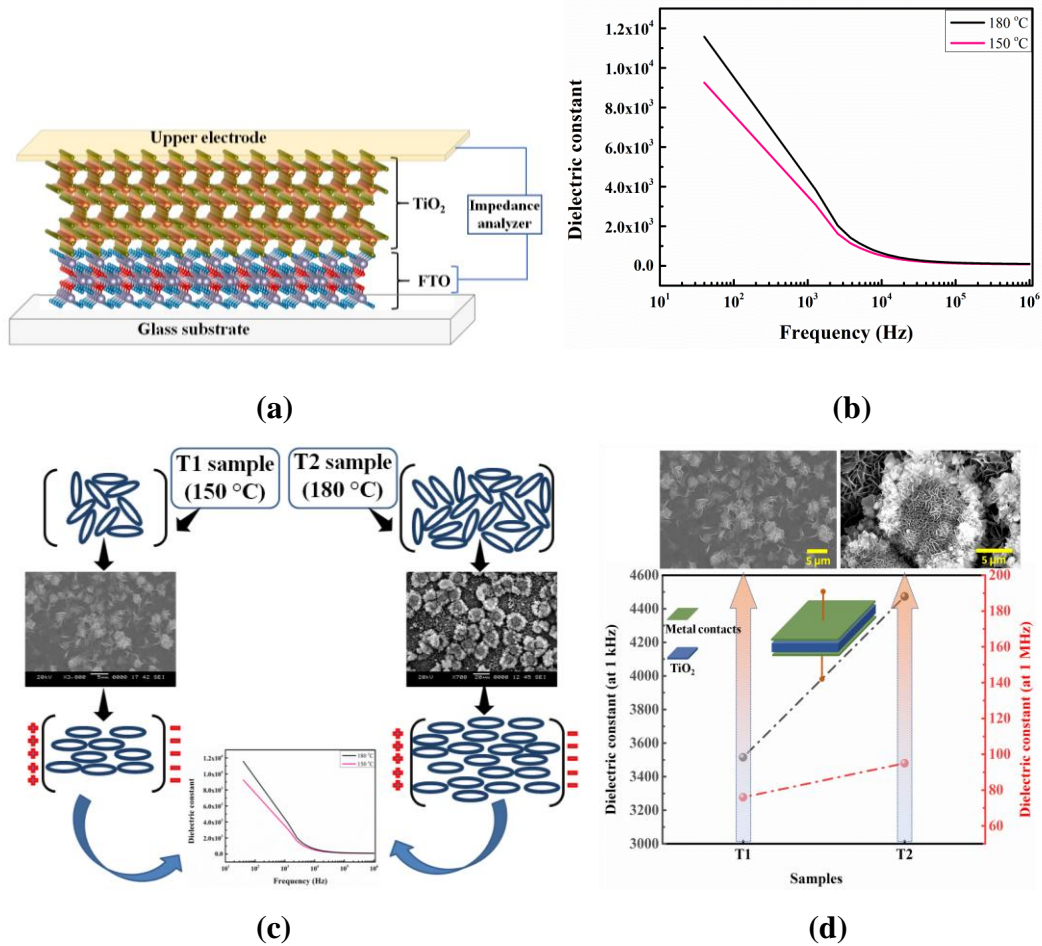


Fig. 5.7 (a) The schematic representation of crystallographic structure of TiO<sub>2</sub>-dielectric material grown on FTO coated glass in parallel plate capacitor setup, (b) variation of dielectric constant against frequency for TiO<sub>2</sub> samples, (c) schematic representation of variation of dielectric constant for T1 and T2 TiO<sub>2</sub> samples and (d) graphical abstract showing variation of dielectric constant for T1 and T2 samples at 1 kHz and 1 MHz.

The sample T2 has the higher number of grain boundaries than that of the T1, where most of the charge carriers (electron-hole pairs) are trapped and scattered, which is popularly known as the grain boundary scattering. When the voltage is applied, many charges are stored at the grain boundaries as a result of charge trapping. This phenomenon affects the dielectric behaviour of the materials (Wypych et al.

2014a). At lower frequencies, the dipole moment can facily follow the transmutations in the electric field. It is schematically represented in Fig. 5.7 (c).

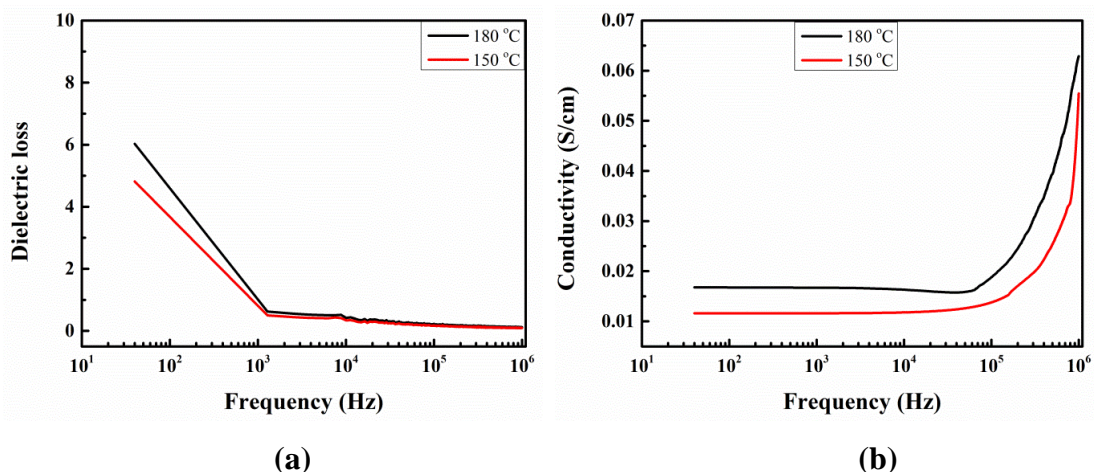


Fig. 5.8 The plots of (a) dielectric loss and (b) conductivity vs. frequency for the T1 and T2 TiO<sub>2</sub> samples.

The dielectric constant of the T2 (flower-like) sample is higher than that of the T1 due to the increased rotational and space charge polarization effects (Rabin et al. 2018). This phenomenon occurs mainly at the interfaces and affects the dielectric constant (Kumar et al. 2006; Singh et al. 2013). For the easy understanding of variation of dielectric constant at different frequency sweeps for samples T1 and T2, Fig. 5.7 (c) and Fig. 5.7 (d) were plotted. The dielectric constant at 1 kHz and 1 MHz of any material is important for researcher’s interest (Singh et al. 2013). Hence, the variation of dielectric constant for T1 and T2 samples at 1 kHz and 1 MHz was separately plotted, as shown in Fig. 5.7 (d). At 40 Hz, the dielectric constant is 11,571 and 9,256 for T2 and T1 samples, respectively. As the frequency increases, the dielectric constant decreases. The dielectric constant at 1 kHz is found to be 3515 and 4473 for T1 and T2 samples, respectively. The magnitude is superior to previously published studies (Avinash et al. 2016). Even at high frequencies, the TiO<sub>2</sub> retains an excellent dielectric strength. At 1 MHz, the dielectric constant is found to be 76 and 95 for T1 and T2 samples, respectively. As shown in Fig. 5.8 (a), the dielectric loss also decreases with an increase in frequency for both the TiO<sub>2</sub> samples. The loss angle has almost the same magnitude at higher frequencies (Prasad et al. 2011). The dielectric loss occurs due to the following reasons: (a) the charge associated with the

TiO<sub>2</sub> orient along the direction of the applied electric field; (b) a part of the applied electric energy is utilized by the charge on TiO<sub>2</sub> to overcome the internal friction forces (Kumar et al. 2006); (c) another small quantity of the applied electric energy is utilized for the rotation of charges from one position to another (Sagadevan 2013). Furthermore, in nanophase TiO<sub>2</sub> materials, the dielectric loss occurs due to inhomogeneities (defects). The loss also occurs due to space charge formation at the interface layers which create an absorption current (Brus et al. 2015; Paraffin et al. 2010; Tripathy et al. 2018). The dielectric loss calculated at 1 kHz is 0.78 and 1.02 for the T1 and T2 samples, respectively. Figure 5.8 (b) shows the variation of conductivity as a function of frequency. Initially, the conductivity observed is very low followed by an exponential enhancement. The conductivity is high at a higher frequency (Tripathy et al. 2018). The conductivity for T1 and T2 samples at 1 kHz frequency calculated from the Fig. 5.8 (b) is 0.0108 S/cm and 0.0161 S/cm, respectively. This is due to the reason that the dielectric material loses its strength and makes the electric charge to flow through the material which is also called as dielectric breakdown.

## 5.9 Conclusions

A single-step facile hydrothermal route to synthesize porous flower-like TiO<sub>2</sub> material in the mixed solvents of diethanolamine and distilled water is presented in the study. The XRD patterns of synthesized TiO<sub>2</sub> correspond to the phase pure-anatase and the BET results along with the SEM micrographs, reveal higher surface area as well. Further, the Raman spectroscopic analysis is in-line with the XRD results depicting phase purity. The exposed high surface of the TiO<sub>2</sub> sample resulted in charge storage in terms of the polarization effect. The effective surface utilized for charge storage was much higher in the flower-like morphology of the TiO<sub>2</sub>-T2 sample compared to that of T1. At 1 kHz, the dielectric constant ( $\epsilon_r$ ) for the TiO<sub>2</sub> samples synthesized at 180 °C (T2) and 150 °C (T1) were found to be 4473 and 3515, respectively. Also, the conductivity increases with an increase in frequency. At higher frequencies, the TiO<sub>2</sub> becomes almost a good conductor due to the polar molecules' alignment along the applied electric field. The TiO<sub>2</sub> flower-like morphology has features for the application as high dielectric strength.

# CHAPTER 6

The content of this chapter have been published in *Journal of Measurement Science and Technology, IOP Science, 32 (9), 095119, 2021, doi.org/10.1088/1361-6501/abe6d2.*

And

**Journal of Materials Science: Materials in Electronics (Accepted, June 2021,  
Manuscript #JMSE-D-21-00656)**

*Page intentionally left blank*

## CHAPTER 6

### ASSESSMENT OF TRIBOELECTRIC PROPERETY OF DIFFERENT NANOCRYSTALS PREPARED BY HYDROTHERMAL TECHNIQUE

*This chapter deals with the hydrothermal synthesis and characterization of the  $La_2O_3$  and ZnO nanocrystals. Further, it is demonstrated the usage of synthesized nanocrystals in the triboelectric nanogenerator devices using Teflon as a counter material.*

#### 6.1 Introduction

The demand for industrial machineries, advanced medical devices, sensors and thin film-electronic devices has increased tremendously due to the increased comfort life of human being. The energy requirements for such devices are the challenging task for the present scenario. The battery powered devices needs frequent replacement of the power source (battery) and the performance of such devices degrades after a prolonged usage. Many researchers have focused on self-powered device to fulfil the energy requirements of the devices. The self-powered devices with piezoelectric and triboelectric materials have evolved as an alternative for battery-powered devices. The major problem associated with piezoelectric device is, it undergoes continuous fatigue loading. Due to this phenomenon, the performance of the devices shrinks/degrades (Kim et al. 2020). Whereas, triboelectric devices have overcome many drawbacks associated with battery-powered and piezoelectric devices. Triboelectric devices can be used as self-powered devices, due to their various advantages, like simple device fabrication, high efficiency, cost effectiveness and large power output. The triboelectric performance undergoes negligible decay even after  $10^6$  cycles of operation. The triboelectricity is a surface phenomenon. The working principle of triboelectric device is explained further (Wang 2017).

When two materials (with different electron affinity) come in contact and separate, the surface charges gets attracted from the material with less electron affinity to the material with high electron affinity (Wang et al. 2017). This is due to the contact electrification and electrostatic effects on the surface of the two dissimilar

materials. This action causes static charges to deposit on the surface. The static charges cause an electric field around the surface which induces mirror charges on respective counter material. Thus, a potential difference is created between the two electrodes in the external circuit and it causes the charge to flow from one electrode to other. When these two surfaces come in contact, the electric field around the surface collapses and thus the potential difference between the electrodes collapses. Hence, the reverse flow of charges will bring the circuit to the equilibrium. Currently, the efforts of many researchers are focused on enhancing the conversion efficiency and output performance of the TENGs. This can be achieved by selecting suitable triboelectric materials with large triboelectric polarities differences and nanomaterials which have high effective surface area (Guo et al. 2013) (Mathew et al. 2021).

Teflon (polytetrafluoroethylene) produces nonreactive and nonstick surface. It has a strong electronegative fluorine groups and an excellent choice for counter surface in triboelectric device. The material demonstrates strong negative triboelectric properties and increased triboelectric charge density on the surface. Thus, Teflon is selected as the counter surface against the triboelectric material.

The hydrothermally synthesized nanocrystals of  $\text{La}_2\text{O}_3$  and  $\text{ZnO}$  are selected for the triboelectric performance study.  $\text{ZnO}$  and  $\text{La}_2\text{O}_3$  nanocrystals are selected owing to their various advantages (Guo et al. 2013)(Salavati-Niasari et al. 2011b). The hydrothermal synthesis of different nanocrystals is a simple, one-step and low cost technique. The synthesized nanoparticles will be of uniform morphology throughout and easily reproducible technique. The method is scalable to large amount of nanoparticles synthesis. This method produces materials with high-effective surface area which further enhances the triboelectric efficiency.

In the first section of the chapter, a single-step hydrothermal synthesis of  $\text{La}_2\text{O}_3$  nanocrystals is presented. The processing is simple, cost effective and demands a minimal thermal budget (Jafari Nejad et al. 2010). The  $\text{La}_2\text{O}_3$  nanocrystals synthesized with this technique possess uniform morphology and size distribution. The synthesized  $\text{La}_2\text{O}_3$  nanocrystals were characterized to study its morphological and structural properties. The synthesized nanocrystals were ground with suitable capping agent to form paste for the screen printing technique without modifying its base

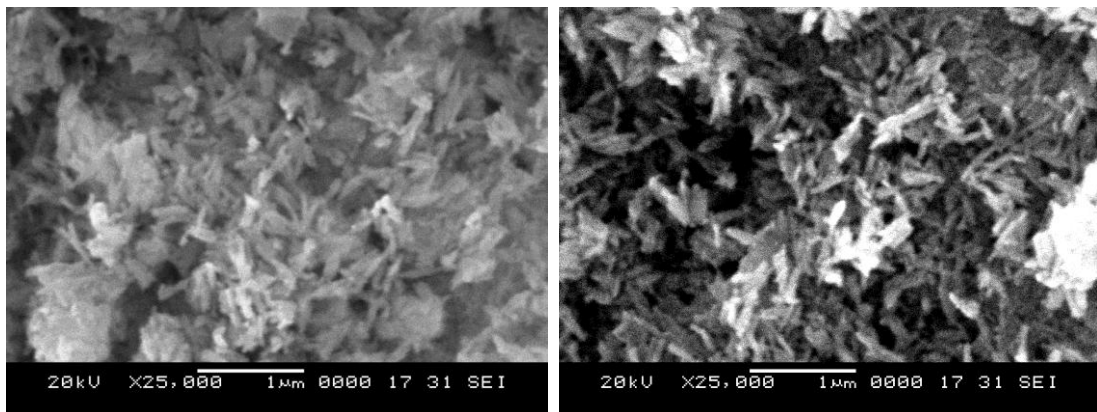


properties. The  $\text{La}_2\text{O}_3$  film was fabricated using synthesized nanocrystals and suitable reagents by the screen printing technique. The prepared film was then examined to study the triboelectric properties.

The second section of the chapter focuses on a single-step microwave hydrothermal synthesis of the ZnO nanoparticles. The synthesized ZnO nanoparticles were characterized using XRD and SEM technique to study the phase and morphology. The synthesized ZnO nanoparticles were further screen-printed on the conductive copper tape. The fabricated film is subjected to triboelectric property assessment using fluoropolymer (Teflon) as the counter surface.

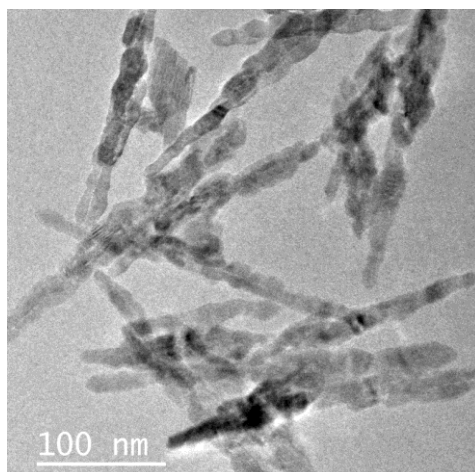
## 6.2 Results and Discussion of Triboelectric Property Assessment of $\text{La}_2\text{O}_3$ Nanocrystals

### 6.2.1 Morphology of $\text{La}_2\text{O}_3$ nanocrystals

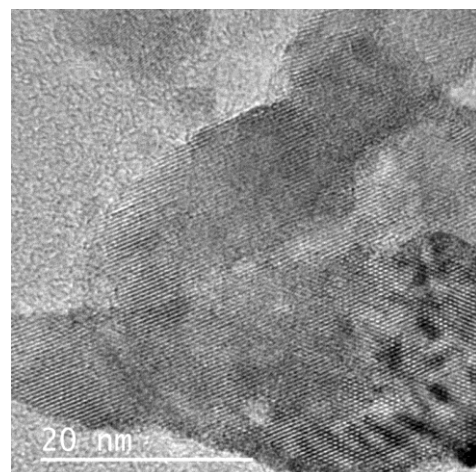


(a)

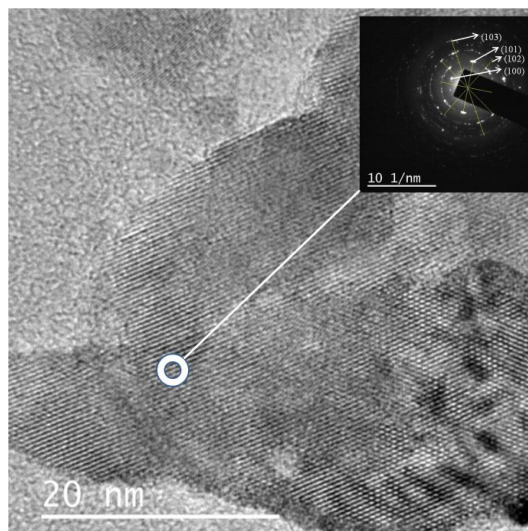
(b)



(c)



(d)



(e)

Fig. 6.1 Morphology of  $\text{La}_2\text{O}_3$  nanocrystals captured using, (a) & (b) SEM, (c) TEM, (d) corresponding magnified high-resolution micrograph and (e) selected area electron diffraction (SAED) ring depicting the polycrystalline nature of  $\text{La}_2\text{O}_3$  nanocrystals.

The micrographs of  $\text{La}_2\text{O}_3$ , captured using electron microscope (Fig. 6.1 (a-e)) depict the rod-like morphology. The synthesized  $\text{La}_2\text{O}_3$  nanocrystals are uniform in size and shape, showing its homogeneous formation during the synthesis. The micrographs at different locations present the uniform morphology with dimensions varying in few hundreds of nanometers. The diameter of the  $\text{La}_2\text{O}_3$  nanocrystals is in the range of 5 to 30 nm and length is 100 to 300 nm (Fig. 6.1 (a & b)). Figure 6.1 (c) shows the TEM micrograph of the  $\text{La}_2\text{O}_3$  nanocrystals, corresponding high-resolution image (Fig. 6.1 (d)) and SAED ring pattern (Fig. 6.1 (e)). The TEM analysis shows the crystalline structure of  $\text{La}_2\text{O}_3$ . The interplanar spacing is 0.334 nm (from Fig. 6.1 (d)). The ring pattern with intense spot in Fig. 6.1 (e) indicates the  $\text{La}_2\text{O}_3$  nanocrystals formation. The intense diffraction spots suggest the formation of crystalline nanoparticles.

## 6.2.2 Morphology of $\text{La}_2\text{O}_3$ screen-printed film

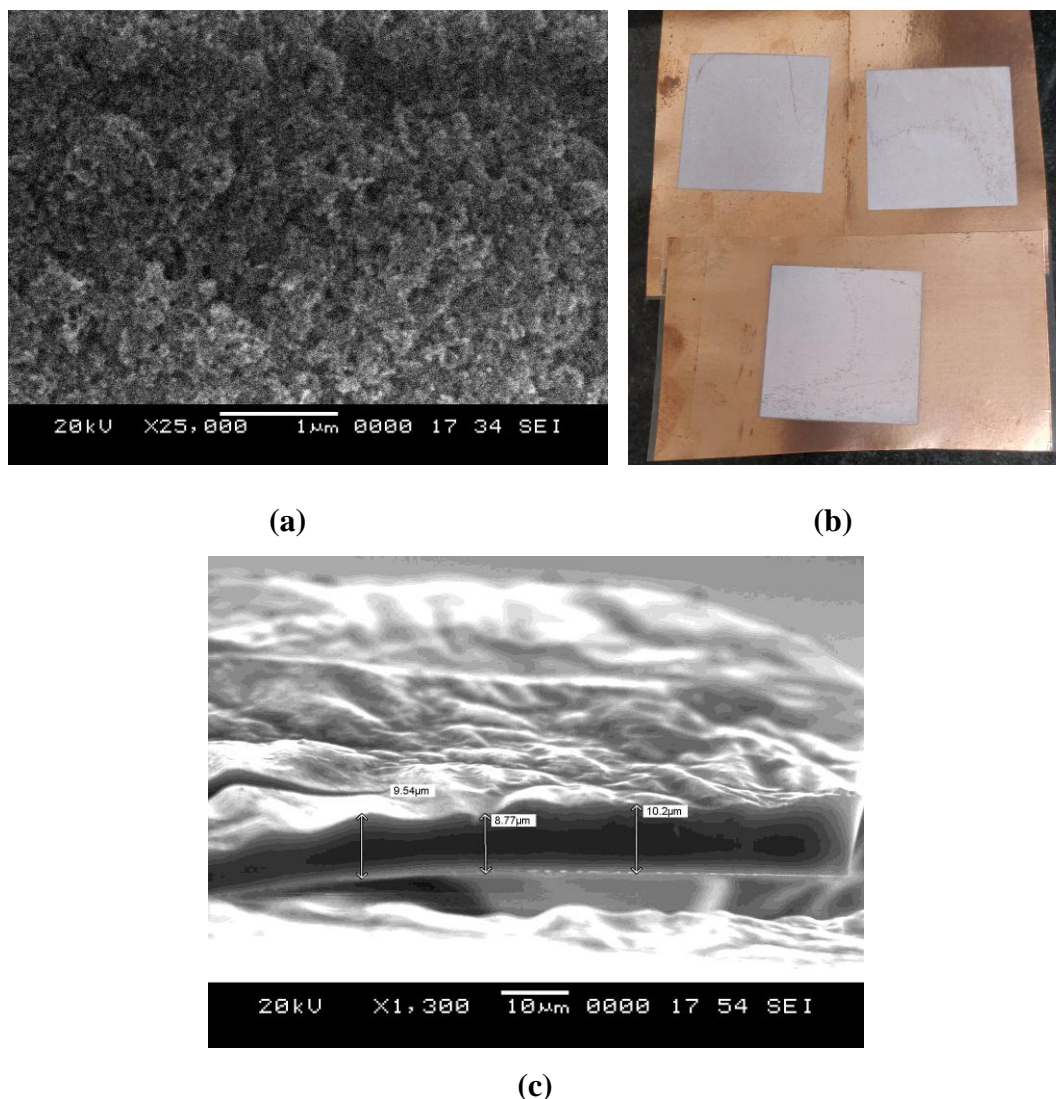


Fig. 6.2 (a) SEM morphology of  $\text{La}_2\text{O}_3$  screen printed film on the copper foil, (b) photograph of the  $\text{La}_2\text{O}_3$  screen printed film on the copper foil and (c) cross sectional SEM micrograph showing the film thickness.

The screen printable paste is prepared using ethylcellulose and terpinol. The film is printed on conductive copper tape using screen-printer. The surface micrograph of  $\text{La}_2\text{O}_3$  screen printed on the copper foil is shown in Fig. 6.2 (a & b). The surface defects like pin holes, defects or cracks are not seen in the micrographs. The film is uniform and defect free throughout the sample. The film thickness is measured from cross sectional sample of the printed film. It is shown in Fig. 6.2 (c). The average cross sectional film thickness is found to be 10 μm.

### 6.2.3 Crystal structure of $\text{La}_2\text{O}_3$ using XRD

The XRD of hydrothermally synthesized  $\text{La}_2\text{O}_3$  nanocrystals is shown in Fig. 6.3. The synthesized  $\text{La}_2\text{O}_3$  nanocrystals are of high purity and pattern is indexed with hexagonal phase (space group  $P-3m1$  with cell constant  $a = 3.9397 \text{ \AA}$ ,  $b = 3.9397 \text{ \AA}$  and  $c = 6.1359 \text{ \AA}$ , ICDD 83-1344) (Salavati-Niasari et al. 2011b).

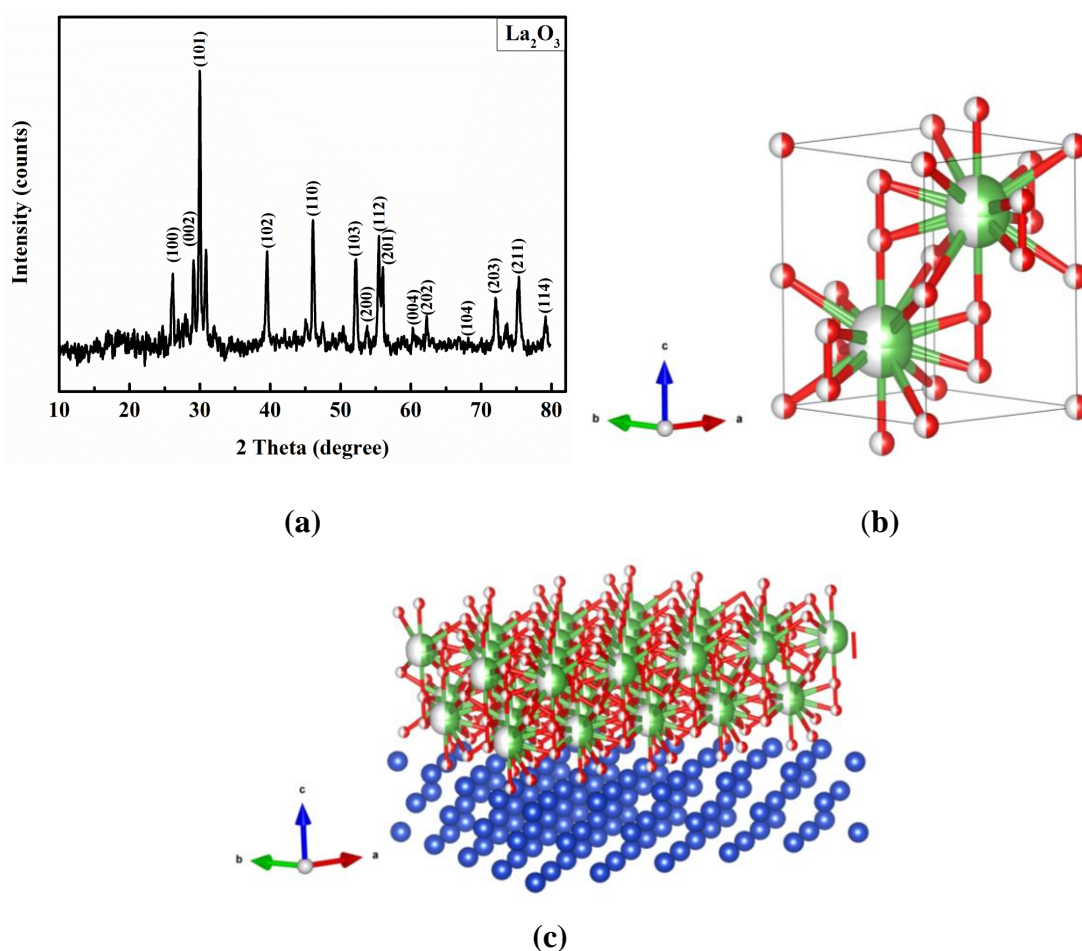


Fig. 6.3 (a) The XRD spectrum of hydrothermally synthesized  $\text{La}_2\text{O}_3$  nanocrystals, (b) the crystal structure of  $\text{La}_2\text{O}_3$  (green-lanthanum and red-oxygen) and (c) the crystal structure of  $\text{La}_2\text{O}_3$  on copper (Blue-copper, red-oxygen and green-lanthanum).

The sharp diffraction peaks at respective Bragg angles indicate that the high crystallinity achieved at considerably low-temperatures (Fig. 6.3 (a)). Thus, both morphological and structural analysis concludes the quality of the synthesized nanocrystals. Also, the broad peaks with large FWHM depict the nanocrystalline nature, which is in good agreement with high-resolution TEM studies presented in

Fig. 6.1 (c & d). The crystal lattice structure is shown in Fig. 6.3 (b). The parameters for drawing  $\text{La}_2\text{O}_3$  crystallographic structure were selected from ICDD 83-1344.

#### 6.2.4 Chemical composition of $\text{La}_2\text{O}_3$ nanocrystals using XPS

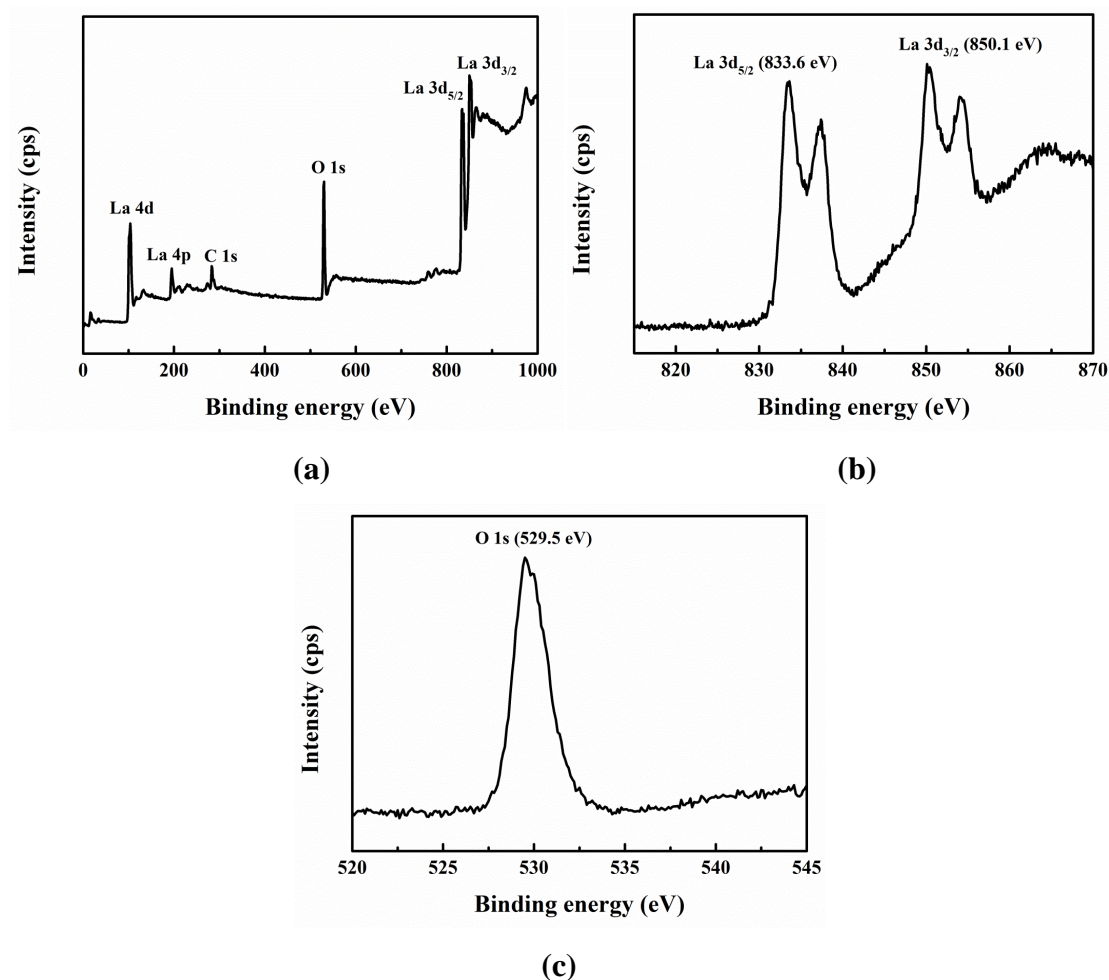


Fig. 6.4 XPS spectra of the  $\text{La}_2\text{O}_3$  showing both (a) low and high-resolution scans, (b) La 3d region and (c) O 1s region.

Further the evidence for the composition is illuminated by the XPS of the  $\text{La}_2\text{O}_3$ . The binding energies obtained in the XPS analysis are corrected for specimen by referencing the C 1s to 284.7 eV (Sunding et al. 2011). The survey XPS spectrum of the sample (Fig. 6.4(a)) suggests that there are no other elements on the surface except lanthanum and oxygen. The presence of minor C 1s peak (Fig. 6.4 (a)) is due to the surface adsorbed carbon atoms/molecules during the hydrothermal synthesis. Figure 6.4 (b) shows that the binding energy of La 3d<sub>5/2</sub> and La 3d<sub>3/2</sub> are 833.6 and

850.1 eV, respectively (Boukha et al. 2010; Li et al. 2019). In Fig. 6.4 (c), it is seen that the O 1s profile is asymmetric, which indicates that two oxygen species are present in the nearby region. The peak which is about 529.5 eV can be indexed to the O<sup>2-</sup> in the La<sub>2</sub>O<sub>3</sub> (Li et al. 2019).

### 6.2.5 BET surface area analysis

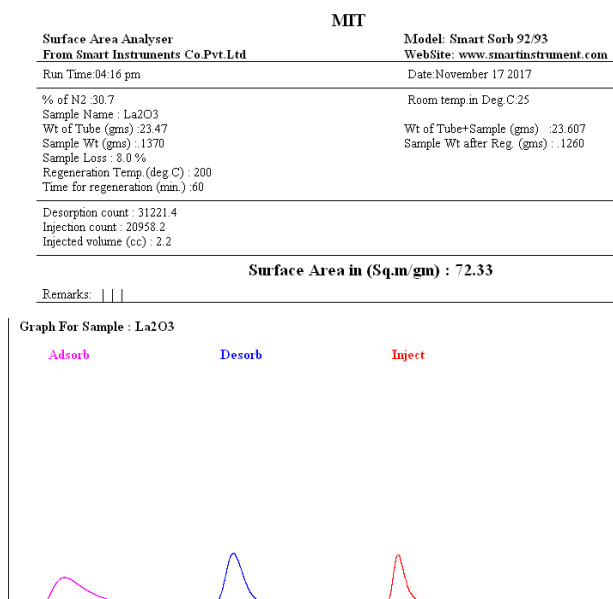


Fig. 6.5 Nitrogen (N<sub>2</sub>) adsorption/desorption isotherms for La<sub>2</sub>O<sub>3</sub> nanocrystals.

Table 6.1 Reported specific surface area of La<sub>2</sub>O<sub>3</sub> nanocrystals.

Method	Specific surface area (m <sup>2</sup> /g)	References
La <sub>2</sub> O <sub>3</sub> -SiO <sub>2</sub> - sol-gel and combustion method	16.7	(Nowicki et al. 2017)
La <sub>2</sub> O <sub>3</sub> - homogeneous precipitation method	18.76	(Liu et al. 2017)
La <sub>2</sub> O <sub>3</sub> - reverse micelle method	12.5	(Sovizi and Mirzakhani 2020)
La <sub>2</sub> O <sub>3</sub> - hydrothermal method	35.61	(Jafari Nejad et al. 2010)
Precipitation method	34	(Badawy and Ibrahim 2016)
Physical mixing and impregnation method	19.44	(Ngaosuwan et al. 2021)
La <sub>2</sub> O <sub>3</sub> – Hydrothermal method	72.33	Present work.

Brunauer–Emmett–Teller (BET) nitrogen gas adsorption-desorption measurements were used to find out the specific surface area of the  $\text{La}_2\text{O}_3$  nanocrystals. The isotherm shows that the particles are porous (Fig. 6.5). The specific surface area of  $\text{La}_2\text{O}_3$  from the BET apparatus is measured to be  $72.33 \text{ m}^2/\text{g}$ . The value is predominant compared to already published literatures (Deng et al. 2009) (Liu et al. 2017) (Nowicki et al. 2017). The specific surface areas of the already reported values are tabulated in Table 6.1.

### 6.2.6 Identification of chemical bonding by FTIR

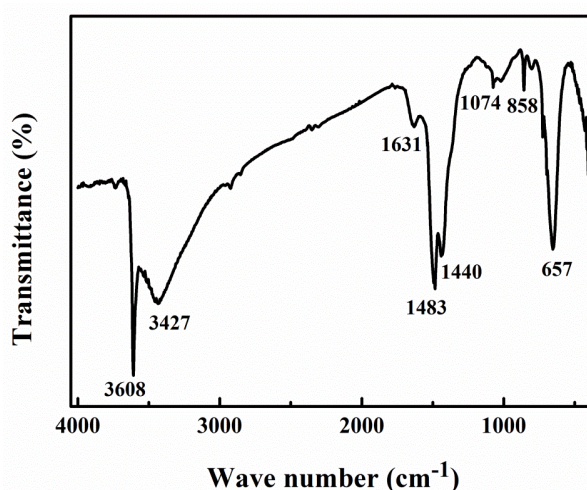


Fig. 6.6 FTIR analysis of  $\text{La}_2\text{O}_3$  nanocrystals.

The FTIR spectrum is recorded to show the functional group of the  $\text{La}_2\text{O}_3$  nanocrystals. The absorption peaks at  $3427$  and  $1631 \text{ cm}^{-1}$  (in Fig. 6.6) were attributed to the stretching vibration of the O-H bond and bending vibration of H-O-H from the moisture on the sample (Hu et al. 2007). The band at  $3608 \text{ cm}^{-1}$  was attributed to the tension of hydroxyl groups of lanthanum oxide. Further, the bands at  $1483 \text{ cm}^{-1}$  and  $1440 \text{ cm}^{-1}$  are attributed to asymmetric stretching mode of the C-O bond (Salavati-Niasari et al. 2011b). The absorption bands at  $858$  and  $657 \text{ cm}^{-1}$  were assigned to bending out of plane vibrations and La-O stretching vibration, respectively (Khosrow-Pour et al. 2013).

### 6.2.7 DSC spectrum of lanthanum oxide nanoparticles

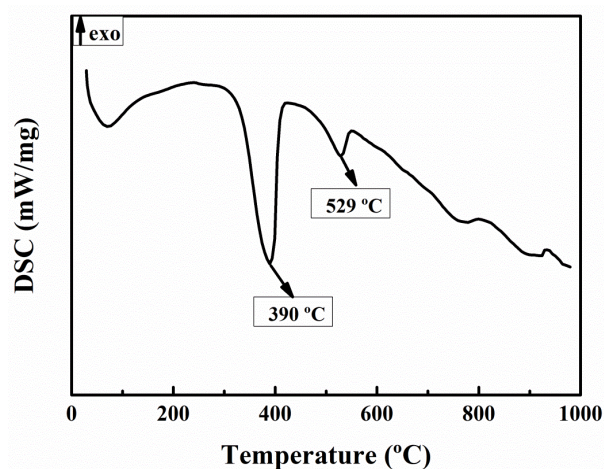


Fig. 6.7 DSC spectrum of lanthanum oxide.

The DSC spectrum, as shown in Fig. 6.7, is indicating that from room temperature to 244 °C the curve is exhibiting exothermic behaviour. It is due to the gradual heat release in the DSC curve, which is attributed to residual organic compound elimination. Two endothermic sharp peaks at 390 and 529 °C are resultant of decomposition of lanthanum compound (Wang et al. 2006). Further, there is no decomposition beyond 550 °C. The sample absorbs heat beyond 550 °C and exhibits endothermic nature. The endothermic peaks beyond 600 °C are due to the decomposition of residuals  $\text{La}(\text{OH})_3$  and  $\text{La}_2\text{O}_2\text{CO}_3$  formed during the synthesis (Kang et al. 2015).

### 6.2.8 Raman spectrum of lanthanum oxide nanoparticles

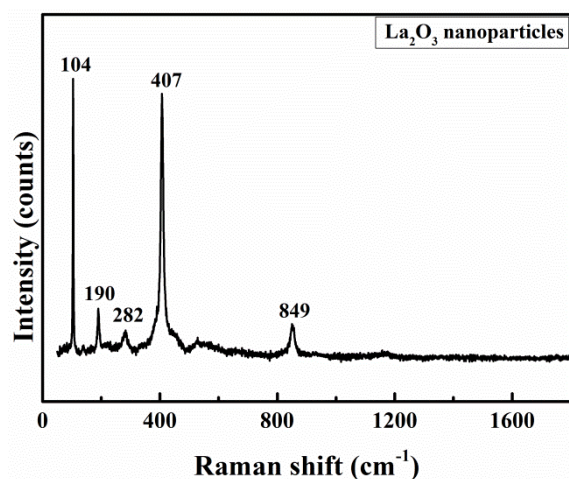


Fig. 6.8 Raman spectrum of  $\text{La}_2\text{O}_3$  nanocrystals.



The Raman spectrum of  $\text{La}_2\text{O}_3$  nanocrystals from  $1600$  to  $50\text{ cm}^{-1}$  is shown in Fig. 6.8. The Raman shifts for  $\text{La}_2\text{O}_3$  are present at  $104$ ,  $190$ ,  $282$ ,  $407$  and  $849\text{ cm}^{-1}$ , respectively. The observed bands are in good agreement with the already reported literature (Zarembowitch et al. 1979) (Yang et al. 2019). The Raman peaks are due to the polycrystalline nature of  $\text{La}_2\text{O}_3$  nanocrystals.

### 6.2.9 Output characteristics of triboelectric nanogenerators

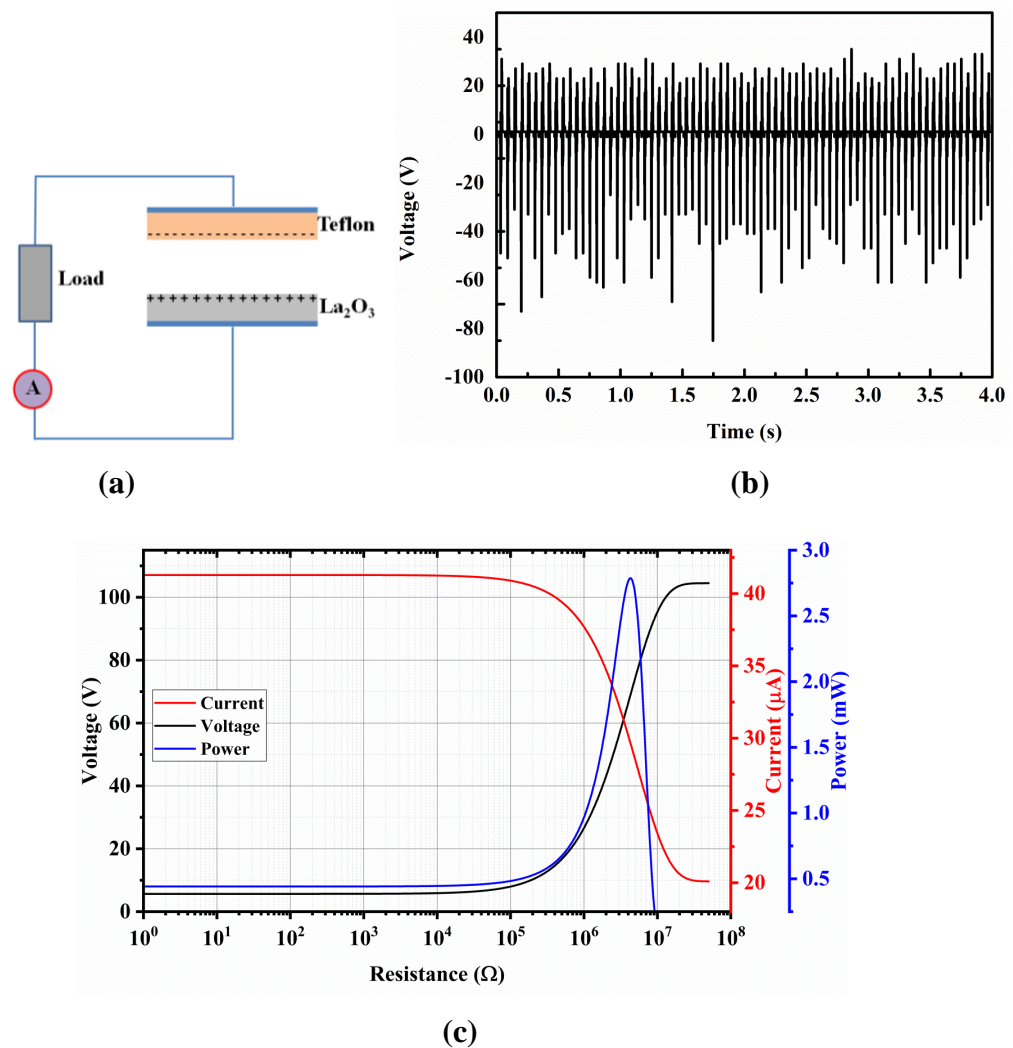


Fig. 6.9 (a) The schematic of TENG device circuit connection, the characteristic electrical output of the  $\text{La}_2\text{O}_3$  triboelectric device showing dependency of (b) voltage and (c) power output on the external load resistance.

To evaluate the maximum power generated by the device, TENG device is connected to an electrical load (resistor)s (Liang et al. 2015a), as shown in Fig. 6.9

(a). The obtained voltage and power output is as shown in the Fig. 6.9 (b & c), respectively. The resistance value was swept from 0 to 50 M $\Omega$ . Respective voltage and current produced by the TENG device are plotted against the external load resistance. The product of the same (i.e., voltage and current) gives the power value. It is found to be maximum at the point where current and voltage intersect each other at 30 M $\Omega$ .

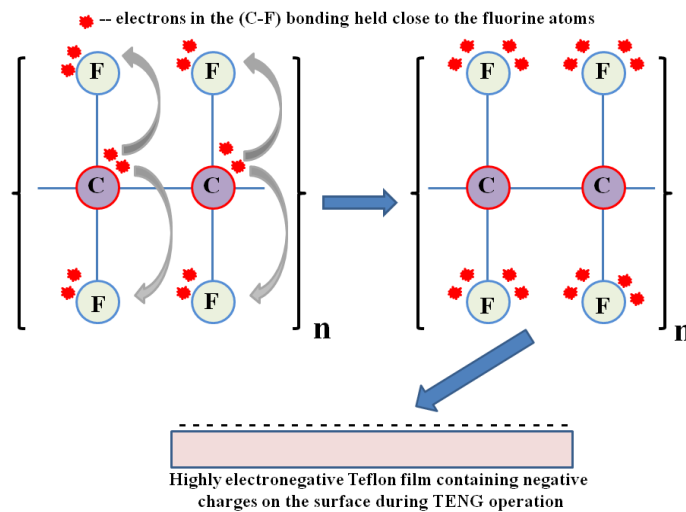


Fig. 6.10 The schematic representation of fluorine tending to hold the electrons in the carbon-fluorine bonds closely to itself, creating highest electron negative polarity over the surface.

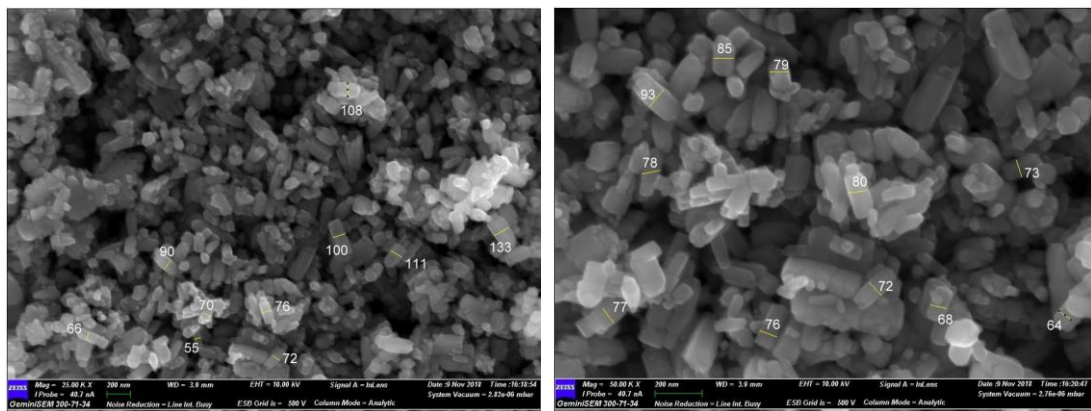
The current amplitude drops with increasing load resistance owing to resistive loss, while the voltage increases. Oscilloscope is used to record the voltage and current generated by La<sub>2</sub>O<sub>3</sub>-TENG device. The performance of the device is tested by tapping the TENG using the motorized fixture (Fig. 3.9). The resistivity of the triboelectric material changes due to chemisorptions of the molecular oxygen species by the Teflon and La<sub>2</sub>O<sub>3</sub> film surface (Wen et al. 2017; Zhang and Wang 2018). The fluorine content in the Teflon is highly reactive with highest electronegativity. The electronegativity of carbon in the Teflon polymer chain is lower than that of the fluorine. Consequentially, the carbon-fluorine bonding electrons are pulled towards fluorine from the carbon (Fig. 6.10). This phenomenon results in high electron polarity around the fluorine atoms. When Teflon and La<sub>2</sub>O<sub>3</sub> nanorod films come into contact, spontaneous polarization occurs (Dewi et al. 2020) on La<sub>2</sub>O<sub>3</sub> and Teflon surface. This result in the dipole moments on Teflon film and La<sub>2</sub>O<sub>3</sub> surface and thus

voltage generates. The device produces an open circuit voltage of 120 V and a short circuit current of 23.7  $\mu\text{A}$ . The device yields a maximum power of 2.85 mW at load resistance of 30  $\text{M}\Omega$ , as shown in Fig. 6.9 (c). The corresponding power density of the  $\text{La}_2\text{O}_3$  TENG device was calculated to be 7.125  $\text{W}/\text{m}^2$ .

### 6.3 Results and Discussion of Triboelectric Property Assessment of ZnO Nanoparticles

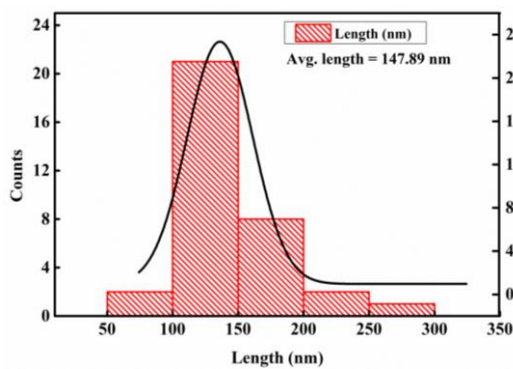
This section focuses on a single-step microwave hydrothermal synthesis of ZnO nanoparticles. The synthesized ZnO nanoparticles were characterized using XRD and SEM technique to study the phase and morphology. The synthesized ZnO nanoparticles were further screen-printed on the conductive copper tape. The screen-printed film was subjected to triboelectric property assessment using fluoropolymer (Teflon) as the counter surface.

#### 6.3.1 Morphology of ZnO nanoparticles

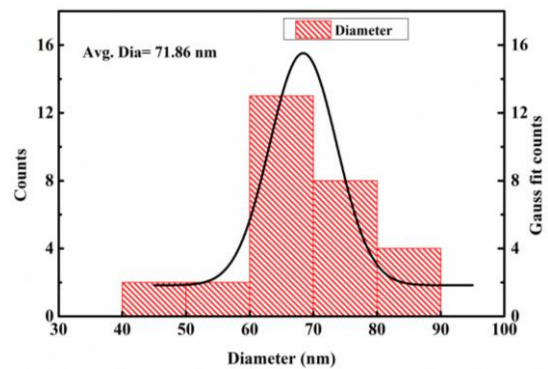


(a)

(b)



(c)



(d)

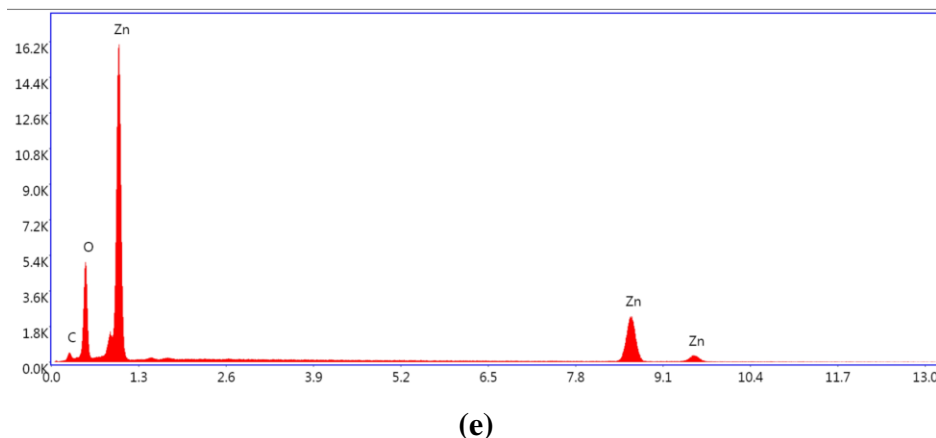


Fig. 6.11 (a) and (b) high resolution SEM micrographs, (c) and (d) particle size distribution with Gauss fit for length and diameter of the ZnO nanoparticles and (e) SEM-EDS spectrum of the ZnO nanoparticles.

Table 6.2 Respective elemental composition of ZnO nanoparticles (in Fig. 6.11 (a)) obtained from the SEM-EDS spectrum is tabulated.

Element	Weight %	Atomic %
C K	8.16	17.76
O K	31.85	54.28
Zn K	59.99	27.96

Figure 6.11 (a) and (b) show the morphology of synthesized ZnO nanoparticles at different magnifications using scanning electron microscope technique. The diameter of the as synthesized ZnO nanoparticles dimensions is in the range of few tens of nanometer and length in few hundreds of nanometers. The ZnO nanocrystals are grown in [0001] direction during the microwave heating. The necessary activation energy for the ZnO crystals is provided by the microwave energy. The micrographs also show that the synthesized nanoparticles are uniform throughout. The particle size distribution graph for length and diameter of the ZnO nanoparticles is shown in Fig. 6.11 (c) and (d). The Gauss fit equation (Eq. 6.1) is used for finding out the average length and diameter of the ZnO nanoparticles. The average length and diameter of the ZnO nanoparticle from the graphs are found to be 147 nm and 71 nm, respectively.

$$y = y_0 + \frac{A}{w\sqrt{\pi/2}} e^{-2\frac{(x-x_c)^2}{w^2}} \quad (\text{Eq. 6.1})$$

The SEM-EDS spectrum is shown in Fig. 6.11 (e). The EDS spectrum shows the presence of only zinc and oxygen elements. The elemental percentage composition is tabulated in Table 6.2. The atomic percentage of the ZnO nanoparticle composition for Zn and O elements are 27.96 and 54.28, respectively. The presence of carbon in the EDS spectrum is due to the carbon-tape substrate.

### 6.3.2 XRD characteristics of ZnO nanoparticles

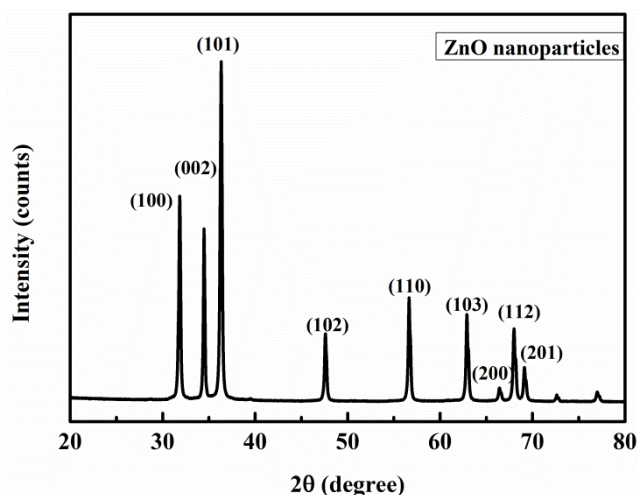


Fig. 6.12 XRD spectrum of ZnO nanoparticles.

Figure 6.12 shows the XRD spectrum of as-synthesized ZnO nanoparticles. The diffraction pattern in the XRD spectrum consists of well resolved high intense peaks of the ZnO. The ZnO nanoparticles obtained are indexed to Bragg angle positions for the  $P63mc$  space group in wurtzite symmetry (ICDD 36-145) (Wang et al. 2012). The  $2\theta$  values for three major peaks of the ZnO nanoparticles are at  $31.68^\circ$ ,  $34.41^\circ$  and  $36.19^\circ$  which are attributed to (100), (002) and (101) planes, respectively, while minor peaks at  $47.45^\circ$ ,  $56.62^\circ$ ,  $62.77^\circ$ ,  $66.67^\circ$ ,  $68.06^\circ$  and  $69.19^\circ$ , correspond to (102), (110), (103), (200), (112) and (201) planes, respectively. The observed diffraction peaks provide a clear evidence for the formation of a single phase wurtzite structure for the ZnO. The average crystallite size of the synthesized ZnO nanoparticles calculated using the *Scherrer equation* is 23.326 nm. The interlayer

spacing “ $d$ ” for the ZnO nanoparticles calculated using the Bragg’s equation for the plane (100) is 0.278 nm (Nipane et al. 2015).

### 6.3.3 Rietveld refinement study of ZnO nanoparticles

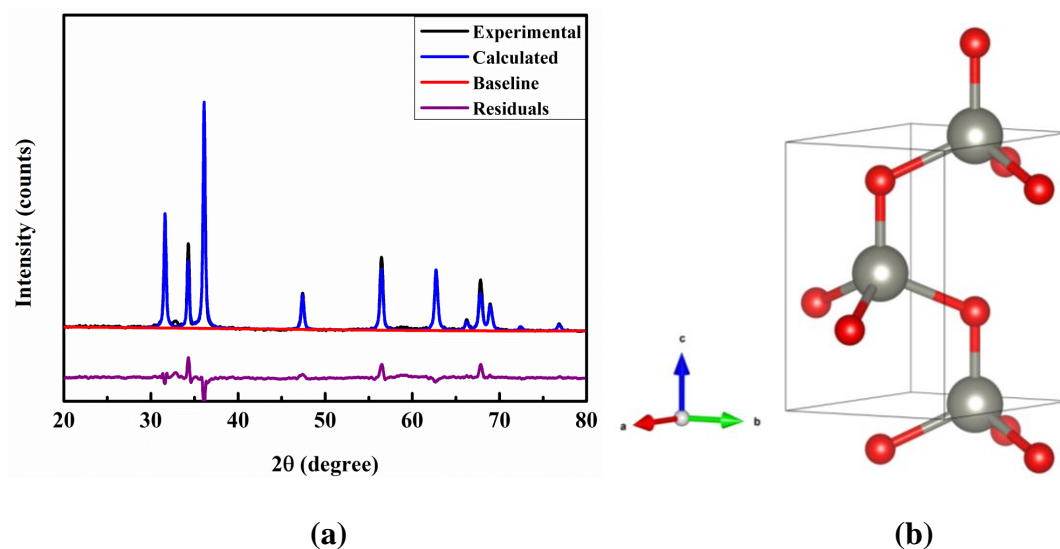


Fig. 6.13 (a) Rietveld refined XRD spectra of the ZnO nanoparticles and (b) crystallographic structure of the ZnO (red colour-oxygen and grey colour-zinc).

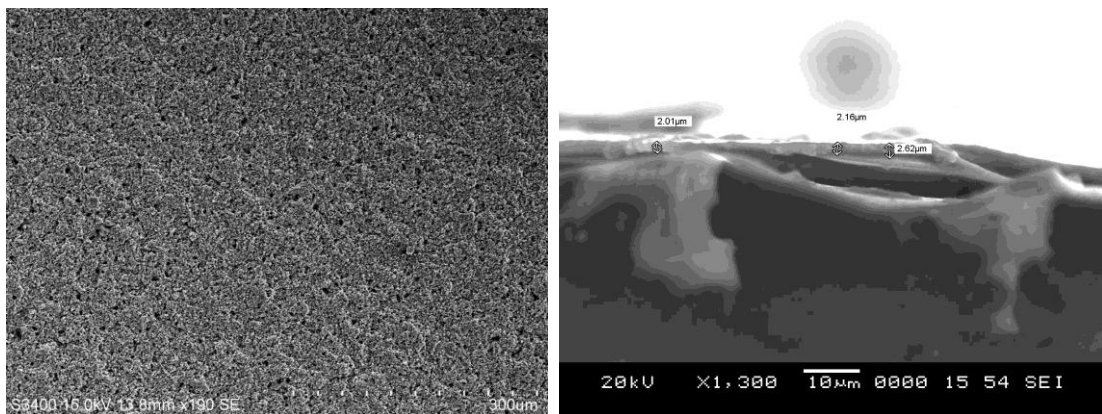
Table 6.3 The refined parameters and crystal data of ZnO nanoparticles.

Parameters	Results
Crystal structure	Wurtzite
Space group	$P6_3mc$
$a$ (Å)	3.251837
$b$ (Å)	3.251837
$c$ (Å)	5.208672
$\alpha$ (°)	90
$\beta$ (°)	90
$\gamma$ (°)	120
$R_p$ (profile factor)	15.1 %
$R_{wp}$ (weighted profile factor)	19.24 %
Cell volume	47.489

Figure 6.13 (a) shows the experimental, calculated and residual XRD profiles for the ZnO nanoparticles after the Rietveld refinement. The major refinement parameters,  $\chi^2$  and  $R_{wp}$ , are well within the acceptable range (Meti et al. 2018). The obtained values of ZnO after the Rietveld refinement are listed in Table 6.3. The lattice parameters calculated from the refined data are  $a = b = 3.251837 \text{ \AA}$  and  $c = 5.208672 \text{ \AA}$ . The crystallographic structure was drawn using the lattice parameters obtained from the Rietveld refinement. It is shown in Fig. 6.13 (b). The crystallographic structure drawn in Fig. 6.13 (b) is hexagonal wurtzite structure of the ZnO.

### 6.3.4 SEM micrographs of screen printed ZnO film

Figure 6.14 (a) shows the morphology of the screen-printed ZnO film. It is observed from the figure that the film has neither cracks, voids nor any other surface defects. The figure shows that the film is uniform over a large area. The ZnO nanoparticles used for this film are intact and bound to each other densely, making the film defect free. The cross sectional SEM micrographs of screen-printed ZnO film in Fig. 6.14 (b) shows the thickness of the film. The average thickness of the film shown is  $2 \mu\text{m}$ .



(a)

(b)

Fig. 6.14 (a) SEM micrographs of screen-printed ZnO (b) cross sectional SEM micrographs of ZnO film showing the thickness.

### 6.3.5 XRD spectrum of screen printed ZnO film

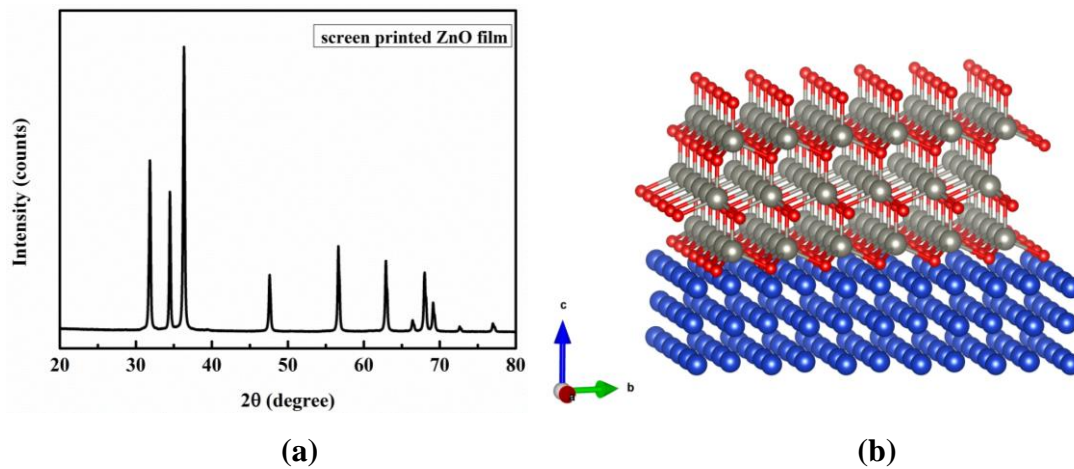


Fig. 6.15 (a) The XRD spectrum of screen-printed ZnO film on the copper tape and (b) the crystal structure of screen-printed ZnO on the copper (Blue-copper, red-oxygen and grey-lanthanum).

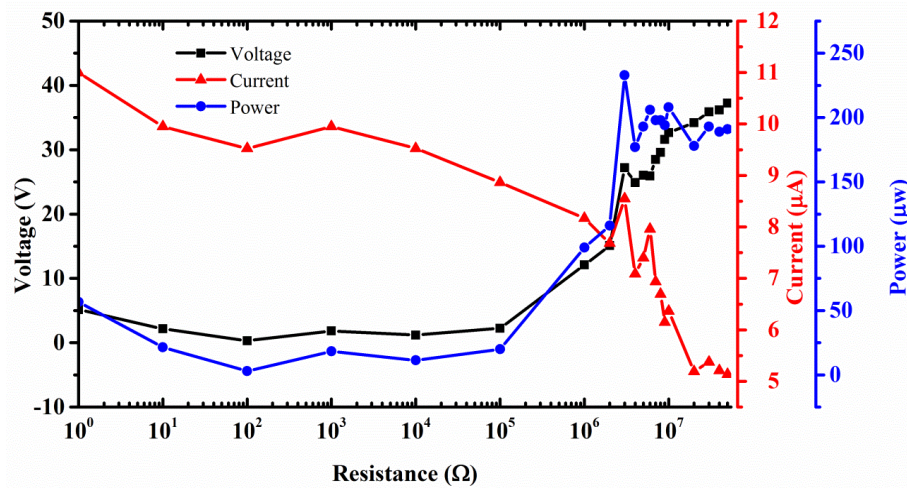
Figure 6.15 (a) shows the XRD spectrum of screen-printed ZnO film. The XRD spectrum shows similar intense sharp peaks at the similar positions to that of ZnO nanoparticles (in Fig. 6.12) without any impurity phases. The diffraction peaks obtained are indexed to Bragg angle positions for the  $P63mc$  space group in wurtzite with hexagonal phase (ICDD 36-145) (Wang et al. 2012). The result indicates that the obtained ZnO film is pristine and has neither undergone any phase transformation during paste preparation nor after screen-printing. Figure 6.15 (b) shows the pictorial representation of crystal structure of ZnO on the copper lattice.

### 6.3.6 Triboelectric property assessment of ZnO film

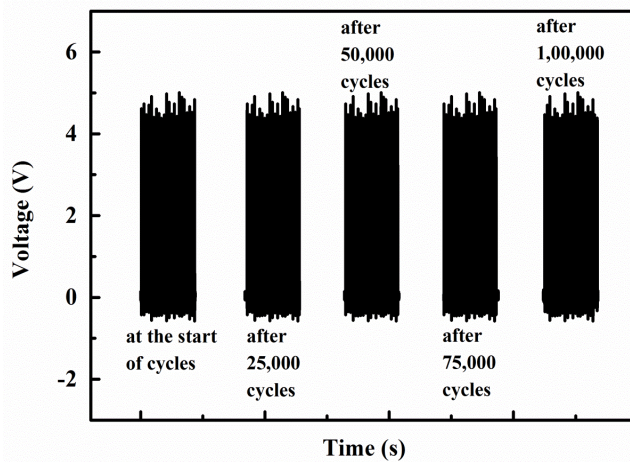
Resistors are used as the external loads to investigate the short circuit current, voltage and output power of the ZnO TENG device. The graph is as shown in the Fig. 6.16 (a). The product of the voltage and current gives the power produced by the TENG. From the figure, it is seen that current drops with increase in the external loading owing to the ohmic loss, while the voltage increases. Due to this phenomenon, the instantaneous peak power ( $V_{\text{peak}}^2/R$ ) is maximized at an external load resistance of 3 MΩ. The maximum power produced by the TENG device is 0.362 mW at 3 MΩ. The corresponding peak power density produced by the device is



0.58 W/m<sup>2</sup>. The TENG device junction (ZnO film and Teflon) is subjected to impulsive load. The durability of the film is important for the application point of view. The durability of the TENG device is examined using an in-house built motorized tapping fixture.



(a)



(b)



(c)

Fig. 6.16 (a) Dependence of voltage, current and the peak power output on the external load resistance (The points represent peak value of electric signals while lines are fitted results), (b) Durability test for TENG active layer: voltage waveform at the beginning, after 25,000 cycles, 50,000 cycles, 75,000 cycles and one lakh cycles of operation and (c) image of the screen-printed ZnO tribo active layer after one lakh cycles of operation.

The Teflon is attached to the tapping shaft surface, while the ZnO film is held stationary below the shaft. The fixture applies a load of 300 gf (gram-force) to make the proper contact between the heterojunction at approximately 15 Hz. This applied load is higher than that of the normal device operation. The data recording during durability test is performed using Arduino. The voltage is first set to 4 – 5 V to reduce the damage to the Arduino board due to the large open circuit voltage of the device. Snippets of the voltage amplitude are recorded at different intervals throughout the durability test measurement (as shown in Fig. 6.16 (b)). It is shown from the durability test that the TENG is still functional even after  $10^5$  cycles of operation without any voltage decay. The voltage amplitude is consistent throughout the durability testing.

The screen-printed ZnO TENG has many advantages. The TENG produces high power density output leading to greatly enhanced effective device performance. Teflon tape and ZnO film creates necessary surface modifications to increase the effective contact area between two contact surfaces. The ZnO nanoparticles used for the TENG greatly increases the effective contact area, necessary high surface and thus increases the triboelectric charges. There is no or negligible decay in the output voltage of the TENG, even after  $10^5$  cycles of operation. It shows that the device can still perform efficiently. The film surface after  $10^5$  cycles of tapping is still intact showcasing that the binding of the ZnO nanoparticles is excellent and adherent to the copper tape (as shown in Fig. 6.16 (c)). The TENG does not rely on direct interaction of the external force and thus it can be easily sealed in the container. The screen-printed ZnO based TENG can be used in external environment with extreme harsh conditions, thereby greatly expanding its applicability to different applications. This makes the device to be used in the areas where human reach is difficult in the constrained or hazardous environment.

## 6.4 Conclusions

In the summary, the synthesis of high surface area ( $\sim 72.33 \text{ m}^2/\text{g}$ )  $\text{La}_2\text{O}_3$  nanocrystals using the hydrothermal technique is presented with its direct utilization in the form of screen-printed film in TENGs. Further, TEM-SAED pattern of  $\text{La}_2\text{O}_3$

nanocrystals showed high intense discrete diffraction spots indicating that the particles were well crystallized. The results are in comparison to that of the XRD technique. The FTIR analysis showed the presence of La-O bond. XPS analysis showed the chemical nature of the nanocrystals. The film of  $\text{La}_2\text{O}_3$  was investigated for its triboelectric behavior and the results depict that the peak output power density could reach up to  $7.125 \text{ W/m}^2$  at an external load resistor of  $30 \text{ M}\Omega$ . Thus, these results suggest that  $\text{La}_2\text{O}_3$  film based TENG device could be used for the self-powered devices and many improvements could be done to increase the power density to use it in various energy harvesting applications.

The synthesized ZnO nanocrystals are directly utilized in the form of screen-printed film to fabricate the TENGs. From the XRD results, it is concluded that the synthesized ZnO nanocrystals showed high intense well resolved peaks. The Rietveld analysis of the XRD spectrum is used to calculate the lattice parameters and phase. The SEM characterization techniques for the ZnO showed that the crystals are uniform throughout and the average crystal size was found to be  $23.326 \text{ nm}$ . The triboelectric characterization of the ZnO is studied with tribonegative fluoropolymer (Teflon). The enhancement in the performance of the TENGs is significant with power and power density of  $0.362 \text{ mW}$  and  $0.58 \text{ W/m}^2$ , at an external load resistance of  $3 \text{ M}\Omega$ . The nanocrystals of ZnO not only enhance the effective surface area, but also lead to preferential polarization of the dipoles, further improving the triboelectric charge accumulation. This enhancement assists in charge injection by triboelectric film on the surface of the ZnO layer, improving the power density value. The facile synthesis of ZnO nanocrystals alongside with simple screen-printing technique provides an easy route to fabricate high-performance TENG device, which could be an excellent candidate for self-powered electronic systems.

*Page intentionally left blank*

# CHAPTER 7

**The content of this chapter have been published in *Journal of Applied Surface Science*, 451, 67-75, 2018, [doi.org/10.1016/j.apsusc.2018.04.138](https://doi.org/10.1016/j.apsusc.2018.04.138).**

*Page intentionally left blank*

## CHAPTER 7

### PHOTOCATALYTIC ACTIVITY OF REDUCED GRAPHENE OXIDE – ZINC OXIDE NANOCOMPOSITES

*This chapter demonstrates the properties of hydrothermally synthesized graphene oxide. Further, it is demonstrated the usage of the hydrothermally synthesized graphene oxide in the preparation of reduced graphene oxide – zinc oxide nanocomposites by using the microwave assisted hydrothermal technique. The synthesized material is characterized and examined for the photocatalytic organic dye (methyl orange) degradation under the UV light.*

#### 7.1 Introduction

The GO/rGO is a two-dimensional mono layer graphite, which are widely used in technological applications in many fields. GO possess extraordinary physical, chemical and mechanical properties. GO and their composites have gained the attention in the field of functional materials due to their improved potential applications. There are number of reports on different methods of synthesis of GO, such as mechanical exfoliation (also called as Scotch-tape method), chemical vapour deposition (CVD), graphite oxide reduction, electron-beam evaporation, epitaxial growth, modified Hummers' method and hydrothermal synthesis (Tang-Lau method). By far, Hummer's method is most widely used technique for the synthesis of GO/rGO. These method involve strong reduction procedures (thermal, chemical, electrochemical), toxic chemicals, high instrumentation cost, tedious procedures and strong reducing agents. Recently, Tang et al. (2012) reported a facile and low cost method for the synthesis of GO utilizing glucose, fructose and sugar as major ingredients. By employing hydrothermal processing, GO is synthesized at much lower temperatures while, at the same time, by varying processing parameters, such as temperature, sugar concentration and duration of heating, the number of layer could be controlled. This method is selected due to the ease of synthesis and requirement of mild chemicals compared to the top-down approach. Also, this can produce relatively

large graphene oxide nanosheets (GONs). The synthesis of GO by Tang Lau method is not explored much in the context of preparation of the nanocomposite.

The ZnO is one of the interesting wide band gap semiconductor materials with a large binding energy, at room temperature. It is an effortless procedure to tune the morphology of micro- and nano-structures of ZnO using various synthesizing techniques, like thermal evaporation, CVD, sol-gel, hydrothermal, aqueous hydrolysis and electrochemical reactions. ZnO finds applications in light emitting diodes, transparent electronic devices, gas sensors, UV filters, acoustic devices, diodes and photocatalytic devices. The optical band gap of ZnO is tuned by the variables, like morphology, composition and size. The composite prepared with carbonaceous species (like GO, rGO, CNT) and ZnO shows tremendous display of improved properties in many applications. The carbonaceous content in the composite assist in charge transfer mobility, thereby improves the optoelectronic, energy storage and photocatalytic properties.

In this chapter, Tang Lau method of synthesizing graphene oxide, with a large lateral dimension, is discussed. The hydrothermally synthesized GO is then successfully reduced and anchored with ZnO nanorods using microwave irradiation. The synthesis method is detailed in section 3.2.5. The addition of rGO to ZnO has resulted in considerable enhancement in the photocatalytic activity when compared to that of the rGO-free ZnO. The effect of rGO content on the photocatalytic performance of the nanocomposite is demonstrated by monitoring the degradation of methyl orange (MO) dye. The difference between rGO, synthesized by modified Hummers' method and hydrothermal method in the preparation of rGO-ZnO nanocomposites, is compared for the photocatalytic ability. The effect of precursors, like zinc chloride and zinc nitrate, in the preparation of rGO-ZnO nanocomposites is also compared for the photocatalytic ability of MO dye degradation.

## **7.2 Characterization of Hydrothermally Synthesized GO**

The initial optimization of hydrothermal synthesis parameters for GO preparation is tuned by variables, like duration of heating and heating temperatures of

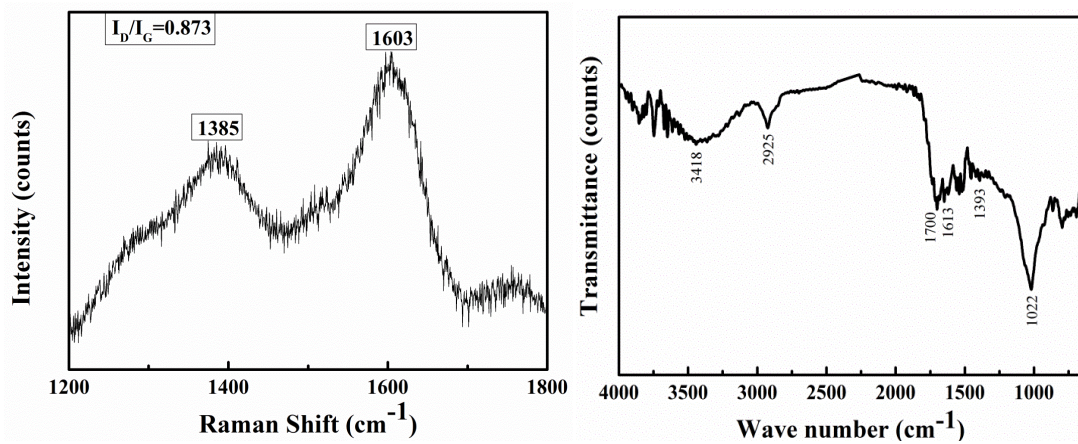


stainless steel autoclave. The heating temperature of autoclave is varied from 165 to 180 °C and time duration from 90 to 110 min. The selected parameters are tabulated in Table 7.1 (Tang Lau et al. 2012). Based on the Raman characteristics of all six samples listed in Table 7.1, the best quality of GO is selected. The glucose and water solution heated in autoclave at 180 °C for 80 min gives the best quality of GO nanosheets. Figure 7.1 (a) shows the Raman spectrum of GONs, where the characteristic D band and G band were observed at 1385 cm<sup>-1</sup> and 1603 cm<sup>-1</sup>, respectively. The G band corresponds to the in-plane stretching motion of the symmetric C-C bond, whereas, the D band is the result of the disruption in symmetric hexagonal graphitic lattice (Bai et al. 2013; Low et al. 2015). The intensity ratio ( $I_D/I_G$ ) is the measure of disorder degree and the average size of the sp<sup>2</sup> domains in graphite materials (Akhavan 2011). The value of  $I_D/I_G$  is observed to be 0.873, which is attributed to the decrease in the size of in-plane sp<sup>2</sup> domains and formation of defects and disorders in the GONs and an increase in the edge planes (Bai et al. 2013).

Table 7.1 Variables in the preparation of GO by hydrothermal method.

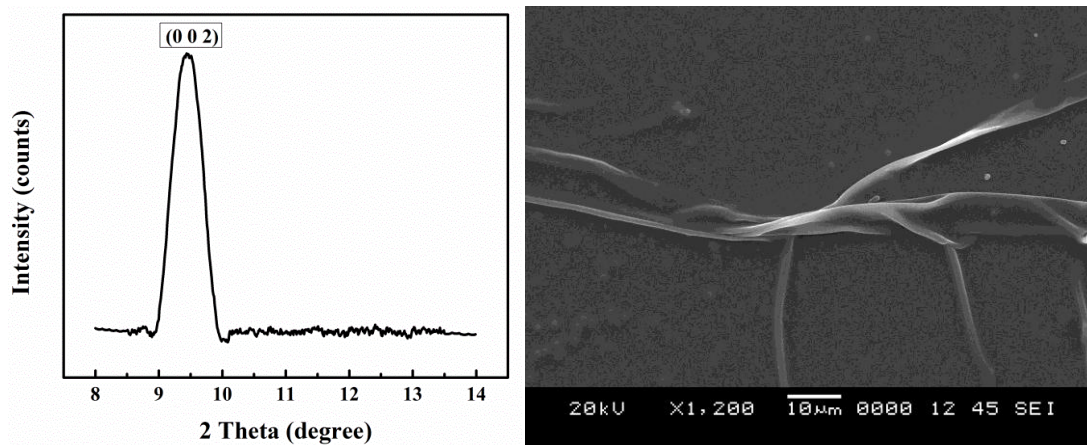
SI. No.	Solution	Concentration	Temperature (in °C)	Time (in min)
1	DI water + glucose	0.5	165	90
2		0.5	170	80
3		0.5	180	80
4		0.5	180	90
5		0.5	180	100
6		0.5	180	110

FTIR spectrum of GONs is shown in Fig. 7.1 (b). The peak response at 2925 cm<sup>-1</sup> is attributed to the stretching vibration of the C-H bond. The broad absorption peak centered at 3418 cm<sup>-1</sup> indicates the presence of hydroxyl (-OH) groups of GONs. The spectrum showed some narrow absorption peaks with position ranging from 3900 - 3600 cm<sup>-1</sup>; which is due to ( $\nu_{OH}$ ) mode vibrations of different isolated hydroxyl groups (Maira et al. 2001). The absorption peaks at 1022, 1393, 1700 and 1613 cm<sup>-1</sup> correspond to alkoxy C-O-C, O=C-O, carbonyl C=O and aromatic C=C stretching vibration modes, respectively (Chen et al. 2015).



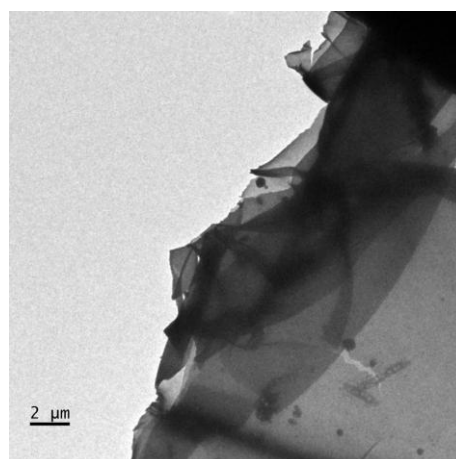
(a)

(b)



(c)

(d)



(e)

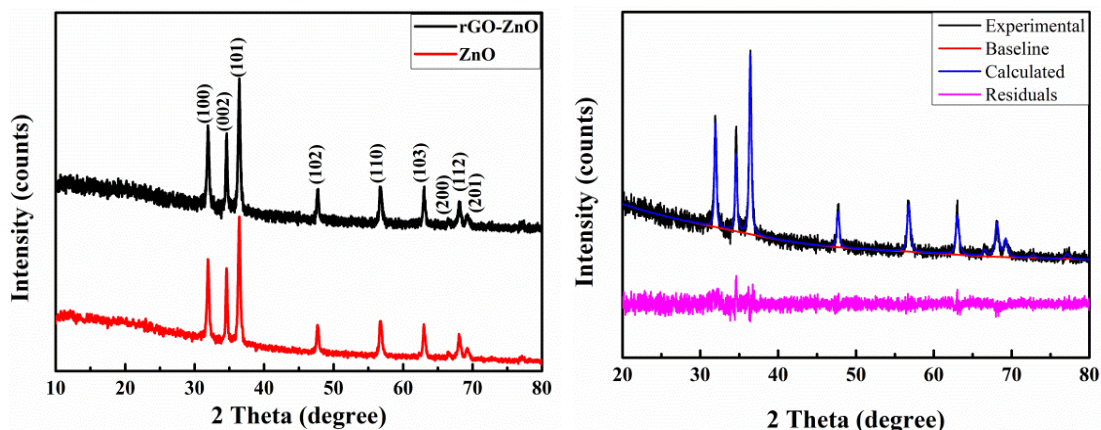
Fig. 7.1 (a) Raman spectrum, (b) FTIR spectrum, (c) XRD spectrum, (d) SEM and (e) TEM micrographs of the hydrothermally synthesized GONs.

These results depict that GONs only have C, H and O elements. C=C and C-C form honeycomb framework with O and H decorating the GONs in –OH, C-H, C-O-C and –C=O groups (Tang et al. 2012). Figure 7.1 (c) shows the XRD pattern of GONs synthesized using sucrose as the reagent in hot air hydrothermal autoclave. The diffraction peak position for (002) reflection is observed at  $9.5^\circ$  ( $2\theta$ ) indicating the  $d$ -spacing of  $9.304 \text{ \AA}$ , which is greater than the reported literature ( $= 8.01 \text{ \AA}$ ) (Štengl et al. 2013a). This incremental deviation from the previous study is attributed to the incorporation of carboxyl, hydroxyl and epoxide groups in graphene sheets during the course of synthesis (Zhou et al. 2012).

The SEM and TEM micrographs of the GONs are shown in Fig. 7.1 (d) and (e). From the micrograph, it is confirmed that the hydrothermally synthesized GONs are made up of large continuous films. The TEM micrograph shows the GONs with different transparency and thickness of sheet like structure. Dark areas in the image are due to the thick stacking of several layers of GONs. Thin transparent region is due to the thinner and few layers of GONs.

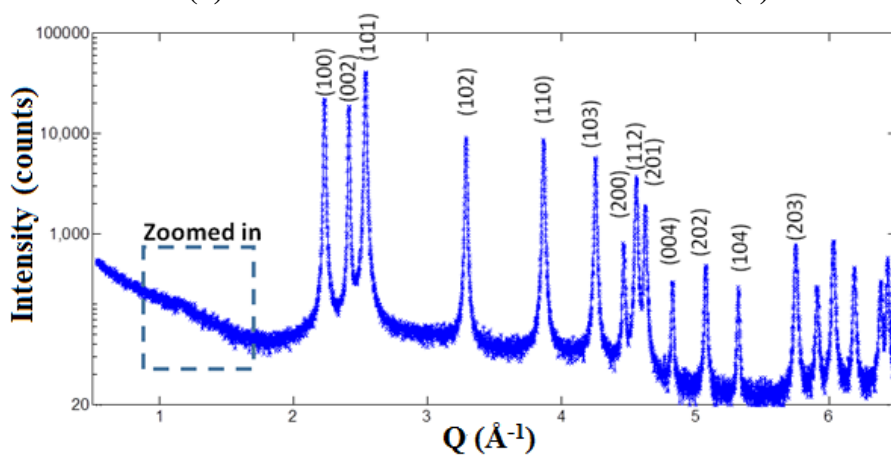
### 7.3 The Structural Characterization of the rGO-ZnO Nanocomposite

The XRD pattern of the rGO-ZnO nanocomposite and ZnO at room temperature is shown in Fig. 7.2 (a). The diffraction pattern consists of well-resolved peaks with significant relative intensity counts. The peaks exhibit Bragg positions for  $P6_3mc$  space group in wurtzite symmetry with a preferred orientation of (101) plane (Kumar et al. 2015c; Prasad and K. Jha 2009). All the peaks of ZnO are in good agreement with the standard ICDD 36-1451 pattern (Lv et al. 2011). The  $2\theta$  values for three major peaks of the ZnO nanopowder are at  $31.7^\circ$ ,  $34.45^\circ$  and  $36.2^\circ$ , which are attributed to (100), (002) and (101) planes, respectively, while minor peaks at  $47.5^\circ$ ,  $56.6^\circ$ ,  $62.8^\circ$ ,  $66.7^\circ$ ,  $68.1^\circ$  and  $69.2^\circ$ , correspond to (102), (110), (103), (200), (112) and (201) planes, respectively. The observed diffraction peaks provide clear evidence for forming a single-phase wurtzite structure for the ZnO. The peak intensities for rGO-ZnO nanocomposite are minimized compared to the ZnO intensities due to the interaction of rGO with ZnO.

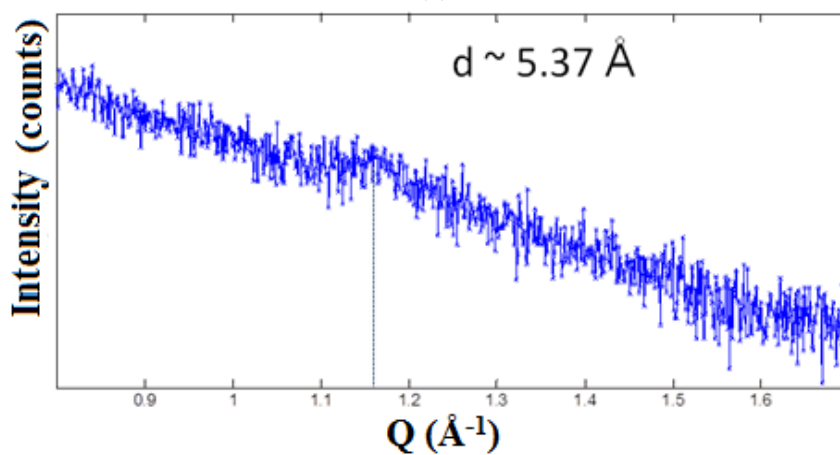


(a)

(b)



(c)



(d)

Fig. 7.2 (a) rGO-ZnO nanocomposite and ZnO XRD pattern, (b) Rietveld refined XRD spectra of rGO-ZnO nanocomposite, (c) Synchrotron XRD pattern and (d) magnified image of the synchrotron XRD pattern showing the presence of the carbon species, graphene (<10%), in the rGO-ZnO nanocomposite.

The XRD pattern of rGO-ZnO shown in Fig. 7.2 (a) is analyzed employing the Rietveld refinement technique with the help of the GSAS software suite. The Rietveld refined data for the XRD pattern is shown in Fig. 7.2 (b). Figure 7.2 (b) shows the experimental, calculated and residual XRD profiles for the rGO-ZnO nanocomposite. The low value of  $\chi^2$  (goodness of fit) and  $R_{wp}$  of 1.110 and 11.9 % are achieved, respectively; which are considered to be good for estimations. The lattice parameters calculated from the refined data are  $a=b= 3.250814 \text{ \AA}$  and  $c= 5.207126 \text{ \AA}$ . These values are in good agreement with those reported in previous studies (Kumar et al. 2015c). No XRD peak related to rGO or any other carbon bearing species is observed. This is attributed to a lower abundance of rGO in rGO-ZnO nanocomposite than the detection limit of XRD.

The XRD studies are further conducted using synchrotron radiation source (Fig. 7.2 (c) and (d)). The intense and relatively broad XRD peaks of ZnO are observed, indicating the nanocrystalline nature of ZnO in the nanocomposite. The crystallite size of ZnO is estimated to be 31 nm using the Scherrer formula. A diffused hump close to the  $Q$  value  $1.17 \text{ \AA}^{-1}$  (corresponding to the  $d$ -spacing of  $5.37 \text{ \AA}$ ) is also observed (depicted in Fig. 7.2 (d)), which is attributed to the presence of rGO. The reduction in the  $d$ -spacing from  $9.304 \text{ \AA}$  to  $5.37 \text{ \AA}$  is attributed to the loss of oxygen, which tends to move the  $d$ -spacing closer to the graphitic structure ( $3.35 \text{ \AA}$ ).

#### **7.4 Chemical Composition Analysis of rGO-ZnO Nanocomposites Using XPS**

Figure 7.3 (a) shows the broad survey XPS spectrum of rGO-ZnO nanocomposite powder. The spectrum reveals the presence of three elements, namely, carbon, oxygen and zinc. The XPS data is matched well with the previously reported data (Akhavan 2011). In Fig. 7.3 (b), two peaks corresponding to Zn  $2p$  core-level is observed at 1022.5 and 1045.7 eV attributed to Zn  $2p_{3/2}$  and Zn  $2p_{1/2}$ , respectively (Feng et al. 2014). These results indicate the chemical state of zinc as Zn (+2 oxidation state). The O  $1s$  peak is centered at 531.5 eV and C  $1s$  peak at 285.75 eV (Fig. 7.3 (a)). From Fig. 7.3 (c), the peak corresponds to O  $1s$  is relatively more comprehensive and can be deconvoluted into three synthetic peaks centered around 531.05, 532.25 and 533.35 eV indicating three kinds of oxygen-containing species.

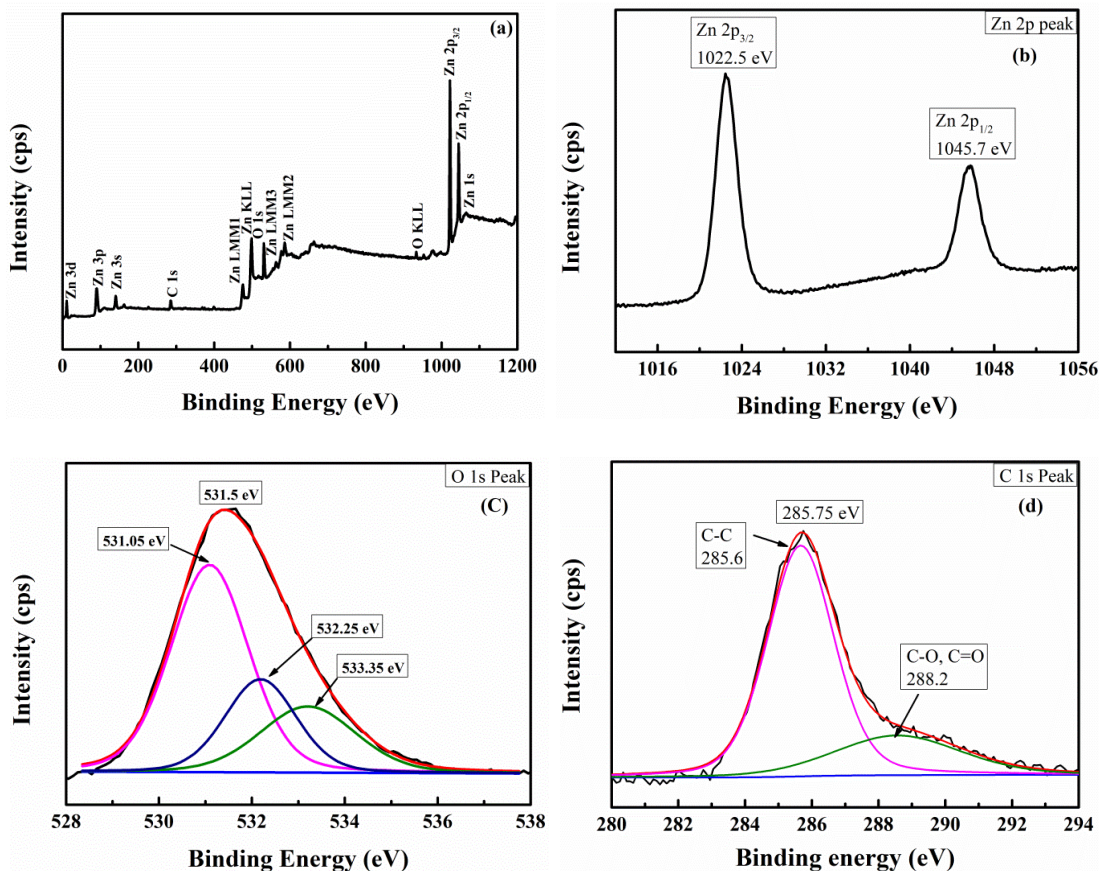


Fig. 7.3 (a) X-ray photoelectron survey spectrum and high-resolution responses of (b) Zn 2p, (c) O 1s and (d) C 1s of rGO-ZnO nanocomposite.

The O 1s peaks centered at 532.25 eV and 531.05 eV are attributed to the oxygen from absorbed water and ZnO, while the O 1s peak centered around 533.35 eV is attributed to oxygen attached to the rGO as C-O bond (Zhao et al. 2014). No peaks corresponding to C=O bonds are observed, which is due to the much lower content of C=O compared to C-O in rGO-ZnO nanocomposite. The C 1s peak centered at 285.75 eV is deconvoluted into two peaks centered around 285.6 eV and 288.2 eV, as shown in Fig. 7.3 (d). The peak centered around 285.6 eV is attributed to C-C bond while the peak centered around 288.2 eV is due to the presence of C-O/C=O bond (Liu et al. 2015). The C-C bond is intense and sharp where as the C-O bond is broadened due to the loss of oxygen during reduction of GO into rGO.

## 7.5 Raman Spectroscopic Analysis of rGO-ZnO and ZnO

The Raman spectra for the rGO-ZnO and the ZnO are shown in Fig. 7.4. The characteristic D and G bands for rGO are observed in the nanocomposite at  $1386\text{ cm}^{-1}$  and  $1604\text{ cm}^{-1}$ , respectively. However, the ratio  $I_D/I_G$  of rGO present in rGO-ZnO nanocomposite is 0.91, which is greater compared to 0.873 (from GO, Fig. 7.1 (c)), confirms the reduction of GO to rGO during microwave heating. This increase in the intensity ratios is due to the decrease in the size of  $\text{sp}^2$  domains of rGO upon reduction and interaction between ZnO and graphene sheets. The Raman shift for ZnO is observed at  $437\text{ cm}^{-1}$ , corresponding to  $E_2$  high-frequency mode of wurtzite structure from  $C_{6v}$  symmetry group (Ashkenov et al. 2003; Lin et al. 2006).

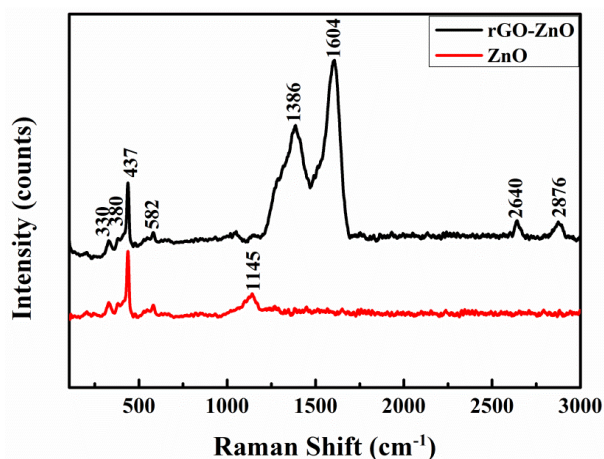


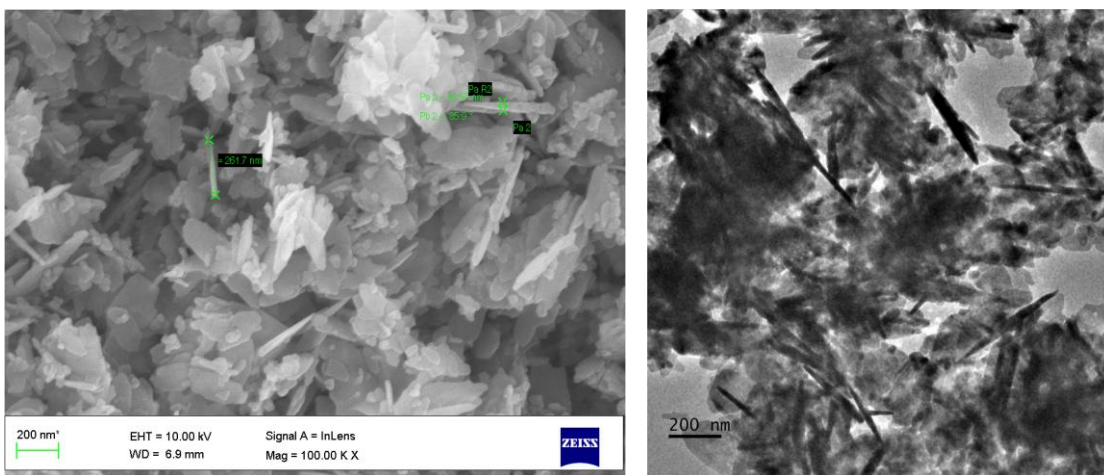
Fig. 7.4 Raman spectra of the ZnO and the rGO-ZnO nanocomposite.

The intensity of  $E_2$  high-frequency mode of the bare ZnO is somewhat lowered by the interaction of the rGO with the ZnO. Group theory predicts that the  $A_1$ ,  $E_1$  and  $E_2$  optical modes are present at the point of Brillion zone.  $A_1$  and  $E_1$  symmetry are polar and get split into longitudinal optical (LO) and transverse optical (TO) phonons, all being Raman and infrared active, and hence exhibit different frequencies (Alim et al. 2005; Pruna et al. 2017b). The peak represents the structural defects in ZnO at  $582\text{ cm}^{-1}$  which is assigned to  $E_1$  (LO) mode. The peak centered around  $380\text{ cm}^{-1}$  and a small shoulder peak at  $410\text{ cm}^{-1}$  are due to  $A_1$  (TO) mode and  $E_1$  (TO) mode frequencies, respectively (Ashkenov et al. 2003). The peaks centered around  $330\text{ cm}^{-1}$  and  $1145\text{ cm}^{-1}$  in the spectrum of ZnO are due to the multiple-phonon scattering process, whereas the intensity of these peaks in rGO-ZnO nanocomposite is

lowered. The Raman peaks corresponding to ZnO in rGO-ZnO nanocomposite are broadened due to higher scattering and interaction of rGO with ZnO.

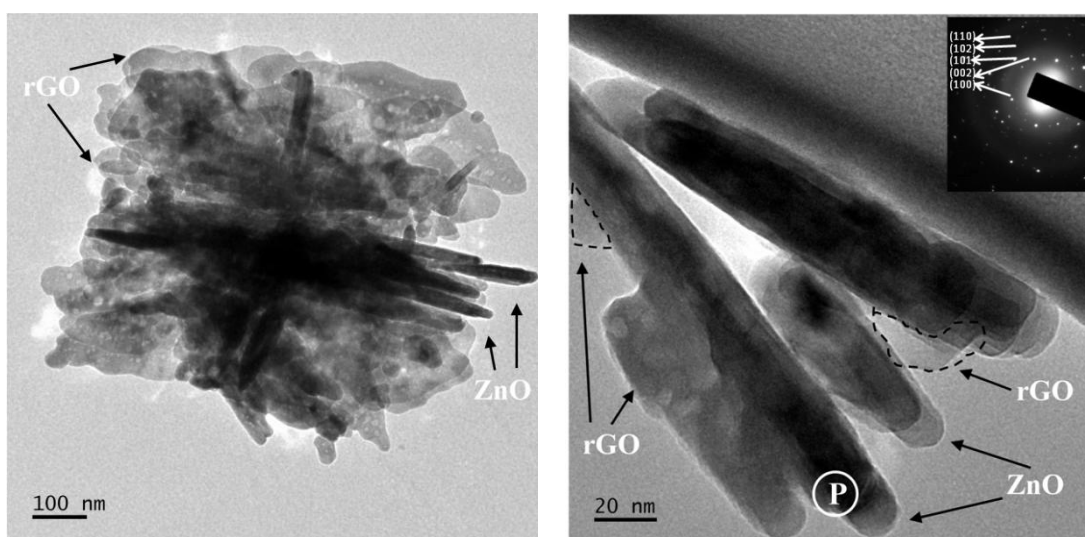
## 7.6 Morphological Analysis of rGO-ZnO Nanocomposites Using FESEM and TEM

The FESEM shows the detailed morphology of the rGO-ZnO nanocomposite. It is observed that the ZnO nanorods are sandwiched between the rGO nanosheets, as shown in Fig. 7.5 (a).



(a)

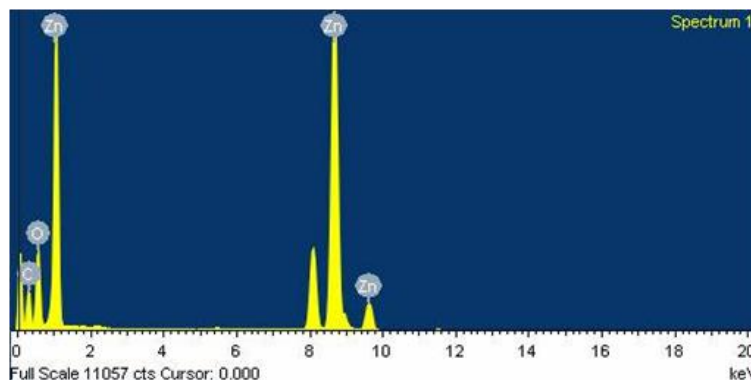
(b)



(c)

(d)





(e)

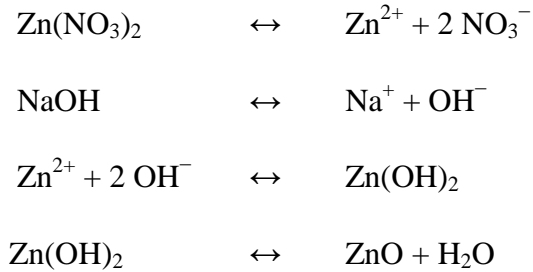
Fig. 7.5 (a) FESEM micrograph presenting morphology of the rGO-ZnO nanocomposite, (b) and (c) TEM micrographs of the microwave-assisted hydrothermally synthesized rGO-ZnO nanocomposite showing ZnO nanorods decorated with rGO, (d) TEM micrograph with selected area electron diffraction (SAED) pattern and (e) TEM-energy dispersive spectroscopy (EDS) of the rGO-ZnO nanocomposite.

The diameter of the ZnO rods is varied in tens of nanometers where as the length in few hundreds of nanometers. In order to complement the results of XRD and FESEM, the microstructure is further investigated by using the TEM. Figure 7.5 (b) and Fig. 7.5 (c) show the TEM micrographs. It shows that the rGO nanosheets are successfully stacked on to the ZnO nanorods. The rGO and ZnO are highlighted in the figures. The selected area electron diffraction (SAED) patterns from the ZnO nanorods showed high intensity diffraction spots indicating well-crystallized ZnO nanorods. One of such SAED patterns is depicted in the inset of Fig. 7.5 (d), from the region marked as “P” in the micrograph. TEM-EDS in Fig. 7.5 (e) spectrum show that C, O and Zn are the only elements present in the nanocomposite.

### 7.7 Growth Mechanism of the ZnO and rGO-ZnO Nanorods

The ZnO crystals are obtained by microwave heating of the  $\text{Zn}(\text{NO}_3)_2$  in a strong alkaline solution using NaOH at 700 W power for 10 min. Zinc dissociates into  $\text{Zn}^{2+}$  ions and the NaOH added to the solution dissociates into sodium ions ( $\text{Na}^+$ ) and hydroxyl ions ( $\text{OH}^-$ ) (Park et al. 2009). The amount of polar molecules and the

hydroxyl ions concentration in the solution are increased. The chemical reaction is predicted as follows:



The thermal energy required is less for the synthesis of ZnO and rGO-ZnO nanocomposite using microwave heating. Since, GO is added to obtain rGO-ZnO nanocomposites during microwave heating, the growth mechanism for the nanocomposite is completely different from the conventional reported mechanisms for either ZnO nanorods or rGO. Microwave primarily interacts with the polar molecules, such as H<sub>2</sub>O to generate heat (Kajbafvala et al. 2009). These molecules absorb microwaves, which results in the rotational molecular motion and heating (ZHU et al. 2009). The rapidly changing electromagnetic field in the microwave chamber causes the movement and polarization of the ions. This phenomenon results in transient and localized high temperature for the reaction system, which facilitates the growth and formation of the rGO anchored ZnO nanocrystals. Prolonged heating during conventional processing usually results in the growth of large crystals. The microwave generates heat within the material and also assists in the molecular motion, which increases the growth kinetics. The activation barrier to nucleation requires lesser thermal energy than the conventional heating. As a result, nucleation is favoured while the growth is restricted mainly due to less time at high temperatures resulting in much finer crystals. It is known that the ZnO has hexagonal lattice structure and the molecule is polar in nature. The ZnO crystals grow along the c-axis of the hexagonal lattice (Wang and Zhu 2004). The inherent asymmetry along the c-axis leads to the anisotropic growth of the ZnO crystallites. Additionally, GONs provide the necessary seed for the nucleation to happen. The growth is more favoured along [0001] direction. The end planes for these ZnO crystals are generally reported to be Zn terminated (0001) surface (Qurashi et al. 2009).

## 7.8 MO Dye Degradation Studies Using rGO-ZnO and ZnO

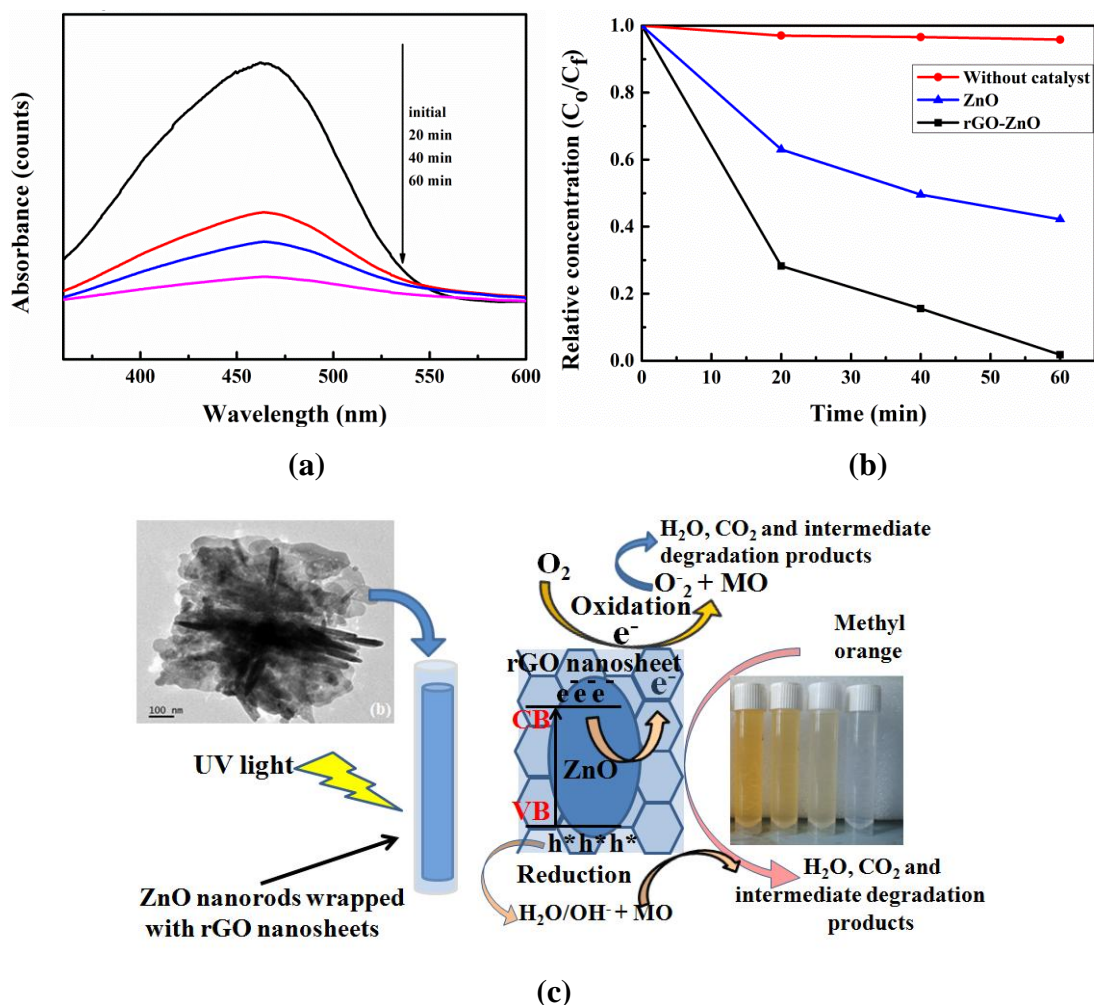


Fig. 7.6 (a) The absorbance spectra of the MO aqueous solution in rGO-ZnO composite after different irradiation time, (b) photocatalytic degradation of the MO aqueous solution in the presence of the rGO-ZnO and the ZnO and (c) the graphical abstract showing the mechanism of MO dye degradation using rGO-ZnO nanocomposite in presence of UV light source.

The photocatalytic ability of the ZnO and the rGO-ZnO is evaluated by the degradation of the methyl orange (MO) under UV irradiation. The absorption spectra of the MO with the rGO-ZnO and the ZnO are recorded for every 20 min. The reduction in the intensity of the absorption peak from MO is depicted in Fig. 7.6 (a). The graph of the concentration changes ( $C_f/C_o$ ) against time is plotted (Fig. 7.6 (b)), where  $C_f$  and  $C_o$  are the final and initial concentration during degradation of the

methyl orange solution, respectively. It is observed that, the degradation of MO molecules is considerably faster in the presence of the rGO-ZnO catalyst in comparison to that with ZnO catalyst. With the rGO-ZnO nanocomposite, almost 98.23% of the MO dye is degraded within 60 minutes, whereas the bare ZnO catalyst resulted in degradation of only 57.78%.

The greater rate of degradation of MO molecules is attributed to the presence of rGO in the rGO-ZnO. The rGO present in the rGO-ZnO composite provides a higher surface area to bind MO molecules through  $\pi$ - $\pi$  conjugation with the offset along the face-to-face direction (Liu et al. 2010). The conduction and valence band of ZnO is at -4.05eV and -7.25 eV, respectively. The work function of the graphene is -4.42 eV (Li and Cao 2011; Qin et al. 2017). In such a case, the ZnO in the rGO-ZnO transfers the photoelectrons from the conduction band to the rGO to attract the MO molecules, enhancing the photocatalytic ability of the rGO-ZnO (Liu et al. 2012b).

The theory behind the high degradation rate is explained as follows: when the rGO-ZnO nanocomposite is exposed to UV light, ZnO emits photoelectrons and holes in the water medium (Kumar and Rao 2017; Sushma and Girish Kumar 2017). The photogenerated electrons then react with surface oxygen on the ZnO to form superoxide radicals ( $O_2^-$ ). The recombination of photogenerated holes and surface oxygen generates hydroxyl radicals ( $OH^-$ ) (Yu et al. 2015). These active oxygen species ( $O_2^-$  and  $OH^-$ ) are responsible for degrading the MO dye.

They react with MO molecules to form  $CO_2$ ,  $H_2O$  and other byproducts. These active species can also recombine within the catalyst without reacting with the MO. This phenomenon is graphically represented in Fig. 7.6 (c). Therefore, the active species must be accepted and delivered away to resist the photoelectrons' recombination with the holes. This role is taken care by the rGO, which offers access to accept and transfer the photoelectrons. The effective charge transfer can reduce the charge recombination and increase the photocatalytic activity of the rGO-ZnO nanocomposite. Another important factor for increase in the photo degradation rate is the possibility of ZnO nanostructure and rGO sheets to connect each other tightly (Zhou et al. 2012).

The photodegradation rates are calculated using pseudo first-order kinetics using Langmuir-Hinshelwood model (Eq. 7.1) (Mohan et al. 2012)

$$\frac{C_0}{C_f} = e^{kt} \quad (\text{Eq. 7.1})$$

The rate constants for the rGO-ZnO and the ZnO are calculated using equation 7.1 are  $0.0523 \text{ min}^{-1}$  and  $0.0143 \text{ min}^{-1}$ , respectively. It is found that the addition of the rGO content to the ZnO has enhanced the photocatalytic ability of the ZnO by more than 3.5 times. A higher rate constant is achieved by using the GO synthesized by the hydrothermal method in comparison with the GO by Hummer's method (Ashkarran and Mohammadi 2015).

### 7.9 Photocatalytic Performance Comparison of rGO-ZnO Prepared from Different Zinc Precursors

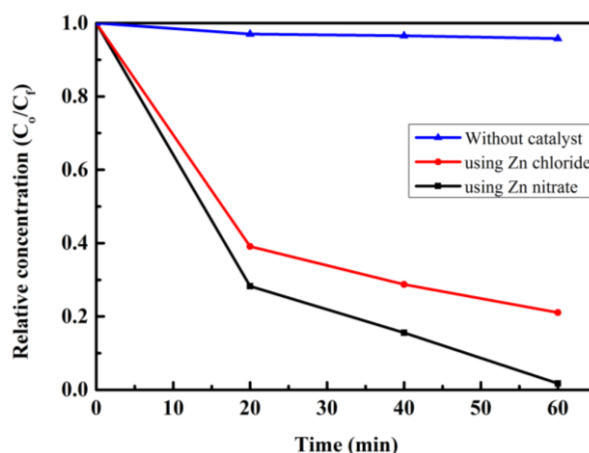


Fig. 7.7 The comparison of absorbance spectra of the MO aqueous solution in the presence of the rGO-ZnO nanocomposite prepared using zinc chloride and zinc nitrate after different UV irradiation times.

The performance of the rGO-ZnO nanocomposite is also compared with the rGO-ZnO nanocomposite synthesized using  $\text{ZnCl}_2$  as a precursor for ZnO. The rGO-ZnO nanocomposite is prepared by using  $\text{ZnCl}_2$  instead of  $(\text{Zn}(\text{NO}_3)_2 \cdot 6 \text{H}_2\text{O})$ . Same quantity of GO and Zn-chloride, in comparison with Zn-nitrate precursor, is taken for synthesizing rGO-ZnO nanocomposite. The microwave energy and heating duration is kept constant. The photocatalytic performance of MO dye by using rGO-ZnO

nanocomposite, synthesized using different zinc precursors, is plotted in Fig. 7.7. It is found that after 60 min; only 78.93% MO degradation is achieved for the rGO-ZnO nanocomposite (where, zinc chloride is the precursor). The Zn-nitrate is always a better choice for preparing rGO-ZnO due to its ability to lower the melting point and ease the decomposition process. The Zn-nitrate precursor doesn't leave any hazardous decomposition products when compared to the Zn-chloride precursor. There are a number of reports on well-crystallized ZnO nanorods synthesis using zinc nitrate as the starting material (Kumar et al. 2015; Sushma et al. 2017). Moreover, one of the highest photocatalytic efficiency is reported for the ZnO nanorods obtained from the zinc nitrate as the starting material (Kumar et. al. 2015). The percentage degradation of the MO by using rGO-ZnO (using  $\text{Zn}(\text{NO}_3)_2 \cdot 6\text{H}_2\text{O}$ ) is 98.23% whereas, it is 78.93 % for rGO-ZnO nanocomposite using  $\text{ZnCl}_2$  precursor.

### 7.10 Photocatalytic Degradation Performance Comparison of rGO-ZnO Nanocomposites with GO Prepared from Tang Lau Method and Hummer's Method

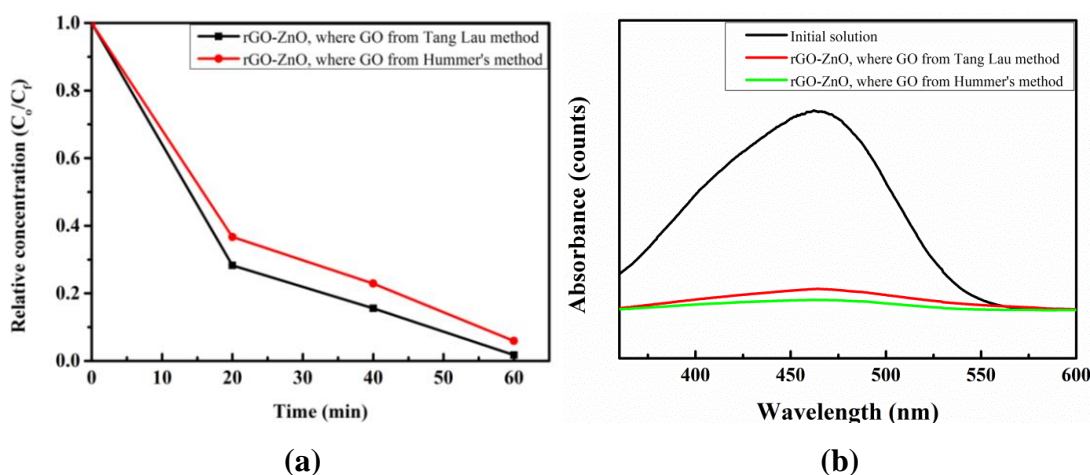


Fig. 7.8 The comparison of absorbance spectra of the MO aqueous solution in the presence of the rGO-ZnO nanocomposite prepared using GO synthesized from Tang Lau method and Hummer's method.

The GO synthesized by Hummer's method is used in the preparation of rGO-ZnO nanocomposite. The photocatalytic performance of such rGO-ZnO (where GO prepared by Hummer's method) is also compared with rGO-ZnO (where GO prepared

with Tang Lau method). The effect of using GO, synthesized by Hummer's method in the preparation of rGO-ZnO nanocomposite, is examined for the degradation of MO dye. Similar testing parameters are maintained throughout. Similar quantity of GO is taken for synthesizing rGO-ZnO nanocomposite. Figure 7.8 shows the UV-visible spectra for the MO dye degradation and performance comparison. It is found that the synthesized nanocomposite showed better performance when compared to the rGO-ZnO (where GO synthesized from Hummer's method). After 1 hour of exposure of the MO dye and photocatalyst, 95.83% of the MO dye is degraded, where as it is 98.23% for rGO-ZnO (where GO synthesized from the Tang Lau method). These degradation results showed the prepared rGO-ZnO nanocomposite is having better degradation ability.

### 7.11 The Recycling Ability of rGO-ZnO Nanocomposites

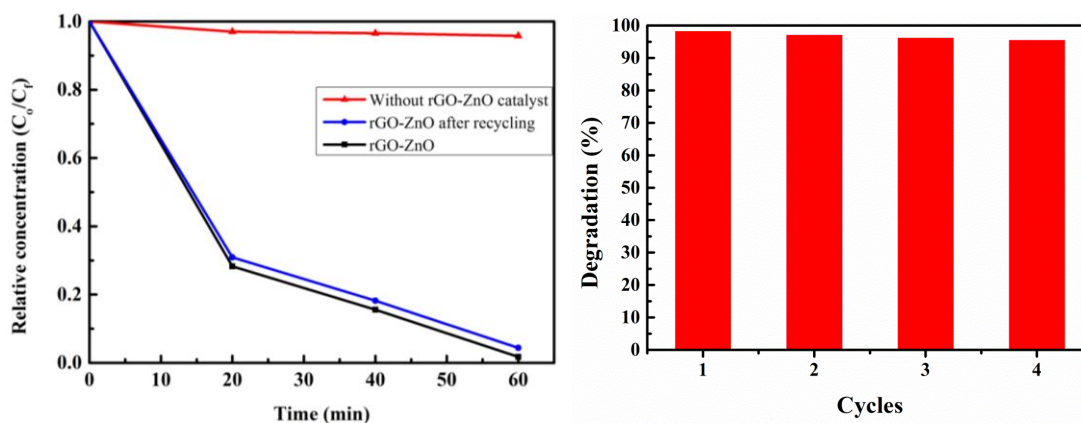


Fig. 7.9 The recycling ability of rGO-ZnO nanocomposite for the MO aqueous solution.

The recycling ability of the rGO-ZnO nanocomposite is tested and plotted in Fig. 7.9. The figure shows the photocatalytic ability of the prepared rGO-ZnO nanocomposite is almost constant for all the cycles. The degradation efficiency is 98.23% and 95.65%, for the first and fourth cycle, respectively. It is seen that a negligible decrease (only 2.58%) in the degradation percentage even after the fourth cycle. Here by, it is conclude that the synthesized nanocomposite has features for the application in the domain of photocatalytic activity to reduce the contaminants.

## 7.12 Conclusions

The chapter demonstrates the use of hydrothermally synthesized GONs in the preparation of rGO-ZnO nanocomposite. The hydrothermal method of GONs synthesis can replace the conventional Hummer's method (where harmful chemicals, like  $\text{KMnO}_4$ ,  $\text{H}_2\text{SO}_4$ ,  $\text{HCl}$  are used). Using the energy of microwaves, the ZnO nanoparticles and rGO-ZnO nanocomposites are synthesized in much shorter time periods (of the order of few min) compared to conventional methods, requiring elaborated time periods and hence reducing thermal budgets. The presence of the rGO in the rGO-ZnO is qualitatively as well as quantitatively analyzed by using XPS, SEM, Raman spectroscopy and synchrotron XRD. SEM micrographs show the growth of the ZnO nanorods with diameters, in the range of 30 to 90 nm and an increased order in the longitudinal direction-length (200 to 400 nm). TEM micrographs revealed that the rGO is attached to the ZnO nanorods to form a sandwich structure. SAED pattern shows the intense discrete diffraction spots confirming that the ZnO nanorods are well-crystallized. Photocatalytic activity of the rGO-ZnO nanocomposite is compared with the bare ZnO using MO dye as the probe. The degradation performance of the prepared photocatalyst is found to be superior compared to the rGO-ZnO nanocomposite synthesized using different Zn-precursor ( $\text{ZnCl}_2$ ) and the rGO-ZnO nanocomposite (where GO synthesized from Hummer's method is used). These synthesized nanocomposites have features for the applications in the domain of the photocatalytic activity to reduce the contaminants.



# CHAPTER 8

*Page intentionally left blank*

## CHAPTER 8

### SUMMARY AND CONCLUSIONS

In the present work, the tailoring of the nature, morphology and dimensions of the nanomaterials by hydrothermal method was carried out. Several parameters were carried out to optimize nature of the synthesized nanomaterials. The synthesized nanomaterials were characterized by using XRD, FESEM, FTIR, TEM, XPS, DSC, TGA, BET, RAMAN, LCR, UV-visible and synchrotron-XRD to study the nature, microstructure, morphology and salient features of the nanomaterials.

In the case of parallel plate capacitor applications, the Nylon-6/TiO<sub>2</sub> polymer nanocomposite films were fabricated by using the hydrothermally synthesized TiO<sub>2</sub>-nanorods (with 5, 10 and 20 weight percents) with the help of spin-coating technique. The coating parameters were optimized prior to the coating of the functional films. The fabricated N6/TiO<sub>2</sub> PNCs were subjected to the impedance spectrometer in the parallel plate capacitor architecture. The study revealed that the dielectric constant of the Nylon-6 polymer matrix was enhanced with the reinforcement of the twenty weight percent of the TiO<sub>2</sub> nanorods. The dielectric loss and AC conductivity was found to be high for the NT20 sample due to the presence of increased content of the TiO<sub>2</sub> nanorods. The TiO<sub>2</sub> content had resulted in the increased conductive path for the charge movements in the material.

The direct growth of the TiO<sub>2</sub> film on FTO-coated glass slides with unique morphology was achieved by the hydrothermal technique. It was observed that the morphology of the direct grown TiO<sub>2</sub> can be tuned by varying the heating temperature of the autoclave. It was also observed that the increase in hydrothermal heating temperature had resulted in the high surface area for TiO<sub>2</sub> film. The surface area of the TiO<sub>2</sub> film grown at 180 °C was found to be superior and possess higher dielectric constant. Also, the dielectric loss and AC conductivity was observed to be high due to the increased conductive path

In the case of triboelectric nanogenerator device applications, the hydrothermally synthesized La<sub>2</sub>O<sub>3</sub> and ZnO nanomaterials were utilized. The first of its kind approach of fabrication of the La<sub>2</sub>O<sub>3</sub>-based TENG devices was examined

using the Teflon as the counter surface. The Teflon is proven to be highly negative triboelectric material. The screen printed  $\text{La}_2\text{O}_3$  film on the copper foils was considered as the tribo positive material. The  $\text{La}_2\text{O}_3$ -based TENG device was fabricated which operated on the vertical contact separation mode mechanism. The  $\text{La}_2\text{O}_3$ -based TENG device is first of its kind due to the less/no literature available on the TENG using  $\text{La}_2\text{O}_3$  material. It was found that the power generated by the  $\text{La}_2\text{O}_3$ -based TENG device was competitive enough to generate the energy required for the self-powered devices.

Similar to the above results, ZnO-based TENG device was fabricated following the same procedure. The Teflon was used as the counter tribonegative material with the conductive copper foil as electrodes. The fabricated device was tested for the power density output which was found to be enough to generate the energy required to drive the self-powered devices. The ZnO-based TENG device was also examined for the durability testing for more than one lakh cycles of operations. It was found that there was a negligible decay in the voltage generated by the TENG after one lakh cycles of operations. This concludes that the fabricated TENG device can be utilized in the case of self-powered vibration sensors and self-powered biomedical devices, where frequent replacement of the power source could be avoided.

In the case of photocatalytic applications, there were many reports on the graphene-ZnO nanocomposites based photocatalyst materials. It was found that the GO synthesized by modified Hummers' method was frequently used. The hydrothermal synthesis of GO can replace the GO synthesized by Hummers' method. The hydrothermally synthesized GO only used water and sugar as target chemicals. In this way, it was observed that utilization of harmful oxidizing and reducing agents can be avoided in the preparation of GO. The photocatalytic performance of the hydrothermally synthesized rGO-ZnO nanocomposite was explored successfully by degrading methyl orange dye. The degradation performance of the rGO-ZnO nanocomposite, where GO synthesized by Hummers' method, was also compared with the rGO-ZnO, where GO synthesized by using hydrothermal method. It was observed that negligible deference in the photocatalytic performance was observed. The effect of usage of the zinc chloride as target chemical for the preparation of the

rGO-ZnO was also compared with the rGO-ZnO performance (where zinc nitrate was the target chemical). The recycling ability of the functional rGO-ZnO nanocomposite materials was also shown to exhibit negligible decrease in the photocatalytic performance after the fourth cycle of operation.

Overall, the hydrothermally synthesized functional nanomaterials proved to be simple, economical, scalable and low-temperature method. The nanomaterials showed uniform characteristics and can be tailored depending on the targeted applications.

### **Scope for Future Studies**

The results and analysis of the present work are focused on the low-temperature single-step synthesis of the functional nanomaterials for energy (dielectrics and triboelectric) and photocatalytic applications. The hydrothermal technique enables the nanomaterials to be grown with desired morphology and dimensions by altering the synthesis parameters. The titanium oxide material has proven to be used as high-dielectric constant material, which can be used in commercial supercapacitors. There is a need of future scope to fabricate the commercial parallel-plate capacitors and supercapacitors using titanium oxide as dielectric medium. Lanthanum oxide and zinc oxide materials have shown predominant triboelectric properties. These materials have the ability to be used in the commercial self-powered miniaturized devices. Further, the synthesis and the fabrication of graphene based composites with titanium oxide, lanthanum oxide and zinc oxide can improve the performance of the functional devices. The advantages of direct growth of the functional materials on the desired substrates and doping of different elements on the nanomaterials by the hydrothermal technique have the future scope. Further, the hydrothermal method can be extended to develop ternary and quaternary elemental nanocomposites to develop functional devices for energy applications.

*Page intentionally left blank*

## REFERENCES

- Abdal-hay, A., Lim, J., Shamshi Hassan, M., and Lim, J. K. (2013). "Ultrathin conformal coating of apatite nanostructures onto electrospun nylon 6 nanofibers: Mimicking the extracellular matrix." *Chem. Eng. J.*, 228, 708–716.
- Agrawal, H., Awasthi, K., and Saraswat, V. K. (2014). "Non-isothermal crystallization kinetics of TiO<sub>2</sub> nanoparticle-filled poly(ethylene terephthalate) with structural and chemical properties." *Polym. Bull.*, 71(6), 1539–1555.
- Ahmad, M. I., Campen, D. G. Van, Fields, J. D., Yu, J., Pool, V. L., Parilla, P. A., Ginley, D. S., Hest, M. F. A. M. Van, and Toney, M. F. (2015). "Rapid thermal processing chamber for in-situ x-ray diffraction." *Rev. Sci. Instrum.*, 86(1), 13902.
- Ahmed, G., Hanif, M., Khan, A. J., Zhao, L., Zhang, J., and Liu, Z. (2018). "ZnO flowers and graphene oxide hybridization for efficient photocatalytic degradation of o-xylene in water." *Mater. Chem. Phys.*, 212, 479–489.
- Akhavan, O. (2011). "Photocatalytic reduction of graphene oxides hybridized by ZnO nanoparticles in ethanol." *Carbon N. Y.*, 49(1), 11–18.
- Alim, K. A., Fonoberov, V. A., Shamsa, M., and Balandin, A. A. (2005). "Micro-Raman investigation of optical phonons in ZnO nanocrystals." *J. Appl. Phys.*, 97(12), 1–5.
- Allenspach, P., and Gasser, U. (2000). "Rare earth magnetism in high-temperature and borocarbide superconductors." *J. Alloys Compd.*, 311(1), 1–10.
- Alvarado, J. A., Maldonado, A., Juarez, H., and Pacio, M. (2013). "Synthesis of Colloidal ZnO Nanoparticles and Deposit of Thin Films by Spin Coating Technique." *J. Nanomater.*, 2013.
- Amoghavarsha, M., Neil, P. Y., and Patrick, S. G. (2014). "Core-shell nanoparticles and enhanced polarization in polymer based nanocomposite dielectrics." *Nanotechnology*, 25(47), 475706.
- Ashkarran, A., and Mohammadi, B. (2015). "ZnO nanoparticles decorated on graphene sheets through liquid arc discharge approach with enhanced photocatalytic

performance under visible-light.” *Appl. Surf. Sci.*, 342, 112–119.

Ashkenov, N., Mbenkum, B. N., Bundesmann, C., Riede, V., Lorenz, M., Spemann, D., Kaidashev, E. M., Kasic, A., Schubert, M., Grundmann, M., Wagner, G., Neumann, H., Darakchieva, V., Arwin, H., and Monemar, B. (2003). “Infrared dielectric functions and phonon modes of high-quality ZnO films.” *J. Appl. Phys.*, 93(1), 126–133.

Atchudan, R., Edison, T. N. J. I., Perumal, S., Karthikeyan, D., and Lee, Y. R. (2016). “Facile synthesis of zinc oxide nanoparticles decorated graphene oxide composite via simple solvothermal route and their photocatalytic activity on methylene blue degradation.” *J. Photochem. Photobiol. B Biol.*, 162, 500–510.

Atchudan, R., Edison, T. N. J. I., Perumal, S., Shanmugam, M., and Lee, Y. R. (2017). “Direct solvothermal synthesis of zinc oxide nanoparticle decorated graphene oxide nanocomposite for efficient photodegradation of azo-dyes.” *J. Photochem. Photobiol. A Chem.*, 337, 100–111.

Atuchin, V. V., Gavrilova, T. A., Grivel, J.C., and Kesler, V. G. (2008). “Electronic structure of layered titanate  $\text{Nd}_2\text{Ti}_2\text{O}_7$ .” *Surf. Sci.*, 602(19), 3095–3099.

Atuchin, V. V., Grigorieva, T. I., Kalabin, I. E., Kesler, V. G., Pokrovsky, L. D., and Shevtsov, D. I. (2005). “Comparative analysis of electronic structure of  $\text{Ti}:\text{LiNbO}_3$  and  $\text{LiNbO}_3$  surfaces.” *J. Cryst. Growth*, 275(1–2), e1603–e1607.

Atuchin, V. V., Kesler, V. G., Pervukhina, N. V., and Zhang, Z. (2006). “Ti 2p and O 1s core levels and chemical bonding in titanium-bearing oxides.” *J. Electron Spectros. Relat. Phenomena*, 152(1–2), 18–24.

Atuchin, V. V., Lebedev, M. S., Korolkov, I. V., Kruchinin, V. N., Maksimovskii, E. A., and Trubin, S. V. (2018). “Composition-sensitive growth kinetics and dispersive optical properties of thin  $\text{Hf}_x\text{Ti}_{1-x}\text{O}_2$  ( $0 \leq x \leq 1$ ) films prepared by the ALD method.” *J. Mater. Sci. Mater. Electron.*, 1–12.

Atuchin, V. V., Kesler, V. G., Meng, G., and Lin, Z. S. (2012). “The electronic structure of  $\text{RbTiOPO}_4$  and the effects of the A-site cation substitution in  $\text{KTiOPO}_4$  - family crystals.” *J. Phys. Condens. Matter*, 24(40), 405503.



- Avinash B, S. and Lamani, A. R. (2016). "Influence of particle size on band gap and dielectric properties of TiO<sub>2</sub> nanomaterials." *AIP Conf. Proc.*, AIP Publishing LLC, 20347.
- Ayana, D. G., Ceccato, R., Collini, C., Lorenzelli, L., Prusakova, V., and Dirè, S. (2016). "Sol-gel derived oriented multilayer ZnO thin films with memristive response." *Thin Solid Films*, 615, 427–436.
- Baby, T. T., and Ramaprabhu, S. (2010). "Investigation of thermal and electrical conductivity of graphene based nanofluids." *J. Appl. Phys.*, 108(12), 124308.
- Backes, C., Abdelkader, A. M., Alonso, C., Andrieux-Ledier, A., and Arenal, et al. (2020). "Production and processing of graphene and related materials." *2D Mater.*, 7(2).
- Badawy, A. A., and Ibrahim, S. M. (2016). "The influence of La<sub>2</sub>O<sub>3</sub>-doping on structural, surface and catalytic properties of nano-sized cobalt–manganese mixed oxides." *Int. J. Ind. Chem.*, 7(3), 287–296.
- Bai, X., Wang, L., Zong, R., Lv, Y., Sun, Y., and Zhu, Y. (2013). "Performance enhancement of ZnO photocatalyst via synergic effect of surface oxygen defect and graphene hybridization." *Langmuir*, 29(9), 3097–3105.
- Bar-Cohen, Y. (2004). Electroactive polymer (EAP) actuators as artificial muscles : reality, potential, and challenges. *SPIE Press*.
- Barratt, N. M. (1965). "Book Review: Capacitors, Magnetic Circuits and Transformers." *Int. J. Electr. Eng. Educ.*, 3(3), 473–474.
- Béguin, F., Presser, V., Balducci, A., and Frackowiak, E. (2014). "Carbons and Electrolytes for Advanced Supercapacitors." *Adv. Mater.*, 26(14), 2219–2251.
- Bera, S., Pal, M., Naskar, A., and Jana, S. (2016). "Hierarchically structured ZnO-graphene hollow microspheres towards effective reusable adsorbent for organic pollutant via photodegradation process." *J. Alloys Compd.*, 669, 177–186.
- Boukha, Z., Fitian, L., López-Haro, M., Mora, M., Ruiz, J. R., Jiménez-Sanchidrián, C., Blanco, G., Calvino, J. J., Cifredo, G. A., Trasobares, S., and Bernal, S. (2010).

“Influence of the calcination temperature on the nano-structural properties, surface basicity, and catalytic behavior of alumina-supported lanthana samples.” *J. Catal.*, 272(1), 121–130.

Boukrouh, S., Bensaha, R., Bourgeois, S., Finot, E., and Marco de Lucas, M. C. (2008). “Reactive direct current magnetron sputtered TiO<sub>2</sub> thin films with amorphous to crystalline structures.” *Thin Solid Films*, 516(18), 6353–6358.

Brus, V. V., Kyaw, A. K. K., Maryanchuk, P. D., and Zhang, J. (2015). “Quantifying interface states and bulk defects in high-efficiency solution-processed small-molecule solar cells by impedance and capacitance characteristics.” *Prog. Photovoltaics Res. Appl.*, 23(11), 1526–1535.

Bu, I. Y. Y., and Huang, R. (2015a). “One-pot synthesis of ZnO/reduced graphene oxide nanocomposite for supercapacitor applications.” *Mater. Sci. Semicond. Process.*, 31, 131–138.

Bunch, J. S., Zande, A. M. van der, Verbridge, S. S., Frank, I. W., Tanenbaum, D. M., Parpia, J. M., Craighead, H. G., and McEuen, P. L. (2007). “Electromechanical Resonators from Graphene Sheets.” *Science* (80-. ), 315(5811), 490–493.

Cao, V. A., Lee, S., Kim, M., Alam, M. M., Park, P., and Nah, J. (2020). “Output power density enhancement of triboelectric nanogenerators via ferroelectric polymer composite interfacial layers.” *Nano Energy*, 67.

Chamoli, P., Shukla, R. K., Bezbaruah, A. N., Kar, K. K., and Raina, K. K. (2021). “Microwave-assisted rapid synthesis of honeycomb core-ZnO tetrapods nanocomposites for excellent photocatalytic activity against different organic dyes.” *Appl. Surf. Sci.*, 555.

Chebil, W., Boukadhaha, M. A., and Fouzri, A. (2016). “Epitaxial growth of ZnO on quartz substrate by sol-gel spin-coating method.” *Superlattices Microstruct.*, 95, 48–55.

Chen, F., Zhang, L., Wang, X., and Zhang, R. (2017a). “Applied Surface Science Noble-metal-free NiO @ Ni-ZnO / reduced graphene oxide / CdS heterostructure for efficient photocatalytic hydrogen generation.” 422, 962–969.

- Chen, J., and Wang, Z. L. (2017). “Reviving Vibration Energy Harvesting and Self-Powered Sensing by a Triboelectric Nanogenerator.” *Joule*, Cell Press.
- Chen, J., Zhu, G., Yang, W., Jing, Q., Bai, P., Yang, Y., Hou, T. C., and Wang, Z. L. (2013). “Harmonic-resonator-based triboelectric nanogenerator as a sustainable power source and a self-powered active vibration sensor.” *Adv. Mater.*, 25(42), 6094–6099.
- Chen, Q., Liu, Q., Hubert, J., Huang, W., Baert, K., Wallaert, G., Terryn, H., Delplancke-Ogletree, M.P., and Reniers, F. (2017b). “Deposition of photocatalytic anatase titanium dioxide films by atmospheric dielectric barrier discharge.” *Surf. Coatings Technol.*, 310, 173–179.
- Chen, S. N., Huang, M. Z., Lin, Z. H., and Liu, C. P. (2019a). “Enhancing charge transfer for ZnO nanorods based triboelectric nanogenerators through Ga doping.” *Nano Energy*, 65, 104069.
- Chen, X., Luo, L., Zeng, Z., Jiao, J., Shehzad, M., Yuan, G., Luo, H., and Wang, Y. (2020). “Bio-inspired flexible vibration visualization sensor based on piezo-electrochromic effect.” *J. Mater.*, 6(4), 643–650.
- Chen, Y. C., Katsumata, K. I., Chiu, Y. H., Okada, K., Matsushita, N., and Hsu, Y. J. (2015). “ZnO-graphene composites as practical photocatalysts for gaseous acetaldehyde degradation and electrolytic water oxidation.” *Appl. Catal. A Gen.*, 490(November 2014), 1–9.
- Chen, Y., Wang, H., Dang, B., Xiong, Y., Yao, Q., Wang, C., Sun, Q., and Jin, C. (2017c). “Bio-Inspired nacre-like nanolignocellulose-poly (vinyl alcohol)-TiO<sub>2</sub> composite with superior mechanical and photocatalytic properties.” *Sci. Rep.*, 7(1), 1823.
- Cheng, G. E., Zhang, Y., Ke, H. Z., Hao, T. T., and Wang, Y. Z. (2014a). “Hydrothermal synthesis of TiO<sub>2</sub>/reduced graphene oxide nanocomposite with enhanced photocatalytic activity.” *Micro Nano Lett.*, 9(12), 932–934.
- Cheng, G., Zhang, Y., Ke, H., Hao, T., and Wang, Y. (2014b). “Hydrothermal synthesis of TiO<sub>2</sub> / reduced graphene oxide nanocomposite with enhanced photocatalytic activity.” 9, 932–934.

Choi, W. M., Shin, K.S., Lee, H. S., Choi, D., Kim, K., Shin, H.J., Yoon, S.M., Choi, J.Y., and Kim, S.W. (2011). “Selective Growth of ZnO Nanorods on SiO<sub>2</sub> /Si Substrates Using a Graphene Buffer Layer.” *Nano Res*, 4(5), 440–447.

Chowdhury, S., Parshetti, G. K., and Balasubramanian, R. (2015). “Post-combustion CO<sub>2</sub> capture using mesoporous TiO<sub>2</sub>/graphene oxide nanocomposites.” *Chem. Eng. J.*, 263, 374–384.

Chu, D., Masuda, Y., Ohji, T., Kato, K. (2010). “Formation and photocatalytic application of ZnO nanotubes using aqueous solution”. *Langmuir*, 26, 2811–2815.

Chu, L., Qin, Z., Yang, J., and Li, X. (2015). “Anatase TiO<sub>2</sub> Nanoparticles with Exposed {001} Facets for Efficient Dye-Sensitized Solar Cells.” *Sci. Rep.*, 5(1), 12143.

Constantin, D. G., Moura, C., Munteanu, D., and Cunha, L. (2012). “The influence of oxygen flow during deposition on the structural, mechanical and tribological properties of titanium oxide magnetron sputtered thin films.” *J. Optoelectron. Adv. Mater.*, 14(11–12), 964–970.

Cortes, F. J. Q., and Phillips, J. (2015a). “Tube-super dielectric materials: Electrostatic capacitors with energy density greater than 200 J·cm<sup>-3</sup>.” *Materials (Basel)*, 8(9), 6208–6227.

Cortes, F. J. Q., and Phillips, J. (2015b). “Novel Materials with Effective Super Dielectric Constants for Energy Storage.” *J. Electron. Mater.*, 44(5), 1367–1376.

Dang, Z.M., Lin, Y.H., and Nan, C.W. (2003). “Novel Ferroelectric Polymer Composites with High Dielectric Constants.” *Adv. Mater.*, 15(19), 1625–1629.

Dang, Z.M., Yao, S.H., and Xu, H.P. (2007). “Effect of tensile strain on morphology and dielectric property in nanotube/polymer nanocomposites.” *Appl. Phys. Lett.*, 90(1), 12907.

Darr, J. A., Zhang, J., Makwana, N. M., and Weng, X. (2017). “Continuous Hydrothermal Synthesis of Inorganic Nanoparticles: Applications and Future Directions.” *Chem. Rev.*, 117(17), 11125–11238.

Demes, T., Ternon, C., Riassetto, D., Roussel, H., Rapenne, L., Gélard, I., Jimenez, C., Stambouli, V., and Langlet, M. (2016). “New insights in the structural and morphological properties of sol-gel deposited ZnO multilayer films.” *J. Phys. Chem. Solids*, 95, 43–55.

Deng, J., Zhang, L., Au, C. T., and Dai, H. (2009). “Template-free synthesis of high surface area single-crystalline lanthanum hydroxide nanorods via a low-temperature solution route.” *Mater. Lett.*, 63(6–7), 632–634.

Deng, W., Zhang, B., Jin, L., Chen, Y., Chu, W., Zhang, H., Zhu, M., and Yang, W. (2017). “Enhanced performance of ZnO microballoon arrays for a triboelectric nanogenerator.” *Nanotechnology*, 28(13).

Dewi, A. S. P., Mufti, N., Fibriyanti, A. A., Diantoro, M., Taufiq, A., Hidayat, A., Sunaryono, and Nur, H. (2020). “The improvement of Triboelectric effect of ZnO Nanorods/PAN in flexible Nanogenerator by adding TiO<sub>2</sub> nanoparticle.” *J. Polym. Res.*, 27(6).

Dissado, L. A., and Fothergill, J. C. (1992). “Electrical Degradation and Breakdown in Polymers”.

Dong, H., Wang, D., Sun, G., and Hinstroza, J. P. (2008). “Assembly of Metal Nanoparticles on Electrospun Nylon 6 Nanofibers.pdf.” *Chem. Mater.*, 20(3), 6627–6632.

Dou, P., Tan, F., Wang, W., Sarreshteh, A., Qiao, X., Qiu, X., and Chen, J. (2015). “One-step microwave-assisted synthesis of Ag/ZnO/graphene nanocomposites with enhanced photocatalytic activity.” *J. Photochem. Photobiol. A Chem.*, 302(302), 17–22.

Du, G., Wang, X., Zhang, L., Feng, Y., and Li, Y. (2013). “Controllable synthesis of different ZnO architectures decorated reduced graphene oxidenanocomposites.” *Mater. Lett.*, 96, 128–130.

Dudem, B., Kim, D. H., Mule, A. R., and Yu, J. S. (2018). “Enhanced Performance of Microarchitected PTFE-Based Triboelectric Nanogenerator via Simple Thermal Imprinting Lithography for Self-Powered Electronics.” *ACS Appl. Mater. Interfaces*,

10(28), 24181–24192.

Džunuzović, E., Marinović-Cincović, M., Vuković, J., Jeremić, K., and Nedeljković, J. M. (2009). “Thermal properties of PMMA/TiO<sub>2</sub> nanocomposites prepared by in-situ bulk polymerization.” *Polym. Compos.*, 30(6), 737–742.

Ernest Ravindran, R. S., Thomas, P., and Renganathan, S. (2017). “Studies on the structural, thermal, and dielectric properties of fabricated Nylon 6,9/CaCu<sub>3</sub>Ti<sub>4</sub>O<sub>12</sub> nanocomposites.” *Sci. Eng. Compos. Mater.*, 24(2), 185–194.

Esfahani, H., Prabhakaran, M. P., Salahi, E., Tayebifard, A., Keyanpour-Rad, M., Rahimpour, M. R., and Ramakrishna, S. (2015). “Protein adsorption on electrospun zinc doped hydroxyapatite containing Nylon 6 membrane: Kinetics and isotherm.” *J. Colloid Interface Sci.*, 443, 143–152.

Fan, F. R., Tian, Z. Q., and Lin Wang, Z. (2012). “Flexible triboelectric generator.” *Nano Energy*, 1(2), 328–334.

Fan, J., Li, Z., Zhou, W., Miao, Y., Zhang, Y., Hu, J., and Shao, G. (2014). “Dye-sensitized solar cells based on TiO<sub>2</sub> nanoparticles/nanobelts double-layered film with improved photovoltaic performance.” *Appl. Surf. Sci.*, 319, 75–82.

Fan, W., Zhang, L., and Liu, T. (2017). “Graphene-Carbon Nanotube Hybrids for Energy and Environmental Applications.” *Graphene-Carbon Nanotub. Hybrids Energy Environ. Appl.*, 21–50.

Fan, X., Chen, J., Yang, J., Bai, P., Li, Z., and Wang, Z. L. (2015). “Ultrathin, rollable, paper-based triboelectric nanogenerator for acoustic energy harvesting and self-powered sound recording.” *ACS Nano*, 9(4), 4236–4243.

Fang, B., Zhang, W., Wang, G., Liu, H., and Wei, S. (2008a). “Microwave-assisted preparation of a carbon nanotube/La(OH)<sub>3</sub> nanocomposite, and its application to electrochemical determination of adenine and guanine.” *Microchim. Acta*, 162(1–2), 175–180.

Fang, J., Wang, F., Qian, K., Bao, H., Jiang, Z., and Huang, W. (2008b). “Bifunctional N-Doped Mesoporous TiO<sub>2</sub> Photocatalysts.” *J. Phys. Chem. C*, 112(46),

18150–18156.

Fang, L., Zhang, B., Li, W., Zhang, J., Huang, K., and Zhang, Q. (2014). “Fabrication of highly dispersed ZnO nanoparticles embedded in graphene nanosheets for high performance supercapacitors.” *Electrochim. Acta*, 148, 164–169.

Feng, Y., Feng, N., Wei, Y., and Zhang, G. (2014). “An in situ gelatin-assisted hydrothermal synthesis of ZnO–reduced graphene oxide composites with enhanced photocatalytic performance under ultraviolet and visible light.” *RSC Adv.*, 4(16), 7933.

Gould, R. J. (2020). “Classical Electrodynamics.” *Electromagn. Process.*, 37–74.

Grabowski, C. A., Fillery, S. P., Koerner, H., Tchoul, M., Drummy, L., Beier, C. W., Brutchey, R. L., Durstock, M. F., and Vaia, R. A. (2016). “Dielectric performance of high permittivity nanocomposites: impact of polystyrene grafting on BaTiO<sub>3</sub> and TiO<sub>2</sub>.” *Nanocomposites*, 2(3), 117–124.

Gritsenko, D. V., Shaïmeev, S. S., Atuchin, V. V., Grigor’eva, T. I., Pokrovskii, L. D., Pchelyakov, O. P., Gritsenko, V. A., Aseev, A. L., and Lifshits, V. G. (2006). “Two-band conduction in TiO<sub>2</sub>.” *Phys. Solid State*, 48(2), 224–228.

Guo, W., Liu, T., Sun, R., Chen, Y., Zeng, W., and Wang, Z. (2013). “Hollow, porous, and yttrium functionalized ZnO nanospheres with enhanced gas-sensing performances.” *Sensors Actuators, B Chem.*, 178, 53–62.

Gupta, A. K., Hsu, C.H., Lai, S.N., and Lai, C.S. (2020). “ZnO-Polystyrene Composite as Efficient Energy Harvest for Self-Powered Triboelectric Nanogenerator.” *ECS J. Solid State Sci. Technol.*, 9(11), 115019.

Haarindraprasad, R., Hashim, U., Gopinath, S. C. B., Perumal, V., Liu, W.W., and Balakrishnan, S. R. (2016). “Fabrication of interdigitated high-performance zinc oxide nanowire modified electrodes for glucose sensing.” *Anal. Chim. Acta*, 925, 70–81.

Hashim, N., Muda, Z., Hussein, M. Z., Isa, I. M., Mohamed, A., Kamari, A., Bakar, S. A., Mamat, M., and Jaafar, A. (2016). “A brief review on recent graphene oxide-

based material nanocomposites: Synthesis and applications.” *Environ. Sci*, 7(9), 3225–3243.

He, F., Lau, S., Chan, H. L., and Fan, J. (2009). “High Dielectric Permittivity and Low Percolation Threshold in Nanocomposites Based on Poly(vinylidene fluoride) and Exfoliated Graphite Nanoplates.” *Adv. Mater.*, 21(6), 710–715.

Héctor, A. B., Jie, M., Zunfeng, L., Randall, M. Stoltenberg Zhenan, B., and Yongsheng, C. (2008). “Evaluation of Solution-Processed Reduced Graphene Oxide Films as as Transparent Conductors.” *ACS Nano*, 2(3), 463–470.

Hosseini, S. A., and Babaei, S. (2017). “Graphene oxide/zinc oxide (GO/ZnO) nanocomposite as a superior photocatalyst for degradation of methylene blue (MB)-process modeling by response surface methodology (RSM).” *J. Braz. Chem. Soc.*, 28(2), 299–307.

Hu, C., Liu, H., Dong, W., Zhang, Y., Bao, G., Lao, C., and Wang, Z. L. (2007). “La(OH)<sub>3</sub> and La<sub>2</sub>O<sub>3</sub> nanobelts-synthesis and physical properties.” *Adv. Mater.*, 19(3), 470–474.

Hu, Y., Yang, J., Jing, Q., Niu, S., Wu, W., and Wang, Z. L. (2013). “Triboelectric nanogenerator built on suspended 3d spiral structure as vibration and positioning sensor and wave energy harvester.” *ACS Nano*, 7(11), 10424–10432.

Hu, Z., Zhao, L., Guo, H., Wang, S., Li, W., Yang, X., Dong, B., and Wan, L. (2018). “Novel double-layered photoanodes based on porous-hollow TiO<sub>2</sub> microspheres and La(OH)<sub>3</sub>:Yb<sup>3+</sup>/Er<sup>3+</sup> for highly efficient dye-sensitized solar cells.” *J. Mater. Sci. Mater. Electron.*, 1–9.

Huang, C., Zhang, Q. M., and Su, J. (2003). “High-dielectric-constant all-polymer percolative composites.” *Appl. Phys. Lett.*, 82(20), 3502–3504.

Huang, X., Jiang, P., and Xie, L. (2009). “Ferroelectric polymer/silver nanocomposites with high dielectric constant and high thermal conductivity.” *Appl. Phys. Lett.*, 95(24), 242901.

Hussien, B. (2011). The D.C and A.C Electrical Properties of (PMMA-Al<sub>2</sub>O<sub>3</sub>)



Composites. *Eur. J. Sci. Res.*

Izaki, M., and Omi, T. (1998). "Transparent zinc oxide films prepared by electrochemical reaction." *Appl. Phys. Lett.*, 68(17), 2439.

Jackson, J. D. (2013). "Classical electrodynamics. Solutions." *J. Chem. Inf. Model.*, 53(9), 1689–1699.

Jafari Nejad, S., Abolghasemi, H., Moosavian, M. A., Golzary, A., and Maragheh, M. G. (2010). "Fractional factorial design for the optimization of hydrothermal synthesis of lanthanum oxide nanoparticles under supercritical water condition." *J. Supercrit. Fluids*, 52(3), 292–297.

Jayachandiran, J., Yesuraj, J., Arivanandhan, M., Raja, A., Suthanthiraraj, S. A., Jayavel, R., and Nedumaran, D. (2018). "Synthesis and Electrochemical Studies of rGO/ZnO Nanocomposite for Supercapacitor Application." *J. Inorg. Organomet. Polym. Mater.*, 28(5), 2046–2055.

Jayalakshmi, M., Palaniappa, M., and Balasubramanian, K. (2008). "Single Step Solution Combustion Synthesis of ZnO/carbon Composite and its Electrochemical Characterization for Supercapacitor Application." *Int. J. Electrochem. Sci.*, 3, 96–103.

Jianwen, X., Bhattacharya, S., Pramanik, P., and Wong, C. P. (2006). "High dielectric constant polymer-ceramic (epoxy varnish-barium titanate) nanocomposites at moderate filler loadings for embedded capacitors." *J. Electron. Mater.*, 2009–2015.

Jin, F., Tong, H., Shen, L., Wang, K., and Chu, P. K. (2006). "Micro-structural and dielectric properties of porous TiO<sub>2</sub> films synthesized on titanium alloys by micro-arc discharge oxidization." *Mater. Chem. Phys.*, 100(1), 31–33.

Jin, J., Qi, R., Su, Y., Tong, M., and Zhu, J. (2013). "Preparation of high-refractive-index PMMA/TiO<sub>2</sub> nanocomposites by one-step in situ solvothermal method." *Iran. Polym. J.*, 22(10), 767–774.

Kajbafvala, A., Shayegh, M. R., Mazloumi, M., Zanganeh, S., Lak, A., Mohajerani, M. S., and Sadrezaad, S. K. (2009). "Nanostructure sword-like ZnO wires: Rapid synthesis and characterization through a microwave-assisted route." *J. Alloys Compd.*,

469(1–2), 293–297.

Kalabin, I. E., Grigorieva, T. I., Pokrovsky, L. D., Sheglov, D. V., Shevtsov, D. I., and Atuchin, V. V. (2003). “Nanofaceting of LiNbO<sub>3</sub> X-cut surface by high temperature annealing and titanium diffusion.” *Opt. Commun.*, 221(4–6), 359–363.

Kalygina, V. M., Egorova, I. S., Prudaev, I. A., Tolbanov, O. P., and Atuchin, V. V. (2016). “Photoelectrical characteristics of TiO<sub>2</sub> -N-SI heterostructures.” *Microw. Opt. Technol. Lett.*, 58(5), 1113–1116.

Kalygina, V. M., Egorova, I. S., Prudaev, I. A., Tolbanov, O. P., and Atuchin, V. V. (2017). “Conduction mechanism of metal-TiO<sub>2</sub>-Si structures.” *Chinese J. Phys.*, 55(1), 59–63.

Kang, J., G., Kim, Y., I., Cho, D. W., Sohn, Y., (2015). “Synthesis and physicochemical properties of La(OH)<sub>3</sub> and La<sub>2</sub>O<sub>3</sub> nanostructures”. *Mater. Sci. Semicond. Process.*, 40, 737-743.

Kango, S., Kalia, S., Celli, A., Njuguna, J., Habibi, Y., and Kumar, R. (2013). “Surface modification of inorganic nanoparticles for development of organic–inorganic nanocomposites—A review.” *Prog. Polym. Sci.*, 38(8), 1232–1261.

Kaur, M., and Verma, N. K. (2014). “CaCO<sub>3</sub>/TiO<sub>2</sub> Nanoparticles Based Dye Sensitized Solar Cell.” *J. Mater. Sci. Technol.*, 30(4), 328–334.

Kavitha, T., Iyengar, A., Lee, K., and Park, S. (2012). “Glucose sensing , photocatalytic and antibacterial properties of graphene – ZnO nanoparticle hybrids.” *Carbon N. Y.*, 50(8), 2994–3000.

Ke, Q., and Wang, J. (2016). “Graphene-based materials for supercapacitor electrodes – A review.” *J. Materiomics*.

Kellar, J. A., Alaboson, J. M. P., Wang, Q. H., and Hersam, M. C. (2010). “Identifying and characterizing epitaxial graphene domains on partially graphitized SiC(0001) surfaces using scanning probe microscopy.” *Appl. Phys. Lett.*, 96(14), 143103.

Khosrow-Pour, F., Aghazadeh, M., Dalvand, S., and Sabour, B. (2013). “Large scale

and uniform La(OH)<sub>3</sub> nanorods prepared by template-free pulsed electrodeposition method.” *Mater. Lett.*, 104, 61–63.

Kilbride, B. E., Coleman, J. N., Fraysse, J., Fournet, P., Cadek, M., Drury, A., Hutzler, S., Roth, S., and Blau, W. J. (2002). “Experimental observation of scaling laws for alternating current and direct current conductivity in polymer-carbon nanotube composite thin films.” *J. Appl. Phys.*, 92(7), 4024–4030.

Kim, D. S., and Kwak, S. Y. (2007). “The hydrothermal synthesis of mesoporous TiO<sub>2</sub> with high crystallinity, thermal stability, large surface area, and enhanced photocatalytic activity.” *Appl. Catal. A Gen.*, 323, 110–118.

Kim, D. W., Lee, J. H., Kim, J. K., and Jeong, U. (2020). “Material aspects of triboelectric energy generation and sensors.” *NPG Asia Mater*, 12 (6).

Kolodziejczak-Radzimska, A., and Jesionowski, T. (2014). “Zinc oxide-from synthesis to application: A review.” *Materials (Basel)*, 7(4), 2833–2881.

Koltzenburg, S., Maskos, M., and Nuyken, O. (2017). “Polymer chemistry”. *Springer Nat.*, Switzerland.

Kruchinin, V. N., Perevalov, T. V., Atuchin, V. V., Gritsenko, V. A., Komonov, A. I., Korolkov, I. V., Pokrovsky, L. D., Shih, C. W., and Chin, A. (2017). “Optical Properties of TiO<sub>2</sub> Films Deposited by Reactive Electron Beam Sputtering.” *J. Electron. Mater.*, 46(10), 6089–6095.

Konstantin S. N., AK, G., SV, M., Jiang, D., Zhang, Y., SV, D., IV, G., and AA, F. (2004). “Electric Field Effect in Atomically Thin Carbon Films.” *Science* 80, 306 (5696), 666–669.

Kumar, A., Singh, B. P., Choudhary, R. N. P., and Thakur, A. K. (2006). “Characterization of electrical properties of Pb-modified BaSnO<sub>3</sub> using impedance spectroscopy.” *Mater. Chem. Phys.*, 99(1), 150–159.

Kumar, K. S., Pittala, S., Sanyadanam, S., and Paik, P. (2015a). “A new single/few-layered graphene oxide with a high dielectric constant of 10<sup>6</sup>: Contribution of defects and functional groups.” *RSC Adv.*, 5(19), 14768–14779.

Kumar, N., Mittal, H., Reddy, L., Nair, P., Ngila, J. C., and Parashar, V. (2015b). “Morphogenesis of ZnO nanostructures: role of acetate ( $\text{COOH}^-$ ) and nitrate ( $\text{NO}_3^-$ ) ligand donors from zinc salt precursors in synthesis and morphology dependent photocatalytic properties.” *RSC Adv.*, 5(48), 38801–38809.

Kumar, S. G., and Rao, K. S. R. K. (2015). “Zinc oxide based photocatalysis: tailoring surface-bulk structure and related interfacial charge carrier dynamics for better environmental applications.” *RSC Adv.*, 5(5), 3306–3351.

Kumar, S. G., and Rao, K. S. R. K. (2017). “Comparison of modification strategies towards enhanced charge carrier separation and photocatalytic degradation activity of metal oxide semiconductors ( $\text{TiO}_2$ ,  $\text{WO}_3$  and ZnO).” *Appl. Surf. Sci.*, 391, 124–148.

Kumar, V., Kumari, S., Kumar, P., Kar, M., and Kumar, L. (2015c). “Structural analysis by rietveld method and its correlation with optical properties of nanocrystalline zinc oxide.” *Adv. Mater. Lett.*, 6(2), 139–147.

Larson, A. C., and Dreele, R. B. Von. (2004). “GENERAL STRUCTURE ANALYSIS SYSTEM”. 86-748.

Lee, W. J., and Sung, Y. M. (2012). “Synthesis of anatase nanosheets with exposed (001) facets via chemical vapor deposition.” *Cryst. Growth Des.*, 12(11), 5792–5795.

Lewin, M., and Pearce, E. M. (1998). Handbook of Fiber Chemistry. (L. Menachem, ed.), *CRC Press, Taylor & Francis*.

Li, B., and Cao, H. (2011). “ZnO@graphene composite with enhanced performance for the removal of dye from water.” *J. Mater. Chem.*, 21(10), 3346–3349.

Li, H., Wei, Y., Zhang, Y., Zhang, C., Wang, G., Zhao, Y., Yin, F., and Bakenov, Z. (2016a). “In situ sol-gel synthesis of ultrafine ZnO nanocrystals anchored on graphene as anode material for lithium-ion batteries.” *Ceram. Int.*, 42(10), 12371–12377.

Li, J. P. H., Zhou, X., Pang, Y., Zhu, L., Vovk, E. I., Cong, L., Bavel, A. P. Van, Li, S., and Yang, Y. (2019). “Understanding of binding energy calibration in XPS of lanthanum oxide by: In situ treatment.” *Phys. Chem. Chem. Phys.*, 21(40), 22351–22358.

- Li, X., Wang, Z., Qiu, Y., Pan, Q., and Hu, P. (2015). "3D graphene/ZnO nanorods composite networks as supercapacitor electrodes." *J. Alloys Compd.*, 620, 31–37.
- Li, X., Yu, J., Wageh, S., Al-Ghamdi, A. A., and Xie, J. (2016b). "Graphene in Photocatalysis: A Review." *Small*, 12(48), 6640–6696.
- Li, Z., Zhou, Z., Yun, G., Shi, K., Lv, X., and Yang, B. (2013). "High-performance solid-state supercapacitors based on graphene-ZnO hybrid nanocomposites." *Nanoscale Res. Lett.*, 8(1), 473.
- Liang, Q., Yan, X., Gu, Y., Zhang, K., Liang, M., Lu, S., Zheng, X., and Zhang, Y. (2015a). "Highly transparent triboelectric nanogenerator for harvesting water-related energy reinforced by antireflection coating." *Sci. Rep.*, 5.
- Liang, Q., Zhanga, Z., Yan, X., Gu, Y., Zhao, Y., Zhang, G., Lu, S., Liao, Q., and Zhang, Y. (2015b). "Functional triboelectric generator as self-powered vibration sensor with contact mode and non-contact mode." *Nano Energy*, 14, 209–216.
- Liao, L., and Duan, X. (2010). "Graphene-dielectric integration for graphene transistors." *Mater. Sci. Eng. R Reports*, 70(3–6), 354–370.
- Lin, K.-F., Cheng, H.-M., Hsu, H.C., and Hsieh, W.F. (2006). "Band gap engineering and spatial confinement of optical phonon in ZnO quantum dots." *Appl. Phys. Lett.*, 88(26), 263117.
- Liu, A., Zhu, H., Sun, H., Xu, Y., and Noh, Y.Y. (2018). "Solution Processed Metal Oxide High- $\kappa$  Dielectrics for Emerging Transistors and Circuits." *Adv. Mater.*, 30(33), 1706364.
- Liu, J., Bai, H., Wang, Y., Liu, Z., Zhang, X., and Sun, D. D. (2010). "Self-assembling TiO<sub>2</sub> nanorods on large graphene oxide sheets at a two-phase interface and their anti-recombination in photocatalytic applications." *Adv. Funct. Mater.*, 20(23), 4175–4181.
- Liu, J., Wang, G., Lu, L., Guo, Y., and Yang, L. (2017). "Facile shape-controlled synthesis of lanthanum oxide with different hierarchical micro/nanostructures for antibacterial activity based on phosphate removal." *RSC Adv.*, 7(65), 40965–40972.

- Liu, Q., Liu, Z., Zhang, X., Zhang, N., Yang, L., Yin, S., and Chen, Y. (2008). "Organic photovoltaic cells based on an acceptor of soluble graphene." *Appl. Phys. Lett.*, 92(22), 223303.
- Liu, S., Liu, C., Wang, W., Cheng, B., and Yu, J. (2012a). "Unique photocatalytic oxidation reactivity and selectivity of TiO<sub>2</sub>-graphene nanocomposites." *Nanoscale*, 4(10), 3193.
- Liu, S., Wang, Z., Zhang, Y., Dong, Z., and Zhang, T. (2015). "Preparation of zinc oxide nanoparticle-reduced graphene oxide-gold nanoparticle hybrids for detection of NO<sub>2</sub>." *RSC Adv.*, 5(111), 91760-91765.
- Liu, W. M., Li, J., and Zhang, H. Y. (2020). "Reduced graphene oxide modified zinc oxide composites synergistic photocatalytic activity under visible light irradiation." *Optik (Stuttg.)*, 207.
- Liu, X., Pan, L., Zhao, Q., Lv, T., Zhu, G., Chen, T., Lu, T., Sun, Z., and Sun, C. (2012b). "UV-assisted photocatalytic synthesis of ZnO-reduced graphene oxide composites with enhanced photocatalytic activity in reduction of Cr(VI)." *Chem. Eng. J.*, 183, 238-243.
- Liu, Y.-Z., Li, Y.-F., Yang, Y.-G., Wen, Y.-F., and Wang, M.-Z. (2013). "A one-pot method for producing ZnO-graphene nanocomposites from graphene oxide for supercapacitors." *Scr. Mater.*, 68(5), 301-304.
- Low, J., Cheng, B., and Yu, J. (2017). "Surface modification and enhanced photocatalytic CO<sub>2</sub> reduction performance of TiO<sub>2</sub>: a review." *Appl. Surf. Sci.*, 392, 658-686.
- Low, J., Yu, J., and Ho, W. (2015). "Graphene-Based Photocatalysts for CO<sub>2</sub> Reduction to Solar Fuel." *J. Phys. Chem. Lett.*, 6(21), 4244-4251.
- Lowell, J., and Rose-Innes, a. C. (1980). "Contact electrification." *Adv. Phys.*, 29(6), 947-1023.
- Lu, T., Pan, L., Li, H., Zhu, G., Lv, T., Liu, X., Sun, Z., Chen, T., and Chua, D. H. C. (2011). "Microwave-assisted synthesis of graphene-ZnO nanocomposite for

- electrochemical supercapacitors.” *J. Alloys Compd.*, 509(18), 5488–5492.
- Lv, K., Zuo, H., Sun, J., Deng, K., Liu, S., Li, X., and Wang, D. (2009). “(Bi, C and N) codoped TiO<sub>2</sub> nanoparticles.” *J. Hazard. Mater.*, 161(1), 396–401.
- Lv, T., Pan, L., Liu, X., Lu, T., Zhu, G., and Sun, Z. (2011). “Enhanced photocatalytic degradation of methylene blue by ZnO-reduced graphene oxide composite synthesized via microwave-assisted reaction.” *J. Alloys Compd.*, 509(41), 10086–10091.
- Lv, T., Pan, L., Liu, X., and Sun, Z. (2012a). “Enhanced photocatalytic degradation of methylene blue by ZnO-reduced graphene oxide-carbon nanotube composites synthesized via microwave-assisted reaction.” *Catal. Sci. Technol.*, 2, 2297–2301.
- Lv, T., Pan, L., Liu, X., and Sun, Z. (2012b). “Enhanced photocatalytic degradation of methylene blue by ZnO-reduced graphene oxide-carbon nanotube composites synthesized via microwave-assisted reaction.” *Catal. Sci. Technol.*, 2(11), 2297.
- Mahadevegowda, A., Young, N. P., and Grant, P. S. (2014). “Electron microscopy of multi-layered polymer-nanocomposite based dielectrics.” *J. Phys. Conf. Ser.*, 522 (1).
- Mahadevegowda, A., Young, N. P., and Grant, P. S. (2015). “Engineering the nanostructure of a polymer-nanocomposite film containing Ti-based core-shell particles to enhance dielectric response †.” *Nanoscale*, 7, 15727.
- Maira, A. J., Coronado, J. M., Augugliaro, V., Yeung, K. L., Conesa, J. C., and Soria, J. (2001). “Fourier transform infrared study of the performance of nanostructured TiO<sub>2</sub> particles for the photocatalytic oxidation of gaseous toluene.” *J. Catal.*, 202(2), 413–420.
- Maliakal, a., Katz, H., Cotts, P. M., Subramoney, S., and Mirau, P. (2005). “Inorganic oxide core, polymer shell nanocomposites as a high gate dielectric for flexible electronics application.” *J. Am. Chem. Soc.*, 127(19), 14655–14662.
- Marinel, S., Choi, D. H., Heuguet, R., Agrawal, D., and Lanagan, M. (2013). “Broadband dielectric characterization of TiO<sub>2</sub> ceramics sintered through microwave and conventional processes.” *Ceram. Int.*, 39(1), 299–306.

Marlinda, A. R., Huang, N. M., Muhamad, M. R., An'Amt, M. N., Chang, B. Y. S., Yusoff, N., Harrison, I., Lim, H. N., Chia, C. H., and Kumar, S. V. (2012). "Highly efficient preparation of ZnO nanorods decorated reduced graphene oxide nanocomposites." *Mater. Lett.*, 80, 9–12.

Maruthupandy, M., Qin, P., Muneeswaran, T., Rajivgandhi, G., Quero, F., and Song, J. M. (2020). "Graphene-zinc oxide nanocomposites (G-ZnO NCs): Synthesis, characterization and their photocatalytic degradation of dye molecules." *Mater. Sci. Eng. B Solid-State Mater. Adv. Technol.*, 254.

Mathew, A. A., Chandrasekhar, A., and Vivekanandan, S. (2021). "A review on real-time implantable and wearable health monitoring sensors based on triboelectric nanogenerator approach." *Nano Energy*.

Matsch, L. W. (1964). *Capacitors, Magnetic Circuits, and Transformers*. Prentice-Hall, Univ. Michigan.

Mazarji, M., Nabi-Bidhendi, G., and Mahmoodi, N. M. (2017). "One-pot synthesis of a reduced graphene oxide–ZnO nanorod composite and dye decolorization modeling." *J. Taiwan Inst. Chem. Eng.*, 80, 439–451.

McCusker, L. B., Dreele, R. B. Von, Cox, D. E., Louër, D., and Scardi, P. (1999). "Rietveld refinement guidelines." *J. Appl. Crystallogr.*, 32(1), 36–50.

Meti, S., K, U. B., Rahman, M. R., and Jayalakshmi, M. (2015). "Photocatalytic Behaviour of Nanocomposites of Sputtered Titanium Oxide Film on Graphene Oxide Nanosheets." *Am. J. Mater. Sci.*, 5(3C), 12–18.

Meti, S., Rahman, M. R., Ahmad, M. I., and Bhat, K. U. (2018). "Chemical free synthesis of graphene oxide in the preparation of reduced graphene oxide-zinc oxide nanocomposite with improved photocatalytic properties." *Appl. Surf. Sci.*, 451, 67–75.

Mi, H. Y., Jing, X., Meador, M. A. B., Guo, H., Turng, L. S., and Gong, S. (2018a). "Triboelectric Nanogenerators Made of Porous Polyamide Nanofiber Mats and Polyimide Aerogel Film: Output Optimization and Performance in Circuits." *ACS Appl. Mater. Interfaces*, 10(36), 30596–30606.



- Mi, H. Y., Jing, X., Zheng, Q., Fang, L., Huang, H. X., Turng, L. S., and Gong, S. (2018b). "High-performance flexible triboelectric nanogenerator based on porous aerogels and electrospun nanofibers for energy harvesting and sensitive self-powered sensing." *Nano Energy*, 48, 327–336.
- Mohamed, M. M., Ghanem, M. A., Khairy, M., Naguib, E., and Alotaibi, N. H. (2019). "Zinc oxide incorporated carbon nanotubes or graphene oxide nanohybrids for enhanced sonophotocatalytic degradation of methylene blue dye." *Appl. Surf. Sci.*, 487, 539–549.
- Mohan, R., Krishnamoorthy, K., and Kim, S. J. (2012). "Enhanced photocatalytic activity of Cu-doped ZnO nanorods." *Solid State Commun.*, 152(5), 375–380.
- Mohanty, N., and Berry, V. (2008). "Graphene-Based Single-Bacterium Resolution Biodevice and DNA Transistor: Interfacing Graphene Derivatives with Nanoscale and Microscale Biocomponents." *Nano Lett.*, 8(12), 4469–4476.
- Möhmel, S., Kurzawski, I., Uecker, D., Müller, D., and Ge, W. (2002). "The influence of a hydrothermal treatment using microwave heating on the crystallinity of layered double hydroxides." *Cryst. Res. Technol.*, 37(4), 359–369.
- Motta, F. V., Lima, R. C., Marques, A. P. A., Li, M. S., Leite, E. R., Varela, J. A., and Longo, E. (2010). "Indium hydroxide nanocubes and microcubes obtained by microwave-assisted hydrothermal method." *J. Alloys Compd.*, Elsevier.
- Moussa, H., Girot, E., Mozet, K., Alem, H., Medjahdi, G., and Schneider, R. (2016). "ZnO rods/reduced graphene oxide composites prepared via a solvothermal reaction for efficient sunlight-driven photocatalysis." *Appl. Catal. B Environ.*, 185, 11–21.
- Mukherjee, S. K., Nebatti, A., Mohtascham, F., Schipporeit, S., Notthoff, C., and Mergel, D. (2014). "Influence of thickness on the structural properties of radio-frequency and direct-current magnetron sputtered TiO<sub>2</sub> anatase thin films." *Thin Solid Films*, 558, 443–448.
- Murphy, C. J., Sau, T. K., Gole, A. M., Orendorff, C. J., Gao, J., Gou, L., Hunyadi, S. E., and Li, T. (2005). "Anisotropic metal nanoparticles: Synthesis, assembly, and optical applications." *J. Phys. Chem. B*, 109(29), 13857–13870.

- Murugan, A. V., and Viswanath, A. K. (2006). "Eu<sup>3+</sup> doped lanthanum oxide nanowhiskers: microwave hydrothermal synthesis, characterization and photoluminescence properties." *J. Phys. D. Appl. Phys.*, 39, 3974–3977.
- Nan, C.-W. (2001a). "Comment on 'Effective dielectric function of a random medium.'" *Phys. Rev. B*, 63(17), 176201.
- Nan, C. W. (2001b). "Comment on 'Effective dielectric function of a random medium.'" *Phys. Rev. B - Condens. Matter Mater. Phys.*, 63(17), 5–7.
- Narasimulu, A. A., Zhao, P., Soin, N., Prashanthi, K., Ding, P., Chen, J., Dong, S., Chen, L., Zhou, E., Montemagno, C. D., and Luo, J. (2017). "Significant triboelectric enhancement using interfacial piezoelectric ZnO nanosheet layer." *Nano Energy*, 40, 471–480.
- Naumenko, D., Snitka, V., Snopok, B., Arpiainen, S., and Lipsanen, H. (2012). "Graphene-enhanced Raman imaging of TiO<sub>2</sub> nanoparticles". *Nanotechnology*, 23, 465703.
- Neher, B., Rahman Bhuiyan, M. M., Gafur, M. A., Kabir, H., Hoque, M. A., Bashar, M. S., Ahmed, F., and Hossain, M. A. (2015). "Study of the electric properties of palm fiber-reinforced acrylonitrile butadiene styrene composites." *J. Reinf. Plast. Compos.*, 34(15), 1253–1260.
- Nenavathu, B. P., Kandula, S., and Verma, S. (2018). "Visible-light-driven photocatalytic degradation of safranin-T dye using functionalized graphene oxide nanosheet (FGS)/ZnO nanocomposites." *RSC Adv.*, 8(35), 19659–19667.
- Ngaosuwan, K., Chaiyariyakul, W., Inthong, O., Kiatkittipong, W., Wongsawaeng, D., and Assabumrungrat, S. (2021). "La<sub>2</sub>O<sub>3</sub>/CaO catalyst derived from eggshells: Effects of preparation method and La content on textural properties and catalytic activity for transesterification." *Catal. Commun.*, 149, 106247.
- Niewa, R., Shlyk, L., and Blaschkowski, B. (2011). "Rare-earth metal transition metal borocarbide and nitridoborate superconductors." *Zeitschrift fur Krist.*, 226(4), 352–384.

- Nikitenko, S. I., Chave, T., Cau, C., Brau, H. P., and Flaud, V. (2015). “Photothermal Hydrogen Production Using Noble-Metal-Free Ti@TiO<sub>2</sub> Core-Shell Nanoparticles under Visible-NIR Light Irradiation.” *ACS Catal.*, 5(8), 4790–4795.
- Niu, S., Wang, S., Lin, L., Liu, Y., Zhou, Y. S., Hu, Y., and Wang, Z. L. (2013). “Theoretical study of contact-mode triboelectric nanogenerators as an effective power source.” *Energy Environ. Sci.*, 6(12), 3576.
- Nowicki, W., Piskula, Z. S., Kuźma, P., and Kirszensztejn, P. (2017). “Synthesis and characterization of a binary system La<sub>2</sub>O<sub>3</sub>–SiO<sub>2</sub> prepared by combustion method.” *J. Sol-Gel Sci. Technol.*, 82(2), 574–580.
- O’Neill, A., Bakirtzis, D., and Dixon, D. (2014). “Polyamide 6/Graphene composites: The effect of in situ polymerisation on the structure and properties of graphene oxide and reduced graphene oxide.” *Eur. Polym. J.*, 59, 353–362.
- Orlov, A., Ulianova, V., Zazerin, A., Bogdan, O., Pashkevich, G., and Yakymenko, Y. (2016). “Active elements on a basis of ZnO nanorods for energy harvesting devices.” *Radioelectron. Commun. Syst.*, 59(2), 60–65.
- Pace, G., Ansaldo, A., Serri, M., Lauciello, S., and Bonaccorso, F. (2020). “Electrode selection rules for enhancing the performance of triboelectric nanogenerators and the role of few-layers graphene.” *Nano Energy*, 76.
- Pai, K. R. N., Anjusree, G. S., Deepak, T. G., Subash, D., Nair, S. V., and Nair, A. S. (2014). “High surface area TiO<sub>2</sub> nanoparticles by a freeze-drying approach for dye-sensitized solar cells.” *RSC Adv.*, 4(69), 36821–36827.
- Pant, H. R., Bajgai, M. P., Nam, K. T., Seo, Y. A., Pandeya, D. R., Hong, S. T., and Kim, H. Y. (2011). “Electrospun nylon-6 spider-net like nanofiber mat containing TiO<sub>2</sub> nanoparticles: A multifunctional nanocomposite textile material.” *J. Hazard. Mater.*, 185(1), 124–130.
- Pant, H. R., Kim, H. J., Bhatt, L. R., Joshi, M. K., Kim, E. K., Kim, J. I., Abdal-Hay, A., Hui, K. S., and Kim, C. S. (2013a). “Chitin butyrate coated electrospun nylon-6 fibers for biomedical applications.” *Appl. Surf. Sci.*, 285(PARTB), 538–544.

Pant, H. R., Pant, B., Park, C. H., Kim, H. J., Lee, D. S., Tijing, L. D., Hwang, B. S., Kim, H. Y., and Kim, C. S. (2013b). "RGO/Nylon-6 composite mat with unique structural features and electrical properties obtained from electrospinning and hydrothermal process." *Fibers Polym.*, 14(6), 970–975.

Para, T. A., Reshi, H. A., Pillai, S., and Shelke, V. (2016). "Grain size disposed structural, optical and polarization tuning in ZnO." *Appl. Phys. A*, 122(8), 730.

Paraffin, T., Shell, C., Balasubramanian, B., Kraemer, K. L., Reding, N. A., Skomski, R., Ducharme, S., and Sellmyer, D. J. (2010). "Synthesis of Monodisperse Properties." *ACS Nano*, 4(4), 1893–1900.

Park, S. K., Park, J. H., Ko, K. Y., Yoon, S., Chu, K. S., Kim, W., and Do, Y. R. (2009). "Hydrothermal - Electrochemical Synthesis of ZnO Nanorods." *Cryst. Growth Des.*, 9(8), 3615–3620.

Pecharromás, C., and Moya, J. S. (2000). "Experimental Evidence of a Giant Capacitance in Insulator-Conductor Composites at the Percolation Threshold." *Adv. Mater.*, 12(4), 294–297.

Peulon, S., and Lincot, D. (1996). "Cathodic electrodeposition from aqueous solution of dense or open-structured zinc oxide films." *Adv. Mater.*, 8(2), 166–170.

Pourshaban, E., Abdizadeh, H., and Golobostanfard, M. R. (2016). "A close correlation between nucleation sites, growth and final properties of ZnO nanorod arrays: Sol-gel assisted chemical bath deposition process." *Ceram. Int.*, 42(13), 14721–14729.

Prabhu, S., Pudukudy, M., Sohila, S., Harish, S., Navaneethan, M., Navaneethan, D., Ramesh, R., and Hayakawa, Y. (2018). "Synthesis, structural and optical properties of ZnO spindle/reduced graphene oxide composites with enhanced photocatalytic activity under visible light irradiation." *Opt. Mater. (Amst.)*, 79, 186–195.

Prasad, B. V., Rao, G. N., Chen, J. W., and Suresh Babu, D. (2011). "Abnormal high dielectric constant in SmFeO<sub>3</sub> semiconductor ceramics." *Mater. Res. Bull.*, 46, 1670–1673.

- Prasad, K., and K. Jha, A. (2009). “ZnO Nanoparticles: Synthesis and Adsorption Study.” *Nat. Sci.*, 1(2), 129–135.
- Pratap, A., Joshi, N. J., Rakshit, P. B., Grewal, G. S., and Shrinet, V. (2013). “dielectric behavior of nano barium titanate filled polymeric composites.” *Int. J. Mod. Phys. Conf. Ser.*, 22, 1–10.
- Pruna, A., Cembrero, J., Pullini, D., Mocioiu, A. M., and Busquets-Mataix, D. (2017a). “Effect of reduced graphene oxide on photocatalytic properties of electrodeposited ZnO.” *Appl. Phys. A Mater. Sci. Process.*, 123(12).
- Pruna, A., Shao, Q., Kamruzzaman, M., Li, Y. Y., Zapien, J. A., Pullini, D., Busquets Mataix, D., and Ruotolo, A. (2017b). “Effect of ZnO core electrodeposition conditions on electrochemical and photocatalytic properties of polypyrrole-graphene oxide shelled nanoarrays.” *Appl. Surf. Sci.*, 392, 801–809.
- Pu, X., Zhang, D., Gao, Y., Shao, X., Ding, G., Li, S., and Zhao, S. (2013). “One-pot microwave-assisted combustion synthesis of graphene oxide–TiO<sub>2</sub> hybrids for photodegradation of methyl orange.” *J. Alloys Compd.*, 551, 382–388.
- Qi, K., Cheng, B., Yu, J., and Ho, W. (2017). “Review on the improvement of the photocatalytic and antibacterial activities of ZnO.” *J. Alloys Compd.*, 727, 792–820.
- Qi, L., Petersson, L., and Liu, T. (2014). “Review of Recent Activities on Dielectric Films for Capacitor Applications.” *J. Int. Counc. Electr. Eng.*, 4(1), 1–6.
- Qin, J., Zhang, X., Yang, C., Cao, M., Ma, M., and Liu, R. (2017). “ZnO microspheres-reduced graphene oxide nanocomposite for photocatalytic degradation of methylene blue dye.” *Appl. Surf. Sci.*, 392, 196–203.
- Qin, X., Shi, D., Guo, B. et al., (2020). “Anion-regulated synthesis of ZnO 1D necklace-like nanostructures with high photocatalytic activity”. *Nanoscale Res. Lett.*, 15, 206.
- Qurashi, A., Tabet, N., Faiz, M., and Yamzaki, T. (2009). “Ultra-fast microwave synthesis of ZnO nanowires and their dynamic response toward hydrogen gas.” *Nanoscale Res. Lett.*, 4(8), 948–954.

Qureshi, A., Singh, D., Singh, N. L., Ataoglu, S., Gulluoglu, A. N., Tripathi, A., and Avasthi, D. K. (2009). "Effect of irradiation by 140 MeV  $\text{Ag}^{11+}$  ions on the optical and electrical properties of polypropylene/ $\text{TiO}_2$  composite." *Nucl. Instruments Methods Phys. Res. Sect. B Beam Interact. with Mater. Atoms*, 267(20), 3456–3460.

Rabieh, S., Nassimi, K., and Bagheri, M. (2016). "Synthesis of hierarchical ZnO-reduced graphene oxide nanocomposites with enhanced adsorption-photocatalytic performance." *Mater. Lett.*, 162, 28–31.

Rabin, N. N., Ida, S., Karim, M. R., Islam, M. S., Ohtani, R., Nakamura, M., Koinuma, M., Lindoy, L. F., and Hayami, S. (2018). "Super Dielectric Materials of Two-Dimensional  $\text{TiO}_2$  or  $\text{Ca}_2\text{Nb}_3\text{O}_{10}$  Nanosheet Hybrids with Reduced Graphene Oxide." *ACS Omega*, 3(2), 2074–2083.

Rajeswari, V., Jayavel, R., and Clara Dhanemozhi, A. (2017). "Synthesis And Characterization Of Graphene-Zinc Oxide Nanocomposite Electrode Material For Supercapacitor Applications." *Mater. Today Proc.*, 4(2), 645–652.

Ramadoss, A., and Kim, S. J. (2013). "Improved activity of a graphene- $\text{TiO}_2$  hybrid electrode in an electrochemical supercapacitor." *Carbon N. Y.*, 63, 434–445.

Ramana, C. V., Atuchin, V. V., Becker, U., Ewing, R. C., Isaenko, L. I., Khyzhun, O. Y., Merkulov, A. A., Pokrovsky, L. D., And, A. K. S., and Zhurkov, S. A. (2007). "Low-Energy  $\text{Ar}^+$  Ion-Beam-Induced Amorphization and Chemical Modification of Potassium Titanyl Arsenate (001) Crystal Surfaces." *J. Phys. Chem. C*, 111(6), 2702–2708.

Ramaswamy, S. H., Shimizu, J., Chen, W., Kondo, R., and Choi, J. (2019). "Investigation of diamond-like carbon films as a promising dielectric material for triboelectric nanogenerator." *Nano Energy*, 60, 875–885.

Ranjith, K. S., Manivel, P., Rajendrakumar, R. T., and Uyar, T. (2017). "Multifunctional ZnO nanorod-reduced graphene oxide hybrids nanocomposites for effective water remediation: Effective sunlight driven degradation of organic dyes and rapid heavy metal adsorption." *Chem. Eng. J.*, 325, 588–600.

Rui, X., Tan, H., and Yan, Q. (2014). "Nanostructured metal sulfides for energy

storage.” *Nanoscale*, 6(17), 9889.

Run Liu, Alexey A. Vertegel, Eric W. Bohannon, Thomas A. Sorenson, and, and Switzer, J. A. (2001). “Epitaxial Electrodeposition of Zinc Oxide Nanopillars on Single-Crystal Gold.”

Rusu, G., and Rusu, E. (2011). “Nylon 6/TiO<sub>2</sub> Composites by in situ Anionic Ring-Opening Polymerization of  $\epsilon$ -Caprolactam: Synthesis, Characterization, and Properties.” *Int. J. Polym. Anal. Charact.*, 16(8), 561–583.

Saadatnia, Z., Mosanenzadeh, S. G., Esmailzadeh, E., and Naguib, H. E. (2019a). “A High Performance Triboelectric Nanogenerator Using Porous Polyimide Aerogel Film.” *Sci. Rep.*, 9(1).

Saadatnia, Z., Mosanenzadeh, S. G., Li, T., Esmailzadeh, E., and Naguib, H. E. (2019b). “Polyurethane aerogel-based triboelectric nanogenerator for high performance energy harvesting and biomechanical sensing.” *Nano Energy*, 65.

Sagadevan, S. (2013). “Synthesis and Electrical Properties of TiO<sub>2</sub> Nanoparticles Using a Wet Chemical Technique.” *Am. J. Nanosci. Nanotechnol.*, 1(1), 27–30.

Sajan, C. P., Wageh, S., Al-Ghamdi, A. A., Yu, J., and Cao, S. (2016). “TiO<sub>2</sub> nanosheets with exposed {001} facets for photocatalytic applications.” *Nano Res.*, 9(1), 3–27.

Salavati-Niasari, M., Hosseinzadeh, G., and Davar, F. (2011a). “Synthesis of lanthanum hydroxide and lanthanum oxide nanoparticles by sonochemical method.” *J. Alloys Compd.*, 509(10), 4098–4103.

Salavati-Niasari, M., Hosseinzadeh, G., and Davar, F. (2011b). “Synthesis of lanthanum carbonate nanoparticles via sonochemical method for preparation of lanthanum hydroxide and lanthanum oxide nanoparticles.” *J. Alloys Compd.*, 509(1), 134–140.

Saravanakumar, B., Mohan, R., Thiyagarajan, K., and Kim, S. J. (2013). “Fabrication of a ZnO nanogenerator for eco-friendly biomechanical energy harvesting.” *RSC Adv.*, 3(37), 16646–16656.

Seger, B., and Kamat, P. V. (2009). "Electrocatalytically Active Graphene-Platinum Nanocomposites. Role of 2-D Carbon Support in PEM Fuel Cells." *J. Phys. Chem. C*, 113(19), 7990–7995.

Sellappan, R., Sun, J., Galeckas, A., Lindvall, N., Yurgens, A., Kuznetsov, A. Y., and Chakarov, D. (2013a). "Influence of graphene synthesizing techniques on the photocatalytic performance of graphene–TiO<sub>2</sub> nanocomposites." *Phys. Chem. Chem. Phys.*, 15(37), 15528–15537.

Sellappan, R., Sun, J., Galeckas, A., Lindvall, N., Yurgens, A., Kuznetsov, A. Y., and Chakarov, D. (2013b). "Influence of graphene synthesizing techniques on the photocatalytic performance of graphene-TiO<sub>2</sub> nanocomposites." *Phys. Chem. Chem. Phys.*, 15(37), 15528–15537.

Seol, M. L., Lee, S. H., Han, J. W., Kim, D., Cho, G. H., and Choi, Y. K. (2015). "Impact of contact pressure on output voltage of triboelectric nanogenerator based on deformation of interfacial structures." *Nano Energy*, 17, 63–71.

Shahriary, L., and Athawale, A. a. (2014). "Graphene Oxide Synthesized by using Modified Hummers Approach." *Int. J. Renew. Energy Environ. Eng.*, 2(1), 58–63.

Shandilya, M., Rai, R., and Singh, J. (2016). "Review: hydrothermal technology for smart materials." *Adv. Appl. Ceram.*, 115(6), 354–376.

Shen, Y., Lin, Y., Li, M., and Nan, C.-W. (2007). "High Dielectric Performance of Polymer Composite Films Induced by a Percolating Interparticle Barrier Layer." *Adv. Mater*, 19, 1418–1422.

Sheng, J., Zhang, S., Lv, S., and Sun, W. (2007). "Surfactant-assisted synthesis and characterization of lanthanum oxide nanostructures." *J. Mater. Sci.*, 9565–9571.

Shinde, A. V., Pande, S. A., Joshi, S. S., and Acharya, S. A. (2016). "Novel ceramic-polyamide nanocomposites approach to make flexible film of PZT ceramics: Structural and dielectric study." *Ferroelectrics*, 502(1), 187–196.

Siddabattuni, S., and Schuman, T. P. (2014). "Polymer-ceramic nanocomposite dielectrics for advanced energy storage." *ACS Symp. Ser.*, 1161, 165–190.



- Singh, D., Yadav, P., Singh, N., Kant, C., Kumar, M., Sharma, S. D., and Saini, K. K. (2013). "Dielectric properties of Fe-doped TiO<sub>2</sub> nanoparticles synthesised by sol-gel route." *J. Exp. Nanosci.*, 8(2), 171–183.
- Singh, M., Mulla, M. Y., Santacroce, M. V., Magliulo, M., Franco, C. Di, Manoli, K., Altamura, D., Giannini, C., Cioffi, N., Palazzo, G., Scamarcio, G., and Torsi, L. (2016). "Effect of the gate metal work function on water-gated ZnO thin-film transistor performance." *J. Phys. D. Appl. Phys.*, 49(27), 275101.
- Sivasankaran, S., and Kishor Kumar, M. J. (2015). "A novel sonochemical synthesis of nano-size silicon nitride and titanium carbide." *Ceram. Int.*, 41(9), 11301–11305.
- Song, W.-T., Xie, J., Liu, S.-Y., Zheng, Y.-X., Cao, G.-S., Zhu, T.-J., and Zhao, X.-B. (2012). "Graphene Decorated with ZnO Nanocrystals with Improved Electrochemical Properties Prepared by a Facile In Situ Hydrothermal Route." *Int. J. Electrochem. Sci.*, 7, 2164–2174.
- Sovizi, M. R., and Mirzakhani, S. (2020). "A chemiresistor sensor modified with lanthanum oxide nanoparticles as a highly sensitive and selective sensor for dimethylamine at room temperature." *New J. Chem.*, 44(12), 4927–4934.
- Sreeprasad, T. S., and Pradeep, T. (2013). "Noble metal nanoparticles." *Springer Handb. Nanomater.*, 303–388.
- Srinivasan, A., and Bandyopadhyay, S. (2017). *Advances in polymer materials and technology.* CRC Press, Taylor & Francis.
- Stankovich, S., Dikin, D. A., Dommett, G. H. B., Kohlhaas, K. M., Zimney, E. J., Stach, E. A., Piner, R. D., Nguyen, S. T., and Ruoff, R. S. (2006). "Graphene-based composite materials." *Nature*, 442(7100), 282–286.
- Štengl, V., Bakardjieva, S., Grygar, T. M., Bludská, J., and Kormunda, M. (2013a). "TiO<sub>2</sub>-graphene oxide nanocomposite as advanced photocatalytic materials." *Chem. Cent. J.*, 7(1), 1–12.
- Stoller, M. D., Park, S., Zhu, Y., An, J., and Ruoff, R. S. (2008). "Graphene-Based Ultracapacitors." *Nano Lett.*, 8(10), 3498–3502.

Stouwdam, J. W., Hebbink, G. A., Huskens, J., and Veggel, F. C. J. M. Van. (2003). “Lanthanide-Doped Nanoparticles with Excellent Luminescent Properties in Organic Media.” *Chem. Mater.*, 15(24), 4604–4616.

Sun, J., Lindvall, N., Cole, M. T., Wang, T., Booth, T. J., Bggild, P., Teo, K. B. K., Liu, J., and Yurgens, A. (2012). “Controllable chemical vapor deposition of large area uniform nanocrystalline graphene directly on silicon dioxide.” *J. Appl. Phys.*, 111(4).

Sunding, M. F., Hadidi, K., Diplas, S., Løvvik, O. M., Norby, T. E., and Gunnæs, A. E. (2011). “XPS characterisation of in situ treated lanthanum oxide and hydroxide using tailored charge referencing and peak fitting procedures.” *J. Electron Spectros. Relat. Phenomena*, 184(7), 399–409.

Sushma, C., and Girish Kumar, S. (2017). “Advancements in the zinc oxide nanomaterials for efficient photocatalysis.” *Chem. Pap.*, 71(10), 2023–2042.

Swamy, V., Menzies, D., Muddle, B. C., Kuznetsov, A., Dubrovinsky, L. S., Dai, Q., and Dmitriev, V. (2006). “Nonlinear size dependence of anatase TiO<sub>2</sub> lattice parameters.” *Appl. Phys. Lett.*, 88(24), 243103.

Tang, L., Li, X., Ji, R., Teng, K. S., Tai, G., Ye, J., Wei, C., and Lau, S. P. (2012). “Bottom-up synthesis of large-scale graphene oxide nanosheets.” *J. Mater. Chem.*, 22(12), 5676.

Tang, Y., Zheng, Q., Chen, B., Ma, Z., and Gong, S. (2017). “A new class of flexible nanogenerators consisting of porous aerogel films driven by mechanoradicals.” *Nano Energy*, 38, 401–411.

Tao, J., Dong, X., Zhu, H., Tao, H., and He, P. (2012). “Enhanced photocatalytic properties of ultra-long nanofiber synthesized from pure titanium powders.” *Rare Met.*, 31(1), 39–42.

Terzioglu, P., Altin, Y., Kalemtaş, A., and Celik Bedeloglu, A. (2020). “Graphene oxide and zinc oxide decorated chitosan nanocomposite biofilms for packaging applications.” *J. Polym. Eng.*, 40(2), 152–157.

Thomas, P., Ernest Ravindran, R. S., and Varma, K. B. R. (2014). “Structural, thermal

and electrical properties of poly(methyl methacrylate)/CaCu<sub>3</sub>Ti<sub>4</sub>O<sub>12</sub> composite sheets fabricated via melt mixing.” *J. Therm. Anal. Calorim.*, 115(2), 1311–1319.

Tie, W., Bhattacharyya, S. S., Wang, Y., He, W., and Lee, S. H. (2017). “Facile in-situ synthesis of a zinc oxide crystals/few-layered graphene flake composite for enhanced photocatalytic performance.” *J. Photochem. Photobiol. A Chem.*, 348, 89–95.

Tiwari, S. K., Sahoo, S., Wang, N., and Huczko, A. (2020). “Graphene research and their outputs: Status and prospect.” *J. Sci. Adv. Mater. Devices*.

Toby, B. H., and ExpGUI. (2001). “EXPGUI, a graphical user interface for GSAS.” *J. Appl. Cryst.*, 34, 210–213.

Tripathy, A., Sharma, P., and Sahoo, N. (2018). “Synthesis, morphological, electromechanical characterization of (CaMgFe<sub>x</sub>)Fe<sub>1-x</sub>Ti<sub>3</sub>O<sub>12-δ</sub>/PDMS nanocomposite thin films for energy storage application.” *IOP Conf. Ser. Mater. Sci. Eng.*, 323(1), 1–6.

Troitskaia, I. B., Gavrilova, T. A., and Atuchin, V. V. (2012). “Structure and micromorphology of titanium dioxide nanoporous microspheres formed in water solution.” *Phys. Procedia*, 23, 65–68.

Tuan, P. Van, Phuong, T. T., Tan, V. T., Nguyen, S. X., and Khiem, T. N. (2020). “In-situ hydrothermal fabrication and photocatalytic behavior of ZnO/reduced graphene oxide nanocomposites with varying graphene oxide concentrations.” *Mater. Sci. Semicond. Process.*, 115.

Uvarov, V., and Popov, I. (2007). “Metrological characterization of X-ray diffraction methods for determination of crystallite size in nano-scale materials.” *Mater. Charact.*, 58(10), 883–891.

Vasanthan, N., and Salem, D. R. (2001). “FTIR spectroscopic characterization of structural changes in polyamide-6 fibers during annealing and drawing.” *J. Polym. Sci. Part B Polym. Phys.*, 39(5), 536–547.

Vivekchand, S. R. C., Rout, C. S., Subrahmanyam, K. S., Govindaraj, A., and Rao, C.

- N. R. (2008). "Graphene-based electrochemical supercapacitors." *J. Chem. Sci.*, 120(1), 9–13.
- Wang, C. C., Shieu, F. S., and Shih, H. C. (2020). "Enhanced photodegradation by RGO/ZnO core-shell nanostructures." *J. Environ. Chem. Eng.*, 8(1).
- Wang, G., Huang, X., and Jiang, P. (2017). "Mussel-inspired Fluoro-Polydopamine Functionalization of Titanium Dioxide Nanowires for Polymer Nanocomposites with Significantly Enhanced Energy Storage Capability." *Sci. Rep.*, 7(December 2016), 1–12.
- Wang, H. H., and Lin, M. F. (1998). "Synthesis and properties of nylon 6 modified with various aromatic polyamides." *J. Appl. Polym. Sci.*, 68(7), 1031–1043.
- Wang, H., Liang, Y., Mirfakhrai, T., Chen, Z., Casalongue, H. S., and Dai, H. (2011a). "Advanced asymmetrical supercapacitors based on graphene hybrid materials." *Nano Res.*, 4(8), 729–736.
- Wang, H., Shi, M., Zhu, K., Su, Z., Cheng, X., Song, Y., Chen, X., Liao, Z., Zhang, M., and Zhang, H. (2016). "High performance triboelectric nanogenerators with aligned carbon nanotubes." *Nanoscale*, 8(43), 18489–18494.
- Wang, J., Gao, Z., Li, Z., Wang, B., Yan, Y., Liu, Q., Mann, T., Zhang, M., and Jiang, Z. (2011b). "Green synthesis of graphene nanosheets/ZnO composites and electrochemical properties." *J. Solid State Chem.*, 184(6), 1421–1427.
- Wang, J. X., Dong, X. T., Cui, Q. Z., Song, C., Liu, G. X., and Yu, W. S. (2013). "Electrospinning: A versatile method for preparation of La(OH)<sub>3</sub> mesoporous nanotubes and chain-shaped nanofibers." *Optoelectron. Adv. Mater. Rapid Commun.*, 7(7–8), 505–508.
- Wang, S., Xie, Y., Niu, S., Lin, L., and Wang, Z. L. (2014). "Freestanding triboelectric-layer-based nanogenerators for harvesting energy from a moving object or human motion in contact and non-contact modes." *Adv. Mater.*, 26(18), 2818–2824.
- Wang, S., Zhao, Y., Chen, J., Xu, R., Luo, L., and Zhong, S. (2010). "Self-assembled

3D  $\text{La}(\text{OH})_3$  and  $\text{La}_2\text{O}_3$  nanostructures: Fast microwave synthesis and characterization.” *Superlattices Microstruct.*, 47(5), 597–605.

Wang, W. W., and Zhu, Y. J. (2004). “Shape-controlled synthesis of zinc oxide by microwave heating using an imidazolium salt.” *Inorg. Chem. Commun.*, 7(9), 1003–1005.

Wang, X., Wang, M., Song, H., and Ding, B. (2006). “A simple sol-gel technique for preparing lanthanum oxide nanopowders.” *Mater. Lett.*, 60(17–18), 2261–2265.

Wang, Y., Xiao, X., Xue, H., and Pang, H. (2018). “Zinc Oxide Based Composite Materials for Advanced Supercapacitors.” *ChemistrySelect*, 3(2), 550–565.

Wang, Z. L. (2014). “Triboelectric nanogenerators as new energy technology and self-powered sensors - Principles, problems and perspectives.” *Faraday Discuss.*

Wang, Z. L. (2017). “On Maxwell’s displacement current for energy and sensors: the origin of nanogenerators.” *Mater. Today*.

Wang, Z. L., and Song, J. (2006). “Piezoelectric nanogenerators based on zinc oxide nanowire arrays.” *Science (80-. )*, 312(5771), 242–246.

Wen, X., Yang, W., Jing, Q., and Wang, Z. L. (2014). “Harvesting broadband kinetic impact energy from mechanical triggering/vibration and water waves.” *ACS Nano*, 8(7), 7405–7412.

Wen, Z., Shen, Q., and Sun, X. (2017). “Nanogenerators for self-powered gas sensing.” *Nano-Micro Lett.*, 9 (4), 45.

Wojnarowicz, J., Chudoba, T., and Lojkowski, W. (2020). “A review of microwave synthesis of zinc oxide nanomaterials: Reactants, process parameters and morphologies.” *Nanomaterials*, 10 (6).

Wong, M. H., Berenov, A., Qi, X., Kappers, M. J., Barber, Z. H., Illy, B., Lockman, Z., Ryan, M. P., and MacManus-Driscoll, J. L. (2003). “Electrochemical growth of ZnO nano-rods on polycrystalline Zn foil.” *Nanotechnology*, 14(9), 968–973.

Wu, J., Shen, X., Jiang, L., Wang, K., and Chen, K. (2010). “Solvothermal synthesis and characterization of sandwich-like graphene/ZnO nanocomposites.” *Appl. Surf.*

*Sci.*, 256(9), 2826–2830.

Wu, N., She, X., Yang, D., Wu, X., Su, F., and Chen, Y. (2012). “Synthesis of network reduced graphene oxide in polystyrene matrix by a two-step reduction method for superior conductivity of the composite.” *J. Mater. Chem.*, 22(33), 17254.

Wypych, A., Bobowska, I., Tracz, M., Opasinska, A., Kadlubowski, S., Krzywaniakaliszewska, A., Grobelny, J., and Wojciechowski, P. (2014a). “Dielectric Properties and Characterisation of Titanium Dioxide Obtained by Different Chemistry Methods.” *J.Nano.Mat.*, 1–9.

Xiang, L., Zhao, X., Yin, J., and Fan, B. (2012a). “Well-organized 3D urchin-like hierarchical TiO<sub>2</sub> microspheres with high photocatalytic activity.” *J. Mater. Sci.*, 47(3), 1436–1445.

Xiang, Q., Yu, J., and Jaroniec, M. (2012b). “Graphene-based semiconductor photocatalysts.” *Chem. Soc. Rev.*, 41(2), 782–796.

Xiao, X., Huang, Y., and Dong, F. (2014a). “Synthesis and application of one-dimensional La(OH)<sub>3</sub> nanostructures: An overview.” *J. Chem.*, 1-9.

Xiao, Y., Feng, Z., Huang, X., Huang, L., Long, Z., Wang, Q., and Hou, Y. (2014c). “Synthesis of lanthanum oxide nanosheets by a green carbonation process.” *Chinese Sci. Bull.*, 59 (16), 1864-1867.

Xu, J., and Wong, C. P. (2005). “Low-loss percolative dielectric composite.” *Appl. Phys. Lett.*, 87(8), 82907.

Xu, N., Zhang, Q., Yang, H., Xia, Y., and Jiang, Y. (2017). “In-situ preparation of hierarchical flower-like TiO<sub>2</sub>/carbon nanostructures as fillers for polymer composites with enhanced dielectric properties.” *Sci. Rep.*, 7(1), 43970.

Xu, T., Zhang, L., Cheng, H., and Zhu, Y. (2011). “Significantly enhanced photocatalytic performance of ZnO via graphene hybridization and the mechanism study.” *Appl. Catal. B Environ.*, 101(3–4), 382–387.

Yadav, R., Kumar, V., Saxena, V., Singh, P., and Singh, V. K. (2019). “Preparation of controlled lotus like structured ZnO decorated reduced graphene oxide

nanocomposites to obtain enhanced photocatalytic properties.” *Ceram. Int.*, 45(18), 24999–25009.

Yahia, M. Ben, Lemoigno, F., Beuvier, T., Filhol, J. S., Richard-Plouet, M., Brohan, L., and Doublet, M. L. (2009). “Updated references for the structural, electronic, and vibrational properties of TiO<sub>2</sub>(B) bulk using first-principles density functional theory calculations.” *J. Chem. Phys.*, 130(20).

Yang, H. G., Liu, G., Qiao, S. Z., Sun, C. H., Jin, Y. G., Smith, S. C., Zou, J., Cheng, H. M., Qing, G., and Lu, M. (2009). “Solvothermal Synthesis and Photoreactivity of Anatase TiO<sub>2</sub> Nanosheets with Dominant {001} Facets.” *Synthesis (Stuttg.)*, 131(8), 4078–4083.

Yang, J., Chen, J., Liu, Y., Yang, W., Su, Y., and Wang, Z. L. (2014). “Triboelectrification-based organic film nanogenerator for acoustic energy harvesting and self-powered active acoustic sensing.” *ACS Nano*, 8(3), 2649–2657.

Yang, N., Zhai, J., Wang, D., Chen, Y., and Jiang, L. (2010). “Two-Dimensional Graphene Bridges Enhanced Photoinduced Charge Transport in Dye-Sensitized Solar Cells.” *ACS Nano*, 4(2), 887–894.

Yang, T.-I., and Kofinas, P. (2007). “Dielectric properties of polymer nanoparticle composites.” *Polymer (Guildf.)*, 48(3), 791–798.

Yang, W., Chen, J., Zhu, G., Yang, J., Bai, P., Su, Y., Jing, Q., Cao, X., and Wang, Z. L. (2013a). “Harvesting energy from the natural vibration of human walking.” *ACS Nano*, 7(12), 11317–11324.

Yang, Y., Yu, Y., Ma, G., Nan, J., Chen, H., Zhang, Z., and Lin, W. (2019). “High-performance lithium–sulfur batteries fabricated from a three-dimensional porous reduced graphene oxide/La<sub>2</sub>O<sub>3</sub> microboards/sulfur aerogel.” *Ceram. Int.*, 45(7), 9017–9024.

Yang, Y., Zhang, H., Chen, J., Jing, Q., Zhou, Y. S., Wen, X., and Wang, Z. L. (2013b). “Single-electrode-based sliding triboelectric nanogenerator for self-powered displacement vector sensor system.” *ACS Nano*, 7(8), 7342–7351.

Yao, H., Li, F., Lutkenhaus, J., Kotaki, M., and Sue, H. J. (2016). “High-performance photocatalyst based on nanosized ZnO-reduced graphene oxide hybrid for removal of Rhodamine B under visible light irradiation.” *AIMS Mater. Sci.*, 3(4), 1410–1425.

Yi, F., Wang, X., Niu, S., Li, S., Yin, Y., Dai, K., Zhang, G., Lin, L., Wen, Z., Guo, H., Wang, J., Yeh, M. H., Zi, Y., Liao, Q., You, Z., Zhang, Y., and Wang, Z. L. (2016). “A highly shape-adaptive, stretchable design based on conductive liquid for energy harvesting and self-powered biomechanical monitoring.” *Sci. Adv.*, 2(6).

Yu, A., Ramesh, P., Itkis, M. E., Bekyarova, E., and Haddon, R. C. (2007). “Graphite Nanoplatelet - Epoxy Composite Thermal Interface Materials.” *J. Phys. Chem. C*, 111, 7565–7569.

Yu, J., Xu, C., Tian, Z., Lin, Y., and Shi, Z. (2016a). “Facilely synthesized N-doped carbon quantum dots with high fluorescent yield for sensing  $\text{Fe}^{3+}$ .” *New J. Chem.*, 40(3), 2083–2088.

Yu, M., Ma, Y., Liu, J., Li, X., Li, S., and Liu, S. (2016b). “Sub-coherent growth of ZnO nanorod arrays on three-dimensional graphene framework as one-bulk high-performance photocatalyst.” *Appl. Surf. Sci.*, 390, 266–272.

Yu, W., Sisi, L., Haiyan, Y., and Jie, L. (2020). “Progress in the functional modification of graphene/graphene oxide: A review.” *RSC Adv.*

Yu, W., Xu, D., and Peng, T. (2015). “Enhanced photocatalytic activity of g- $\text{C}_3\text{N}_4$  for selective  $\text{CO}_2$  reduction to  $\text{CH}_3\text{OH}$  via facile coupling of ZnO: a direct Z-scheme mechanism.” *J. Mater. Chem. A*, 3(39), 19936–19947.

Zarembowitch, J., Gouteron, J., and Lejus, A. M. (1979). “Raman spectra of lanthanide sesquioxide single crystals with A-type structure.” *Phys. status solidi*, 94(1), 249–256.

Zeng, H. B., Bando, Y., Xu, J., Li, L., Zhai, Y., Fang, X. S., and Golberg, D. (2010). “Heteroepitaxial Growth of ZnO Nanorod Arrays on GaAs (111) Substrates by Electrochemical Deposition.” *Eur. J. Inorg. Chem.*, 4339-4343.

Zhang, B., Zhang, L., Deng, W., Jin, L., Chun, F., Pan, H., Gu, B., Zhang, H., Lv, Z.,



- Yang, W., and Wang, Z. L. (2017a). "Self-Powered Acceleration Sensor Based on Liquid Metal Triboelectric Nanogenerator for Vibration Monitoring." *ACS Nano*, 11(7), 7440–7446.
- Zhang, C., and Wang, Z. L. (2018). "Triboelectric Nanogenerators." *Micro Electro Mechanical Systems. Micro/Nano Technologies. Springer*, Singapore, 1335–1376.
- Zhang, L. S., Wong, K. H., Zhang, D. Q., Hu, C., Yu, J. C., Chan, C. Y., Wong, P. K. (2009). "Zn:In(OH)<sub>y</sub>S<sub>z</sub> solid solution nanoplates: synthesis, characterization, and photocatalytic mechanism". *Envi. Sci. Technol.*, 43, 7883–7888.
- Zhang, N., Tao, C., Fan, X., and Chen, J. (2017b). "Progress in triboelectric nanogenerators as self-powered smart sensors." *J. Mater. Res.*
- Zhang, X., Huang, Y., Wang, Y., Ma, Y., Liu, Z., and Chen, Y. (2009). "Synthesis and characterization of a graphene–C<sub>60</sub> hybrid material." *Carbon N. Y.*, 47(1), 334–337.
- Zhang, Z. bin, Qiu, Y. fang, Dai, Y., Wang, P. feng, Gao, B., Dong, Z. ming, Cao, X. hong, Liu, Y. hai, and Le, Z. gao. (2016). "Synthesis and application of sulfonated graphene oxide for the adsorption of uranium(VI) from aqueous solutions." *J. Radioanal. Nucl. Chem.*, 310(2), 547–557.
- Zhao, X., Koos, A. A., Chu, B. T. T., Johnston, C., Grobert, N., and Grant, P. S. (2009). "Spray deposited fluoropolymer/multi-walled carbon nanotube composite films with high dielectric permittivity at low percolation threshold." *Carbon N. Y.*, 47(3), 561–569.
- Zhao, Y., Chen, G. and Wang, Y. . (2014). "Facile synthesis of graphene/ZnO composite as an anode with enhanced performance for lithium ion batteries." *J. Nanomater.*, 2014.
- Zhao, Y., Liu, L., Cui, T., Tong, G., and Wu, W. (2017). "Enhanced photocatalytic properties of ZnO/reduced graphene oxide sheets (rGO) composites with controllable morphology and composition." *Appl. Surf. Sci.*, 412, 58–68.
- Zhen Wen, Qingqing Shen, and Xuhui Sun. (2017). "Nanogenerators for Self-Powered Gas Sensing." *Nano-Micro Lett.*, 9(4), 45 (19 pp.).

- Zheng, L., Cheng, G., Chen, J., Lin, L., Wang, J., Liu, Y., Li, H., and Wang, Z. L. (2015). "A Hybridized Power Panel to Simultaneously Generate Electricity from Sunlight, Raindrops, and Wind around the Clock." *Adv. Energy Mater.*, 5(21).
- Zhou, M., Zang, D., Zhai, X., Gao, Z., Zhang, W., and Wang, C. (2016). "Preparation of biomorphic porous zinc oxide by wood template method." *Ceram. Int.*, 42(9), 10704–10710.
- Zhou, X., Shi, T., and Zhou, H. (2012). "Hydrothermal preparation of ZnO-reduced graphene oxide hybrid with high performance in photocatalytic degradation." *Appl. Surf. Sci.*, 258(17), 6204–6211.
- Zhou, Y., Deng, W., Xu, J., and Chen, J. (2020). "Engineering Materials at the Nanoscale for Triboelectric Nanogenerators." *Cell Reports Phys. Sci.*, Cell Press.
- Zhu, G., Zhou, Y. S., Bai, P., Meng, X. S., Jing, Q., Chen, J., and Wang, Z. L. (2014). "A shape-adaptive thin-film-based approach for 50% high-efficiency energy generation through micro-grating sliding electrification." *Adv. Mater.*, 26(23), 3788–3796.
- Zhu, J., Zhang, J., Zhou, H., Qin, W., Chai, L. and Hu, Y. (2009). "Microwave-assisted synthesis and characterization of ZnO-nanorod arrays." *Trans. Nonferrous Met. Soc. China (English Ed.)*, 19(6), 1578–1582.
- Zhu, Y. J., and Chen, F. (2014). "Microwave-assisted preparation of inorganic nanostructures in liquid phase." *Chem. Rev.*, 114(12), 6462–6555.
- Zi, Y., Niu, S., Wang, J., Wen, Z., Tang, W., and Wang, Z. L. (2015). "Standards and figure-of-merits for quantifying the performance of triboelectric nanogenerators." *Nat. Commun.*, 6.
- Zimmermann, L. M., Baldissera, P. V, and Bechtold, I. H. (2016). "Stability of ZnO quantum dots tuned by controlled addition of ethylene glycol during their growth." *Mater. Res. Express*, 3(7), 75018.
- Zou, W., Zhu, J., Sun, Y., and Wang, X. (2011). "Depositing ZnO nanoparticles onto graphene in a polyol system." *Mater. Chem. Phys.*, 125(3), 617–620.

## List of Publications

### Journal Papers

1. Sunil Meti, Mohammad R. Rahman, Md. I. Ahmad and Udaya Bhat K. (2018). “Chemical free synthesis of graphene oxide in the preparation of reduced graphene oxide-zinc oxide nanocomposite with improved photocatalytic properties” *Appl. Surf. Sci.*, 451, 67–75.  
[doi.org/10.1016/j.apsusc.2018.04.138](https://doi.org/10.1016/j.apsusc.2018.04.138).
2. Sunil Meti, Sagar P. Hosangadi, Mohammad R. Rahman and Udaya Bhat K. (2019). “A single step unique microstructural growth of porous colossal dielectric constant titanium oxide” *Appl. Phys. A*, 125 (3), 1-10.  
[doi.org/10.1007/s00339-019-2477-0](https://doi.org/10.1007/s00339-019-2477-0).
3. Sunil Meti, Udaya Bhat K., M. Rizwanur Rahman (2020). “Colossal dielectric permittivity of Nylon-6 matrix-based composites with nano-TiO<sub>2</sub> fillers” *Appl. Phys. A*, 126 (4), 1-11.  
[doi.org/10.1007/s00339-020-3445-4](https://doi.org/10.1007/s00339-020-3445-4).
4. Hosangadi Prutvi Sagar, Sunil Meti, Udaya Bhat K., and Dipti Gupta (2021). “Triboelectric effect based self-powered compact vibration sensor for predictive maintenance of industrial machineries” *Measurement Science and Technology, IOP Science*, 32 (9), 095119.  
[doi.org/10.1088/1361-6501/abe6d2](https://doi.org/10.1088/1361-6501/abe6d2).
5. Sunil Meti, Hosangadi Prutvi Sagar, Mohammad Rizwanur Rahman, Udaya Bhat K. (2021). “Assessment of triboelectricity in colossal-surface-area-lanthanum oxide nanocrystals synthesized via low-temperature hydrothermal process” *J. Mater. Sci: Mater Electron*, 32, 20351-20361.  
[doi.org/10.1007/s10854-021-06545-7](https://doi.org/10.1007/s10854-021-06545-7)

## **Book Chapters**

1. Udaya Bhat K., Sunil Meti. (2020). “Chapter 7. Graphene-Based ZnO Nanocomposites for Supercapacitors Applications” in the book edition entitled "Graphene as Energy Storage Material for Supercapacitors" Materials Research Foundations, *Materials Research Forum LLC. USA*, 64, pp. 181-208.  
*doi.org/10.21741/9781644900550.*
2. Udaya Bhat K., Sunil Meti, C. Prabukumar, Suma Bhat. (2019). “Chapter 4. Metal Sulfides for Lithium-ion Batteries” in the book edition entitled “Lithium-ion Batteries Materials and Applications” Materials Research Foundations, *Materials Research Forum LLC. USA*, 80, pp. 91-122.  
*doi.org/10.21741/9781644900918-4.*

## **Conference**

Sunil Meti, Udaya Bhat K. (2019). “A simple one-step hydrothermal synthesis of high surface area lanthanum oxide nanoparticles”. Jan 15-17, *CTFM-2020*, NITK Surathkal, India.

## **BIO DATA**

Name : Sunil  
Father's name : Virupakshappa Meti  
Date of birth : 15<sup>th</sup> December 1990  
Permanent address : V. B. Meti, teacher  
Opp: Khadri house  
Railway station road  
Koppal – 583231  
Karnataka, India.  
Mobile : +91-8050402810  
E-mail : meti.sunil@gmail.com

### **Academic qualification:**

Bachelor of Engineering (B.E.) in Mechanical Engineering from B. V. Bhoomaraddi College of Engineering and Technology Hubli, Karnataka, India.

Master of Technology (M.Tech.) in Nanotechnology, Department of Metallurgical and Materials Engineering, from National Institute of Technology Karnataka (NITK), Surathkal, India.

### **List of Publications**

No. of Journals (peer reviewed) : 5

No. of Book Chapters : 2

No. of Conferences : 1